HIRES MOTIVATED NEUTRINO FLUXES AND A LIMIT ON THE ISOTROPIC FLUX OF COSMOGENIC TAU NEUTRINOS

by

Olga Brusova

A dissertation submitted to the faculty of
The University of Utah
in partial fulfillment of the requirements for the degree of

Doctor of Philosophy

in

Physics

Department of Physics and Astronomy

The University of Utah

December 2009

THE UNIVERSITY OF UTAH GRADUATE SCHOOL

SUPERVISORY COMMITTEE APPROVAL

of a dissertation submitted by

Olga Brusova

This dissertation has been read by each member of the following supervisory committee and by majority vote has been found to be satisfactory.

	Chair: Kai Martens
	Pierre Sokolsky
	Brian Saam
	Paolo Gondolo
	Dave Gard

THE UNIVERSITY OF UTAH GRADUATE SCHOOL

FINAL READING APPROVAL

To the Graduate Council of the University of Utah:

I have read the dissertation of Olga Brusova in its final form and have found that (1) its format, citations, and bibliographic style are consistent and acceptable; (2) its illustrative materials including figures, tables, and charts are in place; and (3) the final manuscript is satisfactory to the Supervisory Committee and is ready for submission to The Graduate School.

Date

Kai Martens
Chair, Supervisory Committee

Approved for the Major Department

David Kieda
Chair/Dean

Approved for the Graduate Council

Charles A. Wight
Dean of The Graduate School

ABSTRACT

The detection of ultra high energy cosmic neutrinos is the long standing goal of many high energy particle experiments. After the prediction of the Greisen-Zatsepin-Kuzmin suppression at the highest energy end of the cosmic ray spectrum due to interactions between cosmic ray protons and photons of the cosmic microwave background radiation and the confirmation of this effect by the HiRes experiment, both secondary neutrino and gamma ray fluxes are inevitable. The simple model of a homogeneous population of cosmic ray accelerators injecting protons following a unique power law was used to estimate secondary neutrino and gamma ray fluxes. This model evolves the sources with redshift and adjusts both the redshift evolution m and the exponent in the injecting power law γ to fit the HiRes data. We present neutrino and gamma ray fluxes derived from proton propagation with the HiRes motivated best fits m=3.31 and γ=2.44. These predicted fluxes are too small to be observed by the current experiments.

This study also describes our search for ultra high energy τ-neutrinos in HiRes data. We use a Monte Carlo simulation to model neutrino induced extensive air showers in the vicinity of the HiRes detectors. The event selection criteria were based on Monte Carlo studies to isolate a subset of neutrino-like events in HiRes data. After data reconstruction and reduction no neutrino candidates were found in the remaining events. The upper limit on the tau neutrino flux over the energy range from 10^{18} to 10^{21} eV based on the detector sensitivity to tau neutrino events is $1,883^{146}_{126}$ E^{-2} eV^{-1} cm^{-2} sr^{-1} sec^{-1} at 90% confidence level.

To my mother, Lubov Brusova, and my husband, Stanislav Kovganko, for their support and encouragement.

CONTENTS

LIST OF FIGURES

LIST OF TABLES

ACKNOWLEDGEMENTS

I would like to thank my advisor Dr. Kai Martens for his support, guidance and encouragement. I also wish to thank Dr. Weiran Deng for modifying ANIS Monte Carlo simulation code so it can be used for a fluorescence detector. This work has been supported by US NSF grants PHY-9100221, PHY-9321949, PHY-9322298, PHY-9904048, PHY-9974537, PHY-0073057, PHY-0098826, PHY-0140688, PHY-0245428, PHY-0305516, PHY-0307098, PHY-0649681, and PHY-0703893, and by the DOE grant FG03-92ER40732. I gratefully acknowledge the contributions from the members of the HiRes collaboration and technical staffs of our home institutions. The cooperation of Colonels E. Fischer, G. Harter and G. Olsen, the US Army, and the Dugway Proving Ground staff is greatly appreciated. Special acknowledgement to Martin Cuma and the staff of the Center for High Performance Computing for proving the computational resources and CPU time.

CHAPTER 1

OVERVIEW OF COSMIC RAYS

1.1 Historic Overview of Cosmic Ray Research

The birth of cosmic ray (CR) research is generally associated with the first attempts to understand the mysterious background radiation of extremely penetrating nature that caused the spontaneous discharge of instruments called electroscopes. After the discovery of natural radioactivity by Henri Becquerel in 1896 [37], the only known kinds of radiation that could potentially discharge electroscopes were alpha, beta and gamma rays. Natural radioactivity, however, could not explain why a charged electroscope kept away from radioactive sources would still discharge.

Further attempts to identify the source of this mysterious radiation were associated with the measurements of its intensity as a function of altitude. In 1910, Thomas Wulf took an electroscope up to the top of the Eiffel Tower and concluded that the ionization was not due to Earth's gamma rays [185]. Ionization rates had not dropped as much as was expected, had all of the radiation causing discharge been due to the Earth's radioactivity.

A big step forward in solving this mystery came in 1912 when Victor Hess conducted a series of his famous balloon flights [100]. Hess took an electroscope to the altitude of 5 km. At low altitudes the discharge rate dropped, but as he reached higher altitudes (>1.5 km) the rate went up again. On the basis of his experiments he concluded that the source of that highly penetrating radiation was extra-terrestrial: "The results of my observation are best explained by the assumption that a radiation of very great penetration power enters our atmosphere from above."

In 1914 Werner Kolhörster confirmed Hess' results by measuring the increase in the ionization rates up to 9 km above ground [123]. Hess received the Nobel Prize in Physics in 1936 for his discovery [3].

Hess' discovery was a big breakthrough, but it did not uncover all the mysteries. The physical nature of the phenomenon was still unknown. In 1926 Robert Millikan proposed

a model where radiation will come in the form of gamma rays as a result of the formation of a new type of nuclei [140]. If atomic nuclei were formed out of electrons and ionized hydrogen (these were the only elementary particles known at that time), then the binding energy would be released as gamma rays of higher penetrating power [140, 68]. Millikan introduced the term "cosmic rays" to point to the extra terrestrial origin of these rays.

The hypothesis that cosmic rays are high energy gamma rays was proven wrong by Jacob Clay in 1927 [63]. He made a series of intensity measurements as a function of geomagnetic latitude and found that intensity increased with the latitude. The excess of events arriving from the west compared to the east could only be explained if there was an overall predominance of positively charged particles. His results were confirmed by Arthur Compton in 1932 [65].

In the early 1930s the quest to uncover the origin of cosmic rays led to another dramatic achievement - the birth of the field of particle physics. It all started in 1929 when Dimitry Skobeltzyn detected a cosmic ray particle by its track in a cloud chamber [170]. Laboratory accelerators were already functioning (the first cyclotron was built in the early 1930s), but it was not until 1948 that they could achieve sufficiently high energies to create new particles. Cloud chambers and cosmic rays were the "tools" for particle physicists in the 1930s and 1940s.

In 1932 Carl Anderson, using an improved cloud chamber, discovered the positron [25]. Patrick Blackett and Giuseppe Occhialini in 1933 [54] confirmed Anderson's discovery using Geiger counters to act as a coincidence trigger for a cloud chamber. Muons were found in 1936 [143] by Seth Neddermeyer and Carl Anderson, but originally were thought to be pions (a particle postulated by Hideki Yukawa in 1935 [191]). It was only after emulsion chambers were developed that the real pions were found [149]. In the next few years Kaons, Lambdas and Hyperons were discovered. In the 1950s accelerator physics took a lead in producing new breakthroughs in particles physics, since it was now possible to use well-controlled and well-understood primary beams in the laboratory.

Probably the most important discovery in the history of modern cosmic ray research was made in 1936, when Pierre Auger and his collaborators found evidence for the existence of cosmic ray showers [31]. Auger and his colleagues conducted the pioneering studies of coincidence rates of separated Geiger-Muller counters. They observed coincidences well above the accidental rate for counters separated as much as 300 m and recorded on average 1.5 showers per hour. Their conclusions were that the showers must

contain at least 10^6 particles, that the particles hitting the ground are secondary particles produced by a primary particle interaction at the top of the atmosphere, and that the primary particle must have an energy of at least 10^{15} eV.

It was originally thought that the primary particles were electrons, positrons and gamma rays, that would produce secondary particles according to the electromagnetic cascade theory. Giuseppe Cocconi [64] and Jean Daudin [70] proved this assumption wrong by conducting an experiment in the Alps and measuring a significant muon component and a small number of nucleons in the flux of the secondary particles. The lateral distribution of the muons was much wider than that of the electrons. This was inconsistent with electromagnetic cascade theory. Kaplon et al. [118] suggested protons or nuclei to be the most likely candidates for the role of primary cosmic rays.

Advances in the technology and the low flux of primary cosmic rays, especially at the highest energies, made the construction of the air shower arrays very promising. One of the earliest arrays was built by Bruno Rossi and his team [62, 161] at MIT. They used three liquid scintillators and were trying to determine the size and direction of the showers by changing the configuration of the detectors. They demonstrated that it was possible to obtain the arrival direction from the timing information and calculate the shower size by measuring the density of particles as a function of distance from the shower core. Knowing the shower size it is possible to estimate the energy of the primary cosmic ray. Rossi and his co-workers were able to detect particles with energies ranging from 10^{15} to 10^{18} eV. They also discovered a power law dependence of the number of the particle on their energies with a power index of -2.17 [161].

A cosmic ray detector at Volcano Ranch, New Mexico was specially designed and built by John Linsley [136] in 1959 to study the particle flux above 10^{17} eV. The array was made of 19 scintillator detectors, arranged in two hexagonal grids, and covered an area of 2 m^2 (later expanded to an area of 8 m^2). In February 1962 the Volcano Ranch array claimed detecting a cosmic ray particle with a primary energy of 10^{20} eV [134]. It was not all just about the enormous energy of the particle, most important was the fact that nothing in our galaxy was thought to be able to accelerate charged particles to such energies [134]. But the full importance of that discovery was not realized until after 1965, the year when the cosmic microwave background (CMB) radiation was discovered. It took Kenneth Griesen [92] and independently Georgi Zatsepin and Vadem Kuzmin [192] only a year to realize that the CMB would cause substantial energy losses for the highest

energy protons. That suggested that a 10^{20} eV event had to come from within a distance of about a hundred mega parsecs (Mpc) rather than cosmic distances.

1967 was the year when Kenneth Greisen at Cornell University made the first attempt to exploit a new idea to observe extensive air showers (EAS) by air fluorescence [58]. The Cornell team realized that the particles from the EAS would produce enough light by exciting nitrogen molecules of the atmosphere to allow the detection of the propagation of those particles. They built the first fully operating fluorescence detector, which employed 500 photo-multiplier tubes, each observing 0.01 steradian of the sky. Unfortunately, during its couple of years of operation, the Cornell Detector was not very successful. There were two reasons for that: collecting light lenses were too small and too much aerosol was in the New York state atmosphere.

Even though the Cornell Experiment did not provide the cosmic ray society with any existing discoveries, the fluorescence technique found a second life in the Fly's Eye experiment. Motivated by their success of observing the fluorescence of EAS in coincidence with the ground array at Volcano Ranch [43], the group at the University of Utah built an improved Air Fluorescence detector on the U. S. Army's Dugway Proving Ground in Western Utah. In 1986 the original Fly's Eye site was joined by a second detector, located 3.4 km away. That design gave the Fly's Eye observatory capability to view events in stereo mode [60]. The experiment ran from 1981 till 1993, and observed the most energetic particle in the history of cosmic ray research. It happened on the 15^{th} of October, 1991. The particle's energy is estimated to be 3.2×10^{20} eV [51].

The next generation of fluorescence detector was also built on Dugway. It was a new and improved design of the Fly's Eye. The High Resolution Fly's Eye began operating as a prototype in conjunction with the Michigan Muon Array (MIA) and was functioning from 1993 till 1996 [12].

In 1996 the High Resolution Fly's Eye or HiRes became fully operational. In 1999 it was joined by a second site for stereo observation. In April 2006 the HiRes observatory stopped taking data after 10 years of operation.

Nowadays the main focus of cosmic ray research is in the highest energy part of the spectrum. Many more ultra hight energy particles were discovered, but we are still asking the same question that Hess and others devoted their lives to find the answer to. Where do these particles come from? HiRes and detectors before HiRes did not have sufficient statistics to give any convincing answer. New gigantic hybrid cosmic ray observatories

such as Telescope Array (TA) and Pierre Auger Observatory are now the tools to move cosmic rays research forward in the attempt to reveal the mysterious nature of these messengers from the universe.

1.2 The Current Status of Cosmic Ray Research

Cosmic rays are highly energetic particles of extraterrestrial origin. The energy of a single particle can reach more than 10^{20} eV ($\sim$ 50 joules), which is equivalent to the energy of a baseball ($\sim$140 g) flying at the speed of 100 km/h ($\sim$ 60 mph). Even modern particle accelerators are far from being able to accelerate particles to such enormous energies, leaving cosmic rays as the only source of ultra high energy (UHE - energy above 10^{18} eV) particles.

Despite the fact that cosmic ray research is more than a hundred years old, no one can claim to fully understand the nature of this phenomenon. Scientists are stilled puzzled by the following questions: What are cosmic rays? Where in the universe do they come from? What physical mechanism is responsible for creating particles with such energies? What happens to the cosmic rays on their way from their creation to Earth?

Due to their extremely small flux especially at the highest energies, the direct observation of cosmic rays is virtually impossible, and all the current knowledge about these particles is gathered from indirect observations through extensive air showers (EASs). Different techniques exist and have been applied successfully to extract information about the energy spectrum, the chemical composition and the anisotropy in the arrival direction of cosmic rays from the properties of EASs. This information helps us to test various astrophysical models of origin, acceleration and propagation of cosmic rays.

1.2.1 The Energy Spectrum

The term "spectrum of cosmic rays" refers to the distribution of the cosmic ray flux over energy. The cosmic ray flux, F, in units of SI is the number of cosmic ray particles, N, which arrives from space within a solid angle Ω of one steradian and within a time interval T of one second and hits an area A of one square meters.

$$F = \frac{N}{TA\Omega} \tag{1.1}$$

For the last half century cosmic rays are being successfully detected and analyzed by a number of cosmic ray observatories. Each experiment has come up with its own

cosmic ray spectrum (Volcano Ranch [136], Fly's Eye [50], Akeno Giant Air Shower Array (AGASA) [29], the HiRes-Mia Prototype [13], HiRes Mono [4]). The general recipe for finding the spectrum is given by the equation below:

$$J(E) = \frac{\frac{dN(E)}{dE}}{A\Omega(E)T} \tag{1.2}$$

where $\frac{dN(E)}{dE}$ is the raw energy distribution and the denominator is the energy dependent exposure of the detector (aperture, $A\Omega(E)$, multiplied by the operation time, T). A is the effective area of the detector, and $\Omega(E)$ is angular acceptance at a particular energy.

Figure 1.1 shows cosmic ray spectra as measured by different experiments [166, 141, 142, 50, 17, 93, 129]. A distinct feature of the spectrum is its great extent. The flux of primary cosmic rays starts at one particle per square meter per second at MeV energies and covers more than 10 orders of magnitude to become less than one particle per square kilometer per century at the highest energies. Below 10^{10} eV, the flux of cosmic ray particles observed on Earth is usually not plotted since it varies significantly during the 11-year solar cycle [81]. Above this energy the cosmic ray spectrum is very consistent and is well described by a power law:

$$J(E) = \frac{dN}{dE} \sim E^{-\gamma} \tag{1.3}$$

where γ is the power law spectrum index, which stays within the boundaries of 2.7 and 3.1 over the whole energy region.

Since the spectrum is steeply falling, not all of its features, such as the change in the slope index, may be clearly visible. To make the spectrum features more evident it is custom to plot the differential flux multiplied by E^{γ}. After multiplying the spectrum with $E^{2.75}$ it should become a flat line if 2.75 is the power law index of the spectrum. This line stays horizontal if the value of gamma stays to be 2.75. Changing γ to the value greater than 2.75 leads to a negative slope, on the other hand if γ becomes less than 2.75 it creates a positive slope. Figure 1.2 shows the spectrum of Figure 1.1 multiplied by $E^{2.75}$.

In Figure 1.2 two more features become evident. There is a break of the spectrum and its subsequent steepening near the energy of $3 \cdot 10^{15}$ eV. This breaking point is known as the knee. The second change in the spectral index happens around $3 \cdot 10^{18}$ eV, where the slope recovers and becomes flatter again. This feature is called the ankle.

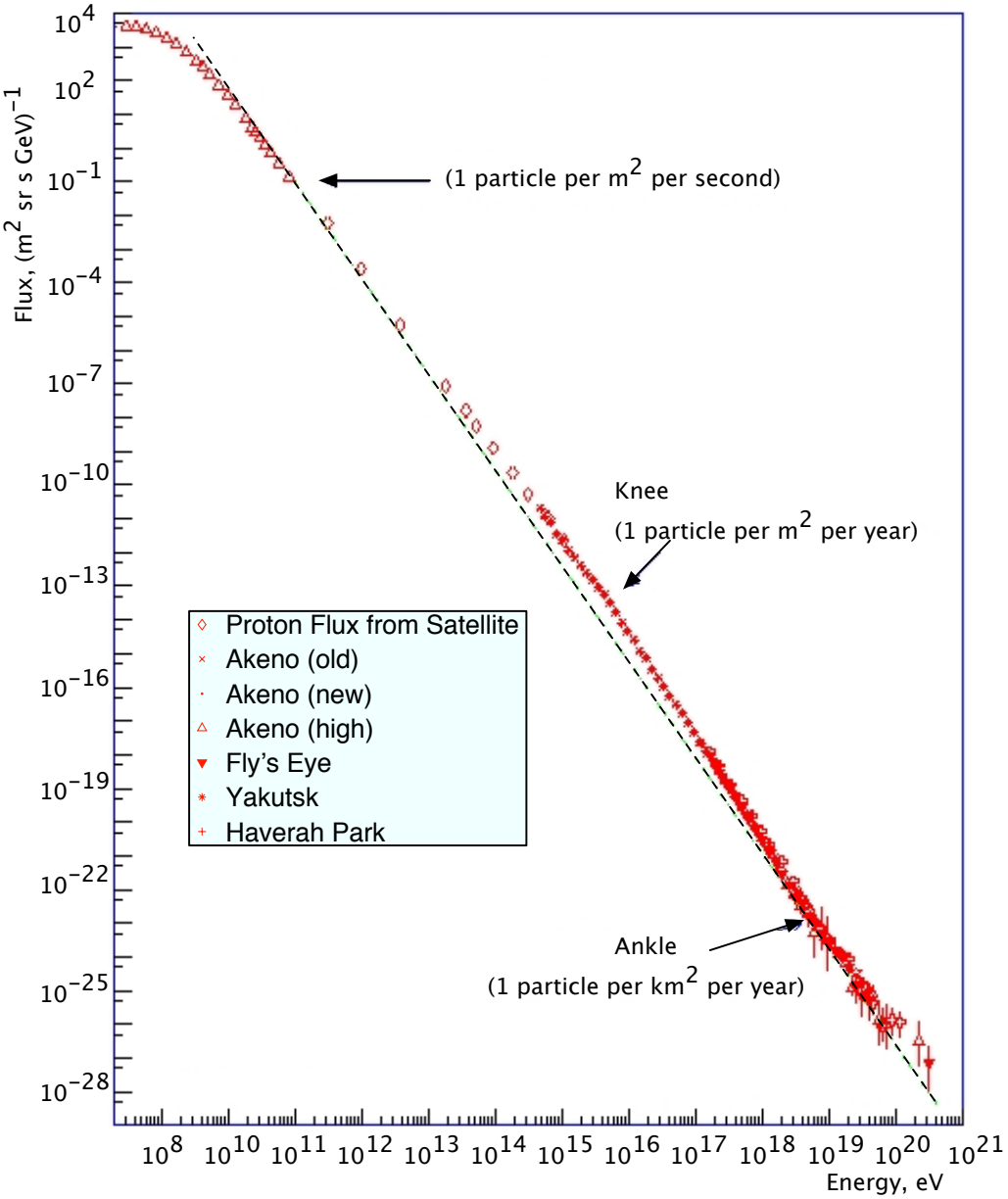

Figure 1.1. Cosmic ray energy spectrum. The dashed line corresponds to the constant power law relationship with the spectral index of 2.7. Adapted from [69].

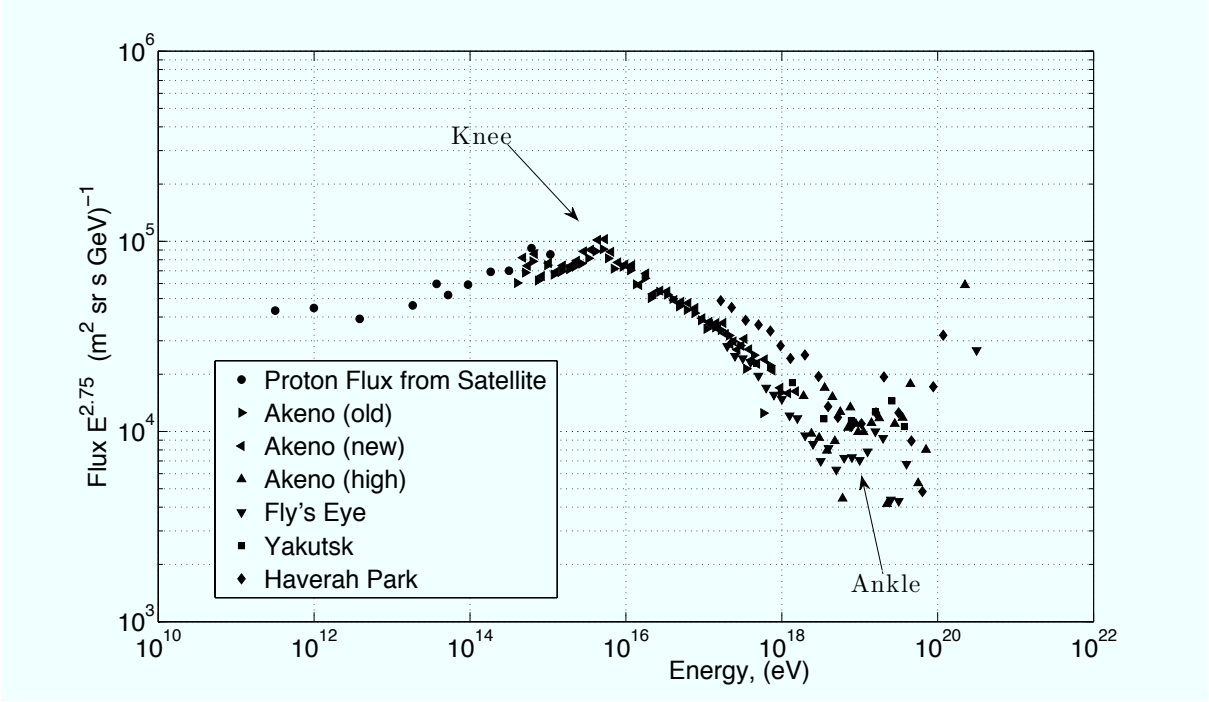

Figure 1.2. Modified cosmic ray spectrum. Adapted from [69].

Since these two features are clearly seen in the spectra of all the experiments mentioned above, which also exploit different detecting techniques, they should not just be artifacts, but should reflect true characteristics of the cosmic ray spectrum.

The fact that the energy spectrum follows an overall power law is a very crucial bit of information for finding the mechanisms of cosmic ray production and acceleration, since it is the sources of cosmic rays that are responsible for the generation of such shape of the spectrum. CR propagation through cosmological distances also changes a shape of the spectrum. Thus the spectrum features are important for obtaining some insight into the possible CR sources and CR propagation.

The accepted explanation for the existence of the breaking points in the energy spectrum is the change in the composition of the cosmic ray primaries at the spectrum transition points [48]. The breaking point at the knee was explained by the so called "leaky box" model. According to this model cosmic ray particles diffuse freely within the galactic disk. At the galactic boundaries they are reflected back but have a finite probability to diffuse out. This probability increases with the particle energy since the Larmor radius of the particle increases. Protons with 1PeV and above will have a good

chance of escaping ("leaking" out of our galaxy) [104]. According to this simple picture, the change in the spectral index arrises from the loss of the protons from the galactic flux and the composition of the flux becomes heavier.

An accepted interpretation of the spectrum change at the ankle relates to e^+e^- pair production energy losses during the UHECR propagation thought the intergalactic space.

The last but not the least interesting feature of the cosmic ray energy spectrum is the very high energy part of it. The most energetic event of $3 \cdot 10^{20}$ eV was observed by the Fly's Eye Experiment, but there were more that have energies of the same order of magnitude. According to Greisen, Zatsepin and Kuzmin, at the energy exceeding $6 \cdot 10^{19}$ eV, cosmic rays will interact with the cosmic microwave background and will loose part of their energy. This interaction reduces the distance over which the UHECR can travel and still arrive at Earth with an energy above the GZK threshold energy. The existence of the GZK cut-off limits the location of the possible CR accelerators to relatively close by.

Some of the CR research groups, such as AGASA [178], claim that there is no cut-off whatsoever. Others, like HiRes, state that they can see the cut-off in their data, observing only 13 events with an energy above the threshold, while expecting 43 with no suppression [9]. These two experiments use different techniques to detect cosmic rays and that can lead to controversial results. It is the new generation of CR experiment such as Telescope Array (TA) and Pierre Auger Observatory that will have to resolve this dilemma. Recently the Pierre Auger Observatory has confirmed the HiRes result [163].

1.2.2 Chemical Composition

The chemical composition of the cosmic rays is of great importance since it restricts the possible astrophysical processes that could have produced the particles. For example, an iron predominance in the composition would make old iron rich objects in our galaxy more favorable [39]. On the other hand, should the primaries be gamma rays, then we look for possible sources of UHE γ-rays.

Up to energies of 10^{14} eV the cosmic ray composition is well understood, since it is possible to measure composition directly on an event-by-event basis. Calorimeters, emulsion tracks, and transition radiation detectors are flown in balloon flights high in the atmosphere or on satellites and the space shuttle. Plans exist to incorporate such experiments in future space stations. For these energies particle physics data from

accelerators are also available, providing good confidence in the accuracy of the measured composition.

At low energies the composition resembles that of the solar abundance, though there are some important differences [171]. Figure 1.3 shows the relative abundance of solar and cosmic ray material. As can be seen from the Figure 1.3, both solar and cosmic ray matter have an excess of nuclei with even atomic numbers over the nuclei with odd ones. This effect can be explained by the fact that the nuclei with even Z and A are more strongly bound than those with odd A and/or Z [168]. There are also several striking differences in the abundances in lithium (Li), beryllium (Be) and boron (B) between the cosmic rays and solar matter. Though the cosmic ray abundance in iron (Fe) matches that of the sun, there is an overabundance in the elements just lighter than iron. Cosmic rays are falling short in hydrogen (H) and helium (He).

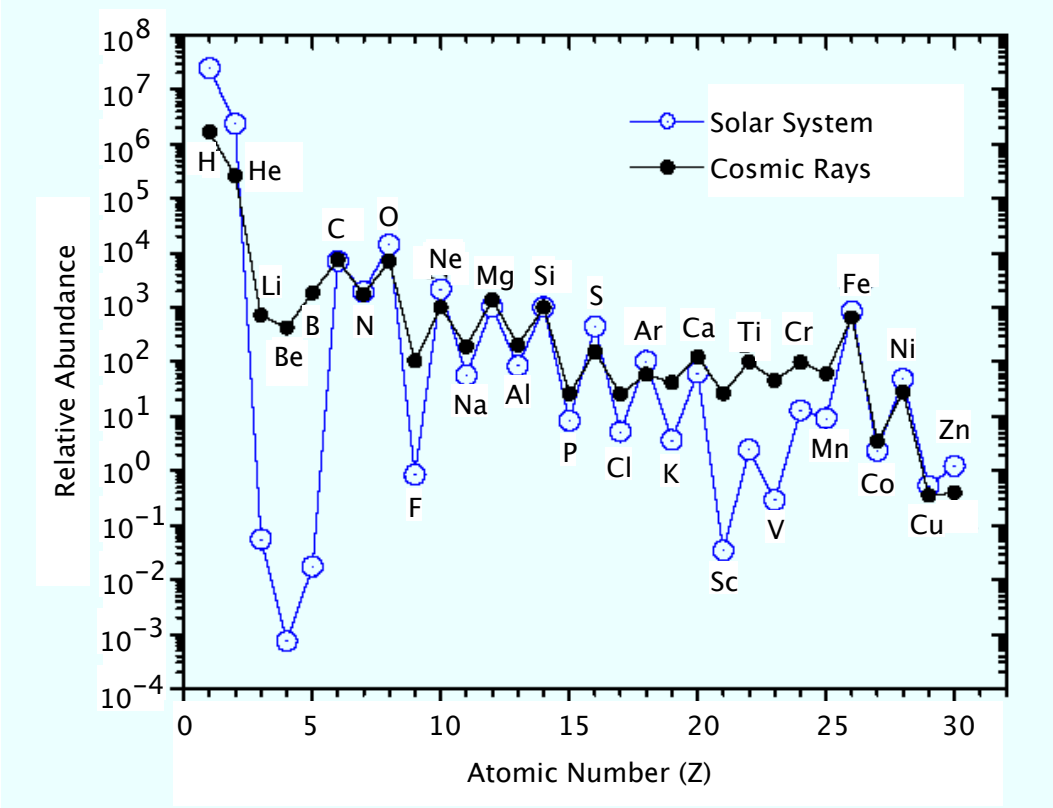

Figure 1.3. Relative solar and cosmic ray abundance of elements. Solar abundances of the elements (H-Zn) compared to element abundance in the primary cosmic ray nuclei, all relative to silicon. Adapted from [168].

Despite all the differences discussed above, cosmic ray primaries are believed to have stellar origin at these energies and all the mismatches in compositions arise from the interactions with the interstellar material on their way to Earth. The heavier nuclei will spallate into lighter ones as a result of such interactions. So the abundance in Li, Be and B is the result of the spallation of carbon (C) and oxygen (O). Similarly, the abundance of Sc, Ti and V is due to spallation of Ni and Fe [168].

The composition of cosmic rays at TeV to PeV energies is approximately 50% protons, 25% alpha-particles, 13% CNO and 12% Fe. Electrons comprise $\leq 10^{-2}$ and gamma rays on the order of 10^{-3} of the cosmic ray flux at these energies [171].

Above 10^{15} eV the flux of primary cosmic rays becomes so small (as small as 1 particle per square kilometer per century at the highest energies), that it is not possible to obtain the composition on an event-by-event basis. In the ultra high energy regime the composition of cosmic rays is determined by indirect measurements of the secondary particles from EAS. Air showers initiated by heavy nuclei (iron) on average are different from those initiated by light ones (protons).

This information is extracted from composition sensitive EAS parameters by comparing the average behavior of such parameters as a function of energy to the Monte Carlo shower simulation predictions (such as CORSIKA [98]). Examples of composition sensitive EAS parameters are X_0 (the first interaction depth in the atmosphere) and X_{max} (depth at the shower maximum).

These methods of composition measurements are model dependent and various simulations yield different and even contradictory result [95]. Models rely on extrapolations from accelerator data obtained at much lower energies, which can have huge uncertainties. Nevertheless all models agree that heavier nuclei tend to have shorter interaction length and will deposit their energy more quickly in the atmosphere than do light nuclei, EASs of which develop deeper and fluctuate more. This results in smaller X_0 and X_{max} parameters for the EASs initiated by the heavy nuclei on average. It is custom to speak in terms of protons (light) and iron nuclei (heavy), as these represent extremes in the cosmic ray composition.

The HiRes experiment uses the X_{max} technique for its composition studies in the energy range from 10^{17} eV to 10^{20} eV. The results are shown in Figure 1.4.

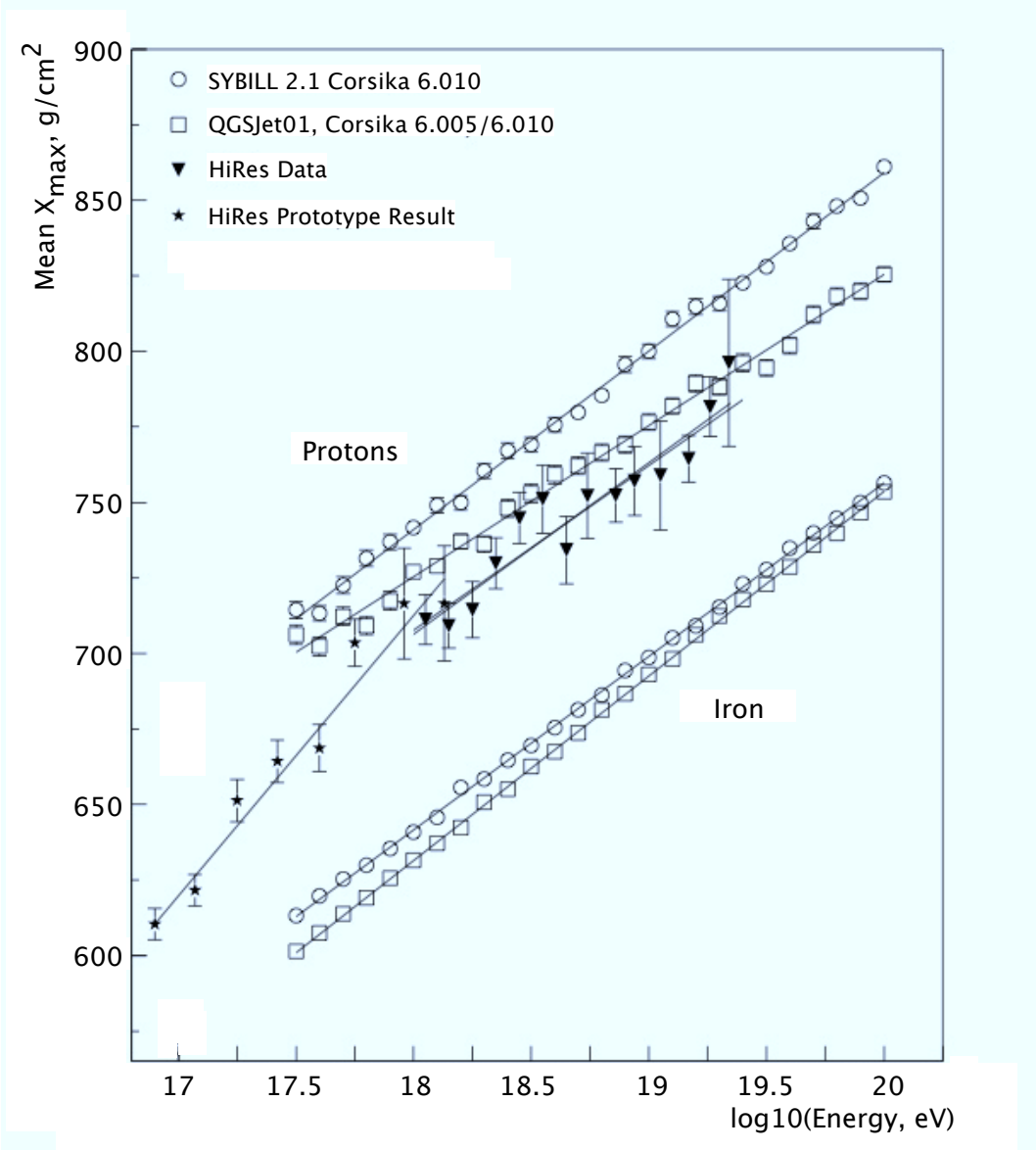

Figure 1.4. HiRes X_{max} composition study. Squares and circles are Monte Carlo results simulated with QGSJET and SIBYLL models respectively. Stars show the HiRes Prototype results. Diamonds are results calculated by Heck. Triangles show the HiRes1 monocular result. Two fit lines are best fit to the data and a fit to the 76% of the events which have hourly atmospheric corrections.

The mean value of X_{max} is plotted as a function of energy. The HiRes measurements are shown as upside down filled triangles. Stars represent the hybrid data as measured by the HiRes Prototype detector, in conjunction with the MIA experiment. The open circles show the simulation results for pure proton (upper line) and pure iron (lower line) composition as predicted by the SIBYLL interaction model. Results from the QGSJET interaction model are indicated by open squares.

Figure 1.4 suggests that the composition of primary cosmic rays is changing from heavy to light as the energy increases.

1.2.3 Anisotropy

The origin of UHECR is still a mystery. Anisotropy studies are very important for solving this mystery. Since most cosmic rays are protons and iron nuclei (charged particles) they are going to experience deflection when traveling in a magnetic field. The amount of deflection by the magnetic field is usually described by the gyro-radius, given by

$$R_g = \frac{\gamma \cdot m \cdot \nu \cdot \sin(\theta)}{z \cdot e} \sim \frac{E(eV)}{z \cdot e \cdot B_\mu}(kpc) \tag{1.4}$$

where $E(eV)$ is the energy of the particle in eV, B_μ is the magnitude of magnetic field in μG and z is the charge number.

The magnitude of the galactic magnetic field lies in the interval from 1 to 10 μG, and the extra-galactic magnetic field is of the order $10^{-3}\mu G$ [137].

From equation 1.4 it is clear that the further a cosmic ray travels the more it is deflected. The galactic propagation distance is on the order of 10 Kpc. Only the highest energy cosmic rays will have a bending angle less that 0.1°. But since cosmic rays are believed to have galactic origin predominantly at the energies below 10^{18} eV, it is not surprising that the measured flux appears to be isotropic at low energies.

For extra galactic sources it is still possible to observe anisotropy in the cosmic ray arrival direction if the energy of the ray is high. The current anisotropy studies from different experimental groups are controversial at the highest energies. The AGASA group has measured a 4.5 σ excess in the direction of 10° from the galactic plane in the energy interval of $10^{18.0}$ to $10^{18.4}$ eV [97]. The Fly's Eye group by searching for large scale anisotropy also saw a small galactic plane enhancement in their data [52] in the range of $10^{17.6}$ to $10^{18.0}$ eV. The Pierre Auger collaboration reports no signs of anisotropy near the

galactic centre above 10^{17} eV [18]. None of the studies report a statistically significant excess from the super-galactic plane.

More recently AGASA has reported evidence for clustering of the highest energy events [27]. The expectation of anisotropy above the GZK threshold was verified by the Pierre Auger collaboration in 2007 [10] at a confidence level of at least 99%. The Pierre Auger group reported that its highest energy cosmic rays (energies greater than $\sim 6\times10^{19}$ eV) show a correlation with the positions of extragalactic nearby active galactic nuclei. Moreover the correlation is maximum for sources located closer than 100 Mpc and angular separation of a few degrees, which is consistent with the hypothesis that UHECRs are accelerated in near-by extragalactic sources. Better statistics from the new generation of detectors will, it is hoped, help to get a better understanding of the origin problem.

1.3 Cosmic Ray Models

The present knowledge about cosmic rays does not allow us to answer the question about their origin. Any proposed mechanisms of cosmic ray production, acceleration and propagation should explain the current empirical cosmic ray data (spectrum features, composition and anisotropy) and that makes the problem of CR origin an extremely complicated one.

There exist various models of cosmic ray production. They may be broken down into two categories: "bottom-up" acceleration models and "top-down" decay models.

1.3.1 "Bottom-up" Acceleration Models

In so called astrophysical acceleration models CR particles have relatively low energies when they are created, but get accelerated later. Generally two major acceleration mechanisms are considered: direct (fast) and statistical (slow) acceleration.

1.3.1.1 Direct acceleration. Fast direct acceleration assumes the existence of a strong electromagnetic field. The magnetic component of the field will keep a particle confined in the e/m region while the electric component boosts its energy.

Fairly simple arguments show that maximum possible energy (in units of 10^{18} eV) reached by a particle in the vicinity of astrophysical shocks is estimated by [125].

$$E_{max}(10^{18}eV) \sim \beta \times Ze \times B(\mu G) \times L(kpc) \tag{1.5}$$

where β is the velocity of the magnetic shock region, Ze is the total particle charge, B is the field strength in micro gauss and L is the size of the e/m region in kilo parsecs.

In other words, a particle can be accelerated in a region of field strength B until its gyro-radius increases beyond the size of the region L and it can escape. The gyro-radius of a particle is given by

$$R_{gyro}(kpc) \sim \frac{E(10^{18}eV)}{Ze \times B(\mu G)} \tag{1.6}$$

Figure 1.5 is the famous "Hillas diagram" from Ref. [105], which displays potential astrophysical acceleration sites on a magnetic field vs. size plot, since these two parameters predict the maximum possible energy of the eZ charged particle. The top dotted diagonal line indicates the size and the magnetic field strength required to accelerate protons to 10^{20} eV, under the realistic assumption of a shock velocity $\beta = 1/300$. All the objects that lie above this line are capable of doing that. Unfortunately, the plot shows that all the known possible CR acceleration site are below the line and thus fail to accelerate protons to the highest energies. The solid diagonal line holds the same argument but for the extreme assumption of $\beta = 1$ (shocks traveling with the speed of light). Even under this unrealistic condition there are not many sources that meet the criteria. The lowest dashed diagonal line corresponds to the 10^{20} eV iron nuclei and shocks at $\beta = 1$.

The picture starts to look even worse when possible energy loss mechanisms are taken into account. The regions of strong e/m fields are usually associated with intense radiation in their vicinity. It is expected that cosmic ray energy will be degraded by photopion production and by synchrotron losses. In addition it is not obvious how this model can produce an $E^{-\gamma}$ particle spectrum [105].

Despite all the limitations of this model, the most likely CR sources are quickly rotating neutron stars, active galactic nuclei (AGN), radio galaxies, galactic clusters and the intergalactic medium (IGM).

1.3.1.2 Statistical acceleration. In the case of statistical acceleration the final energy is gained slowly over many decades of energy. But it is a very attractive acceleration mechanism, because the power law dependence of the spectrum comes in naturally.

One of the first scenarios of statistical acceleration was proposed by Fermi [76]. He showed that charged particles could scatter off magnetic clouds in the interstellar medium and would gain or loose energy depending on the angle at which they enter the cloud.

In the one-dimensional case, a particle of mass m is moving with velocity v and collides with a magnetic cloud of infinite mass, moving with velocity V [171, page 91]. Thus the velocity in the center of mass of the particle-cloud system is V. The energy of the cloud

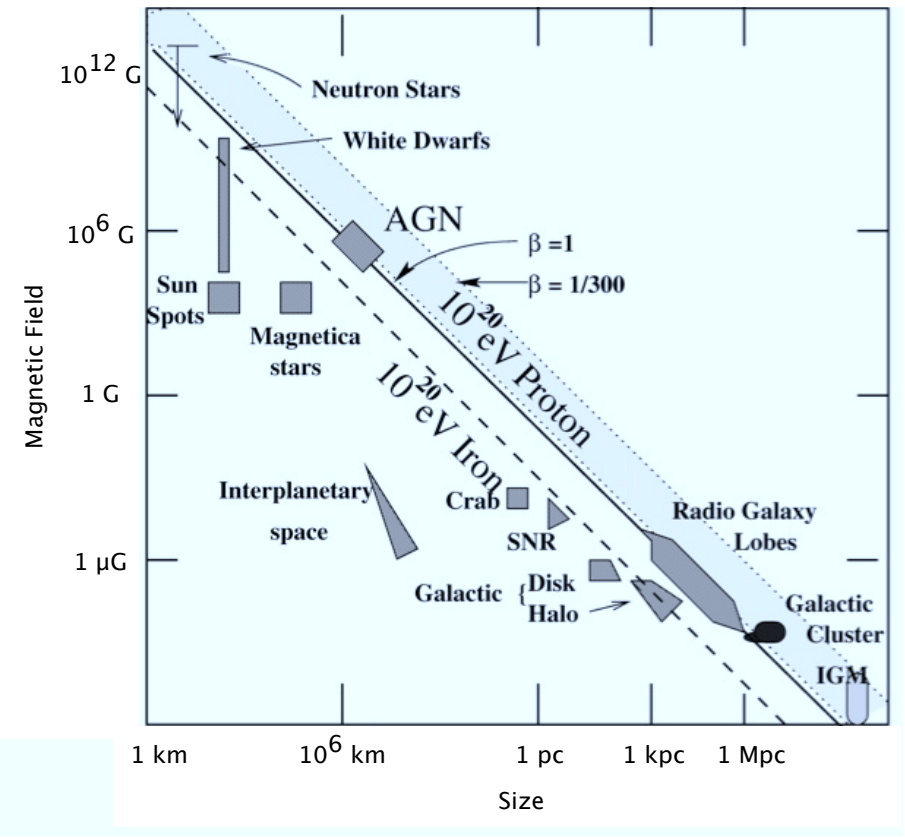

Figure 1.5. Hillas diagram of potential astrophysical acceleration sites from Ref. [105]. Potential astrophysical objects, capable to accelerate cosmic ray particles above 10^{20} eV must lie above the solid line for protons and shock front traveling at the speed $\beta = 1/300$, top dotted line for protons and shock front traveling at the speed $\beta = 1$ and bottom dashed line for iron nuclei and shock front traveling at the speed $\beta = 1$. The abbreviations here correspond to: AGN - active galactic nuclei; SNR - supernova remnants; IGM - intergalactic medium.

should exceed that of a particle. In the case of the head-on collisions the center of mass energy of a particle does not change, but its momentum points to the opposite direction after the collision. The change in the cosmic ray energy is positive and given by

$$\Delta E_{head-on} = \frac{2E_V}{c(1+\frac{v^2}{c^2})}(\frac{V}{c}+\frac{v}{c}) \tag{1.7}$$

In the case of the following collisions the change in the cosmic ray energy is negative and given by

$$\Delta E_{following} = -\frac{2E_V}{c(1+\frac{v^2}{c^2})}(\frac{v}{c} - \frac{V}{c}) \tag{1.8}$$

It was shown that the probability of the head-on collisions is $(v+V)/V$ and is greater than the probability of the following collisions, which is equal to $(v-V)/V$ [171, page 91]. So the conclusion is that on the average a particle will gain energy and the fractional energy gain per collision is approximated as

$$\Delta E/E \sim (\frac{v}{c})^2 \tag{1.9}$$

Since the particle energy gain is proportional to $(v/c)^2$, this mechanism of cosmic ray acceleration is also known as second order Fermi acceleration.

The particle will gain energy until the statistical equilibrium between the degrees of freedom of the chaotically moving clouds and the particle is reached. This limits the possible particle energy. The number of particles with energy E is estimated by Longair [137] to be proportional to

$$N_E \sim E^{1+\tau/T} \tag{1.10}$$

where T is the time a particle stays within the cloud, and τ is given by

$$\tau = \frac{1}{4R(V/c)^2} \tag{1.11}$$

Here R is the number of collisions per second, experienced by a cosmic ray.

The problem with this acceleration mechanism is that in reality V is much smaller the speed of light, and the mean free path for collisions is on the order of one parsec [171, page 92]. The resulting energy gain will be very slow and fails to explain the existence of the highest energy cosmic rays.

A more efficient statistical acceleration mechanisms includes strong shock waves. Due to the turbulent magnetic fields on either side of the shock front, a cosmic ray particle bounces back and forth across it [128, page 467]. By crossing a shock wave, moving at a nonrelativistic velocity V, a particle will gain energy proportional to

$$\Delta E/E \sim (\frac{V}{c}) \tag{1.12}$$

Since this process depends on the first order of V/c, it is often referred to as the first order Fermi acceleration. The shock acceleration mechanism for a plane shock of infinite extent produces a power spectrum with the spectral index equal to 2 [146].

The most promising candidate for shock acceleration is a supernova explosion. Unfortunately, the maximum energy that a particle can achieve is limited by the eventual disintegration of the expanding supernova remnant and is calculated to be no more than 10^{15} eV [128, page 468]. At this energy the gyroradii of the cosmic ray particles are of the same size as the supernova remnant. This threshold also corresponds to the knee in the cosmic ray spectrum, where the spectral index changes from -2.7 to 3. This makes supernovae explosions great candidates for accelerating particles up to the "knee" energy.

A shock can accelerate particles to higher energies if the time the particle spends in the accelerating region and/or the spatial extent of this region are increased. It was pointed out by Jokipii et al. [111], that there might exist a hypothetical galactic wind termination shock wave with galactic dimension and galactic age. The galactic wind if it exists is similar to solar wind, which is a result of the transport of the energy with shock waves from the solar surface [137, page 138]. In other words, the solar wind is a hot gas moving at relativistic velocities and carrying entrapped magnetic fields. A termination shock occurs at the point where the solar wind kinetic pressure is balanced out by the interstellar pressure [171, page 97].

The galactic wind is most probably driven by supernova shocks. Numerical calculations show that galactic wind could accelerate protons to 10 EeV and Fe nuclei up to 100 EeV.

1.3.2 "Top-down" Decay Models

The acceleration mechanisms in forms of both direct and statistical acceleration (except for the galactic wind one) fail to explain the existence of the highest energy (up to 10^{20} eV) cosmic rays especially when all the energy loss processes are taken into account. This made so called "top-down" models gain more popularity. These models are based on the idea that ultrahigh energy cosmic rays originate in the decay or annihilation of some exotic objects produced in the early universe. There are several major types of these objects that are being generally considered.

Supermassive relics or X particles would be long-lived metastable objects produced in the early evolution of the universe [40], with mass larger than 10^{21} eV and lifetime of the order of the age of the universe. In order to explain the observed UHECRs these relics must decay in the current epoch. X particles of such mass decay to leptons and quarks, and the quarks then hadronize to mostly pions and some small number of nucleons [49] at UHE.

Like ordinary matter these relic objects feel gravitational attraction and aggregate to form cold dark matter (CDM), which is thought to be responsible for the observed structure in the universe. This means that if supermassive relic particles are really the sources of UHECR, then there should exist an anisotropy in the arrival direction of cosmic rays toward the galactic center and galactic clusters [40, 73]. At present there is no evidence for such an anisotropy in the empirical data from cosmic ray experiments.

Topological defects (TDs) are predicted to form in the early universe, when it underwent a transition from an absolute symmetry state with massless particles, to the present broken symmetry state and massive particles [121, 47]. During this transition in the early universe, enormous amounts of energy can be freed, some of which can be transfered to UHECR.

Topological defects are classified according to their dimensions: magnetic monopoles are zero-dimensional and point-like; cosmic strings are one-dimensional objects and may also be called superconductive if they carry current; domain walls are two-dimensional and textures are three-dimensional. TDs may annihilate to release X particles trapped inside them [47] or behave as cosmic rays themselves to create extensive air showers.

Z-bosons are produced as resonances when UHE neutrinos from neutron and pion decay interact with the relic neutrino background [75].

$$\nu\ \nu_{background} \longrightarrow Z^* \longrightarrow hadrons$$

The background relic neutrinos decoupled from the thermal photon bath in the first second after the creation of the universe. They were later cooled down by cosmic expansion to the point that they became gravitationally trapped as a part of the hot dark matter halo [189]. This model proposes that UHECR originate as the decay products of massive Z-bozons [195], but can account for a production of light nuclei (protons) only.

Though top-down theories seem to be very attractive to explain the existence of cosmic rays at the highest energies, they are not as efficient in explaining the lower energy portion of the cosmic rays spectrum. Other sources are required to do so.

Only more studies of cosmic ray energy spectrum, composition and anisotropy can show which model is the most realistic about its production of UHECR.

1.3.3 Models of Cosmic Ray Propagation

In order to be detected here on Earth, cosmic rays, no matter how they were created, have to traverse substantial distances from their place of origin. For example, if a particle

has an extragalactic origin, it must travel through first the extragalactic medium, then through the intergalactic medium and finally the interstellar medium of our own galaxy. It is absolutely necessary to consider what happens to the cosmic rays along their way, since it effects the observed cosmic ray energy spectrum, composition and the arrival direction.

The interstellar medium is composed of clouds of neutral gas and gas ionized by starlight (mostly hydrogen) [171, page 11]. There are also chaotic and regular magnetic fields. Studies of the Faraday rotation of the plane of polarization of linearly polarized light and the polarization of synchrotron emission and starlight suggest that the magnitude of the chaotic and regular galactic magnetic fields (GMFs) are about a few micro gauss. The intergalactic medium includes extragalactic magnetic fields (EGMFs), which are much more uncertain but are believed to have strength on the order of $10^{-2} - 10^{-3}$ of the galactic fields [171, page 13] and to be randomly oriented.

Another important component of both the galactic and the extragalactic medium is the Cosmic Microwave Background Radiation (CMBR), that was predicted by George Gamow and Ralph Alpher in 1948 and detected by Arno Penzias and Robert Woodrow Wilson in 1964 [147]. The CMBR has a thermal blackbody spectrum at a temperature of 2.725 K, so the spectrum peaks in the microwave range frequency of 160.2 GHz, corresponding to a 1.9 mm wavelength. The big bang theory suggests that the cosmic microwave background is uniform, fills all of observable space and accounts for most of the radiation energy in the universe ($\sim 5 \times 10^{-5}$ of the total density of the universe).

The composition of the original cosmic rays plays a crucial role, because different particles are subjects to different interaction and behave quite differently while traveling over cosmological distances. Cosmic ray primaries are believed to be mostly charged particles (protons and iron nuclei). This means that the only direct way to identify the sources of UHECRs by pointing cosmic ray arrival direction back toward their origin will not work, since the trajectory of the charged particles is deflected by the magnetic fields. The effect of this deflection is estimated by the following relation

$$\delta = \frac{S}{R_{gyro}} \tag{1.13}$$

where S is a distance, that a particle is traveling in a uniform magnetic field.

Using equation 1.6 for R_{gyro}, the angular deflection δ of the particle from its initial trajectory is given by

$$\delta \sim \frac{Ze \times S(kpc) \times B(\mu G)}{E(10^{18} eV)} \tag{1.14}$$

We can see that angular deflection is proportional to the particle charge; thus Fe nuclei will be deflected more than light protons. Since EGMF is a several of orders of magnitude weaker than GMF, it will deflect cosmic rays trajectories less and can be ignored in many cases. The chaotic orientation of EGMFs also reduces its effect on cosmic rays propagation and in the extreme case may result in a zero deflection. For a particle traveling a distance S through a turbulent field with mean field strength B and correlation length L_c we have for $S >> L_c$ a random walk with $N = S/L_c$ deflections and $\sqrt{N}$ behavior for the net deviation [94]. Thus 1.14 can be rewritten as:

$$\delta \sim \frac{Ze \times B(\mu G)}{E(10^{18} eV)} \times \sqrt{S(kpc) L_c(kpc)} \tag{1.15}$$

Deflection is also inversely proportional to the energy of the particle, so at the highest energies it can be small enough that the arrival directions of the cosmic rays are reasonably correlated with source location. The only problem is the extremely low cosmic ray flux at the these energies and as the result poor statistics. Recently the Auger collaboration has released an analysis of their data of the ultra high energetic cosmic rays [67] where they report to find correlations between the highest energy events and active galactic nuclei (AGN) at a confidence level of 99%. That confirms the extragalactic origin of the UHECR.

The energy of the original cosmic rays, especially if they are of extragalactic origin, will also be affected and degraded as they propagate through the cosmos. It is very important to understand and to consider these processes as their effect on the particle propagation will limit the maximum distance of the possible UHECR sources location from the Earth. The nature of these processes depends on the type of cosmic ray particle and will be discussed next.

One of the energy loss processes that applies to any particle is due to the adiabatic expansion of the universe. As space expands, the wavelengths that correspond to the particles get bigger and their energies get smaller. Universal expansion energy losses do not depend on the particle energy and is parameterized by 1.16:

$$l_H \simeq \frac{c}{H_0} \simeq 3h^{-1}\ Gpc \tag{1.16}$$

Protons (except for the very high energy ones) have a negligible probability of interaction due to the very low matter density of the universe. An average cosmic ray particle travels through ~ 0.2 g/cm^2 of matter in intergalactic space and ~ 10 g/cm^2 in a galaxy [27], but its mean free path is an order of magnitude higher (about 70 g/cm^2 for a PeV proton). However, CMB radiation can significantly reduce the energy of the most energetic cosmic rays.

For protons with energies between $10^{18.5} < E < 10^{19.5}$ eV, photon pair production described by the equation 1.17 is the dominant energy loss mechanism [55]. The energy loss length $l_p(E)$ for the process reaches its minimum of 2 Gpc in this energy interval [190].

$$\gamma_{CMB} + p \longrightarrow p + e^+ + e^- \tag{1.17}$$

In the UHE regime the energy losses are even bigger. As was originally suggested by Greisen [92] and, independently, by Zatsepin and Kuzmin [192] in 1966, at 2.7 K temperature of this relic radiation, a typical CMB photon will have about 10^{-4} eV in the laboratory reference frame, but about 300 MeV in the 50 EeV proton reference frame. So the protons with energy of the order of 50 EeV will collide inelastically with these photons through the creation of a Δ^* (1232 MeV) resonance, which will decay into a nucleon (proton or neutron) and pion (neutral or positive):

$$\gamma_{CMB} + p \longrightarrow \Delta^*(1232\ MeV) \longrightarrow \begin{cases} n\ \pi^+ \\ p\ \pi^0 \end{cases} \tag{1.18}$$

Because the interaction is inelastic, the original proton will loose energy. Pions will carry a significant amount of the energy of the cosmic ray. This means that there should not be a lot of the protons with an energy above 50 EeV and a suppression of the cosmic ray flux is expected above this energy. This effect is known as Greisen-Zatsepin-Kuzmin (or simply GZK) cut-off. Above the so-called GZK threshold ($\sim 6 \times 10^{19}$ eV) the universe becomes opaque to UHECR and the distance that UHECR can travel is limited to $\sim 50 - 100$ Mpc, which is about the size of our local supercluster of galaxies. Auger analysis [67] of the correlation for the events above GZK threshold holds only for the AGNs located up to a distance of ~ 100 Mpc, which is an independent confirmation of the GZK cut-off.

Figure 1.6 shows the attenuation length of cosmic rays as a function of energy calculated by Yoshida and Teshima from [190]. One can see a sudden decrease in the attenuation length just above the GZK threshold. Attenuation length l_π is an exponential

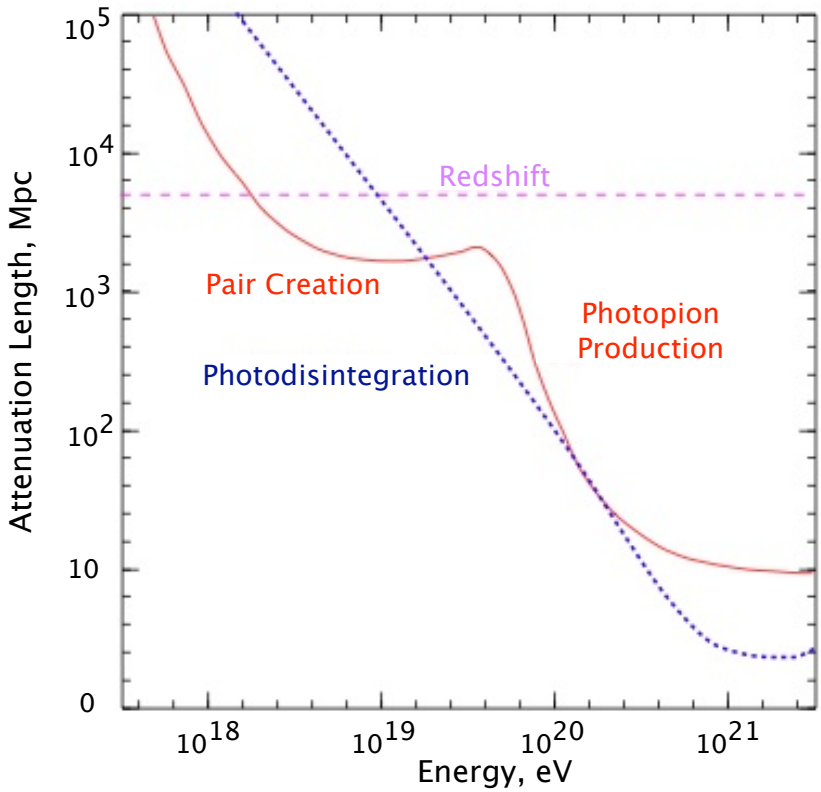

Figure 1.6. Energy dependence of cosmic ray attenuation length. Adapted from [187]. Solid line shows the attenuation length as a function of energy for protons, calculated by Yoshida and Teshima [190]. Dotted line is the energy dependent attenuation length for iron as calculated by Puget et al. [153]. Dashed line locates the redshift bound, corresponding to the adiabatic energy loss for all types of cosmic ray particles.

function of energy and in the range from $10^{19.5} < E < 10^{20.5}$ eV it is parameterized by equation 1.19.

$$l_\pi(E) \simeq 4.8(\frac{E}{E_{th}})^2 e^{E_{th}/E}\ Mpc \tag{1.19}$$

where $E_{th} \simeq (m_\pi m_p c^4)/(2k_b T_{CMB}) \simeq 3 \times 10^{20}$ eV is the threshold energy for photopion production. As proton energy grows more and more CMB photons satisfy the threshold condition for pion production.

The attenuation length for a 7×10^{19} eV energy proton is about 500 Mpc [190]. The sources that contribute to this highest energy part of the spectrum should therefore be located within a 500 Mpc radius from the Earth. For the protons with energy 3×10^{20} eV

this limit is even tighter ($\sim$ 10 Mpc). Only nearby sources can create the highest energy cosmic rays observed. The GZK dilemma is that there is no astrophysical object in our cosmological neighborhood that is energetic enough to produce and accelerate cosmic rays to energies above 10^{20} eV.

Heavier nuclei also interact with the CMB photons through the process known as photo-spallation (photodisintegration). The mean free path for nuclei is even shorter (on the order of 10 Mpc [137]). Figure 1.6 shows a more rapid energy loss due to photodisintegration for heavier nuclei [153]. Hence no nuclei at UHE can be observed at Earth, if the cosmic ray sources are farther than 10 Mpc. Since heavy nuclei break down quickly during propagation (3-4 nucleon per Mpc) for extragalactic source models, protons should dominate an EHECR composition.

If the extragalactic cosmic rays are neutral particles, their arrival direction will point directly toward their sources, since their path is not deflected by magnetic fields. Unfortunately, the fraction of neutral particles (neutrons, gamma rays and neutrinos) in the cosmic rays flux is very small.

Neutrons are expected to be present in the cosmic ray flux as the daughter products of photo-pion production (see equation 1.18). However, these neutrons will decay back to protons with the decay length given by:

$$L_{decay} = \gamma \; c \; \tau_{decay} \sim 1 \; Mpc \; \left(\frac{E}{10^{20} eV} \right) \tag{1.20}$$

Figure 1.7 compares nucleon GZK interaction length with the neutron decay length as a function of energy [175]. At relatively lower energy the decay length of the GZK neutrons is quite small and all the $10^{20} - 10^{21}$ eV neutrons should decay back to proton within 1-10 Mpc. At highest energies neutrons interact with CMB photons, rather than decay, due to the increasing decay length. These interactions will also produce next generation protons and neutrons. All the processes discussed here will result in negligible neutron flux at UHE.

High energy photons (or gamma rays) are also considered as neutral cosmic ray candidates. There are many mechanisms that can be responsible for the production of UHE photons. One of them is GZK photopion production with the subsequent decay of neutral pions into two gamma rays.

$$\pi^0 \longrightarrow \gamma \; \gamma \tag{1.21}$$

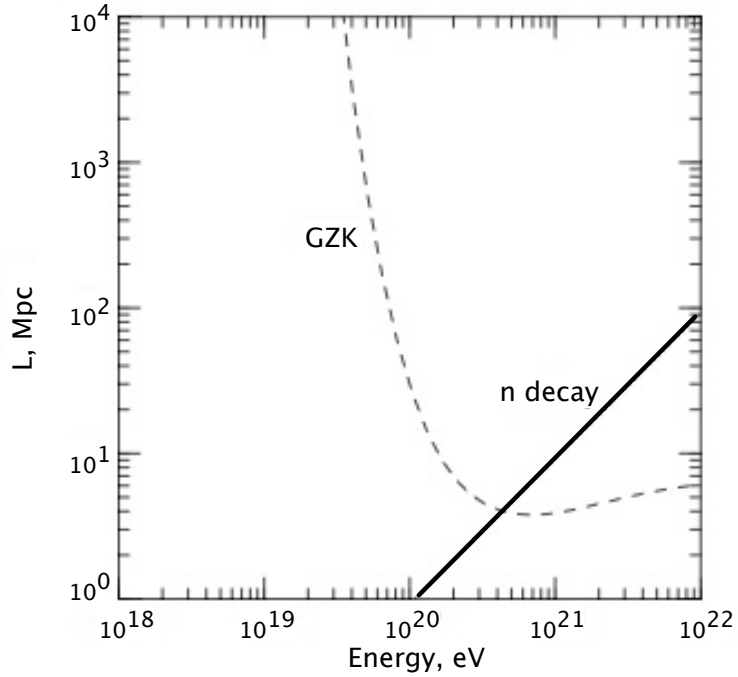

Figure 1.7. Neutron GZK interaction (solid line) and neutron decay (dashed line) lengths. Adapted from [175].

Exotic "top-down" scenarios also predict UHE photon fluxes [167].

The propagation of gamma rays through the universe is complicated by the severe energy losses due to interactions with ambient low energy photons of infrared, radio, microwave and CM backgrounds. EHE photons interact with the background photons via pair production 1.22 and double pair production 1.23:

$$\gamma\ \gamma_b \longrightarrow e^+\ e^- \tag{1.22}$$

$$\gamma\ \gamma_b \longrightarrow e^+\ e^-\ e^+\ e^- \tag{1.23}$$

The magnitude of the magnetic field determines what happens to these electrons and positrons. In case of a strong magnetic field ($\sim$ 1 nG or stronger), synchrotron energy loss is the dominant process. The synchrotron energy loss length is shown in Figure 1.8. It is much shorter than the photon interaction length, so in this scenario pair production is the end of the UHE gamma ray.

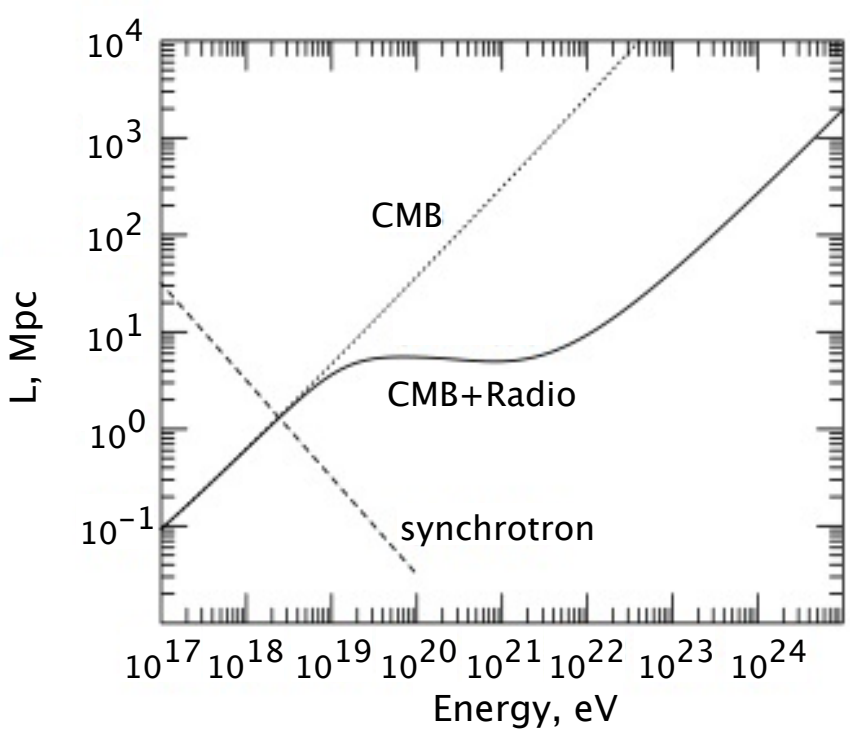

Figure 1.8. Energy dependent synchrotron energy loss (dashed line) and photon interaction lengths. Photon interaction length due to CMB only is shown as dotted line. Solid line is photon interaction length due to CMB plus radio background. Adapted from [175].

If the strength of the magnetic field is low ($\sim$ 0.01 nG), synchrotron energy loss will not play much of a role and inverse Compton scattering will dominate energy loss of electrons and positrons:

$$e\ \gamma_b \longrightarrow \gamma\ e \tag{1.24}$$

Rarely triplet pair production also occurs:

$$e\ \gamma_b \longrightarrow e\ e^+\ e^- \tag{1.25}$$

As the result of pair production and inverse Compton scattering the energy will be lost slowly as this electromagnetic cascade evolves. This would lengthen the propagation

distance of UHE photons. Figure 1.9 shows photon attenuation length due to infrared (IR), cosmic microwave (CM) and radio backgrounds. Photon interaction length due to CMB and CMB plus radio background are shown in Figure 1.8.

Neutrinos are also by-products of the GZK-effect. They are created from the decay of the positive pions through the process:

$$\pi^+ \longrightarrow \nu_\mu \ \mu^+ \tag{1.26}$$

followed by

$$\mu^+ \longrightarrow \bar{\nu_\mu} \ \nu_e \ e^+ \tag{1.27}$$

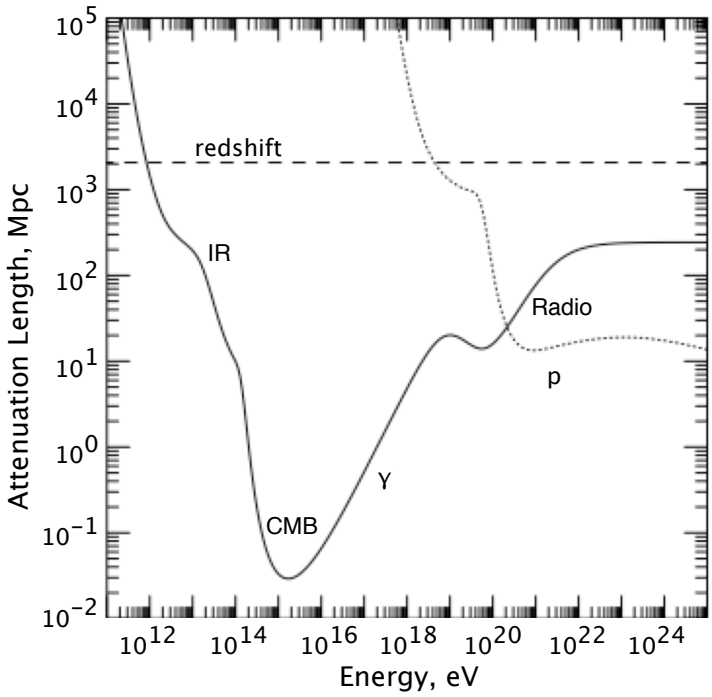

Figure 1.9. Energy dependent photon attenuation length. Photon attenuation length (solid line) due to infrared (IR), cosmic microwave (CM) and radio backgrounds is compared to proton GZK attenuation length (dotted line) and attenuation due to redshift (dashed line). Adapted from [179].

These are the so called GZK-neutrinos or cosmogenic neutrinos. Since they are neutral particles they propagated without any deflection. They also do not easily interact due to their extremely low interaction cross sections. Because they are unlikely to interact with matter, neutrinos are also extremely difficult to detect. The detection of cosmogenic neutrinos, however, will confirm the existence of the GZK effect once and for all and will provide an opportunity to search for cosmic ray sources beyond our cosmic neighborhood.

If they are detected the highest energies neutrinos can answer many question about our universe that still puzzle scientists around the world. This is why neutrino research is so important and huge underground neutrino telescopes have been built to detect neutrinos from extraterrestrial sources. This work is also devoted to the estimation of the neutrino flux, but using a completely different approach.

CHAPTER 2

HIRES MOTIVATED NEUTRINO AND GAMMA RAY FLUXES

It is commonly believed that the cosmic rays of highest energy have an extragalactic origin, rather that being accelerated in our own galaxy. There are some observations that support this argument. First of all, the recent studies of anisotropy in the arrival direction of the cosmic rays do not confirm any clustering of the UHE events along the galactic plane, although there exist a significant indication of the clustering along the super-galactic plane [96, 174]. Composition change from heavy nuclei at lower energies to light protonic at highest also hints towards an extragalactic origin of UHECR [7]. Also, excepts for possibly radio pulsars, there are no sources in our galaxy that are big and/or energetic enough to produce particles in the UHE regime.

As was discussed previously the assumption that the UHECRs are protons accelerated in extragalactic sources gives us an opportunity to connect them with the UHE neutrinos and gamma rays. The highest energy cosmic rays have enough energy to interact with the photons of the cosmic microwave background to produce pions. These collisions result in the suppression of cosmic ray flux at the energies above 10^{20} eV (GZK cut-off), as observed by HiRes [9]. The decay of secondary pions in the photopion production reaction creates UHE neutrinos and gamma rays.

A simple study can be made as an attempt to estimate the expected GZK neutrino and gamma ray fluxes resulting from the propagation of UHE protons. Similar exercises were already done by a group of different authors including [32, 176, 22, 24, 189, 165]. This chapter describes our limits on fluxes of secondary GZK particles based on the HiRes cosmic ray spectrum, assuming a uniform distribution of cosmic ray sources.

2.1 Model Description

This model is an extension of the effort by Douglas Bergman described in Ref. [44]. Originally this model was built to interpret the primary (proton) cosmic ray fluxes that

HiRes measured at Earth. We extended this work to calculate the resulting secondary neutrino and gamma ray fluxes.

In this model an observer on Earth is located at the center of geocentric spheres. Cosmic ray sources are uniformly distributed on the surface of these spheres. There are a total number of 400 spheres or spherical shells, equally spaced in terms of redshift. The first (closest) shell has a radius of $z = 0.01$. The relative distance between these shells is set to be $dz = 0.01$, so that the radius of the last sphere reaches $z = 4$.

The redshift evolution of cosmic ray sources is taken into the account in the model, by making the density of the sources on the surface of the spheres dependent on its radius (redshift) as:

$$n_{sph}(z) = n_0 \mathcal{H}(z) \tag{2.1}$$

where $n_{sph}(z)$ is the density of sources for the sphere at redshift z, n_0 is the density of sources at $z = 0$ and $\mathcal{H}(z)$ expresses an evolution of sources with redshift. Several model of evolution of cosmic ray sources with redshift are considered. We first consider the most simple source redshift evolution of the form:

$$\mathcal{H}(z) = (1 + z)^m \tag{2.2}$$

The next two models are motivated by the optical and x-ray wavelength sky surveys of Quasi Stellar Objects (QSOs) and Active Galactic Nuclei (AGNs) as well as the star formation rates (SFR). The data consistently predict break in the evolution at redshift z_{cr} towards flatter or even constant evolution and a sharp exponential cut-off at $z_{cut-off}$. The explanation for these observations comes from the fact that at earlier times (higher redshifts) the large black holes that power these sources were just forming and at z_{cr} they reached their mature state. There is no consistency among different studies on the values for m, z_{cr} or $z_{cut-off}$. An old estimate of the star formation rate [138] suggests $m = 3$, $z_{cr} = 1.9$ and $z_{cut-off} = 2.7$. More recent estimate of the SFR evolution of reference [57] predicts $m = 3$, $z_{cr} = 1.3$ and $z_{cut-off} = 6$. The recent infrared survey of the Spitzer telescope [148] estimates a stronger evolution with $m = 4$, $z_{cr} = 1$ and $z_{cut-off} = 6$. In case of $m = 3$ the source density follows an evolution similar to that of the universal expansion.

Our second model of the evolution of cosmic ray sources has the following parameterization:

$$\mathcal{H}(z) = \begin{cases} (1+z)^m, & z \leq z_{cr} \\ (1+z_{cr})^m, & z > z_{cr} \end{cases} \tag{2.3}$$

For the model we assume that $z_{cut-off} > 4$ and thus does not effect our calculations. For the final model $z_{cut-off} < 4$. The final model has the form:

$$\mathcal{H}(z) = \begin{cases} (1+z)^m, & z \leq z_{cr} \\ (1+z_{cr})^m, & z_{cr} < z \leq z_{cut-off} \\ (1+z_{cr})^m exp\left(\frac{z_{cut-off}-z}{z_{cut-off}}\right), & z > z_{cut-off} \end{cases} \tag{2.4}$$

Each cosmic ray source (or shell) produces cosmic rays with the same power spectrum of $E^{-\gamma}$. m, z_{cr}, $z_{cut-off}$ and γ are parameters of our model that are later extracted from the measured data.

The flow of the Monte Carlo is as follows. For every single shell 10,000 cosmic rays (we consider only protons) are created with random energies from the energy interval of $10^{7.5} - 10^{12.5}$ GeV. Every single proton is then propagated along the radius to the Earth. Since it is a 1D propagation we do not consider the effect of the EGM and IGM on its propagation.

As they travel through cosmological distances (z), protons loose their energy due to different processes. In order to predict the UHECR spectrum at Earth, we have to consider the modification to the spectrum due to various energy loss mechanisms [42, 101, 41, 154, 188, 19]. The most obvious one is the energy loss due to the expansion of the universe. During propagation in the extragalactic medium protons also interact with the CMB photons through photopion and pair production reactions. Other universal backgrounds such as infrared, optical and ultraviolet have little effect on the UHE proton spectra and can be neglected in the calculation of the UHECR spectrum, if we consider only protons [22].

Electron positron pair production is taken into account using the continuous energy-loss formalism of Berezinsky et al.[41]. According to [101] simple continuous loss approximation does not work to describe photo-pion losses, since it fails to predict the intrinsic spread in energy due to the kinematics of photo-pion production and the Poisson noise in the numbers of photons encountered for a given path length. We use a different approach to find the parameters of photo-pion interaction. In case of photopion interaction pions are not the only particles that are being produced, but due to their lowest mass among mesons they are the most abundant. The possibility of creation of other particles is neglected in this analysis.

Secondary particles (neutrinos and gamma rays) created as the result of proton interaction on CMB are also included in the propagation process. We assume no interaction of UHE neutrinos on any of the universe backgrounds. Generated neutrinos lose their energies only adiabatically due to the expansion of the universe. The fluxes of UHE gamma rays are estimated by developing electro-magnetic cascades through extragalactic space. Different channels of cascade initiation include UHE gamma rays, positrons, electrons from gzk processes as well as e^+e^- pairs from pair production on CMB.

To find the resulting cosmic ray, neutrino and gamma ray fluxes on Earth, we add up the contributions from all the different z shells according to their respective weight in the z evolution under consideration. All m, z_{cr}, $z_{cut-off}$ and γ, are varied to build up a cosmic ray spectrum at the Earth that optimally fits the observed monocular HiRes spectra. In order to account for the contribution to the CR flux from our own galaxy, which plays a significant role at the lowest energies under consideration, the galactic component is added in according to the heavy component identified in the composition measurements of Ref. [6]. The only other free parameter is an overall flux normalization.

Since the neutrino and gamma ray production is calculated with the same Monte Carlo code, the normalization of the simulated cosmic ray spectra to the HiRes monocular results also provides the normalization for the expected neutrino and gamma ray spectra.

2.1.1 Model of the Universe

The Standard Cosmological Model suggests that the universe is uniform (isotropic and homogeneous) at large scales and it is currently expanding. There is also strong evidence that it was hotter and denser in the past. This knowledge comes from the observations of supernovae, galaxies and clusters, the cosmic microwave background radiation, and the abundance of light elements in the cosmos. Together, these data put a strong constraint on possible models of our universe.

The shape of the universe and its ultimate fate is determined by the competition between universal expansion and gravitational pull. The rates of expansion and gravity depend on the pressure and density of matter in the universe. In the case when the pressure is low and can be ignored, density is the crucial parameter for understanding the state of the universe. If the density of the universe is high enough (greater that some critical value), the expansion of the universe, which is described by the Hubble Constant, H_0, will slow and gravity will make the universe contract and eventually collapse on itself ("Big Crunch"). The geometry is closed. Less than critical density will make the universe

expand forever. It is an open universe scenario. If the density is kept at the critical value, this will produce a flat universe.

By making accurate measurements of the cosmic microwave background fluctuations, WMAP (Wilkinson Microwave Anisotropy Probe [106]) is able to measure the basic parameters of the Standard Cosmological Model including the density and composition of the universe. WMAP measurements conclude that universe is flat and its mean energy density is equal to critical. Five years of WMAP data released on 28 February 2008 are summarized in Table 2.1 in form of the basic cosmological parameters (see Appendix A on details of cosmological parameters).

The results in Table 2.1 suggest that only 4.56% of the matter in the universe is made of protons, neutrons and electrons (so called "baryonic matter"). More than 95% of the energy density in the universe is in a form that cannot be directly detected (at least not now). Cold Dark Matter, that interact very weakly with ordinary matter, comprise 23%. There exist many plausible candidates for dark matter (Supermassive Black Holes, Brown Dwarfs, weakly interacting massive particles (WIMPs) and axions). New particle accelerators and direct detections are likely to bring new insight in the coming years. Dark energy, which has a gravitationally repulsive effect, forms 72% of the energy density in the universe. The assumption of dark energy (sometimes referred to as the density of vacuum) explains many cosmological observations at once (the observed distribution of galaxies, accelerated expansion, etc.).

Figure 2.1 plots the confidence regions for density of matter Ω_m (baryonic and Cold Dark matter) vs. vacuum density Ω_Λ with results from three different experimental tech-

Table 2.1. Summary of cosmological parameters. Best-fit cosmological parameters from WMAP five-year results combined with measurements from Type Ia supernova (SNe) and Baryon acoustic oscillations (BAO) [106]

Description	Parameter	Value	Units
Hubble Constant	H_o	$70.5^{+1.3}_{-1.3}$	$km\ s^{-1}\ Mpc^{-1}$
Total Density	Ω_0	$1.005^{+0.0060}_{-0.0061}$	
Baryon Density	Ω_b	$0.0456^{+0.0015}_{-0.0015}$	
Dark Matter Density	Ω_d	$0.228^{+0.013}_{-0.013}$	
Dark Energy Density	Ω_Λ	$0.726^{+0.015}_{-0.015}$	
Spatial Curvature	Ω_k	$0.0179 < \Omega_k < 0.0081$	
Age of the Universe	t_o	$13.72^{+0.12}_{-0.12} \times 10^9$	$years$

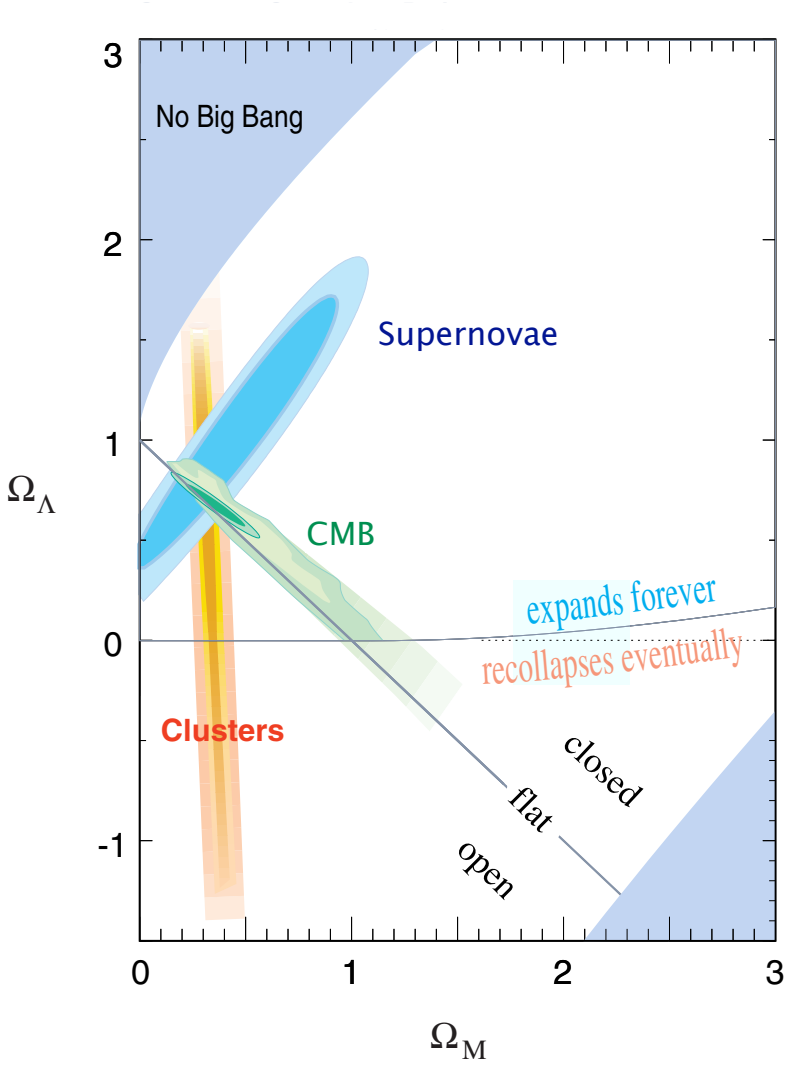

Figure 2.1. Confidence regions of the Ω_m and Ω_Λ (matter density and vacuum energy density, respectively) for current data from supernovae [122], cluster measurements [23], and CMB data [172]. The near horizontal line starting at zero on the vertical axis divides the plot into two regions. Cosmologies above this line will be expanding forever, those that are below the line will eventually stop expanding and recollapse. At high mass densities universe collapse scenario can still win if the vacuum energy density is not big enough, this is reflected in the line beginning to curve upwards as Ω_m increases. The shaded region in the upper left corner labeled "no big bang" corresponds to the "bouncing universe" models [59]. The shaded region in the lower right corner are very young cosmologies (even younger than the oldest heavy element. Cosmological models that reside on solid diagonal line correspond to a flat geometry. Those above the line are closed and open geometries lie below. It can be seen that the expansion future of the universe is not determined by its geometry. Adapted from [122, 172, 23].

niques: measurements of the abundance of galactic clusters [23], redshift measurements of receding supernovae [122], measurements of the cosmic microwave background [172]. Consistent overlap in data from three different experiments confirm that dark energy is the dominant type of energy density, comprising 73% ($\Omega_\Lambda = 0.73$). Density of matter is only 27% ($\Omega_m = 0.27$), which makes a popular assumption of a simple matter dominated universe invalid.

We build our model based on the current state of the universe, meaning that we assume a flat ($\Omega_t = 1$) dark energy density dominated universe with the dark energy and matter energy densities equal to 0.73 and 0.27 correspondingly. We use a Hubble Constant of 71 $km\ s^{-1}\ Mpc^{-1}$.

2.1.2 Model of Proton Propagation

Proton propagation is one of the key features of our model and should be treated very carefully. Though we have made quite a few assumptions that simplify our model, they are well justified for the energy range under consideration.

We begin the propagation simulation by dividing the proton source - observer distance expressed in terms of redshift into 100 equally spaced redshift intervals dz. The same propagation routine is applied to each interval dz. Since it is easier to work with distances expressed in standard cosmological units (Mpc), we start with converting the redshift interval dz to a distance interval ds by exploiting formula A.22 derived in Appendix A. The relationship between the distance and redshift depends mainly on the cosmological model. In case of a flat universe ($k = 0$) and zero radiation energy density the relationship A.22 simplifies to:

$$ds = \frac{c}{H_0} \frac{dz}{(1+z)\sqrt{\Omega_m(1+z)^3 + \Omega_\Lambda}} \tag{2.5}$$

Figure 2.2 shows the distance redshift plots for two flat cosmological models: vacuum energy dominated cosmology with $\Omega_m = 0.27$ and $\Omega_\Lambda = 0.73$ (the cosmological model used in this analysis) and matter dominated cosmology with $\Omega_m = 1$ and $\Omega_\Lambda = 0$. One can see the dramatic difference in the relationship between redshift and distance of these two models.

Proton energy losses over interval ds are estimated by the combination of applying analytical formulas and a Monte Carlo approach. As was mentioned previously there are three main energy loss mechanisms during proton propagation: pair production

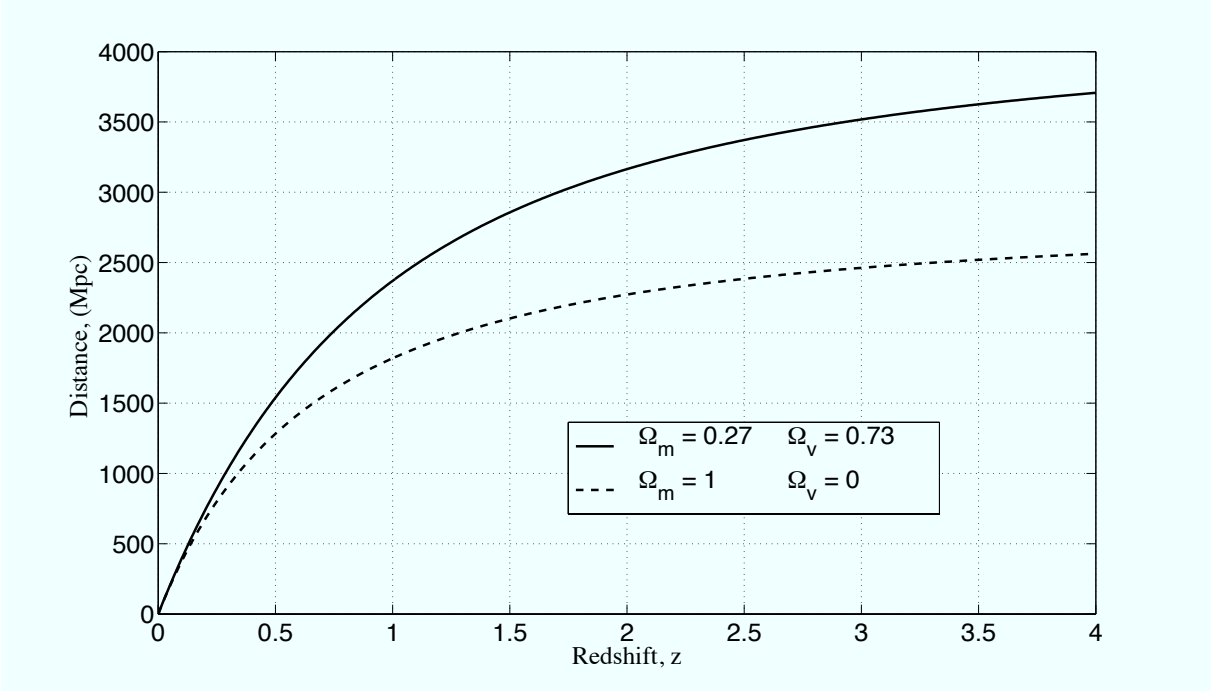

Figure 2.2. Redshift distance relationship for two models of flat cosmologies: vacuum energy dominated with $\Omega_m = 0.27$ and $\Omega_\Lambda = 0.73$ (solid line) and matter dominated with $\Omega_m = 1$ and $\Omega_\Lambda = 0$ (dashed line).

(equation 1.17), photopion reaction(equation 1.18) and energy losses due to the expansion of the universe. According to [41], we define energy losses at $z = 0$ of an ultra relativistic particle with energy E traveling through cosmological distance $ds = c \cdot dt$ as

$$\beta_0(E) = -\frac{1}{E}\frac{dE}{dt} \tag{2.6}$$

Figure 2.3 plots the energy losses β_0 as a function of energy for these processes. For the lowest energies up to $E = 2.4 \times 10^{18}$ eV redshift losses dominate over losses due to interaction on the CMB. In the intermediate energy region $2.4 \times 10^{18} < E < 6 \times 10^{19}$ pair production plays the most important role as an energy loss mechanism. At the highest energies $> 6 \times 10^{19}$ eV photopion energy losses are several orders of magnitude greater than the other two.

To find the energy losses for the cosmological epoch with redshift z one has to apply the following transform:

$$\beta(E, z) = \beta_0(E)(1 + z)^3 \tag{2.7}$$

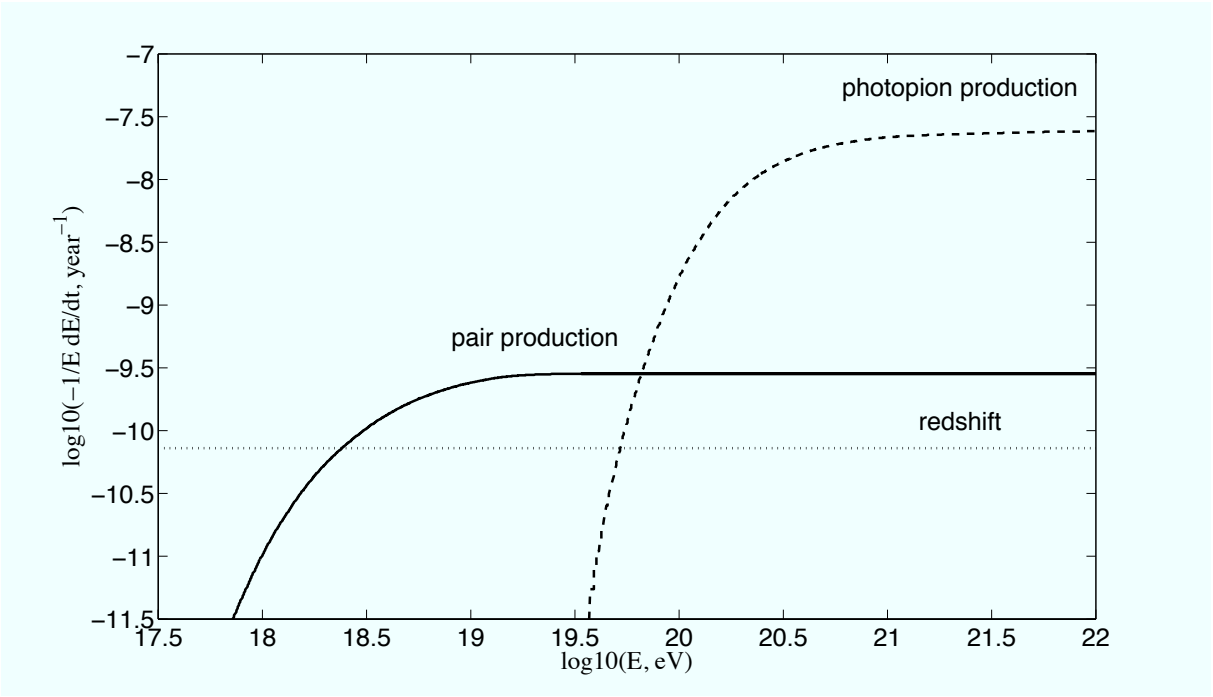

Figure 2.3. UHE proton energy losses at $z = 0$: energy losses due to photopion production, pair production energy losses, and adiabatic energy losses. Based on [41].

There is another way to look at energy losses due to photopion production. One can prove that the final energy of a proton is defined by (for derivation of a more general form of equation 2.8 see Appendix B.4):

$$E_{pf} = (E_{pi} + \epsilon)\left(\frac{s + m_p^2 - m_\pi^2}{2s} - \frac{1}{2s}\sqrt{(s - (m_p - m_\pi)^2)(s - (m_p + m_\pi)^2)}cos(\theta^*)\right) \tag{2.8}$$

Here we assume that $\beta_i^* = 1$ (for a very relativistic particle). E_{pf} is the energy of a proton after the interaction, E_{pi} - energy of the incident proton and ϵ is the energy of the ambient CMB photon. Since $\epsilon << E_{pi}$, we can ignore this term.

$$E_{pf} \simeq E_{pi}\left(\frac{s + m_p^2 - m_\pi^2}{2s} - \frac{1}{2s}\sqrt{(s - (m_p - m_\pi)^2)(s - (m_p + m_\pi)^2)}cos(\theta^*)\right) \tag{2.9}$$

The invariant mass in the case of proton interaction on the CMB photon is

$$s = m_p^2 + 2m_p\epsilon^{'} = m_p^2 + 2E_p\epsilon(1 - \beta cos(\theta)) \tag{2.10}$$

The first term in the brackets of equation 2.9 is also called the mean elasticity

$$K_p = \frac{s + m_p^2 - m_\pi^2}{2s} \tag{2.11}$$

The second term in the equation 2.9 is a measure of the spread of the final energy around the mean:

$$\tilde{K_p} = \frac{\sqrt{(s - (m_p - m_\pi)^2)(s - (m_p + m_\pi)^2)}}{2s} \tag{2.12}$$

Expressing E_{pf} as $E_{pi} - \Delta E$ we get for the amount of energy lost by a proton in the photopion production process:

$$\Delta E \simeq E_{pi}\left(1 - K_p + \tilde{K_p} cos(\theta^*)\right) \tag{2.13}$$

In our model we assume that the angle θ^* is isotropically distributed, thus the mean energy loss per interaction in the observer's frame equals $\Delta E_p = -K_p E_{pi}$ and the energy dispersion is $\Delta E_{rms} \simeq \left(\tilde{K_p}/\sqrt{3}\right)$. The result of 2.13 suggests that the spread in the final proton energy in the observer's frame increases strongly with CMF energy [15] and goes from $K_p \simeq 0.13, \tilde{K_p} \simeq 0$ at the reaction threshold to $K_p = \tilde{K_p} \simeq 1/2$ at the highest energies. The large spread in the final energy at the highest energies does not allow us to apply Berezinsky's formalism of [41] directly. Instead we use it as the first step to calculate the mean number of pion-producing photons $\langle n_{ph} \rangle$ encountered by UHECR proton in a path length $ds = c \cdot dt$ (as suggested by [15]).

$$\langle n_{ph} \rangle = \frac{ds}{K_p \beta(E, z)} \tag{2.14}$$

Following [15], we can approximate the energy loss per interaction using a simple interpolation formula for the mean inelasticity $K_p = \frac{0.2(E_{th}+2.5E)}{E_{th}+E}$, where the threshold energy of the reaction in head-on collisions between protons and low-energy 2.725 K CMB photons is $E_{th} = \frac{m_p m_\pi}{2\epsilon}\left(1 + \frac{m_\pi}{2m_p}\right) \approx 3 \times 10^{11}$ GeV (here $\epsilon = kT \simeq 2.35 \times 10^{-4}$ eV).

The mean number of interactions $\langle n_{ph} \rangle$ is used to find the actual number of photons encountered by an individual particle, which is subject to Poisson statistics. The probability of a particle to encounter zero photons decays as $P(n_{ph} = 0) = e^{-\langle n_{ph} \rangle}$ with the variance in the number of encounters equals to $\chi_n = \langle n_{ph} \rangle^{1/2}$. As pointed out by [15] the

effect of Poisson statistics is important especially for highest energies. For interval ds we draw the number of actual interaction n_{ph} according to the Poisson distribution with the mean equals to $\langle n_{ph} \rangle$ and then divide ds into $n_{ph} + 1$ equal interval, each corresponding to a single photopion creation.

$$dx = \frac{ds}{1 + n_{ph}} \tag{2.15}$$

Now for every interval dx we can find the energy losses.

Photopion production on CMB is the most important energy loss process at the highest energies. Its total cross-section is plotted in Figure 2.4. Figure 2.4 also shows four separate contributions to the total photopion cross-section [33]. They are baryon resonance productions (a resonance is created in the reaction and then it decays into secondary particles); direct production, which refers to residual, non-resonant contributions to direct two-body channels; multipion production; and diffractive scattering. We only use the single-pion ($\Delta^+(1232)$) resonance channel in calculating the cross-section for the reaction. This is a good approximation for the energy range under consideration, since Δ (1232)-resonance has the highest cross section. The direct channel can be also important for highest interaction energies, but is not considered here.

Photopion production through the creation of a Δ (1232)-resonance has the following form:

$$\gamma_{CMB} + p \longrightarrow \Delta^*(1232\ MeV) \longrightarrow \begin{cases} n\ \pi^+ \\ p\ \pi^0 \end{cases} \tag{2.16}$$

As a result of the interaction, a pion and a nucleon are produced. From isospin considerations, the outgoing nucleon has 2/3 probability of being a proton (in this case pion has no charge) and 1/3 probability of being a neutron (positively charged pion is produced). Thus he number ratio of π^0 to π^+ for the reaction is 2:1.

The reaction has a threshold photon energy $\epsilon'_{th} = m_\pi \left(1 + \frac{m_\pi}{2m_p}\right) \simeq 145$ MeV in the proton rest frame, corresponding to zero momentum for the secondary particles. In the observer's frame the threshold energy of a CMB photon will depend on the energy of the CR proton and the angel between two particles and can be approximated as $\epsilon_{th} = \frac{m_p m_\pi}{2E_p} \left(1 + \frac{m_\pi}{2m_p}\right) \simeq \frac{m_\pi}{2\gamma'}$. The photon energies ϵ are drawn randomly from the energy distribution of CMB radiation at epoch z, which is best described by a blackbody spectrum with $kT(z)$. $T(z)$ implies the evolution of the CMB temperature due to the expansion of the universe. An observer on Earth measures CMB corresponding to the

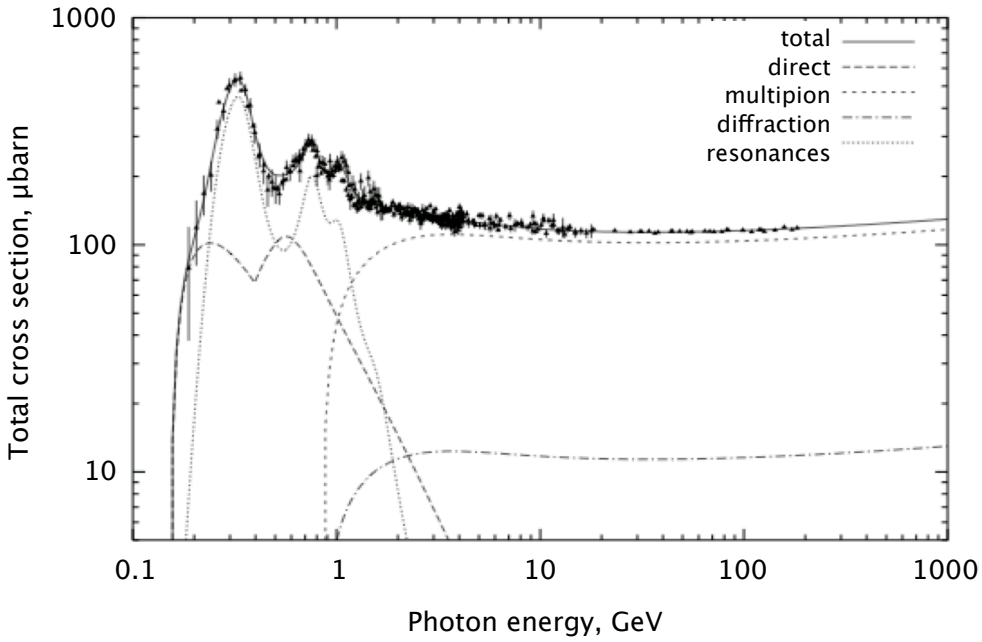

Figure 2.4. Total photopion production cross section as a function of the photon energy in the proton rest frame with four different contributions: baryon resonances, the direct single-pion channel, diffractive scattering, and multipion production. Adapted from [33]

blackbody spectrum with $T_0 = 2.725$ K. The observer at redshift z will measure the same CMB but with the blackbody spectrum corresponding to temperature:

$$T(z) = T_0(1 + z) \tag{2.17}$$

Figure 2.5 shows how the CMB spectrum evolves with redshift. CMB photons are more energetic at higher redshift.

The energies of the secondary nucleon (N) and pion (π) in 2.16 are determined from the collision kinematics (see Appendix B.4). The energies of the particles after the collision in the CMB are:

$$E_N^* = \frac{s + m_N^2 - m_\pi^2}{2\sqrt{s}} \tag{2.18a}$$

$$E_\pi^* = \frac{s + m_\pi^2 - m_N^2}{2\sqrt{s}} \tag{2.18b}$$

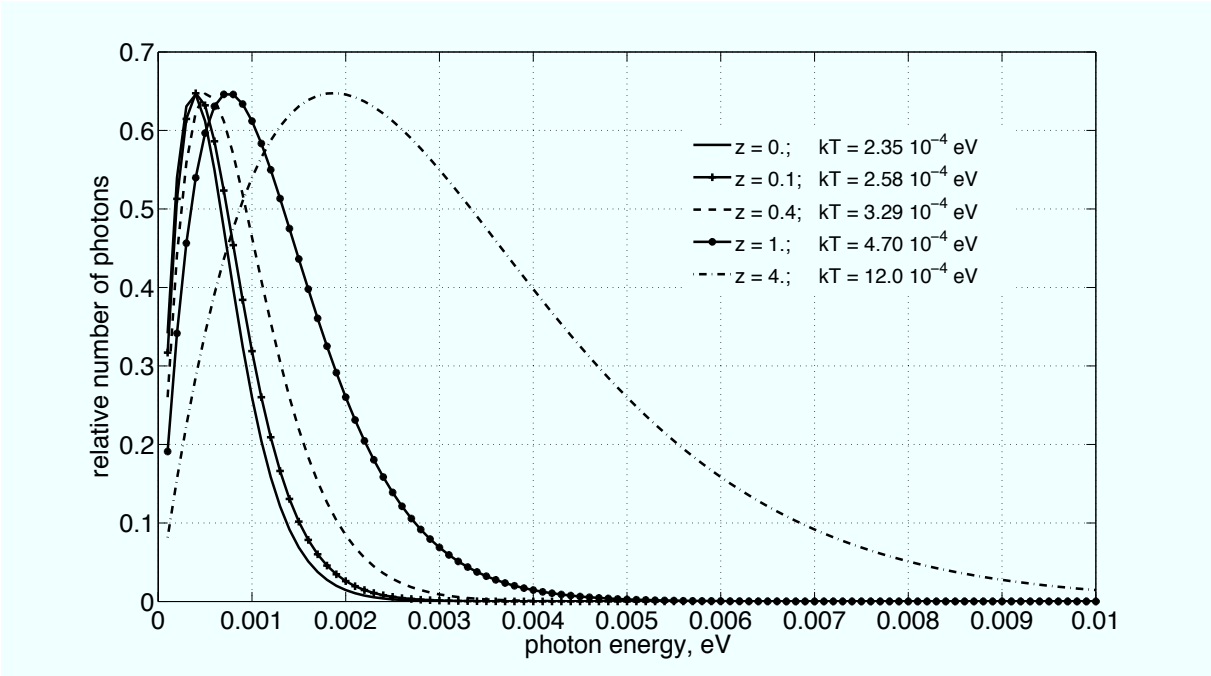

Figure 2.5. CMB blackbody spectra for different redshifts. CMB distribution for current z is described by a thermal blackbody distribution with $kT(z)$.

Here $s = m_p^2 + 2m_p\epsilon^{'}$ is the invariant energy of this system. $\epsilon^{'} = \gamma^{'}\epsilon(1 - \beta^{'}cos(\theta)$ is the photon energy in the proton rest frame. $\gamma^{'} = E_p/m_p$ is the Lorentz boost factor and $\beta = \sqrt{1 - \frac{1}{\gamma'^2}}$. θ is the angle between proton and photon in of and is drawn from a uniform distribution $-1 \leq cos(\theta) \leq 1$. The momenta of secondary particles in CMB are given by (see Appendix B.4):

$$p^* = p_N^* = p_\pi^* = \frac{1}{2\sqrt{s}}\sqrt{(s - (m_N - m_\pi)^2)(s - (m_N + m_\pi)^2)} \tag{2.19}$$

Energies of the particles in the observer reference frame are found by applying inverse Lorenz transforms (see Appendix B.1 for details):

$$E_N = \gamma^* \left(E_N^* + \beta^* p^* cos(\phi^*)\right) \tag{2.20a}$$

$$E_\pi = \gamma^* \left(E_\pi^* + \beta^* p^* cos(\delta^*)\right) \tag{2.20b}$$

where $\phi^* = 180^\circ + \delta^*$ is the production angle in the CMB and is assumed to have a uniform distribution $(-1 \leq cos(\phi^*) \leq 1)$.

In case when a resulting nucleon is a neutron, we assume its instantaneous decay into proton through:

$$n \longrightarrow p\ e^-\ \bar{\nu}_e \tag{2.21}$$

The energies of the decay products in this interaction are found through the three-body decay kinematics discussed in detail in Appendix B.3.

Energy losses at intermediate energies are dominated by the pair production reaction:

$$p\ \gamma_{CMB} \longrightarrow p\ e^+\ e^- \tag{2.22}$$

Pair production energy losses are found using Berezinsky's analytical solution of [41]. Energy losses expressed as $-1/E\ dE/dt$ due to pair production for the current epoch are plotted as a function of proton energy in Figure 2.3. The adjustment for the cosmological epoch with redshift z is done according to 2.7. Thus the amount of energy lost $dE_{e^+e^-}$ in the interval ds by a proton with initial energy E as the result of pair production interactions on the CMB is expressed as:

$$dE_{e^+e^-} = \frac{\beta_{e^+e^-}(E,z)Edx}{c} \tag{2.23}$$

All particles loose energy due to cosmological expansion. The energy loss rate expressed as $-1/E\ dE/dt$ resulting from cosmological redshift is

$$\beta_{rsh} = -\frac{1}{E}\frac{dE}{dt} = \frac{1}{1+z}\frac{dz}{dt} = H(z) \tag{2.24}$$

The universe expansion energy losses for a particle of energy E over interval dx for our universe model are:

$$dE_{rsh} = \frac{EH(z)dx}{c} = \frac{Edx}{c}H_o\sqrt{\Omega_m(1+z)^3+\Omega_\Lambda} \tag{2.25}$$

2.1.3 Model of Neutrino Propagation

Our model of neutrino propagation is quite simple. We consider two processes that contribute to the production of UHE cosmogenic neutrinos associated with photo-pion interaction. As was mentioned earlier (Section 2.1.2) photopion production has a 1/3 probability of creating a positively charged π^+ meson according to:

$$p\gamma_{CMB} \longrightarrow \Delta^*(1232\ MeV) \longrightarrow n\ \pi^+ \tag{2.26}$$

We also learned in section 2.1.2 that the decay of a secondary neutron leads to the production of a proton, an electron and an electron antineutrino:

$$n \longrightarrow p\ e^-\ \bar{\nu}_e \tag{2.27}$$

The other process that contributes to the neutrino production is the decay of an unstable pion ($\tau_{\pi_+} = \gamma \cdot 2.6 \times 10^{-8}$ s) into a muon and a muon neutrino 2.28 and the decay of a muon in $\tau_{\mu_+} = \gamma \cdot 2.197 \times 10^{-6}$ seconds into two neutrinos and a positron 2.29. This results in a total count of two muon neutrinos and one electron neutrino per pion decay:

$$\pi^+ \longrightarrow \mu^+ + \nu_\mu \tag{2.28}$$

$$\mu^+ \longrightarrow e^+ + \nu_e + \bar{\nu}_\mu \tag{2.29}$$

Through the creation of one charged pion in the photopion interaction of UHE protons on the CMB, we end up with four neutrinos (not distinguishing between neutrinos and antineutrinos).

At production, the neutrino flux consists of equal fractions of ν_e, $\bar{\nu}_e$, ν_μ and $\bar{\nu}_\mu$. But due to neutrino oscillation we expect all three neutrino species at Earth. Neutrino oscillation was proven by numerous experiments [130] and can not be ignored. The probability of transition from one neutrino flavor to another is described in a two neutrino approximation as:

$$P_{\nu_i \to \nu_j} = sin^2(2\alpha)\ sin^2(\frac{\Delta m^2 L}{4E}) \tag{2.30}$$

where α is the mixing angle, Δm is the mass difference between the neutrino species and L is the propagation distance.

If the propagation distance is long, it is only essential to account for muon (anti)neutrino oscillations, which currently appear to occur almost exclusively into tau neutrinos (there is little or no oscillation into electron neutrino and this possibility is ignored). The probability of $\nu_\mu \to \nu_\tau$ oscillation is given by $P_{\nu_\mu \to \nu_\tau} = 1/2$, since oscillation lengths are very small in comparison with the distances. Thus on the very long astrophysical path length 50% of the muon neutrinos would be converted to tau neutrinos.

Generated neutrinos lose their energies adiabatically due to the expansion of the universe. Neutrinos generated with energy E at a given z are redshifted to energy:

$$E_\nu(z=0) = \frac{E_\nu(z)}{1+z} \tag{2.31}$$

In our calculations we neglect any possible neutrino interactions along their way to the Earth. This assumption is valid for neutrino energy range considered in our model. If energy of neutrino particles exceeds 10^{15} GeV, their interaction with background relic neutrinos cannot be neglected, since the collision energy can reach the mass of Z-bozons ($Z^0 \sim 90$ GeV). Neutrino interaction cross section is significantly increased for resonance effect described in 1.3.2. Since we do not consider the possibility of the existence of cosmic ray particles above $10^{12.5}$ GeV, the probability of neutrino interaction on relic neutrino background is very small. Cross sections of neutrino interactions with photons of universal backgrounds are several orders of magnitude smaller than neutrino-neutrino interaction and thus are also ignored in this study.

2.1.4 Model of Gamma Ray Propagation

The production and propagation of the UHE gamma rays requires more consideration as compared to neutrino case. GZK gamma rays are created through the decay of neutral pions ($\tau_{\pi_0} = \gamma \cdot 0.87 \times 10^{-16}$ s). There is 2/3 probability of a neutral pion creation in proton interaction on the CMB and the subsequent decay of the Δ^+ resonance:

$$p\ \gamma_{CMB} \longrightarrow \Delta^*(1232\ MeV) \longrightarrow p\ \pi^0 \tag{2.32}$$

Each pion decays into two gamma rays:

$$\pi^0 \longrightarrow \gamma + \gamma \tag{2.33}$$

Following their production, gamma rays will with high probability convert into electron-positron pairs through interaction on the CMB:

$$\gamma\ \gamma_{cmb} \longrightarrow e^+\ e^- \tag{2.34}$$

The probability of pair creation on the CMB is calculated in Ref. [89] and the derivations are repeated in Appendix C.

Figure 2.6 contours photon survival probability $P_{surv} = e^{-\tau}$ in the photon energy and propagation distance diagram. As one can see only very energetic photons that are

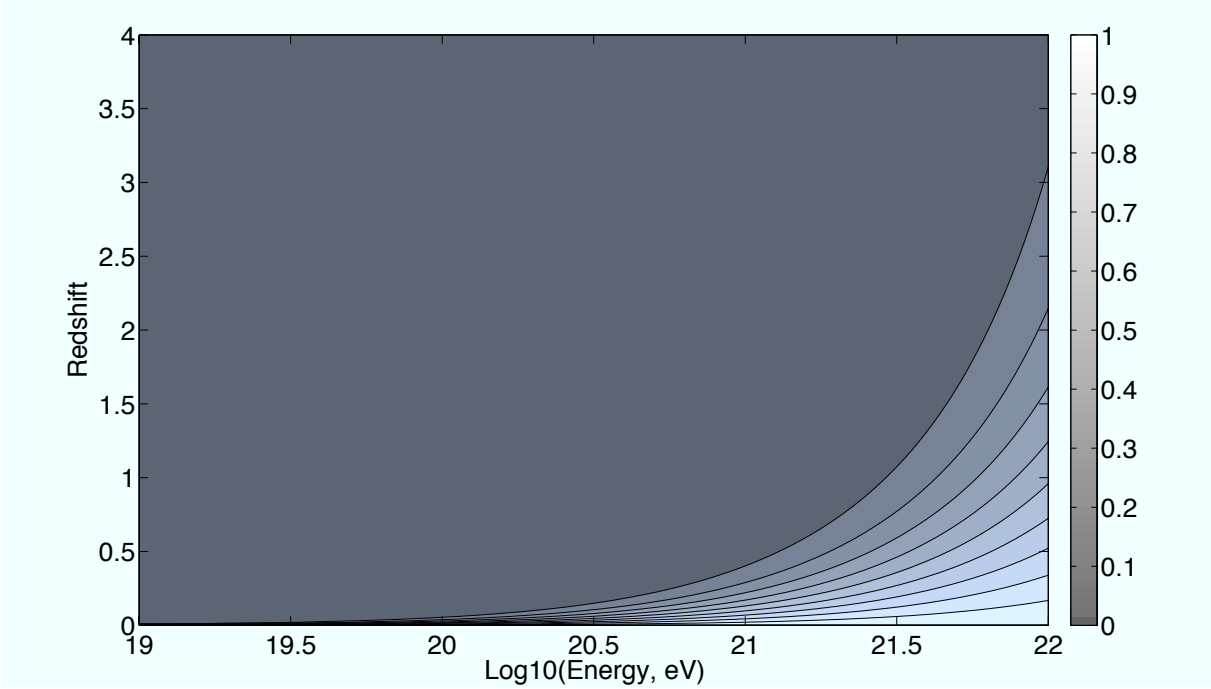

Figure 2.6. Photon survival probability in the CMB as a function of energy and propagation distance (redshift) presented as probability contours (calculations are based on [89]).

created close by have a nonzero probability to reach the observer on Earth. Nevertheless GZK photons can be observed at lower energies and the reason for that is that γ-rays will generate electromagnetic (EM) cascades while propagating. In the extreme Klein-Nishina limit ($s >> m_e^2$) UHE electrons or positrons produced by pair production end up with most of the initial photon energy and later transfer most of the energy back to photons by inverse Compton scattering [131]. Thus the attenuation length of the cascade photons is considerably increased [132].

$$e\ \gamma_{cmb} \longrightarrow e\ \gamma \tag{2.35}$$

Pair production (PP) 2.34 and inverse Compton scattering (ICS) 2.35 are the two main processes that drive the EM cascade. If an extragalactic magnetic field (EGMF) is present, the synchrotron energy loss for the electrons should be considered, which results in the development of the EM cascade being heavily suppressed [132]. For more details refer to Ref. [132]. The synchrotron energy loss rate for a charged particle with mass m, energy E, and charge qe subject to a magnetic field of strength B is given by [108]:

$$\frac{dE}{dt} = -\frac{4}{3}\sigma_T \frac{B^2}{8\pi}\left(\frac{qm_e}{m}\right)^4 \left(\frac{E}{m_e}\right)^2 \tag{2.36}$$

Here σ_T is the Thomson cross section and m_e is the electron rest mass. The loss rate is proportional to the particle's energy and thus has the greatest effect in the UHE regime. It is also inversely proportional to m^4 and at the same energy will be substantial for electron and negligible for protons.

Deflection is the second effect of the magnetic field on the propagation of the charged particles. One dimensional treatment of the propagation of CR particles does not work if the gyroradius of a charged particle is much greater than its propagation distance [131]. The gyroradius of a charged particle with charge qe and energy E propagating in a magnetic field with a component $B_\perp$ perpendicular to the particle motion is given by:

$$R_g \simeq \frac{E}{qeB_\perp} \simeq 1.1 \times 10^3 \frac{1}{q}\left(\frac{E}{10^{21}\ eV}\right)\left(\frac{B_\perp}{10^{-9}\ G}\right)\ Mpc \tag{2.37}$$

In the case of a simple model of a homogeneous and isotropic distribution of CR sources, the influence of the deflection on the resulting shape of the particle spectrum becomes small [131] and a straight line propagation approximation is adequate for many relativistic situations. The argument here is that for any charged particle that becomes deflected away from the line of sight there is always another one that is deflected into the line of sight [28]. This simple model of a homogeneous and isotropic distribution of CR sources is supported by the distribution of large scale structure (LLS) in the observable universe. Some anisotropy is only detectable for LLS within the radius of 50-100 Mpc form the Earth.

HE electrons and positrons produced in 2.27 and 2.29 also initialize electromagnetic cascades and contribute to the gamma ray flux at lower energies. Pairs from proton interaction on CMB also initiate EM cascades which feed the lowest part of the gamma ray spectrum at Earth. Since pair production is considered as a continuous energy loss process, we are following Sigl in [28] to estimate the number of pairs produced by knowing the energy of the primary proton E_p and its energy loss dE_p. Pairs are following a power law distribution of 2.38 in the energy region from $E_{min} \simeq \frac{m_e^2}{8\epsilon}$ till $E_{th} \simeq \frac{4E_p^2\epsilon}{4E_p\epsilon + m_p^2}$. m_p and m_e are the proton and electron masses, respectively, ϵ is the CMB photon energy.

$$\frac{dn_{e^+e^-}}{dE_e} = NE_e^{-7/4} \tag{2.38}$$

where $N = dE_p / \sum_{E_i=E_{min}}^{E_{th}} n_{e^+e^-}(E_i)E_i$.

For the muon and neutron decay the energies of the secondary particles are calculated using the three body decay algorithm of Appendix B.3. The pion decay is calculated using the appropriate two body decay kinematics of Appendix B.2.

To model the development of electromagnetic cascades we used a corresponding module of the CRPropa version 1.3.4 numerical tool [28]. CRPropa was designed as a numerical tool that propagates UHECR and their secondaries through extragalactic distances in a user defined model of the universe. We are only using a one-dimensional transport code that solves electromagnetic cascades propagation that is based on Ref. [131]. The code takes all relevant interactions with background photons into account, including single pair production ($\gamma\gamma_{CMB} \rightarrow e^+e^-$), double pair production ($\gamma\gamma_{CMB} \rightarrow e^+e^-e^+e^-$), inverse Compton scattering ($e\gamma_{CMB} \rightarrow \gamma e$), and triplet pair production ($e\gamma_{CMB} \rightarrow ee^+e^-$). Synchrotron losses of electrons are also taken into account and the resulting lower energy synchrotron photons are followed in the subsequent EM cascades. The photons and pairs are followed until either their energy drops below 100 MeV or they reach the observer.

CRPropa has three different photon backgrounds implemented in its code: CMB, low energy photon infrared background (IRB) and universal radio background (URB). CMB is identical to the one we used for the proton propagation. There are three different IRB distributions that can be chosen which are all consistent with recent limits from blazar observations [28]. The spectrum of the low and high Franceschini [78] and Primack [151] models of IRB are shown in Figure 2.7. IRB has a peak around 1 μm in wavelength due the to direct emission from stars and a second peak at 100 μm due to reprocessing of the starlight by interstellar dust [131]. They become important for EM cascades around the threshold for pair production (at about $10^{12} - 10^{13}$ eV) and are less significant in the UHE region. Since the pair production cross section peaks around $\simeq 3 \times 10^{19}$ eV interactions with URB become more important around this energy and govern the cascade development despite the fact the number density of radio background photons is much smaller than that of CMB photons [131]. Weak and strong versions of URB are implemented based on Ref. [152] and observations [61].

Though the CMB redshift evolution is well known, the redshift evolution of the IRB and URB is more complicated since they not only evolve in time due to the expansion of the universe but also evolve due to the evolution of the respective sources [131] (the evolution of radio galaxies in case of URB and normal galaxies in case of IRB). The nontrivial redshift evolution of the URB is implemented in the cascade module of

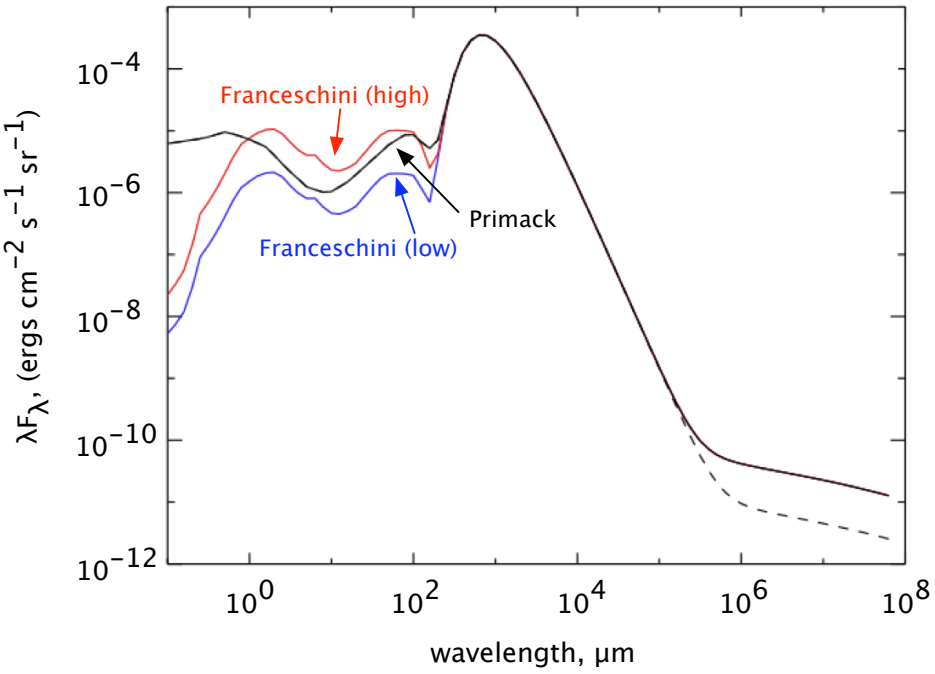

Figure 2.7. Models of infrared background at zero redshift implemented in [28] and used for EM cascade development. Adapted from [28].

CRPropa analogous to [131]:

$$n_{URB}(\epsilon, z) = (1+z)^2 \int_z^{\infty} \frac{4\pi\Phi[(1+z')\epsilon/(1+z), z']}{H(z')} dz' \tag{2.39}$$

where $\Phi_{URB} = \phi_{URB}(\epsilon) g_{URB}(z)$. $\phi_{URB}(\epsilon)$ is motivated by observations [61] and $g_{URB}(z) = 10^{1.18z - 0.28z^2}$ is based on theoretical estimates of [152].

IRB is assumed to come from ordinary galaxies which formed early in the universe, at $z_b = 5$ with the redshift evolution in the form:

$$n_{IRB}(\epsilon, z) = \begin{cases} (1+z)^2 n_b \left(\frac{\epsilon}{1+z}, z=0\right), z \leq z_b \\ 0 \qquad\qquad\qquad\qquad , otherwise \end{cases} \tag{2.40}$$

Here $n_b = 2 \times 10^{-3}$ cm^{-3} is the optical background density today.

In this model we assume a random EGMF with a strengths that can be varied between 10^{-12} G and 10^{-9} G and a correlation length of 10 Mpc.

2.2 Results and Discussion

Our Monte Carlo provides the spectra of cosmic ray protons as well as secondary neutrinos and gamma rays for a total number of 400 source redshifts starting from 0 and going up to $z = 4$. By adding proton spectra assuming different m and γ (and also z_{cr} and $z_{cut-off}$) parameters, we can select those that produce an overall cosmic ray spectrum (up to the normalization constant) that best fits the HiRes data. At lower energies galactic iron is added according to the heavy component identified in the HiRes-MIA composition measurements [7]. The only other free parameter is an overall flux normalization. Then the best fit values of the parameters as well as the flux normalization constant derived from the best fit are used to build up secondary particle (neutrino and gamma ray) spectra.

2.2.1 Simulated Cosmic Ray Energy Spectrum

The proton spectrum at Earth is built by adding resulting spectra of proton propagation from different redshifts. First, spectra of different z-shells are added assuming a uniform energy distribution of primary particles. The spectrum from each shell is weighed with an appropriate weighting function $\mathcal{L}(z)$ to take the cosmological source evolution in the expanding universe into account.

The weighting function $\mathcal{L}(z)$ is a product of two functions as in:

$$\mathcal{L}(z) = \mathcal{H}(z)\eta(z) \tag{2.41}$$

where $\mathcal{H}(z)$ parameterizes the cosmological source evolution and $\eta(z)$ takes care of cosmological expansion. $\eta(z)$ for our cosmological model is defined as

$$\eta(z) = \frac{dt}{dz} = \frac{1}{H_0(1+z)}\sqrt{\Omega_m(1+z)^3 + \Omega_\Lambda} \tag{2.42}$$

We consider three different models of cosmological source evolution: "simple" as in 2.2, "flat" as in 2.3 and "exponential cut-off" as in 2.4. The source function dependence on redshift is plotted for all three of these model in Figure 2.8.

Since our Monte Carlo was generated assuming isotropy in neutrino flux, contributions from z-shell are convolved with the $E^{-\gamma}$ proton injection function to obtain the final extragalactic spectra on Earth. The overall extragalactic GZK flux is obtained by summing up the contributions from all the shells. Figure 2.9 shows how different shells are added to produce the resulting proton GZK flux at Earth. A series of colored lines

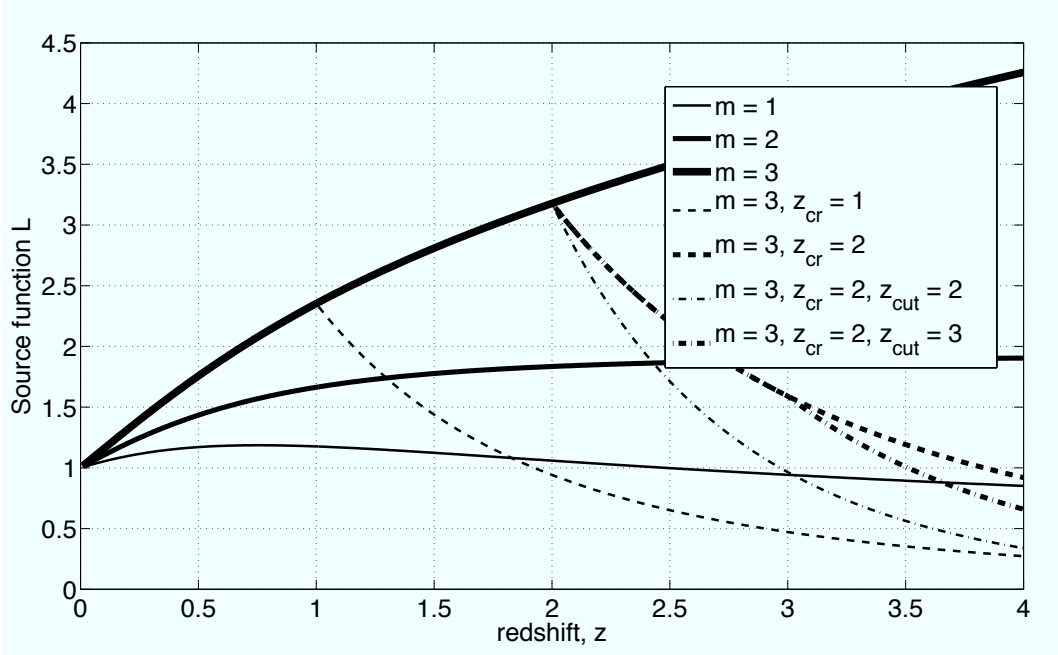

Figure 2.8. Redshift dependence of cosmological source function for three models. Simple model is shown in solid lines for three parameters m=1, m=2 and m=3. For the m=3 case two dashed lines illustrate the flat model behavior with the $z_{cr} = 1$ and $z_{cr} = 2$. For the m=3, $z_{cr} = 2$ case additional dashed-dotted lines are drawn to indicate the cut-off model with $z_{cut-off} = 2$ and $z_{cut-off} = 3$.

in this figure show the contributions from different shells. Not all 400 contributions are present. Instead each line shows the contributions from a range of z shells. The first one marked by z=0.01 corresponds to the flux from protons propagated from z=0.01. It contributed 9% to the total flux. The first shell was set as a standard flux contribution, used to find the subsets of shells that will contribute approximately the same amount to the total flux. Thus the second line on the figure shows that z-shells z=0.01 and z=0.03 together contribute 12%. We can see that as we go higher in redshift the number of z-shell needed to achieve the contribution of the first shell grows. The last line marked by z=4.00 shows the summarized flux of all the shells from z=1.13 to z=4.0. The extragalactic GZK proton flux results from adding the fluxes of all 400 z-shells (Figure 2.9).

Figure 2.9 illustrates that there is a correlation between cosmic ray energies and the average redshift of their origin. Due to the energy loss processes particles coming from different redshifts contribute to different energies of the cosmic rays spectrum on Earth. Thus low redshift shells will shape the highest energy part of the spectrum, while protons

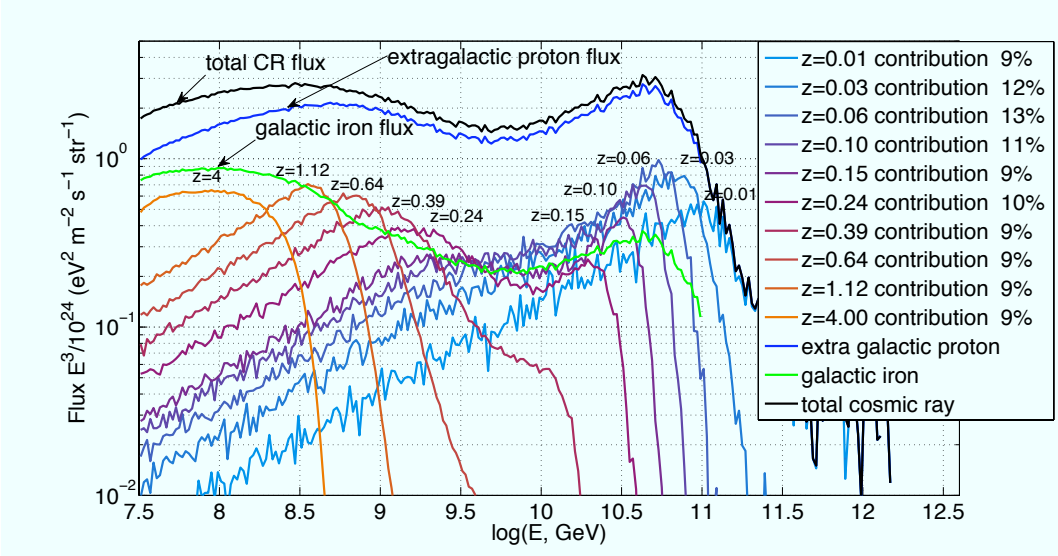

Figure 2.9. The model prediction of CR fluxes from sources at different redshift shells and their contributions to overall extragalactic proton energy spectrum at Earth. Galactic iron is given as a fraction of the light extragalactic component according to the HiRes composition studies. Overall CR flux is the sum of extragalactic proton and galactic iron fluxes.

originated at largest redshifts will loose a significant amount of their initial energy and can only effect the low energy part of the spectrum.

At the last step, the heavy galactic component (Figure 2.9) is added as a fraction of the light extragalactic one according to the HiRes composition studies. The resulting CR flux on Earth is shown as a top line in Figure 2.9. Based on HiRes X_{max} composition study, the galactic component can be parameterized as:

$$Flux = Flux_{ext.}(1 + 0.01\epsilon_{gal}) \tag{2.43a}$$

$$\epsilon_{gal} = \begin{cases} -41.18\ logEeV + 755, & 17.0 \geq logEeV < 17.85 \\ -3.72\ logEeV + 86.42, & 17.85 \geq logEeV < 20.0 \\ 0, & otherwise \end{cases} \tag{2.43b}$$

The results for our first model of source redshift evolution, $(1+z)^m$, are shown in Figure 2.10(a). Fitting to the HiRes monocular spectra suggest the best fit values of $m = 3.31$ and $\gamma = 2.44$. This model fits the spectrum well, reproducing the well known features of the ankle and the GZK cut-off. χ^2 for the fit equals 60.26 for 39° of freedom. χ^2 contours for the fit are shown in Figure 2.10(b).

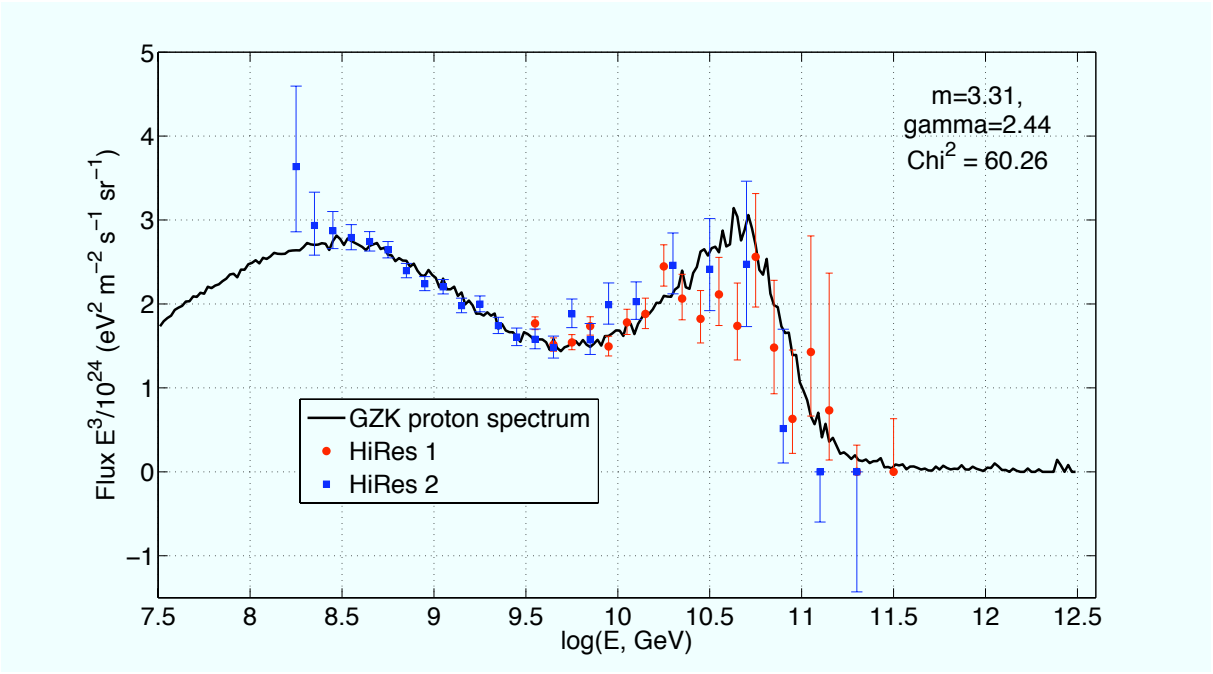

(a) Best USM-plus-galactic fit

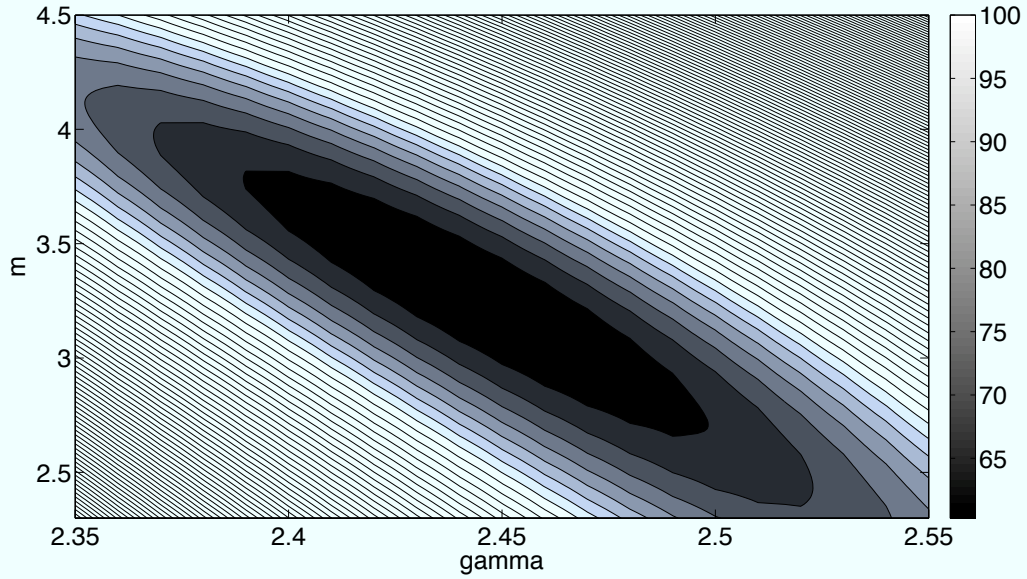

(b) χ^2 contours for the USM-plus-galactic fit

Figure 2.10. Best USM-plus-galactic fit to the HiRes monocular spectra for the simple evolution model.

Between $10^{19.4}$ and $10^{19.7}$ eV our model over estimates the cosmic ray flux, as measured by HiRes. Bergman in [44] claims that this is due to the sharp cut-off in the energy spectrum of our model at $10^{21.5}$ (no particle are generated beyond this energy), which may not reflect the source distribution of maximum energies. Relatively poor agreement at the lowest energies may be due to our estimate of the galactic component.

Following Bergman [44] we studied the sensitivity of the fit to both m and γ. Figure 2.11(a) shows the fits for the best fit γ and several different m values. Fits with best fit m and different γ are presented in Figure 2.11(b). The plots suggest that the spectrum is most sensitive to γ in the "ankle" region and especially around the rise above the ankle, while m mostly effects the low energy part around the second "knee" (this region is also sensitive to gamma). The conclusion is that the fit is more sensitive to the spectral index of the original proton flux rather than to a change in the evolution of sources. It is also interesting to note that an increase in m and γ delays the onset of the so called "second knee" and decreases the flux at highest energies.

Our second model of the source redshift evolution with a constant evolution above z_{cr} suggest the same best fit values for m and γ. It was also discovered, that all the values of $z_{cr} > 2.16$ give the same χ^2 for the fit, which is exactly equivalent to the χ^2 value of the simple model described above. Lowering z_{cr} below 2.16 results in worse fits to the HiRes spectrum. The comparison of the resulting spectra from two models is plotted in Figure 2.12.

The comparison of the two models suggest that z-shell above z=2.16 do not play a significant role building the cosmic ray spectra that will match observed HiRes data. Shells above z=2.16 contribute to the lower energies, where HiRes data are not available and thus they do not participate in choosing the best fit parameters m and γ.

As for the z_{cr} model, the last model of source evolution (with the exponential decay above $z_{cut-off}$), it does not improve the agreement between HiRes data and the simulated GZK cosmic ray flux, but introduces more discrepancy at lower energies.

It is also important to mention that our estimation of the best fit parameters and performance of the source evolution models depend significantly on the estimation of the galactic component of the cosmic rays flux from the composition measurements by X_{max} technique. The galactic component effects the lowers energy bins on the predicted flux, where the main disagreement between the models exists.

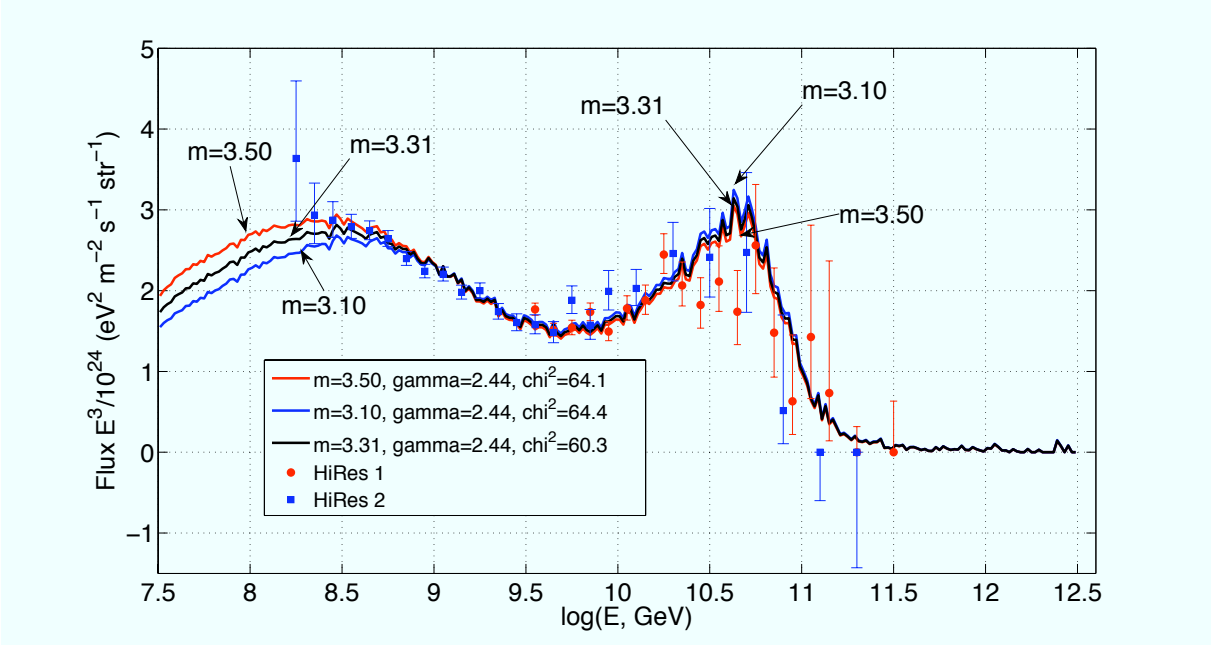

(a) Sensitivity to parameter m

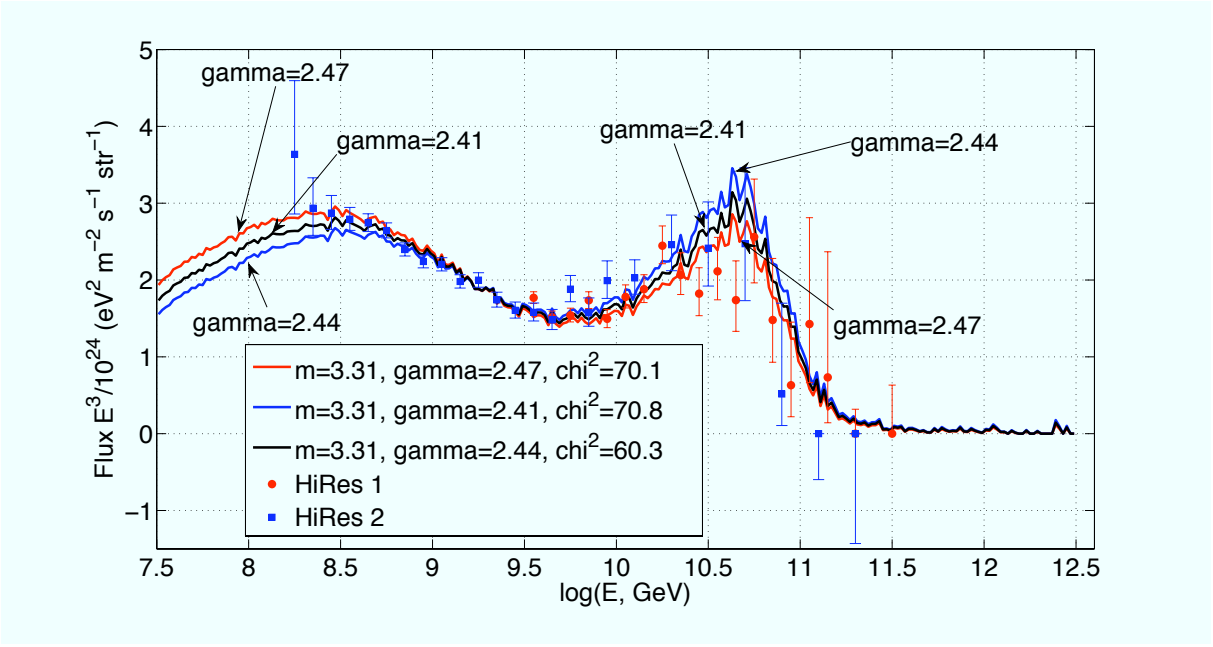

(b) Sensitivity to parameter γ

Figure 2.11. Sensitivity of the USM-plus-galactic fit to parameters m and γ for the simple evolution model.

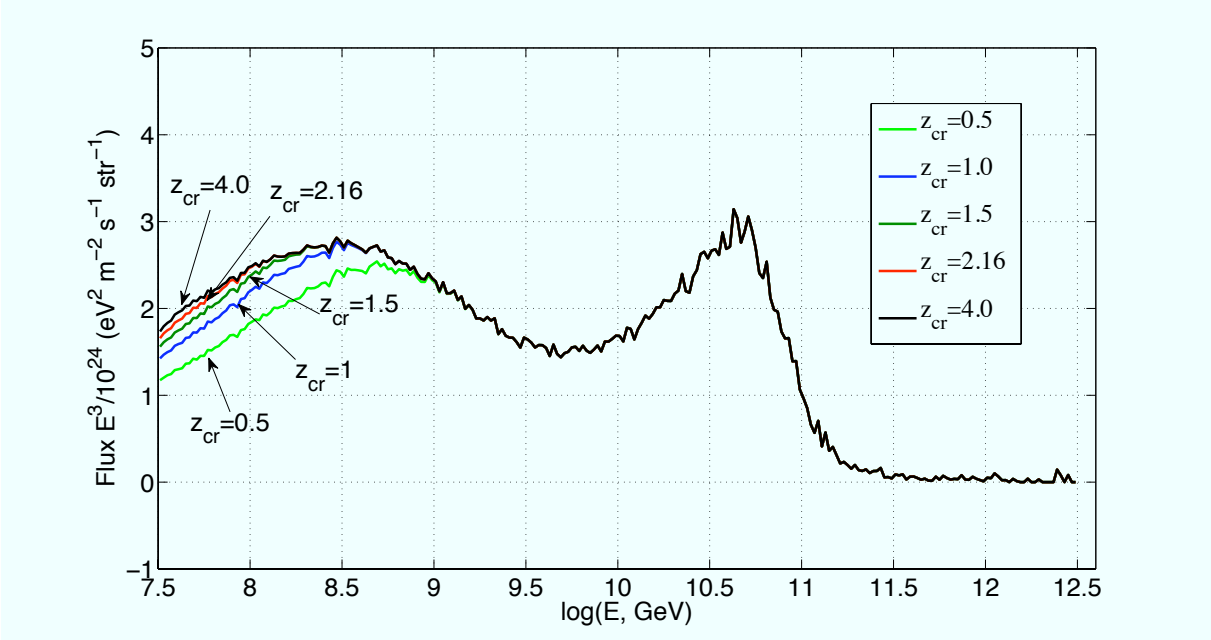

Figure 2.12. Sensitivity of the USM-plus-galactic fit to parameter z_{cr}.

2.2.2 GZK Neutrino Fluxes

The best fit parameters of the previous subsection were used to calculate the resulting cosmogenic neutrino flux. GZK neutrinos are produced in the photopion interactions of UHE protons with the CMB photons. Neutrinos produced in these interactions are followed along straight lines till they reach the observer on Earth. Since the neutrino production is calculated with the same Monte Carlo code, the normalization of the simulated proton spectra to the observed HiRes one provides the normalization for the neutrino fluxes. Figure 2.13 shows the prediction for cosmogenic neutrino fluxes for the best fit parameters $m = 3.31$ and $\gamma = 2.44$.

Figure 2.13 shows that two types of neutrino particles from muon decay (ν_e and $\bar{\nu}_\mu$) have similar contributions to the total GZK neutrino spectrum on Earth, while ν_μ from pion and $\bar{\nu}_e$ from neutron decay contribute to lower energies.

Analogous to the proton spectrum, Figure 2.14 shows the contributions to the total cosmogenic neutrino flux from different z-shells. The shells plotted in the figure are of variable thickness. The shells are marked by their upper boundaries. The lower boundary of the shell corresponds to the upper boundary of the previous shell. The shells were picked so they are accounted approximately for 10% of the total flux.

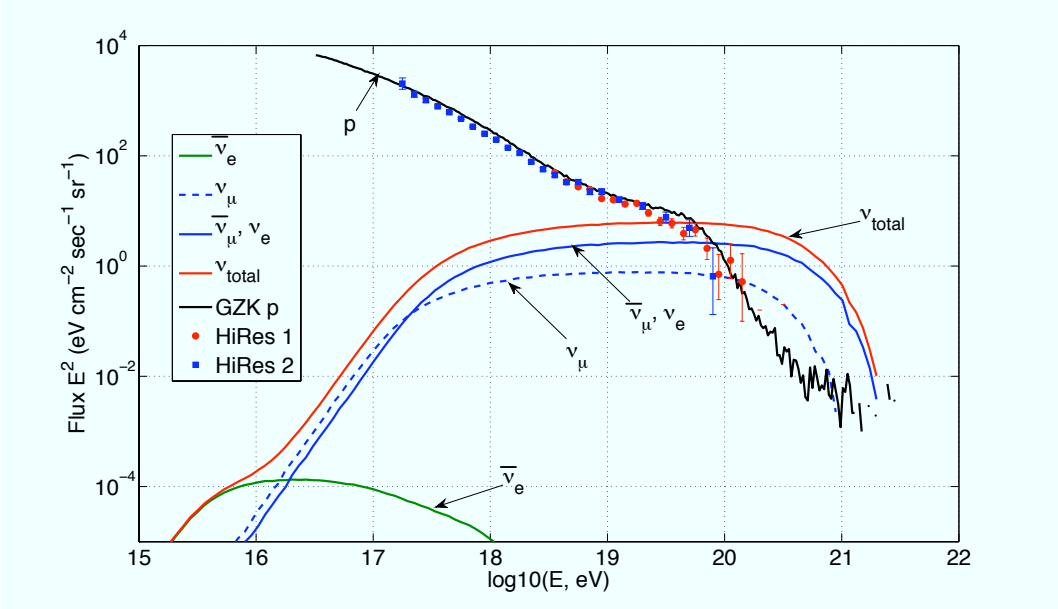

Figure 2.13. HiRes motivated secondary cosmogenic neutrino fluxes based on the USM-plus-galactic best fit to the HiRes monocular data.

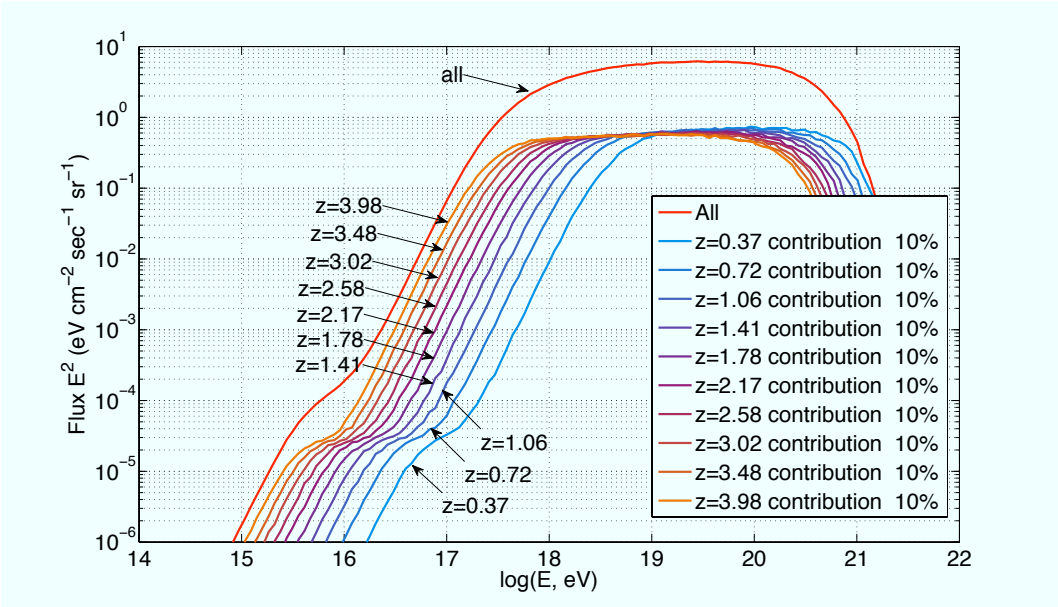

Figure 2.14. Contributions to secondary cosmogenic neutrino flux from z-shells (proton sources at different redshifts) and their contributions to overall extragalactic GZK neutrino energy spectrum at Earth.

As can be seen in Figure 2.14, shells have equal thickness in first approximation. Another interesting observation is that neutrino z-shells are just translated to lower energies with no noticeable relative change in the shape. No difference in the positions of the shells along the vertical axis is observed. Thus one expects the total flux to be broadened as we add more z-shell into our model. Figure 2.15 illustrates the change in the total cosmogenic neutrino flux as we constrain the total number of z-shell that are used to build the spectrum. There is no surprise that as more shells are added total neutrino flux increases. Interesting is the fact that with every new shell its contribution to the total flux is smaller, but is plays a greater role in broadening the peak of the flux.

Based on the observations above one can conclude that by setting the redshift limit at 4, we are probably underestimating the cosmogenic neutrino fluxes at Earth, provided that there are UHE cosmic ray sources located further than z=4. This especially applies to the lower energies. The mistake we are making, however, should not be too big, since the main contribution to the total flux comes from close by shells.

We also study the sensitivity of the neutrino flux to our model parameters m and γ. Figures 2.16 and 2.17 summarize the study. Neutrino fluxes are more sensitive to the spectral index γ. A harder spectrum can actually decrease the neutrino flux by orders of magnitude. A softer spectrum produces a greater flux. The influence of the evolution parameter m on the total neutrino spectrum is not that significant, but still stronger evolution results in a higher neutrino flux.

2.2.3 UHE Gamma Ray Fluxes

Secondary gamma ray flux resulting from UHECR propagation over cosmological distances relates to two different processes that contribute to EM cascades. GZK related photopion production interactions of UHECRs with CMB photons create UHE gamma rays, electrons and positron, that cascade down to GeV - TeV energies, energies at which the universe is no longer opaque to photons. Pair production by protons on low energy photons is the second source of secondary gamma rays. Figure 2.18 presents our estimates of secondary gamma ray fluxes due to both GZK processes and pair production for the best fit parameters $m = 3.31$ and $\gamma = 2.44$.

Figure 2.18 suggests that diffuse gamma ray fluxes from CR propagation are dominated by EM cascades initiated by π^0 decays at higher energies and initiated by pair production at lower energies. The two processes becomes equally important at around 10^{14} eV. π^+ decay products (e^+ and e^-) are not significant in terms of contributing to

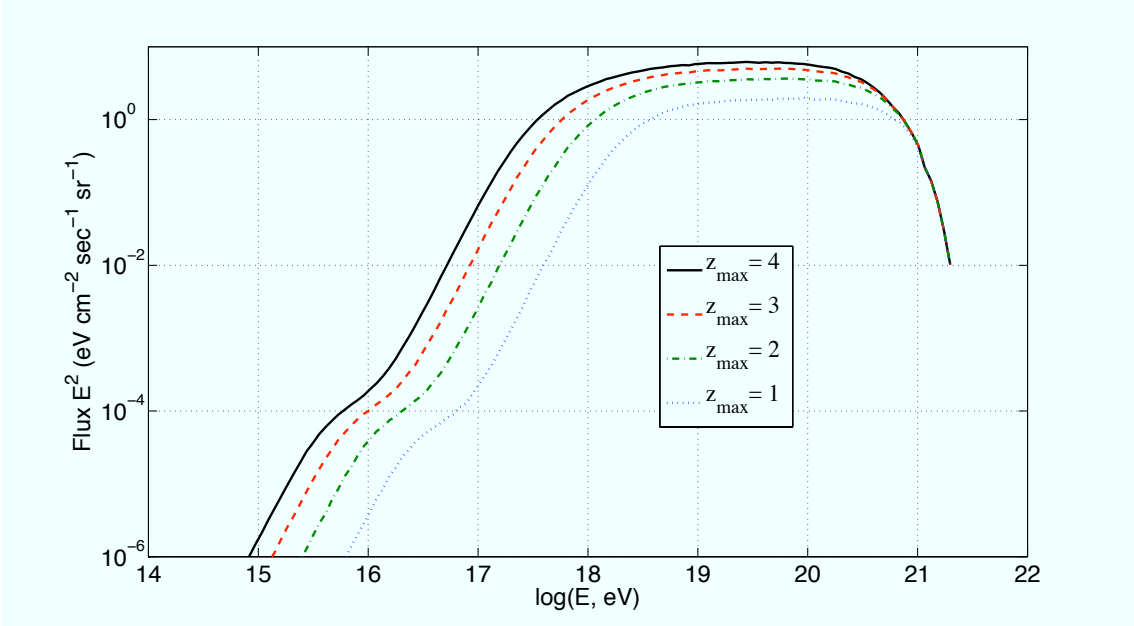

Figure 2.15. Sensitivity of secondary cosmogenic neutrino flux to parameter z_{max}.

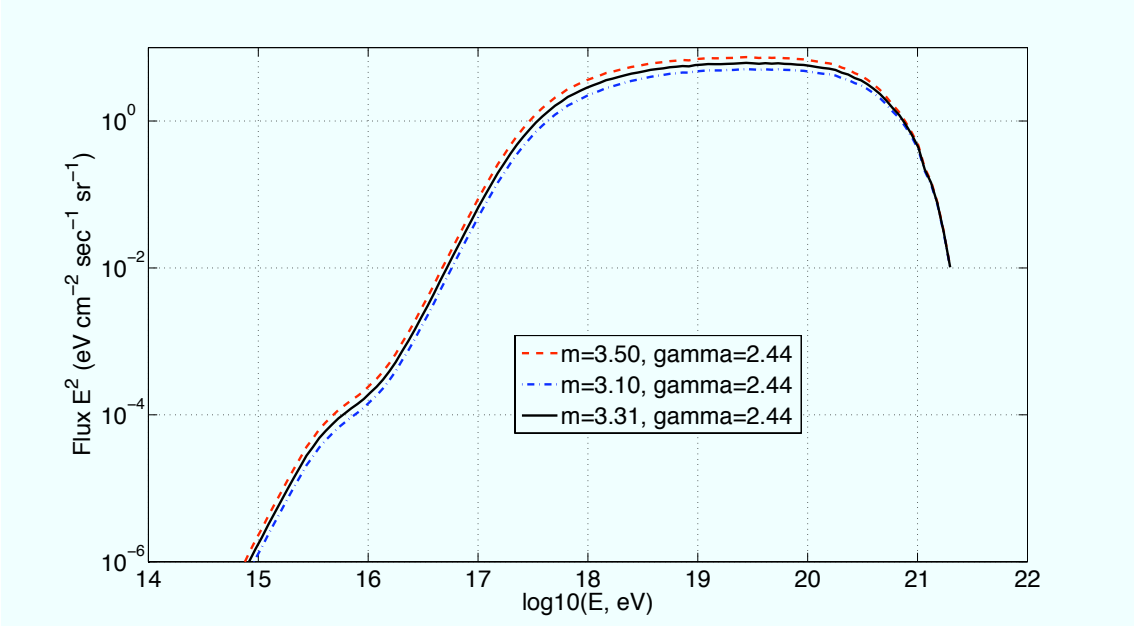

Figure 2.16. Sensitivity of secondary cosmogenic neutrino flux to parameter m.

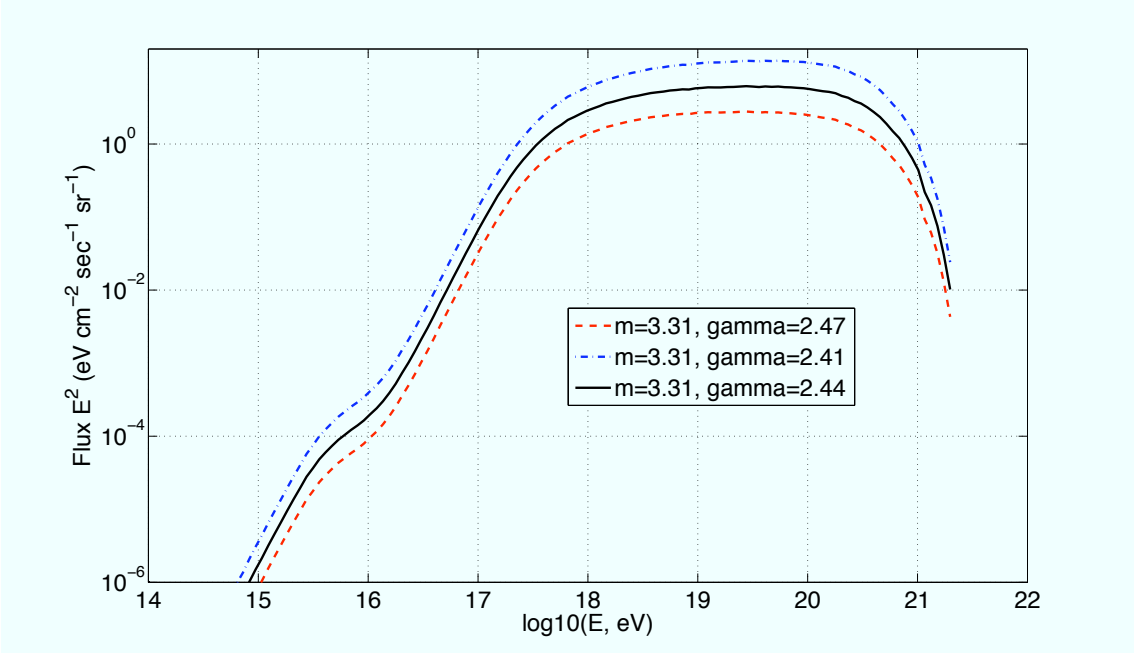

Figure 2.17. Sensitivity of secondary cosmogenic neutrino flux to parameter γ.

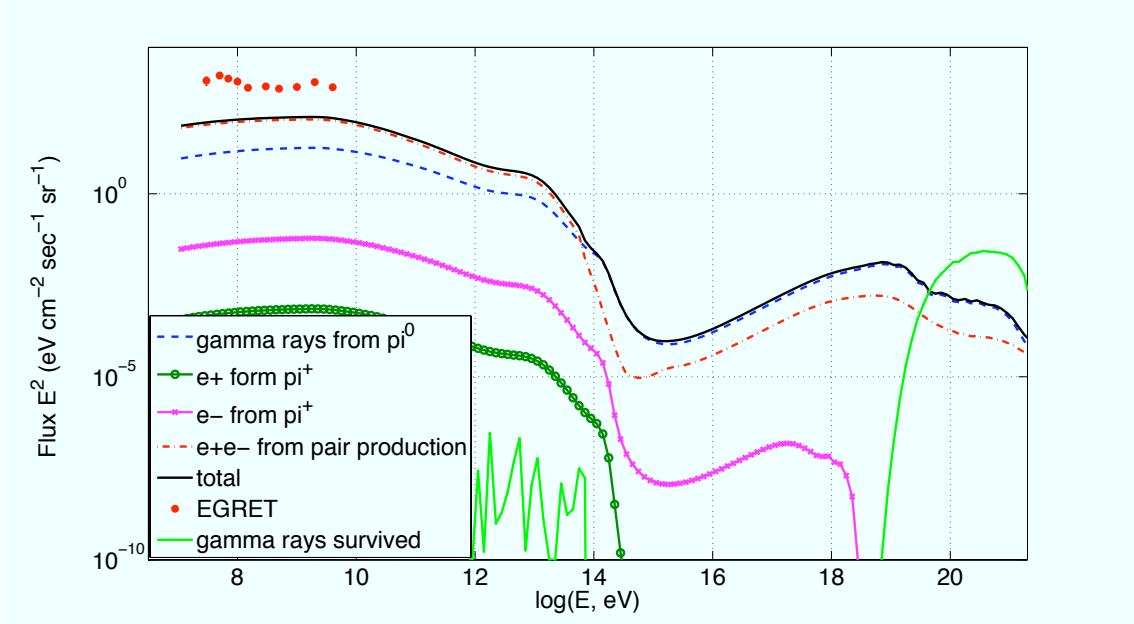

Figure 2.18. HiRes motivated secondary gamma ray fluxes based on the USM-plus–galactic best fit to the HiRes monocular data.

the diffuse secondary gamma ray flux and can be ignored without any effect on the total flux.

The extragalactic diffuse γ-ray background deduced from the Energetic Gamma Ray Experiment Telescope (EGRET) [173] aboard the Compton Gamma-Ray Observatory is shown by filled circles in Figure 2.18. Our estimated gamma ray flux is only a tiny fraction of diffused flux measured by EGRET. More sensitive experiments such as GLAST [88] may be able to detect fluxes of the magnitude, indicated here.

Figure 2.18 also shows our estimated flux for gamma rays that are created in π^0 decays and reach Earth without any interaction with CMB photons. Gamma ray survival probability is calculated based on Ref. [89] (Appendix C). This simple model overestimates γ-flux at highest energies and underestimates it at lower ones, since the development of EM cascades is not considered here.

As in the case of proton and neutrino fluxes we study the sensitivity of our results to different model parameters. Figures 2.19, 2.20 and 2.21 summarize our effort to estimate how much the resulting secondary gamma ray flux changes due to changes in m, γ and z_{max} parameters, respectively.

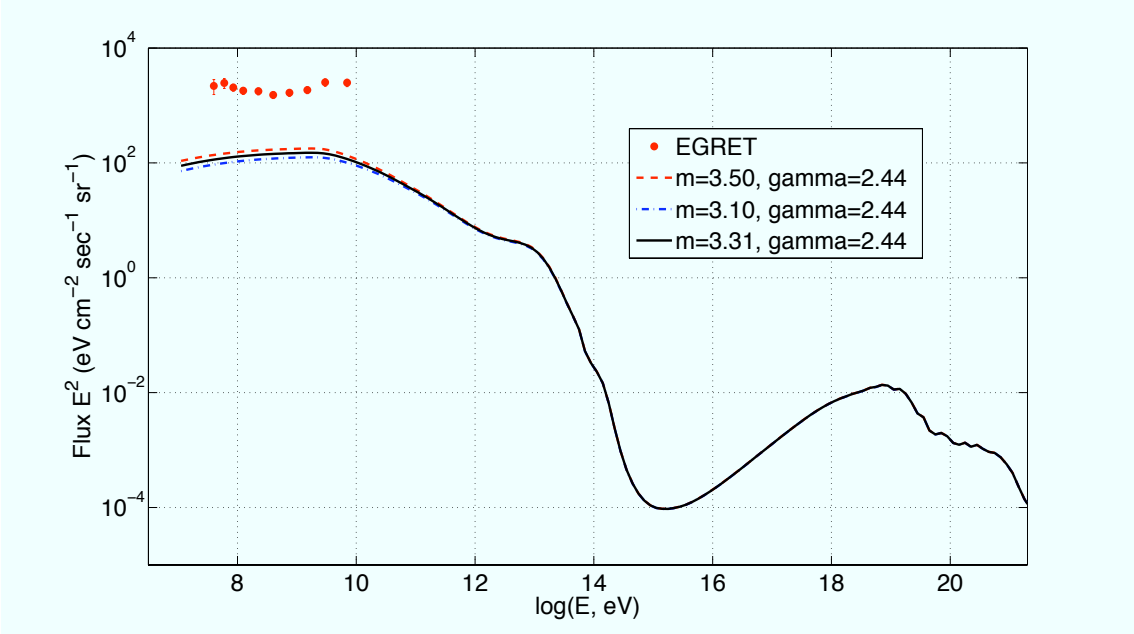

Figure 2.19. Sensitivity of secondary gamma ray flux to parameter m.

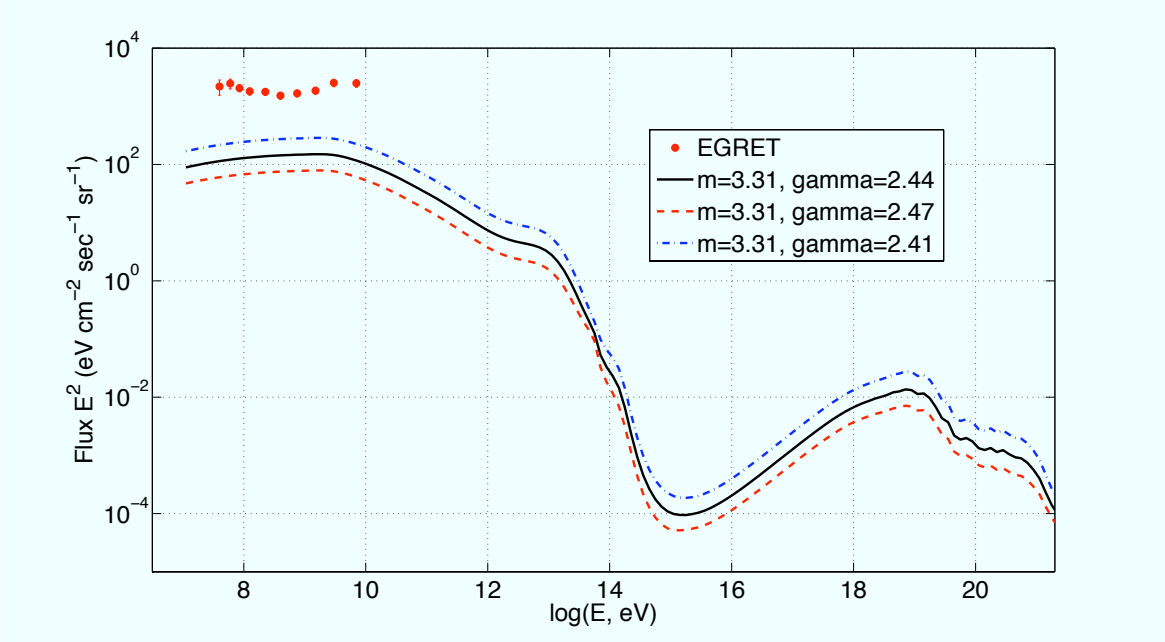

Figure 2.20. Sensitivity of secondary gamma ray flux to parameter γ.

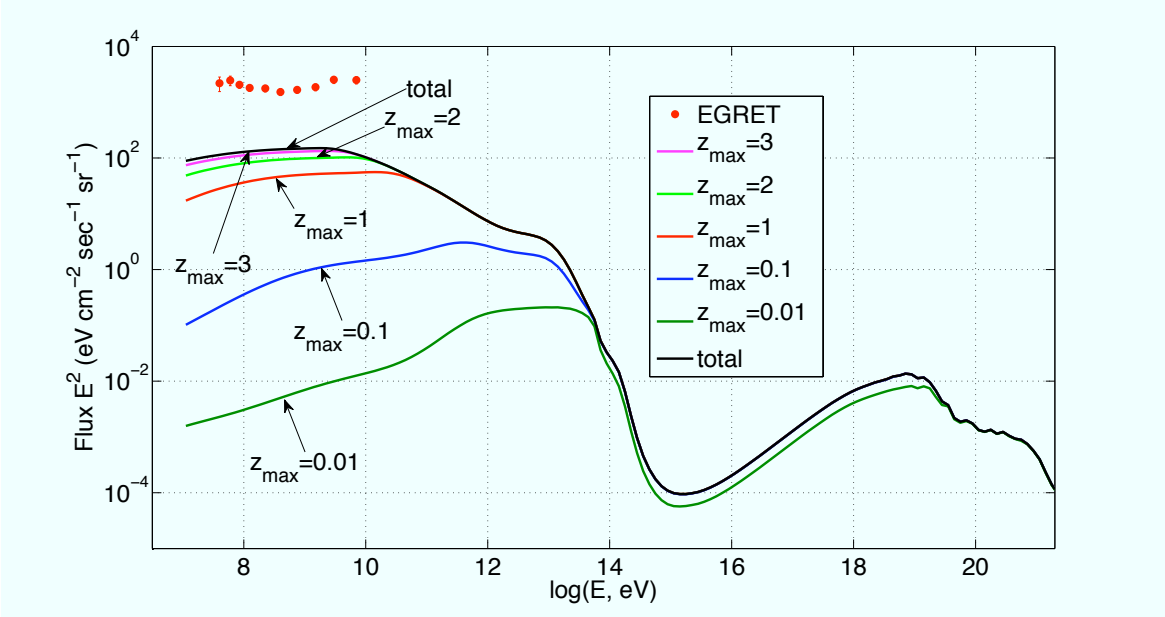

Figure 2.21. Sensitivity of secondary gamma ray flux to parameter z_{max}.

It is no surprise, that the secondary gamma ray flux is most sensitive to the parameter z_{max}, although this sensitivity decreases with the increase in the value of the parameter. Gamma rays traveling from further away will loose a significant amount of energy before reaching Earth and will effect the lower part of the spectrum as compared to those originating from closer CR sources. Our gamma flux is less sensitive to the evolution parameter m. Changes in m are noticeable at the lowest energy end of the spectrum considered here and are insignificant. The parameter γ controls the total amount of energy deposited into EM cascades as the result of CR interactions. This also changes the relative contribution of the modeled flux to the extragalactic diffuse gamma ray flux limit from EGRET. In cosmological scenarios with less steep CR production spectrum, higher secondary gamma ray fluxes are obtained. The shape of the spectrum is not really affected by γ.

Contributions of different z-shell to the total γ-flux are shown in Figure 2.22. The shell are chosen so that each shell contributes 10% to the total flux. The upper boundaries of the shell are given in the legend. The lower boundaries are the same as the upper boundary of the previous shell (0 for the first one). A similar to proton flux case pattern of shell thinning with increase in redshift is observed.

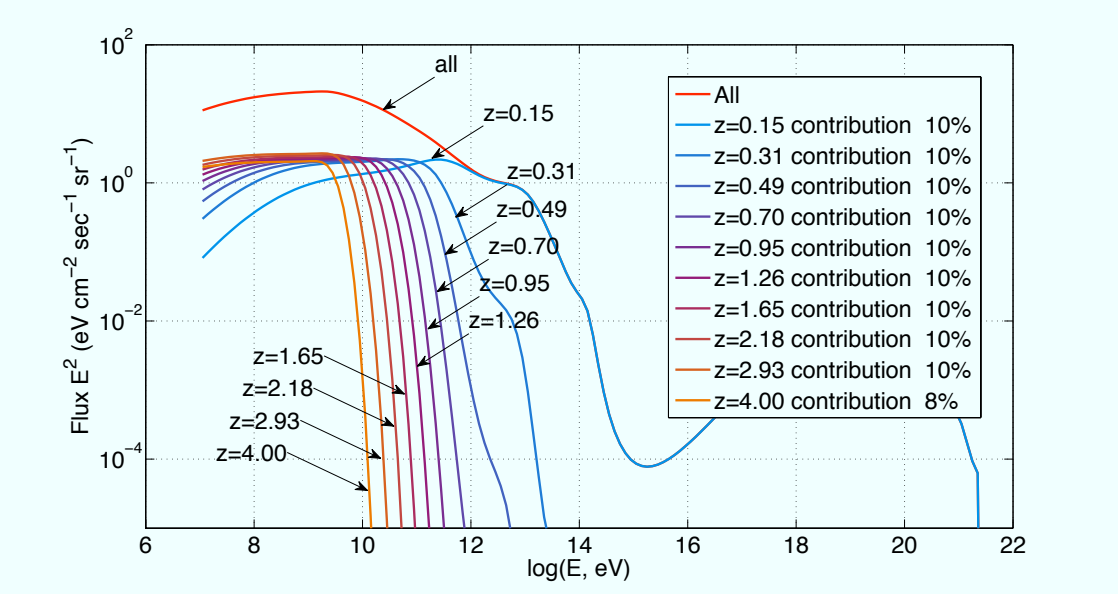

Figure 2.22. Contributions to secondary gamma ray flux from z-shells (proton sources at different redshifts) and their contributions to overall extragalactic gamma ray spectrum at Earth.

In this chapter we described secondary gamma ray and neutrino fluxes produced as consequence of GZK mechanism. The resulting fluxes are built under the assumption a uniform distribution of CR souses and a linear propagation of all particles. Fluxes provided here are model dependent. Model parameters are tuned to have the best possible match between the simulated proton spectrum and CR monocular spectra measured by HiRes.

Figure 2.23 compares our resulting neutrino and gamma ray fluxes with upper limits set by other neutrino (Fly's Eye 85 [36], AGASA 01 [186], RICE 06 [124], Pierre Auger 08 [11], AMANDA 2 [16], Semikoz and Sigl [165]) and gamma-ray (EGRET [173]) experiments and studies. Based on our result we conclude that both neutrino and gamma ray fluxes are too small to be observed by modern experiments. Only the increased sensitivity of a new generation of detectors would allow to measure the secondary gamma ray and neutrino fluxes.

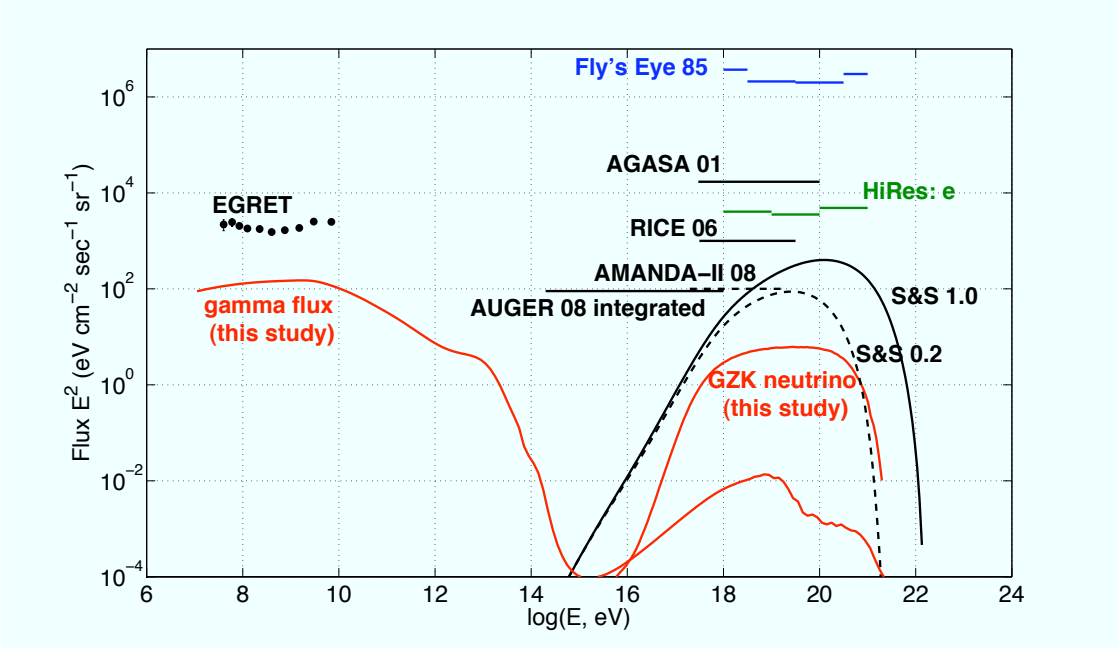

Figure 2.23. Neutrino and gamma-ray fluxes and limits. Fluxes derived in this study are compared to upper limits of other experiments and studies (Fly's Eye 85 [36], AGASA 01 [186], RICE 06 [124], Pierre Auger 08 [11], AMANDA 2 [16], Semikoz and Sigl [165], EGRET [173]).

CHAPTER 3

PHYSICS OF EXTENSIVE AIR SHOWERS (EAS)

At the UHE level, the flux of cosmic rays can be lower than 1 particle per km^2 per century. This makes a direct measurement of the properties of the primary cosmic ray particles extremely difficult. At these energies, the information about cosmic ray primaries is determined through the detection and analysis of extensive air showers (EAS).

An extensive air shower is a cascade of billions of particles moving at the speed of light through the atmosphere. An EAS is born when a relativistic cosmic ray particle enters the upper atmosphere and interacts with an air nucleus (mostly nitrogen and rarely oxygen). In the interaction the primary cosmic ray looses some of its initial energy and likely its identity while new particles are created. These secondaries will again interact with air nuclei to produce more secondary particles, which are added to the EAS. This process repeats and feeds the EAS with more and more particles. As a shower develops the average energy of the particles in a shower is getting lower and lower while the size of EAS keeps getting bigger and bigger. When the average energy of a shower particle drops below the critical value, no more particles are produced and at this point the shower reaches its maximum size. At shower maximum the number of particles can be as high as 10^{11} for a 10^{20} eV primary. The shower can be kilometers long in the atmosphere with the lateral extent up to tens of squared kilometers at the ground level. As it passes its maximum, the number of particles in the EAS gets smaller as they loose their energy and stop, and finally the shower disappears.

The properties of a primary particle such as energy, particle type and arrival direction can be studied by measuring the properties of the shower it created. Rather simple models of shower development relate the observable shower properties to the properties of a primary CR.

EAS can be studied in two principal ways: by ground arrays that detect the shower particles at the ground level or by optical detectors that record the light produced by the

EAS passage through the atmosphere.

This chapter starts with the review of the basic properties of an EAS and its components (electromagnetic, hadronic and muonic) and how they are related to the properties of a CR primary and then introduces the main methods of EAS detection. A special type of tau neutrino initiated EAS is discussed at the end of the chapter.

3.1 EAS Development

3.1.1 Branching "Toy" Model

Before going into the details of EAS development, it is worthwhile to start with the simple model that illustrates some of its main features. Such a model was developed by Heitler [99] and is generally known as branching model. The model is described in details in Gaisser [81].

Suppose a CR primary particle is entering the Earth's atmosphere with the energy E_0 (Figure 3.1). The model assumes a fixed characteristic collision length λ. Thus after traveling length λ the primary will interact and break into two particles, each having half of the energy of the original, $E_0/2$. After the shower develops through slant-depth X (amount of mass in gm/cm^2 along the shower track), there have been $n = X/\lambda$ interactions, and the total number of particles is:

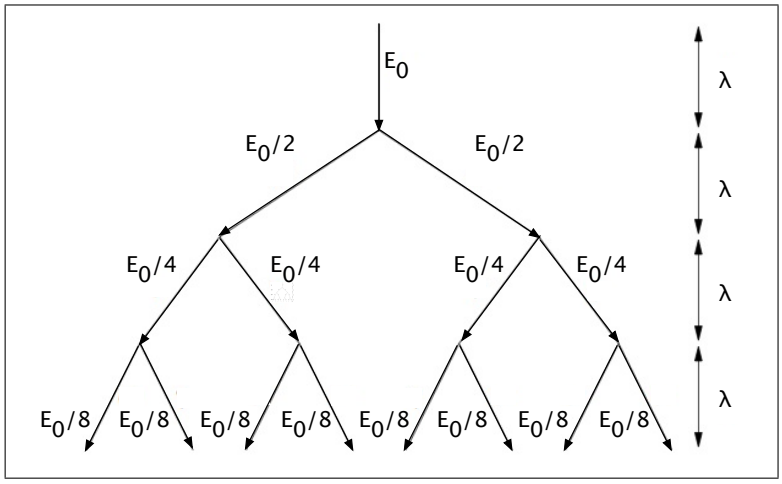

Figure 3.1. Schematics for Heitler's model of EAS development through the branching process.

$$N(X) = 2^{X/\lambda} \tag{3.1}$$

The energy of each particle is given by

$$E(X) = \frac{E_0}{N(X)} = E_0 \cdot 2^{-X/\lambda} \tag{3.2}$$

This branching process continues until the energy of the particles falls below some critical energy, E_c. This point corresponds to the maximum number of particles in the shower

$$N_{max}(X_{max}) = E_0/E_c \tag{3.3}$$

which occurs at the depth

$$X_{max} = \lambda \frac{ln(E_0/E_c)}{ln(2)} \tag{3.4}$$

Though this is a very basic model, it illustrates two important features that hold for the development of a real EAS. The first observation comes from equation 3.3 and predicts that the number of particles at shower maximum is proportional to the primary particle energy:

$$N_{max} \propto E_0 \tag{3.5}$$

The second result is illustrated by equation 3.4 and says that the atmospheric depth of the shower maximum is proportional to the logarithm of the primary particle energy

$$X_{max} \propto ln(E_0) \tag{3.6}$$

Thus this simple model allows us to understand qualitatively that energy of the primary particle can be approximated by measuring N_{max} and X_{max} parameters of an EAS.

If the primary particle is a nucleus of mass A and energy E_0, the same branching model can be applied if the nucleus is treated as a group of A nucleons of energy E_0/A, each of which produces its own shower independently. The shower maximum depth in this case is

$$X_{max} = \lambda \frac{ln(E_0/AE_c)}{ln(2)} \tag{3.7}$$

The message here is that light (proton) and heavy (iron) nuclei initiated showers will have different properties. On average iron primaries will have showers with smaller values of parameter X_{max} or in other words will develop higher in the atmosphere. This makes the X_{max} parameter sensitive to the composition of the CR primaries.

3.1.2 Shower Components

The initial types of the secondary particles in the EAS is determined by the type of the primary one. If the primary particle is an UHE photon, its interaction with the air nucleus can be twofold:

$$\gamma + air\ nucleus \longrightarrow hadron(\pi^{\pm,0}, K^{\pm,0}, ...) \tag{3.8}$$

and

$$\gamma + air\ nucleus \longrightarrow e^+ + e^- \tag{3.9}$$

The relative probability of photo production (equation 3.8) to pair production (equation 3.9) is quite small, $R = \sigma_{\gamma \to hadron}/\sigma_{\gamma \to e^+e^-} = 2.8 \times 10^{-3}$ [81, page 245].

EAS initiated by a gamma ray through the interaction given by equation 3.9 is called an electromagnetic cascade and is composed of electrons, positrons and photons.

If the primary particle is an UHE proton, its interaction with the air nucleus is similar to that of gamma ray in equation 3.8:

$$p + air\ nucleus \longrightarrow hadron(\pi^{\pm,0}, K^{\pm,0}, ...) \tag{3.10}$$

EAS produced through interactions described by equations 3.8 and 3.10 are more complicated than pure electromagnetic showers and in fact have three components: electromagnetic component, hadronic core and muonic component. Figure 3.2 shows a simplified schematic of an EAS generated by a proton with all three components of the shower displayed.

3.1.2.1 Electromagnetic component. As was mentioned above, purely electromagnetic cascades originate from ultra high energy gamma rays. In case of a hadronic primary, UHE gammas are produced in the π^0 decays, with a branching ratio (BR) of 98.4% (see Table 3.1).

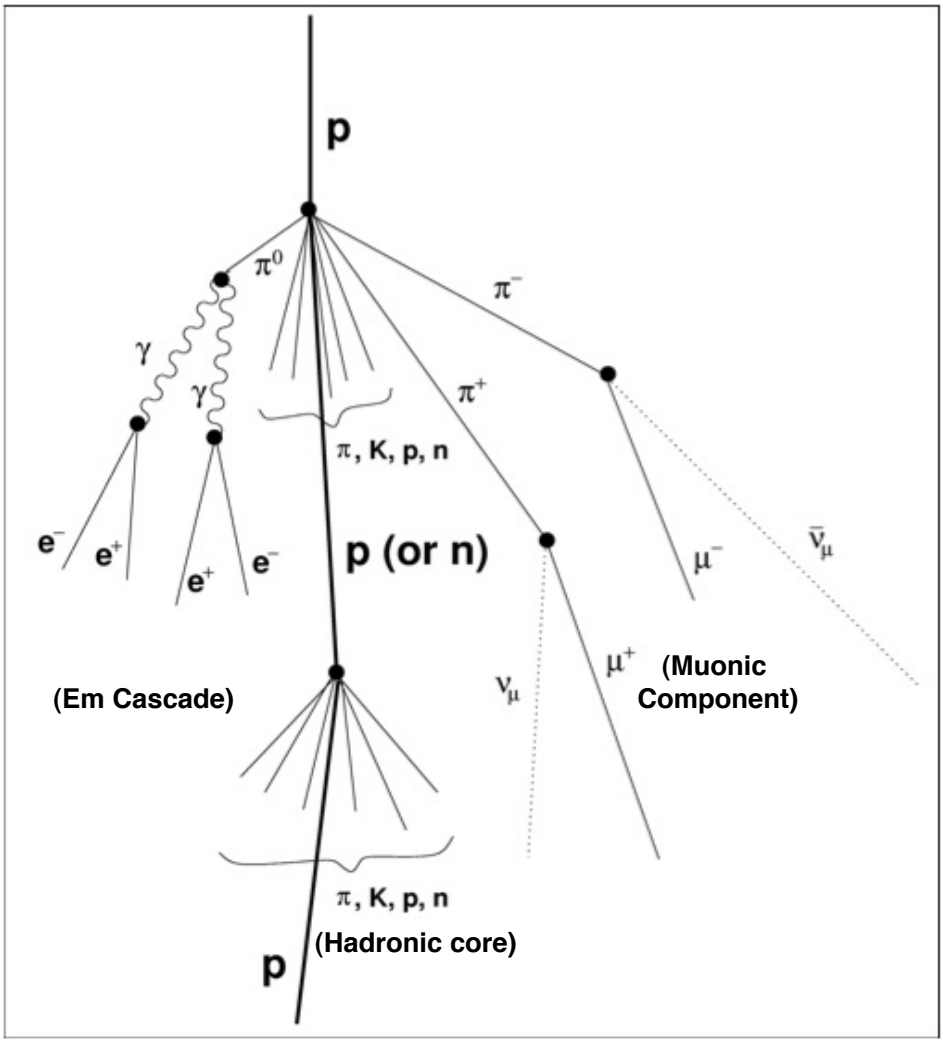

Figure 3.2. Schematics of a hadronic EAS with its components. Adapted from [169].

Table 3.1. Particle properties

Particle	Mass (MeV/c^2)	Half-life (s)	Decay Mode	Relative Fraction
$e^{\pm}$	0.511	stable	stable	-
μ^+	105.7	2.2×10^{-6}	$e^+\nu_e\bar{\nu_\mu}$	100%
μ^-	105.7	2.2×10^{-6}	$e^-\bar{\nu_e}\nu_\mu$	100%
π^0	134.9	8.4×10^{-17}	$\gamma\gamma$	99%
π^+	139.6	2.6×10^{-8}	$\mu^+\nu_\mu$	100%
π^-	139.6	2.6×10^{-8}	$\mu^-\bar{\nu_\mu}$	100%
K_S^0	497.7	8.9×10^{-11}	$\pi^+\pi^-$	69%
			$\pi^0\pi^0$	31%
K_L^0	497.7	5.2×10^{-8}	$\pi^{\pm}e^{\mp}\bar{\nu_e}(\nu_e)$	39%
			$\pi^{\pm}\mu^{\mp}\bar{\nu_\mu}(\nu_\mu)$	27%
			$\pi^0\pi^0\pi^0$	22%
			$\pi^+\pi^-\pi^0$	12%
K^+	493.6	1.2×10^{-8}	$\mu^+\nu_\mu$	64%
			$\pi^+\pi^0$	21%
K^-	493.6	1.2×10^{-8}	$\mu^-\bar{\nu_\mu}$	64%
			$\pi^-\pi^0$	21%

$$\pi^0 \longrightarrow \gamma + \gamma \tag{3.11}$$

These neutral pions are produced directly in the high energy hadron collisions (equations 3.8 and 3.10) or via decays of secondary kaons, such as in following processes:

$$K^{\pm} \longrightarrow \pi^{\pm} + \pi^0$$

$$K_S^0 \longrightarrow \pi^0 + \pi^0$$

$$K_L^0 \longrightarrow \pi^0 + \pi^0 + \pi^0$$

The development of an electromagnetic cascade is well understood. A good description is given by Rossi and Greisen in [162, 90], Allan in [21] and Gaisser in [81] . The general idea is close to that described by the toy model of subsection 3.1.1. The difference is that the interaction length is not constant and the energy is not just split in half during the collisions.

The development of the electromagnetic cascade is controlled by a number of energy loss processes, which are dominating different energy ranges. At the highest energies the

cascade develops through alternating between photon pair production (equation 3.11) and Bremsstrahlung production of photons by electrons and positrons:

$$e^{\pm} \longrightarrow e^{\pm} + \gamma \tag{3.12}$$

When the energy of a photon drops below some critical value (E_c ∼80-90 MeV in air), pair production stops playing the dominant role of gamma energy loss. Compton scattering on atomic electrons is dominant over the energy range from 20 MeV to 100 keV. Below 100 keV the photo-electric effect dominates, in which the photon is absorbed by a nucleus to free one of its electrons.

Bremsstrahlung also is not the only energy loss channel for electrons and positrons. It is most effective above E_c. Below this energy ionisation losses are most important.

Thus the initial development of the electromagnetic cascade is controlled by pair production and Bremsstrahlung (for particle energies $\gtrsim E_c$). The case when we consider only these two processes of energy loss is known as Approximation A. Approximation A is almost identical to the Heitler "toy" model of subsection 3.1.1, since for high energies the interaction length for pair production is approximately equal to that for Bremsstrahlung. This means that the general results of the Heitler model (equations 3.5 and 3.6) are applicable here.

Approximation B takes into account the ionisation losses of electrons. The ionisation losses are treated as continuous and constant at E_c=81 MeV. Under Approximation B, the total number of electrons at depth X produced in a cascade initiated by a photon with energy E_0 is [81]

$$N_e(E_0, t) = \frac{0.31}{\sqrt{X_{max}}} exp\left[X\left(1 - \frac{3}{2}ln(s)\right)\right] \tag{3.13}$$

where N_e is the number of electrons in the shower, X_{max} is the depth of the shower maximum:

$$X_{max} \equiv ln(E_0/E_c) \tag{3.14}$$

Parameter s is called the "shower age" and is defined by

$$s \equiv \frac{3X}{X + 2X_{max}} \tag{3.15}$$

The shower age varies from s = 0 at the origin of the shower to s = 2, corresponding to zero particles remaining in the shower. At the shower maximum s = 1.

For hadronic showers about 90% of the energy of the EAS goes to its EM component, which consists of a large number of electromagnetic cascades generated at different heights.

3.1.2.2 Hadronic core. A primary cosmic ray nucleon (or a nucleus) when it interacts with an air nucleus will produce other hadrons. As indicated in equation 3.10, nucleons, kaons and pions are the most common products of such interactions. But more exotic processes may also occur creating strange baryons, charmed hadrons and other particles.

Most of the secondary hadrons in the EAS are pions. They are created equally in three flavors: positive pion (π^+), negative pion (π^-) and neutral pion (π^0). Neutral pions are unstable and will decay into two gamma rays shortly after their creation and thus contribute to the electromagnetic component of the shower (see section 3.1.2.1). Charged pions have a longer half-life and will either interact or decay, depending on their energy and the altitude. At higher energies time dilation extends their lifetime in the laboratory frame, so they have more time to interact. On the other hand, pions will have their highest energy at the beginning of the shower development, which usually corresponds to the high altitudes and small atmospheric densities. This reduces their chance to interact. If they do not interact, they decay into muons and neutrinos and contribute to the muonic component of the EAS (see Table 3.1).

Kaon are generated at the rate of $\sim 10\%$ of that of pions. There are four species of kaons: $K^+, K^-, K^0, \bar{K^0}$. Neutral kaons have two states distinguished by their half-life time. Half of them will be short lived (equation 3.16), and the other half will be long lived (equation 3.17):

$$|K_S^0 >= \frac{1}{\sqrt{2}}(|K^0 > +|\bar{K^0} >) \tag{3.16}$$

$$|K_L^0 >= \frac{1}{\sqrt{2}}(|K^0 > -|\bar{K^0} >) \tag{3.17}$$

Charged kaons, similarly to charged pions, have a longer half-life than their neutral counterparts and will have an opportunity to interact, rather than decay. For more information on the decay modes of different particles, refer to Table 3.1.

Pions and kaons (and other hadrons) are relatively heavy particles and will have only small changes in the transverse momentum from that of the original particle. As the result a compact hadronic core is formed around the shower axis, which is defined by the

arrival direction of the primary cosmic rays. This core has a lateral extent of the order of a few meters, since higher generation hadrons stay close to the shower axis.

As the cascade develops the hadronic core becomes smaller, because it feeds the electromagnetic and muonic parts, which get bigger and bigger. The core exhausts its potential, when the mean energy of the hadrons falls below the threshold for pion production. The longitudinal development of the electromagnetic part of the hadron initiated shower is well described by the analytical expression known as Gaisser-Hillas (GH) function [82]:

$$N_e(X) = N_{max} \left(\frac{X - X_0}{X_{max} - X_0} \right)^{\frac{X_{max} - X_0}{\lambda}} exp \left[\frac{X_{max} - X}{\lambda} \right] \tag{3.18}$$

where $N_e(X)$ is the number of electrons at the depth X, X_{max} is the depth at the shower maximum ($N = N_{max}$), X_0 is the depth of the first interaction (N=1) and λ is a model dependent constant, which is equal to ~ 70 g/cm^2.

X_0 depends on the collision cross section, and hence the energy and mass composition of a particle (~ 70 g/cm^2 for 10^{15} eV and ~ 80 g/cm^2 for 10^{18} eV). The depth of the shower maximum, X_{max}, is a function of X_0, the shower energy and nature of the primary particle. Typically, X_{max} falls in the range of 600 - 800 g/cm^2. Figure 3.3 shows a 10^{17} eV EAS generated by the shower simulation program CORSIKA and fitted with a GH function.

Another functional form that also describes the development of an air shower is known as Gaussian-in-Age (GA) and is represented as follows:

$$N_e(X) = N_{max} exp \left(\frac{(s-1)^2}{2\sigma^2} \right) \tag{3.19}$$

The function has only three parameters. Parameters N_{max} and X_{max} have the same meaning as for the GH parameterization. $s(X, X_{max})$ is the shower age parameter defined in 3.15. The properties of the function include the symmetry about X_{max}. σ describes the width of the Gaussian function. Figure 3.4 shows one of the CORSIKA generated showers (empty circles) with the Gaussian-in-Age fit (solid line).

It is impossible to give the correct relationships for σ and thus for X_0, X_{max} as the exact physics of hadronic interactions is still unknown in the UHE regime. Various models have been developed to predict the cross-sections of the hadronic interactions. At the highest energies they are based on the information available from particle accelerators at low energies and are trying to extrapolate their predictions to highest energies.

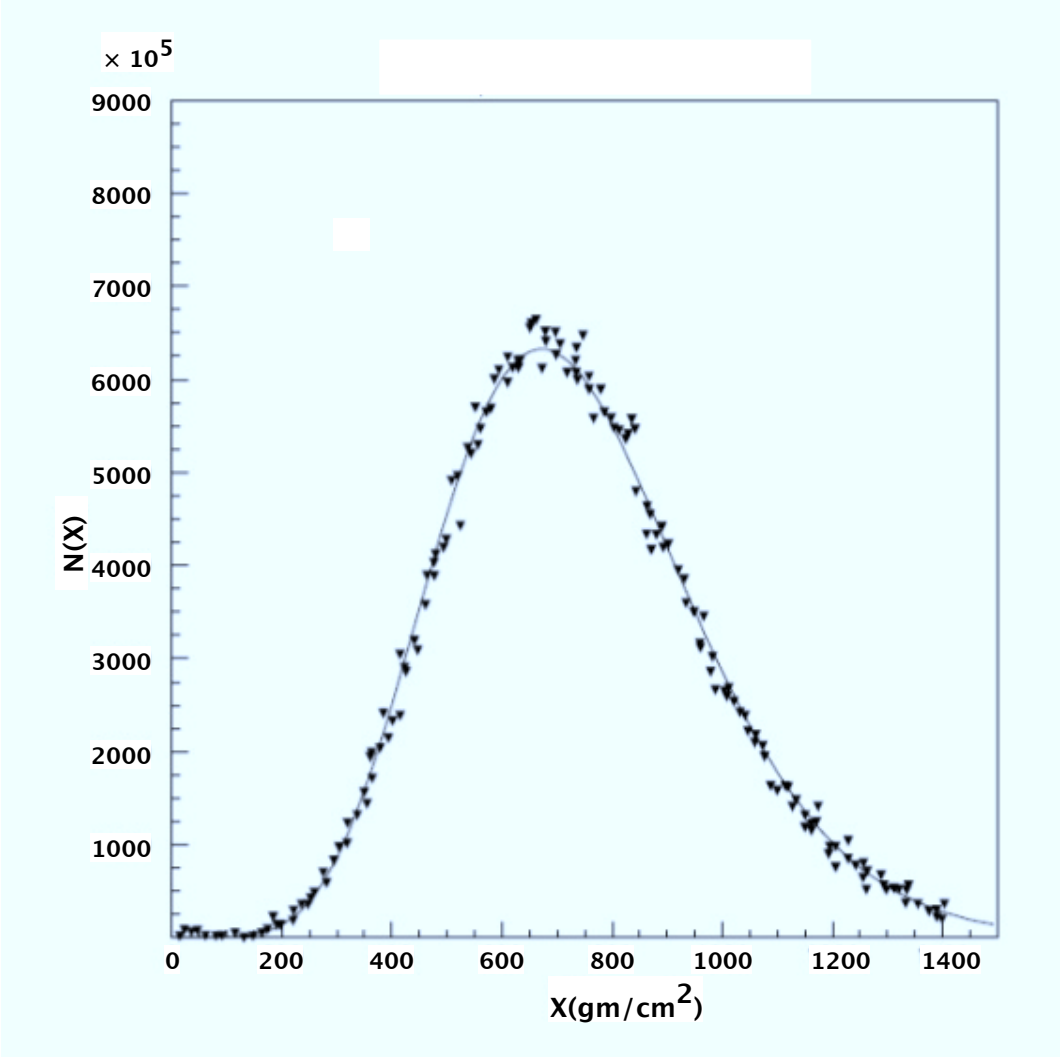

Figure 3.3. Gaisser-Hillas fit to a typical shower profile generated by CORSIKA for 10^{17} eV proton.

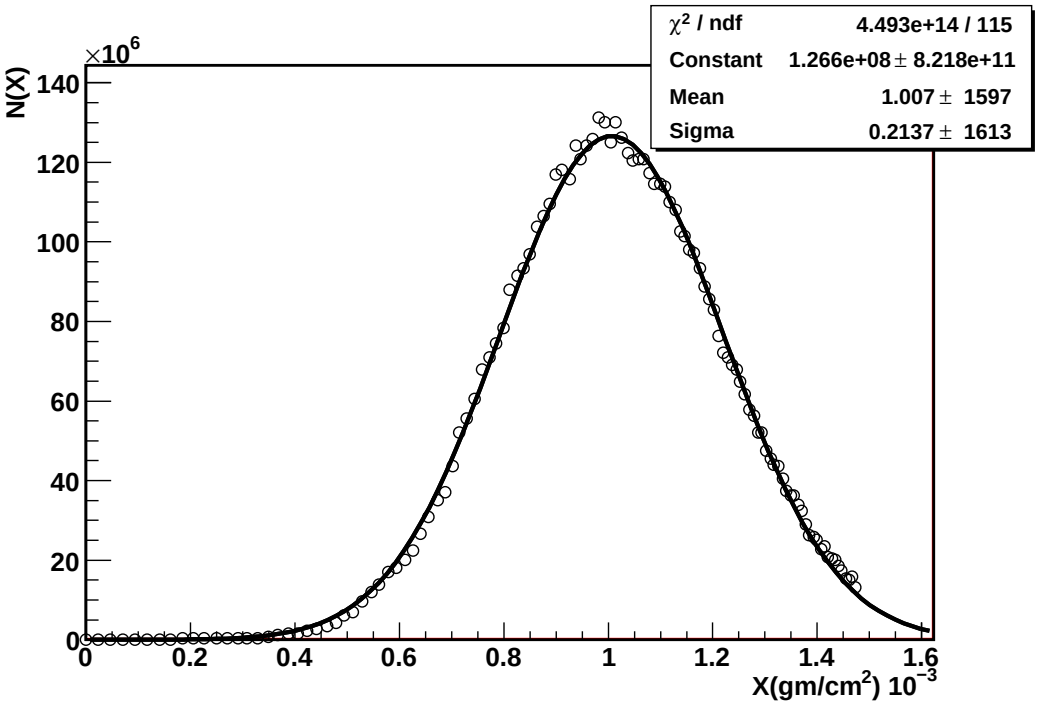

Figure 3.4. Gaussian-in-Age fit to a typical shower profile generated by CORSIKA.

The most popular hadronic models that are widely used for EAS simulations include SIBYLL [77], QGSJET [114, 116], and DPMJET [155].

Light leptons (electrons and muons) form a laterally wider spread cone around the shower core. This lateral spreading is due to Coulomb scattering of the lighter electrons, which compose about 90% of the shower particles. Nishimura and Kamata [117] and Greisen [90] showed that the lateral distribution of electrons in terms of electron density may be approximated by the formula [81, page 226]:

$$\rho(N_e, r) = \frac{N_e}{r_M^2} f_{NKG}(s, r/r_M) \tag{3.20}$$

where N_e is the total number of electrons, s is the shower age, $r_M = x_0(E_s/E_c) \approx 9.3$ g/cm^2 is the Moliere radius for multiple scattering [81] and f_{NKG} is the Nishimura-Kamata-Greisen (NKG) function:

$$f_{NKG}\left(s, \frac{r}{r_M}\right) = \left(\frac{r}{r_M}\right)^{s-2} \left(1 + \frac{r}{r_M}\right)^{s-4.5} \frac{\Gamma(4.5-s)}{2\pi\Gamma(s)\Gamma(4.5-2s)} \tag{3.21}$$

This functional form assumes azimuthal symmetry for the density of the particles. In reality this will not hold for inclined showers. Despite this, the NGK formula is used in fitting the measured density of particles as a function of distance to the core, which is then related to the energy of the primary particle.

3.1.2.3 Muonic component. Muons compose the last but not the least important component of the hadronic shower. Muons are generated from the decay of the charged pions and kaons (see Table 3.1). More muons are produced at the early stages of shower development, since the probability of the decay is greater than the interaction probability at the top of the atmosphere. Pair production ($\gamma \rightarrow \mu^+\mu^-$) will also make a small contribution to the number of muons in the shower.

The lateral spread of muons is a result of their large production angles (transport of the transverse momenta from a parent particle of a hadronic core). Multiple scattering by air nuclei plays a relatively small role, due to the large muon mass. Also since they are generated early in the shower, the spreading gets bigger by the time they reach the ground.

Muons are weakly interacting particles and their half-life is 2.2×10^{-6} seconds. In the laboratory frame, their lifetime will be extended by time dilation, so that muons with the Lorenz factor > 20 will reach sea-level before they decay.

The energy loss of the muons is mostly due to ionisation. The cross sections for bremsstrahlung (radiation) and pair-production are small, which make them second order processes (except for the highest energies). The energy losses of muons can be written as:

$$-\frac{dE}{dx} = a(E) + b(E)E \tag{3.22}$$

where $a(E)$ is the continuous energy loss rate due to ionisation and $b(E)$ represents a discrete energy loss rate due to second order processes. The ionisation energy losses are dominant and have a constant value of ~ 2 MeV / g cm^{-2} [102].

The lateral distribution of the muon density for muons with energies ≥ 1 GeV was first estimated by Greisen [91] and has a form:

$$\rho_\mu(r) = 18r^{-0.75}\left(1 + \frac{r}{320}\right)^{-2.5}\left(\frac{N_e}{10^6}\right)^{0.75} \tag{3.23}$$

where ρ_μ is the density of the muons at a distance r from the shower core and N_e is the number of charged particles.

Because of the slow attenuation of the muonic component of the shower, the measured total muon number N_μ at ground level may be used as a primary particle energy estimator.

3.2 Methods of EAS Detection

There exist three different methods of measuring the properties of an EAS (and eventually the properties of the primary particle). They are employed in three different detector types: Cherenkov light detectors, air fluorescence detectors and ground arrays. The first two techniques observe the passage of a shower via recording the light emitted by ultra relativistic shower particles (Cherenkov light) or nitrogen molecules (air fluorescence). Ground arrays sample the shower particles at ground level. Each method has its advantages and disadvantages. Recently, it became popular to build hybrid detectors that exploit several different methods at the same time to overcome many of the problems of a single detector and get better quality information about cosmic rays.

3.2.1 Cherenkov Light Detectors

About 90% of the energy of a primary cosmic ray eventually ends up in the electromagnetic channel of an EAS. Most of the high energy electrons and positrons are traveling with the speed exceeding the speed of light in the air and produce Cherenkov radiation. The main idea is as follows. A charged particle disrupts the local electromagnetic field (EM) in the medium it is traveling through. Electrons in the atoms of the medium become excited, displaced and polarized by the passing EM field of a charged particle. Photons are emitted as these medium electrons restore themselves to equilibrium. In normal circumstances, these photons destructively interfere with each other and no radiation is detected. In the case when an EM field that travels faster than light is propagating through the insulating medium, the photons constructively interfere in certain directions and intensify the observed radiation.

Figure 3.5 shows a simplified geometry of Cherenkov emission. A shower particle is traveling with speed $v_p = \beta c$, through a medium with an index of refraction n. Arrows represent emitted photons that are traveling with the speed of light in the medium $v_{em} = c/n$. At time $t = 0$ the charged particle is in the position 1. In time t it will cover distance $d_p = \beta ct$ and will be in position 2. For the same time t, emitted electromagnetic light will traverse the distance $d_{em} = \frac{c}{n}t$ and will reach point 3. From solving the right angle triangle $\triangle 123$, we can see that the following relation holds:

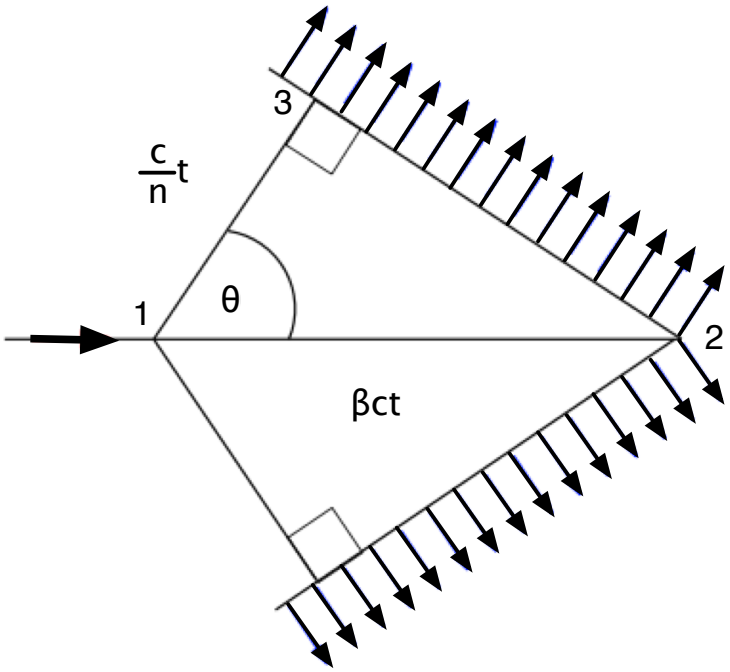

Figure 3.5. Schematics of Cherenkov light production by a charged particle.

$$cos(\theta) = \frac{1}{n\beta} \tag{3.24}$$

Angle θ is the characteristic angle of the Cherenkov radiation. The maximum angle of emission of polarized Cherenkov light is obtained when the particle is traveling at the speed of light $\beta = 1$

$$\theta_{max} = cos^{-1}\left(\frac{1}{n}\right) \sim 1.3^{\circ} \tag{3.25}$$

Since θ is small, Cherenkov radiation is collimated along the shower axis and appears as a pancake-like pool of light about 200 m in diameter and about a meter thick traveling with the particles in the shower.

The amount and the angular distribution of the produced Cherenkov light depends on the number and lateral distribution as well as energy distribution of the electrons and positrons in the shower. Equation 3.26 gives the number of Cherenkov photons per meter generated by a particle of energy E [171, page 51]:

$$\frac{dN_p}{dl} = 4\pi\alpha\left[1 - \left(\frac{E_{min}}{E}\right)^2\right]\int \frac{\delta}{\lambda^2} d\lambda \tag{3.26}$$

where α is the fine structure constant, $\delta = 1 - n$, $E_{min} = \frac{mc^2}{\sqrt{2(n-1)}} = \frac{0.511}{\sqrt{2\delta}}$ (MeV) is Cherenkov threshold energy. For the isothermal atmosphere approximation $\delta = \delta_0 e^{-h/H}$, where $\delta_0 = 2.4 \times 10^{-4}$ and $H_0 \sim 7.3$ km is atmospheric scale height.

The contribution from all the electrons at depth X along the shower is :

$$\frac{dN_{cv}(X)}{dl} = \int_{E_{min}}^{\infty} N_e(X) f(E, X) \frac{dN_p}{dl} dE \tag{3.27}$$

$N_e(X)$ is the number of electrons as a function of depth X. $f(E, X)$ is the energy distribution of the electrons at a given depth, which is found using Monte Carlo approach [171] to be:

$$f(E, X) = \int_{E}^{\infty} \left(\frac{0.89E_0 - 1.2}{E_0 + E}\right)^s (1 + 10^{-4} sE)^{-2} \tag{3.28}$$

Here s is the shower age and $E_0 = 44 - 17(s - 1.46)^2$.

Angular distribution of the Cherenkov light can be approximated as:

$$\frac{d^2 N_{cv}(X)}{dl d\Omega} = \frac{dN_{cv}(X)}{dl} \frac{e^{-\theta/\theta_0}}{sin\theta} \tag{3.29}$$

with $\theta_0 = 0.83 E_{min}^{-0.67}$ [171].

Cherenkov detector measures the lateral distribution of Cherenkov light and reconstructs the primary energy from the distribution. The number of the Cherenkov photons produced depends on the wavelength as $1/\lambda^2$, meaning that much of the light is in the ultraviolet part of the spectrum. Clear atmospheric conditions are favorable for transmitting light down to 290 nm. At this point ozone absorption should be taken into account.

An air Cherenkov detector is composed of one or more optical mirrors. The Cherenkov light is reflected by the mirror and focused on photomultiplier tubes. Tubes are used to convert optical signal from the cosmic ray event into an electronic signal, which is then amplified and recorded by detector electronics.

3.2.2 Air Fluorescence Detectors

As the charged particles travel through the atmosphere, they dissipate some of their energy by exiting nitrogen molecules. The excited molecules relax by emitting ultraviolet

photons isotropically in all directions. Historically this radiation is called fluorescence (also adapted here), but scintillation is the proper name. The nitrogen fluorescence spectrum as measured by Bunner [58] is shown in Figure 3.6. Most of the fluorescence light (about 88%) is concentrated between the wavelengths of 300 and 400 nm, with the strongest bands at 337 nm, 357 nm and 391 nm.

When an air shower develops, the amount of fluorescent light produced from each segment of the shower is proportional to the number of electrons in that segment. The number of photons produced per unit meter per unit solid angle is:

$$\frac{d^2N_\gamma}{dld\Omega} = \frac{YN_e}{4\pi} \tag{3.30}$$

Y is the fluorescence yield, which is the number of photons emitted per charged particle per meter. Fluorescence yield is relatively constant over the range of atmospheric temperatures and pressures and can be approximated by the following empirical formula [113]:

$$Y = \frac{(dE/dx)}{(dE/dx)_{1.4MeV}} \cdot \rho \left\{ \frac{A_1}{1+\rho B_1\sqrt{t}} + \frac{A_2}{1+\rho B_2\sqrt{t}} \right\} \tag{3.31}$$

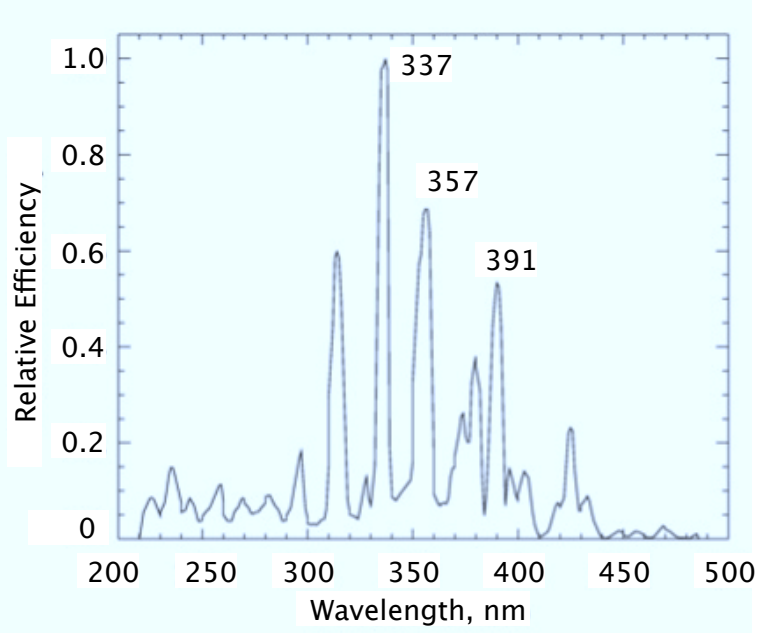

Figure 3.6. Spectrum of nitrogen fluorescence in the near ultraviolet as measured by Bunner [58]. The intensities are normalized to 1.0 at 337 nm.

In this equation ρ is the density in kg/m^3, t is the temperature in K. A_1=89 m^2/kg, A_2=55 m^2/kg, B_1=1.85 m^2/kg$\sqrt{K}$ and B_2=6.50 m^2/kg$\sqrt{K}$ are the constants. dE/dx is the energy loss of electrons in MeV/cm. Y is estimated to be about 4-5 photons per electron per meter. The light yield per particle is quite small, but EAS with energies $> 10^{16}$ eV are detectable during dark sky conditions (no moon or other sources of light) due to the large number of electron and positrons in these showers.

Atmospheric fluorescence detectors (such as HiRes) utilize mirrors and photomultiplier tubes (PMTs) to detect the weak fluorescence signal from EAS. Each PMT has a fixed field of view in the sky and as the shower develops it will move pass the fields of view of a number of subsequent tubes. The amount of light that each PMT detects depends on a number of factors. Among the main factors are the stage of the shower development the PMT views, the distance of the shower relative to the PMT, atmospheric conditions and others.

Not all of the light collected by a PMT is due to atmospheric fluorescence. Some of this light comes as Cherenkov photons. The relative contribution of Cherenkov radiation depends on the shower axis orientation with the respect to the tube. Only the fluorescent component is used in estimation of the shower size and thus the energy of the primary cosmic ray. In order to correctly determine shower properties Cherenkov light should be subtracted.

Fluorescent light (and Cherenkov light also) is attenuated by Rayleigh and Aerosol scattering during its propagation in the atmosphere. It is important to understand and correct for these effects.

3.2.2.1 Rayleigh scattering. Rayleigh (molecular) scattering is a relatively straightforward scattering process in the air and is described by the following relation:

$$\gamma + molecule \longrightarrow \gamma + molecule \tag{3.32}$$

Rayleigh scattering is an elastic scattering of electromagnetic radiation by particles much smaller than the wavelength of the radiation. If the particle is similar or larger than a wavelength, the scattering process has to be described by Mie theory.

The cross section of Rayleigh scattering has a $\frac{1}{\lambda^4}$ wavelength dependence (blue light is scattered much more readily than the red light). The mean free path for scattering at 400 nm is $X_R = 2970$ gm/cm^2 [171, page 201]. The number of photons scattered out of the beam per unit length is defined by the following relationship:

$$\frac{dN_\gamma}{dl} = -\frac{\rho N_\gamma}{X_R}\left(\frac{400\ nm}{\lambda}\right)^4 \tag{3.33}$$

The scattering probability into a given solid angle is given by

$$\frac{d^2N_\gamma}{dld\Omega} = \frac{3}{16\pi}\left|\frac{dN_\gamma}{dl}\right|(1+cos^2\theta) \tag{3.34}$$

Since it has a rather slow angular dependance, Rayleigh scattering should be considered for all emission angles.

The attenuation of light traveling from X_1 slant depth to X_2 for Rayleigh scattering can be written as [171, page 202]

$$T_{Rayleigh} = exp\left[-\frac{|X_1 - X_2|}{X_R}\left(\frac{400\ nm}{\lambda}\right)^4\right] \tag{3.35}$$

3.2.2.2 Aerosol scattering. Aerosol (Mie) scattering is a more complex process. In contrast to Rayleigh scattering, the solution to this scattering depends on the particle size and shape. The aerosol particle sizes in the atmosphere vary from $\sim 10^{-1}\ \mu m$ to $\sim 100\ \mu m$. There is no unique size distribution, it varies from place to place and strongly depends on weather conditions (humidity, wind velocity, etc.). Most aerosols are concentrated near the surface. Aerosol scattering is modeled using the Mie approximation, in which the aerosol particles are assumed to be dielectric spheres. The amount of scattered light is approximated by

$$\frac{dN_\gamma}{dl} \approx -\frac{N_\gamma e^{-h/H_M}}{L_M(\lambda)} \tag{3.36}$$

where $H_M \approx 1.2$ km is a scale height and $L_M(334nm) = 12$ km is the extinction length. The plot of $L_M(\lambda)/L_M(334nm)$ based on the Etterman model is shown in Figure 3.7. The angular distribution is strongly peaked at zero degrees emission angle and is give by

$$\frac{d^2N_\gamma}{dld\Omega} \approx \alpha\ e^{-\theta/\theta_M}\left|\frac{dN_\gamma}{dl}\right| \tag{3.37}$$

where $\alpha = 0.8$ and $\theta_M = 26.7^\circ$. Mie scattering dominates over Rayleigh scattering at small angles.

Analogous to equation 3.35 the attenuation of light traveling from height h_1 to h_2 for Mie scattering [171, page 202] is:

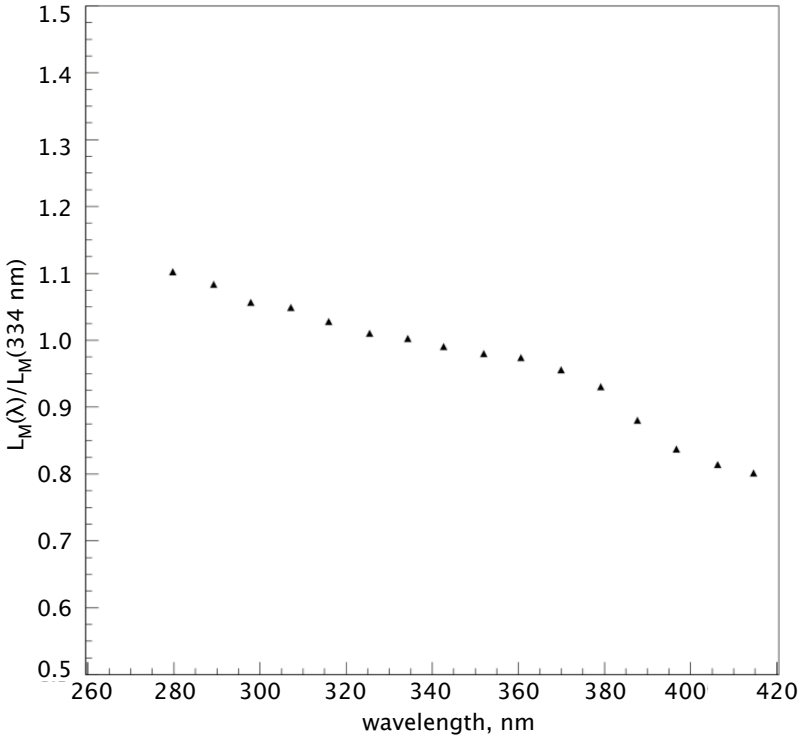

Figure 3.7. Wavelength dependent aerosol extinction length relative to L_M (334 nm) based on the Etterman model. Adapted from [14].

$$T_{Mie} = exp\left[-\frac{H_M}{l_M cos\theta}\left(e^{-h_1/H_M} - e^{-h_2/H_M}\right)\right] \tag{3.38}$$

If multiple scattering of light can be ignored, the total transmission due to scattering becomes:

$$T_{scat} = T_{Rayleigh} T_{Mie} \tag{3.39}$$

For excellent weather conditions, the contribution of Mie scattering is no more than 20% of that of Rayleigh [171, page 202].

3.2.2.3 Ozone absorption. UV attenuation due to absorption on Ozone can be written in the following form:

$$\frac{dN_\gamma}{dl} = -N_\gamma \rho_{O_3}(h) A_{O_3}(\lambda) \tag{3.40}$$

Parameters $\rho_{O_3}(h)$ and $A_{O_3}(\lambda)$ are the Ozone density, which depends on altitude, and an attenuation coefficient, which is highly dependent on wavelength. Ozone concentration as a function of altitude is shown in Figure 3.8. Wavelength dependence of the attenuation coefficient is shown in Figure 3.9.

Similarly to the scattering cases above, we can write the Ozone transmission coefficient as

$$T_{O_3} = exp(-\Delta x_{O_3} A_{O_3}(\lambda)) \tag{3.41}$$

where Δx_{O_3} is the Ozone slant depth. If the Ozone absorption is taken into account, the total amount of shower light that will reach the detector is given by:

$$N_{\gamma\ detector} = N_{\gamma\ EAS}\ T_{Rayleigh}\ T_{Mie}\ T_{O_3} \tag{3.42}$$

The main advantage of an air fluorescence telescope is that it measures energy deposition over a large portion of the shower. This allows a better estimation of the energy of the primary particle. Better reconstruction of the arrival direction is achieved by viewing the shower as it traverses many kilometers. An important improvement in determining the arrival direction of a cosmic ray is obtained if two of such detectors are used to detect the same shower from different vantage points, providing a stereoscopic view.

The main disadvantage of the air fluorescence technique is that it works only during moonless nights with good weather conditions (resulting in 10% duty cycle). Its efficiency strongly depends on the atmospheric conditions and is highest when the sky is clear and dark.

3.2.3 Ground Arrays

A ground array is an array of usually equally spaced particle counters. It is designed to sample the particle density of the shower front at a specific depth (depends on zenith angle). The most famous was the Akeno Giant Air Shower Array (AGASA), that was operated by University of Tokyo. The separation of the counters in the array determines the minimum energy of the showers it is built to detect. Tens of meters is an optimal distance for low energy showers, while order of kilometers in detector separation allows only the detection of UHE showers.

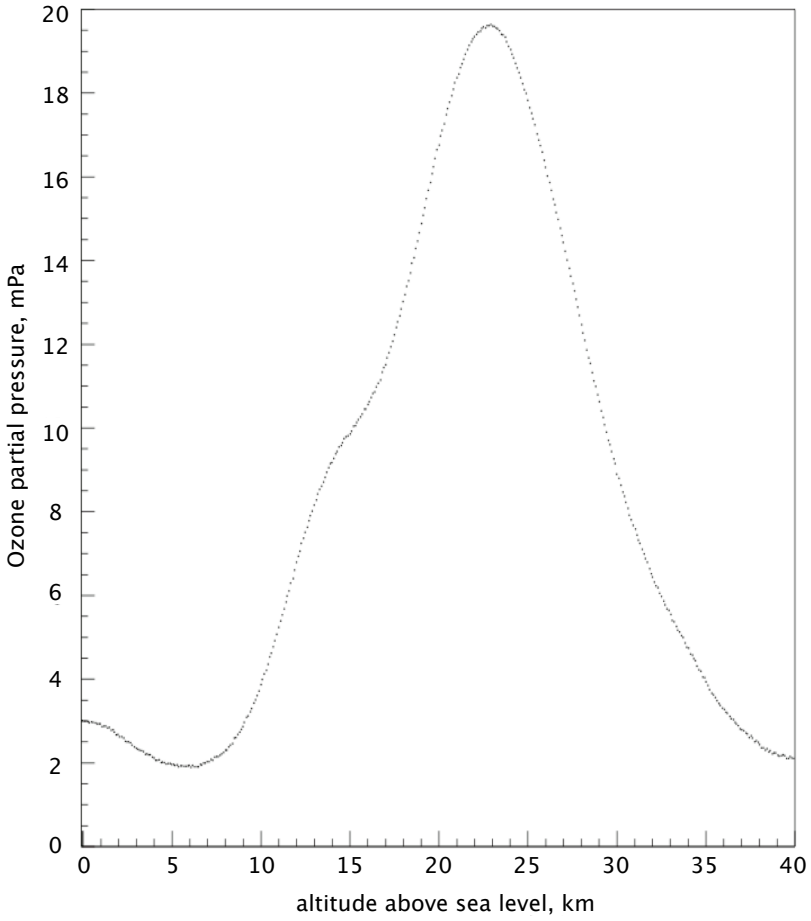

Figure 3.8. Ozone concentration in the atmosphere as a function of altitude as given in [112]. Adapted from [14].

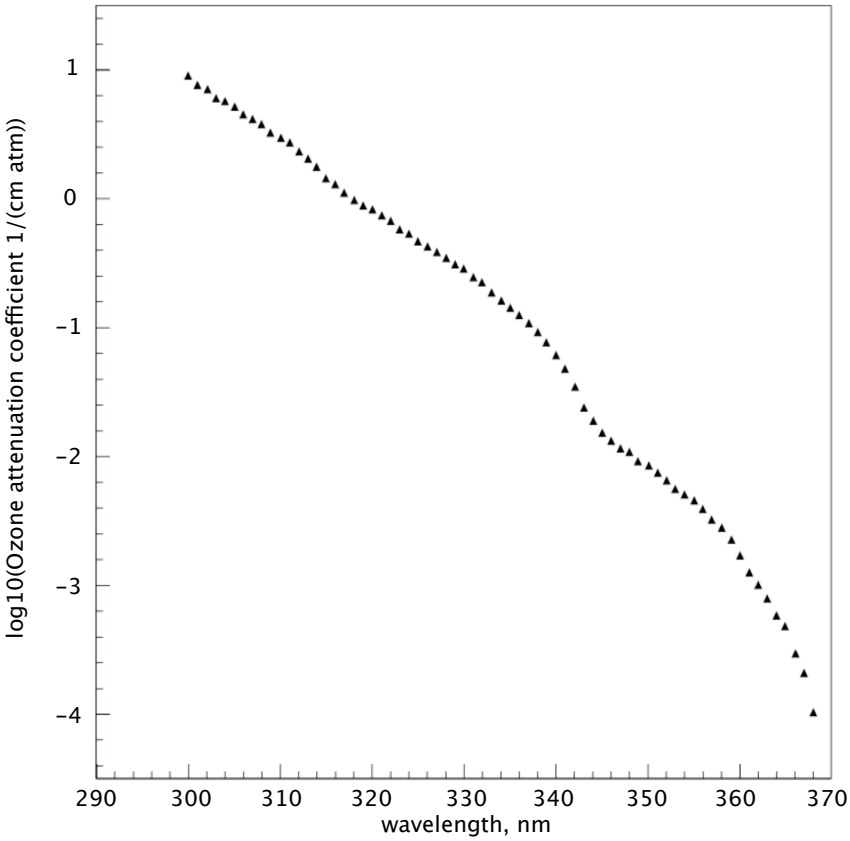

Figure 3.9. Wavelength dependent ozone attenuation coefficient. Adapted from [14].

There are several types of detectors that can be used to count the particles (at the ground level they are mostly γ, $e^{\pm}$ and $\mu^{\pm}$). In the UHE region, the most popular are scintillation counters and water Cherenkov detectors. Scintillation counters (used by AGASA) are composed of PMTs viewing a slab of plastic scintillator. A water Cherenkov detector is a tank filled with high purity water viewed by PMTs. It records Cherenkov light produced by muons and also electrons/positrons or converted photons of the shower. More information on water Cherenkov arrays can be found in the Pierre Auger Project Design Report [66].

The particle density measured by a ground array can then be fitted to a lateral distribution function (equation 3.20 or its modified form [188]), which is one of the steps in determining the primary particle energy. The lateral distribution of the EAS can be also used to measure the core position with great accuracy if the core falls within the array. The arrival direction of the shower is determined by relating the arrival times of the shower front at different array elements.

The greatest advantage of ground arrays is that they can operate at any time of the day and in any weather, so they have up to 100% duty cycle. On the other hand, there are many disadvantages. Since the flux of cosmic rays is low at high energies, ground arrays must cover large areas to be effective. Shower parameters that they measure are also more model dependent. One must heavily rely on the hadronic interaction models.

The problems of each individual detector type discussed above may be overcome by considering a hybrid observation. It is done by measuring the same shower with both a ground array and a fluorescence telescope. The Southern Pierre Auger Observatory is a hybrid cosmic ray observatory in Argentina [66]. The detector consists of 1600 water Cherenkov surface detectors, separated by 1.5 km, covering an area of 3000 km^2 and overlooked by 24 fluorescence telescopes. Utah hosts another hybrid cosmic rays experiment called the Telescope Array (TA). Here cosmic rays are observed at three fluorescence sites and a separate ground array consisting of 512 scintillators set 1.2 km apart from one another. Hybrid cosmic ray detectors are a new generation of air shower experiments that are aiming to better understand the properties of the UHECR.

3.3 Neutrino Initiated EAS

This thesis is devoted to the estimation of neutrino fluxes or their limits based on the data of the HiRes experiment. Being a fluorescence observatory, HiRes extracts infor-

mation on the primary cosmic rays particles through detecting EAS by air fluorescence. Thus, the biggest problem lies in distinguishing between EAS initiated by neutrinos and those initiated by cosmic rays. Fortunately, neutrinos have quite unique properties and impose characteristic features on the EAS. Neutrino properties and how they are reflected in the corresponding EAS will be discussed next.

3.3.1 Neutrino Properties

In the Standard Model (SM) of particle physics neutrinos ν are elementary particles (fermions), members of lepton family, that do not have an electric charge and to the best of our knowledge a mass that it close to zero. There are three known neutrino types (flavors) from three generations of leptons: electron neutrino (ν_e), muon neutrino (ν_μ) and tau neutrino (ν_τ). Neutrinos are known to undergo a flavor oscillation while they propagate through space. In the SM the existence of flavor oscillations requires a nonzero mass of the particles involved, because the probability of transition from one flavor to another is proportional to the mass difference:

$$P = sin^2(2\alpha)sin^2\left(1.27\Delta m^2\frac{L}{m}\right) \tag{3.43}$$

Here α is the mixing angle and L is the propagation distance. If neutrinos have very small masses, they are traveling at a speed which is less than the speed of light, but is very close to it.

In the Standard Model of Particle Physics neutrinos do not participate in electromagnetic or strong interactions, but only in weak interactions. There are two types of neutrino interactions. Neutral Current (NC) interactions are mediated by Z^0 bosons. In a neutral current interaction, a neutrino is transferring some of its energy and momentum to a target particle. All three neutrino flavors regardless of neutrino energy can participate in the NC process. In NC interactions no information about the neutrino flavor can be obtained by analyzing the properties of the recoil particles. The general form of the interaction is given below:

$$\nu_l + X \longrightarrow \nu_l + X, \quad l = e, \mu, \tau \tag{3.44}$$

Electron scattering is the most well known NC process involving neutrino:

$$\nu_e + e^- \longrightarrow Z^0 \longrightarrow \nu_e + e^- \tag{3.45}$$

Neutrino can also interact through Charged Current (CC) interactions by exchanging $W^{\pm}$ bosons. In a CC interaction, a neutrino transforms into its partner lepton (e, μ or τ). The reaction is possible only when the neutrino has sufficient energy to create its heavier partner. In CC the flavor of the incident neutrino can be determined by examining the lepton type created in the reaction. Since the interaction involves the exchange of a charged boson, the target particle has to be changed (e.g., neutron to proton). The general form of CC interaction can be represented as follows:

$$\nu_l + X \longrightarrow l + Y, \quad l = e, \mu, \tau \tag{3.46}$$

The detection of a neutrino is performed indirectly by observing the resulting particles from its interaction with normal matter (protons, neutrons, or electrons). Unfortunately modern Earth based accelerators cannot provide particle beams that are energetic enough to study cross sections at UHE. These cross sections can only be approximated based on theoretical models, extrapolating from low energy data. The interaction cross section of UHE neutrinos with a nucleon can be evaluated by exploiting the parton model [84, 53]. In this model a nucleon if it is broken apart by the exchange boson is represented by a spray of individual quarks. At UHE the neutrino exchanges a boson with a quark inside of the nucleon through a deep inelastic scattering (DIS) process. In case of infinite energy in the neutrino-nucleon center of mass system quarks appear to be free point-like particles that can participate in the interaction independently from the others (but only one per interaction). Thus at the highest energies differential cross section for NC 3.47 and CC 3.48 can be expressed in terms of the Bjorken variables [53] $x = Q^2/2M\nu$ and $y = \nu/E_\nu$ as:

$$\frac{d^2\sigma}{dxdy} = \frac{G_F^2 M E_\nu}{2\pi} \left(\frac{M_Z^2}{Q^2 + M_Z^2} \right) \left[xq^o(x, Q^2) + x\bar{q^o}(x, Q^2)(1-y)^2 \right] \tag{3.47}$$

$$\frac{d^2\sigma}{dxdy} = \frac{2G_F^2 M E_\nu}{\pi} \left(\frac{M_W^2}{Q^2 + M_W^2} \right) \left[xq(x, Q^2) + x\bar{q}(x, Q^2)(1-y)^2 \right] \tag{3.48}$$

$-Q^2$ is the invariant 4-momentum transfer between incident neutrino and outgoing lepton, $\nu = E_\nu - E_{lepton}$ is the energy loss in the nucleon rest frame, M is the nucleon mass, M_Z and M_W are the masses of intermediate bosons and $G_F = 1.16632 \times 10^{-5}$

GeV^{-2} is a Fermi constant. The quantities $q(x,Q^2), \bar{q}(x,Q^2), q^o(x,Q^2)$ and $\bar{q^o}(x,Q^2)$ are parton quark and antiquark distribution functions [84]. For UHE the NC, CC and total neutrino-nucleon cross sections can be approximated according to:

$$\sigma_{NC} \approx 2.3 \times 10^{-36} cm^2 \left(\frac{E_\nu}{1\ GeV}\right)^{0.363} \tag{3.49a}$$

$$\sigma_{CC} \approx 5.5 \times 10^{-36} cm^2 \left(\frac{E_\nu}{1\ GeV}\right)^{0.363} \tag{3.49b}$$

$$\sigma_{total} \approx 7.8 \times 10^{-36} cm^2 \left(\frac{E_\nu}{1\ GeV}\right)^{0.363} \tag{3.49c}$$

When the energy of a neutrino increases (Q^2 gets bigger), the parameter x decreases. At small x the contribution of individual quarks becomes more pronounced. Nowadays experiments can reach $x \sim 10^{-4}$ and in order to get information for smaller x one has to apply extrapolation methods, which introduce large uncertainties.

3.3.2 EAS from UHE Neutrinos

As shown in Chapter 1, the HiRes CR spectrum at the highest energies is readily explained by protons arriving from cosmic accelerators. Cosmogenic neutrinos are then produced through the UHECR interactions on the CMB and their modeled limits are given in section 2.2.

Although at production the ratio of cosmogenic neutrino fluxes is $2:2:0$ for $\nu_e : \nu_\mu : \nu_\tau$, neutrino flavor oscillation leads to approximately equal fluxes of muon and tau flavors after propagation over cosmological distances ($\nu_e : \nu_\mu : \nu_\tau = 2:1:1$). Thus all three neutrino flavors should be considered as the EAS initiators.

Depending on the neutrino flavor (ν_e, ν_μ, ν_τ) and the type of interaction (CN, CC), different scenarios exist for observing a neutrino event with an air fluorescence detector. The channels and the outcomes of different scenarios are summarized in Table 3.2.

In an NC interaction, the recoiled nucleon initiates a hadronic air shower in the atmosphere, but no information is saved about the neutrino type. In a CC interaction, the energy is divided between the recoiling nucleon and the secondary charged lepton that carries the flavor of the initial neutrino. If ν interacts in the atmosphere, the recoiling nucleon will initiate a hadronic air shower. The fate of the lepton is determined by the incident neutrino flavor. In the case of the ν_e CC interaction, an outgoing electron starts a pure electromagnetic air shower. A muon will result from a ν_μ CC interaction. The

Table 3.2. Neutrino shower scenarios

Interaction Type	Reaction	Shower Type
NC	$\nu_l\ X \longrightarrow \nu_l\ X$, $l = e, \mu, \tau$	hadronic shower from recoil
CC	$\nu_e\ X \longrightarrow e\ Y$	hadronic shower from recoil, e/m shower from e
CC	$\nu_\mu\ X \longrightarrow \mu\ Y$	hadronic shower from recoil, long track from μ
CC	$\nu_\tau\ X \longrightarrow \tau\ Y$	hadronic shower from recoil, short track from τ

lifetime of muons is 2 milliseconds ($c\tau$ = 660 m). At the highest energies the decay length becomes so big, that the probability of its decay within the field of view of the detector is negligible. Tau leptons originating from ν_τ CC interaction have much shorter lifetime ($c\tau$ = 87 μm) and have a high probability to decay inside the detector's field of view. The process can induce two showers separated by a distance gap that is on average proportional to the τ energy. These events are known as "Double Bang events" and are a tale-tale signature of tau neutrino EASs.

Due to their extremely small cross sections, neutrino interactions in the atmosphere are rare (a target mass equivalents to thousands of kilometers of water is needed for a single interaction). The passage of a neutrino through the vertical and horizontal depths of the atmosphere is equivalent to passing through 10 and 350 m of water respectively. Even at the highest energies (where the interaction cross section are large) the atmosphere lacks the target mass for a neutrino interaction. On the other hand rock is much denser and can provide enough target mass for neutrino interactions. Unfortunately energy losses also becomes significant in dense materials. Only Earth-skimming UHE neutrinos and those that interact in the mountain ranges surrounding the fluorescence observatory can produce energetic air showers that can exit from the rock and be detected.

Both electron and tau neutrinos interaction in the Earth's crust or in the mountains can produce observable EAS. In the rock muons loose all their energy before they decay. Electromagnetic showers from electrons have a chance of emerging from the rock due to the Landau-Pomeranchuk-Migdal (LPM) effect [127, 139]. Landau and Pomeranchuk in 1953 showed that if the formation length of bremsstrahlung (the length over which the radiation process occurs) becomes comparable to the distance over which the mul-

tiple scattering becomes important, the bremsstrahlung will be suppressed [127]. The quantitative theory of this phenomenon was developed in 1956 by Migdal [139].

Bremsstrahlung is not a point interaction. In this interaction a high energy electron exchanges a virtual photon with a nucleus and emits a photon. The longitudinal momentum transfer between the electron and the nucleus is very small and proportional to

$$q \sim \frac{E_\gamma}{2\gamma^2},\ E_\gamma << E_e \tag{3.50}$$

where γ is E_e/m_e. Since longitudinal momentum transfer is small, the uncertainty principle insists that the exchange of a virtual photon must take place over a finite distance. If while traversing this distance the electron multiple scatters by an angle larger than the photon emission angle $1/\gamma$, the emission is suppressed. This happens when the photon energy is less than E_e^2/E_{LPM}, where E_{LPM} is a material-dependent constant.

The LPM effect results in a significant decrease in the cross sections for bremsstrahlung and pair production, suppressing the development of e/m showers in dense media like rock. Thus the showers are not attenuated as much and have a chance to exit into the Earth's atmosphere with sufficient energy to be observed by a detector. For the analysis of the search for electron neutrino induced showers in the HiRes-II monocular dataset refer to [8].

Due to their short life-time tau leptons decay and transfer energy to the secondary particles before loosing too much energy when they propagate in rock. The decay channels of the tau leptons are summarized in Table 3.3. Tau neutrinos are recreated in the tau decays. For the higher energy tau neutrinos these processes can occur several times. The secondary τ leptons from Earth-skimming ν_τ and those that interact in the mountains can actually exit the rock and decay in the atmosphere producing air showers.

Tau air showers emerging from the Earth crust and the mountains are the most powerful signature of UHE cosmogenic tau neutrinos. These air showers have inclined near horizon tracks. Additionally showers from Earth-skimming neutrinos are up-going as they exit from the Earth's crust into the atmosphere.

The challenge of searching for neutrino events with the fluorescent technique lies in isolating neutrino induced EAS from background a mis-reconstructed down-going cosmic rays events. The main difference between neutrino and cosmic ray events is that cosmic

Table 3.3. Tau neutrino decay channels

Decay mode	Decay Probability	Secondaries	Air Shower Type
$\tau^- \longrightarrow \nu_\tau + e^- + \bar{\nu}_e$	$\sim 17.8\%$	e	electromagnetic
$\tau^- \longrightarrow \nu_\tau + \mu^- + \bar{\nu}_\mu$	$\sim 17.4\%$	μ	unobservable
$\tau^- \longrightarrow \nu_\tau + hadrons$	$\sim 64.8\%$	$\pi^\pm$	hadronic
		$\pi^0 \rightarrow 2\gamma$	electromagnetic

rays interact at the top of the atmosphere and produce down-going showers, whereas neutrino showers can be close to horizontal, originating deep in the atmosphere or in the rock mass surrounding the detector. Cosmic rays events can also produce inclined showers at the top of the atmosphere and they need to be distinguished from the neutrino events.

CHAPTER 4

HIGH RESOLUTION FLY'S EYE (HIRES) EXPERIMENT

This chapter is devoted to the description of the experimental setup and operation of the High Resolution Fly's Eye (HiRes) Experiment. HiRes is a fluorescence observatory, designed to detect the passage of the highest energy cosmic rays through the atmosphere by measuring fluorescent light. For detailed information about the HiRes design refer to [184].

4.1 General Overview of HiRes

HiRes is a second generation fluorescence detector built on the United States Army Dugway Proving Ground (DPG) in the West Desert of Utah 160 km southwest of Salt Lake City. A first fluorescence detector was built back in 1981 and was called the Fly's Eye (FE). For reviews on the Fly's Eye see [35, 60]. It was constructed by the University of Utah group led by George Cassiday on the top of Little Granite Mountain (known to the collaboration as Five Mile Hill). The location of HiRes is shown in Figure 4.1.

DPG provides an optimal location for a fluorescence detector site based on the following arguments:

1. desert elevation (4,500 feet above see level) corresponds to 860 gm/cm^2 (ideal for UHE EAS observation)

2. relative isolation from big light polluters (light is blocked by surrounding mountains)

3. low annual precipitation (increased detector duty cycle)

4. absence of surface water, average humidity 48%, average wind velocity 6 miles/hour (reduced aerosol in the atmosphere compared to the Standard Desert Atmosphere)

5. detector is placed atop a mountain (reduced aerosol influence, since aerosol concentration decreases with height)

Figure 4.1. Location of the High Resolution Fly's Eye experiment relative to Salt Lake City, Utah (the University of Utah). Adapted from [177].

6. available infra-structure (electricity, communication)

7. security for personnel and equipment (military base)

The Fly's Eye detector originally had 67 modules, each containing a spherical mirror accompanied by 12 - 14 PMTs. There were a total number of 880 PMTs, each viewed $5^\circ \times 5^\circ$ region of the sky and together they covered the whole sky. The arrangement of the PMT's and their hexagonal shape gave the detector its famous name because of the resemblance to the compound eye of a fly.

The second site of the Fly's Eye detector was finished in 1986 and contained 36 modules (or mirrors). It was located 3.4 km from the original site. After the construction of the second detector the operation of the Fly's Eye became possible in stereo mode. The FE experiment was taking data until 1992. In November of 1991 the FE detected the world's most energetic cosmic ray event with an energy of 3.2×10^{20} eV.

The first "HiRes" type detector was built as an improvement on the Fly's Eye design and became known as the HiRes Prototype (for more details consult [30]). Comparing to the FE it had bigger mirrors, more PMTs with smaller field of view ($1^\circ \times 1^\circ$) and better sample and hold (S&H) electronics. The modifications to the Fly's Eye were reflected in its new name - High Resolution Fly's Eye. The prototype HiRes detector was located at the original FE site and had 14 mirrors arranged in "five" rings covering from 3° to 70° in elevation. It became fully functional in 1993. Two of its mirrors were oriented to overlook the FE-2 site, the Chicago Air Shower Array (CASA) and the Michigan Muon Array (MIA) (the last two experiments were also located at the FE-2 site). The HiRes-2 24 mirror prototype was deployed in 1994 12.6 km from HiRes-1. The HiRes-2 mirrors were arranged in two rings to overlap with the field of view of HiRes-1 and CASA/MIA. The HiRes prototype was taking data in stereo configuration for only two years. It was shut down in 1996 to be replaced with final configuration of the HiRes experiment.

The new HiRes experiment was aimed to study the high end of the cosmic ray energy spectrum. A study conducted by the HiRes collaboration showed that in order to obtain the maximum aperture for a 10^{20} eV event, the mirrors of a detector should be arranged such that they cover full 360° in azimuthal direction and from 3° to 17° in elevation [14]. This was considered in the design of the new HiRes Detector.

The HiRes experiment, as its prototype, consisted of two separate sites: HiRes-1 and HiRes-2. HiRes-1 began operation in 1997 replacing its ancestor, the HiRes-1 Prototype, at Five Mile Hill (112°50'08.8764"N longitude, 40°11'42.6156"W latitude and 1597 m above sea level). The mirrors of HiRes-1 were arranged in a single ring covering 352° of azimuth and from 3° to 17° in elevation. Figure 4.2(a) presents the HiRes-1 event display that illustrates the orientation of the HiRes-1 cameras.

The HiRes-2 site went online in 1999. It was sitting on the top of Camels Back Ridge (112°57'32.292"W longitude, 40°07'55.452"N latitude and 1553 m above sea level). HiRes-2 had two rings with a total of 42 mirrors covering an azimuth angle of 336° and elevations from 3° to 30°. Figure 4.2(b) is similar to Figure 4.2(a) but shows the HiRes-2 cameras and their relative position.

A basic element of HiRes (also called a camera or a mirror) includes a spherical mirror, a cluster of photo-multiplier tubes (PMTs) and data-acquisition (DAQ) electronics. Figure 4.3 shows a simplified representation of a mirror. Mirrors are used to focus fluorescence light produced by an EAS in the atmosphere onto the PMT cluster. The

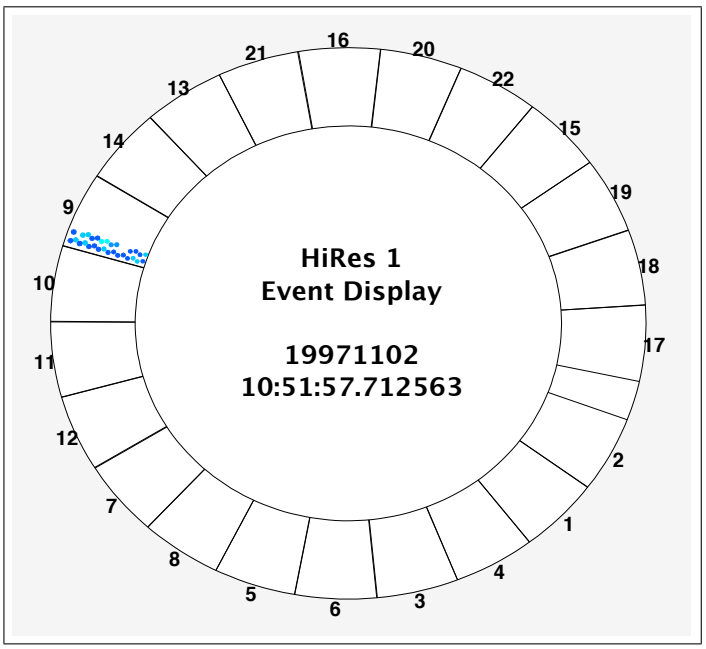

(a) HiRes-1: Camera 7 points at HiRes-2.

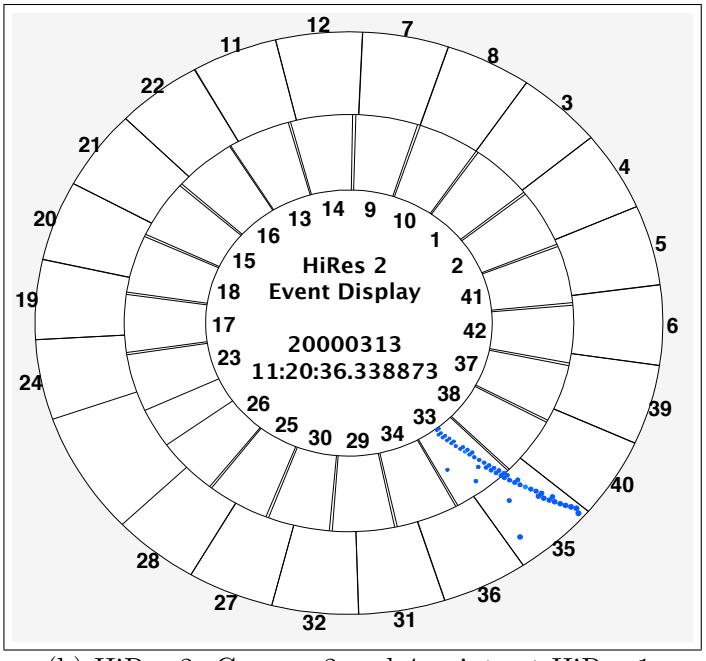

(b) HiRes-2: Camera 2 and 4 points at HiRes-1.

Figure 4.2. HiRes event displays. North is up, the zenith is at the center of each display and the horizon is at the outer edge. Both event date and time are shown in the center of the display. An event can be seen in mirror 9 of HiRes-1 and to cross from mirror 33 into mirror 35 at Hires-2.

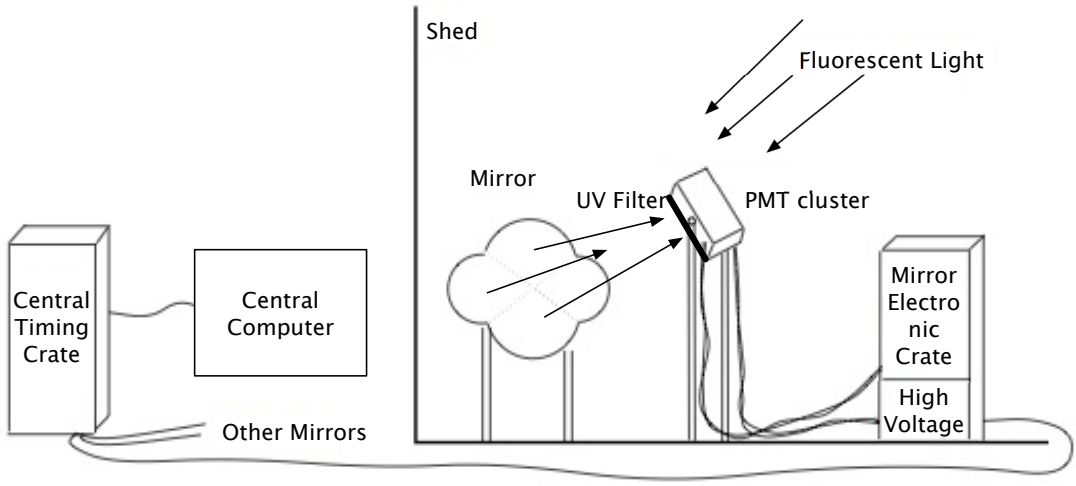

Figure 4.3. Schematic of a basic HiRes detector unit.

camera cluster is located $\sim 2.3\ m$ in front of a mirror, right in its focal plane. In order to improve the signal to noise ratio, reflected light from the mirror is going through a UV-pass filter, which is mounted on the front face of the cluster. The PMTs convert fluorescent light into an electrical signal. The signals from the cluster are digitized by accompanying electronics and collected at a central facility.

The layouts of the HiRes-1 and the HiRes-2 detectors are shown in Figures 4.4(a) and 4.4(b) respectively. Detector units (mirrors) are housed in specially designed mirror shelters, usually in pairs. These mirror shelters are made of steel with large garage-style doors as the front face (Figure 4.5). The doors open for observation during moonless nights and close before sunrise to protect optics and electronics from direct sunlight. Five out of twelve HiRes-1 buildings had been used for the HiRes-1 Prototype and were designed to overlook CASA/MIA. The two round buildings in Figure 4.4(a) are corn silos whose front faces and roof slid back for the observation at the highest elevation angles.

The HiRes-1 detector was operated from a central facility where the rest of the data acquisition (DAQ) system, GPS-based Central Timing (CT) and a YaG laser used for detector calibration were located. Electronics for each camera was connected to the DAQ via Ethernet and to CT via separate timing cables. A dedicated T1 line connected the HiRes-1 site with the outside world. The HiRes- 2 site was also controlled from a central

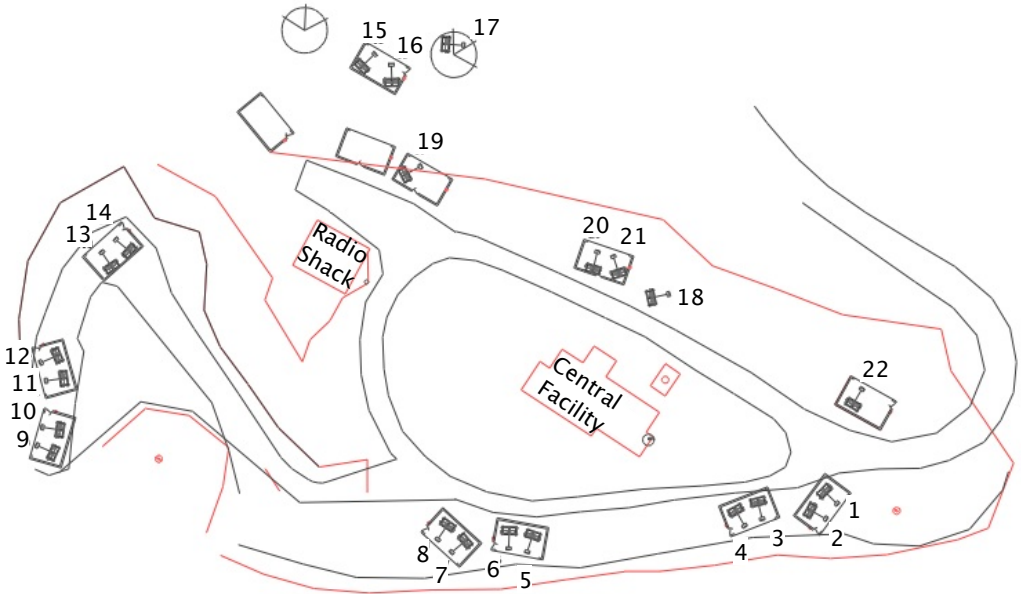

(a) HiRes-1

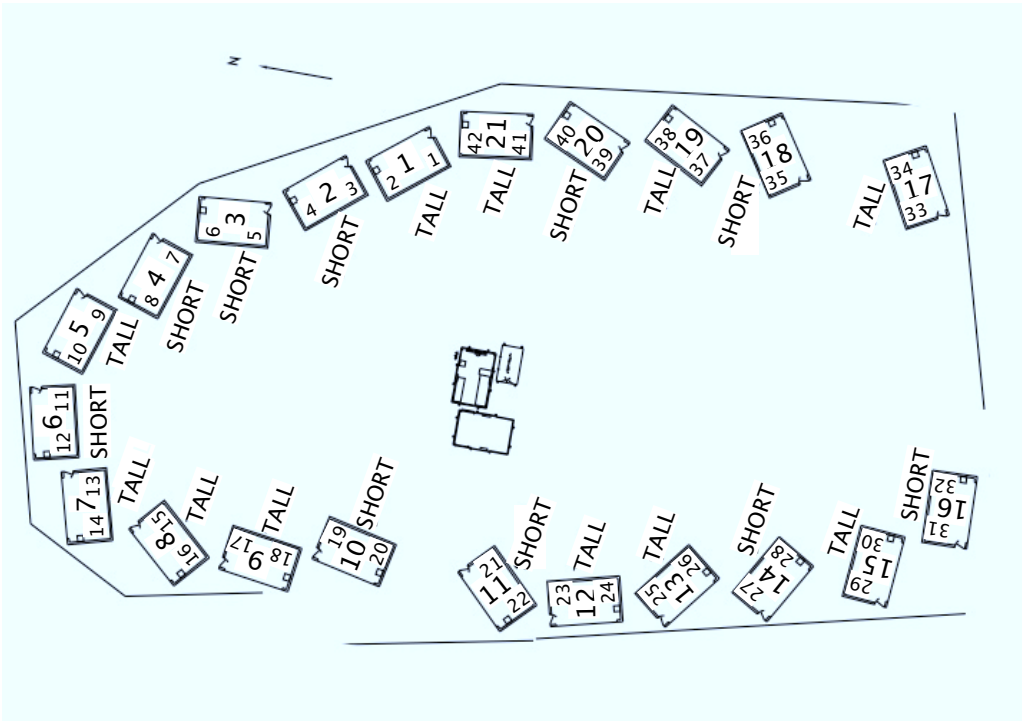

(b) HiRes-2: Short and tall refer to the height of the cluster stands. Tall stands are needed for the upper elevation mirrors.

Figure 4.4. The physical layout of the HiRes detector.

Figure 4.5. Photograph of a HiRes detector building.

facility. The HiRes-2 camera racks communicated via bi-directional, serially connected optical fibers.

The HiRes experiment stopped operation in April of 2006 after almost 10 years of taking data. The experiment has been very successful and made remarkable contributions to cosmic ray research.

4.2 The HiRes Optics

The HiRes optics include spherical mirrors, UV sensitive cameras (clusters of PMTs) and UV filters.

4.2.1 Mirror

A HiRes spherical mirror is serving the purpose of collecting UV light from EASs and focusing it on a PMT cluster. Each mirror is made of glass and coated with aluminum. Mirrors are composed of four separate segments such that the shape of the mirrors resembles a clover leaf (see Figure 4.5). This was done for ease of fabrication. Despite

having a diameter of 2 m the mirrors only have an effective area of 3.8 m^2. Reduction in the area is due to the clover shape of the mirrors and obstruction by the PMT cluster. The radius of curvature of the mirrors is 474 cm.

Mirror reflectivity is about 90% and varies slightly with wavelength. Mirror reflectivity as a function of wavelength is plotted in Figure 4.6. Accumulation of dust on the mirror surface can reduce its reflectivity by 10%. This analysis uses a value of 80% for the mirror reflectivity.

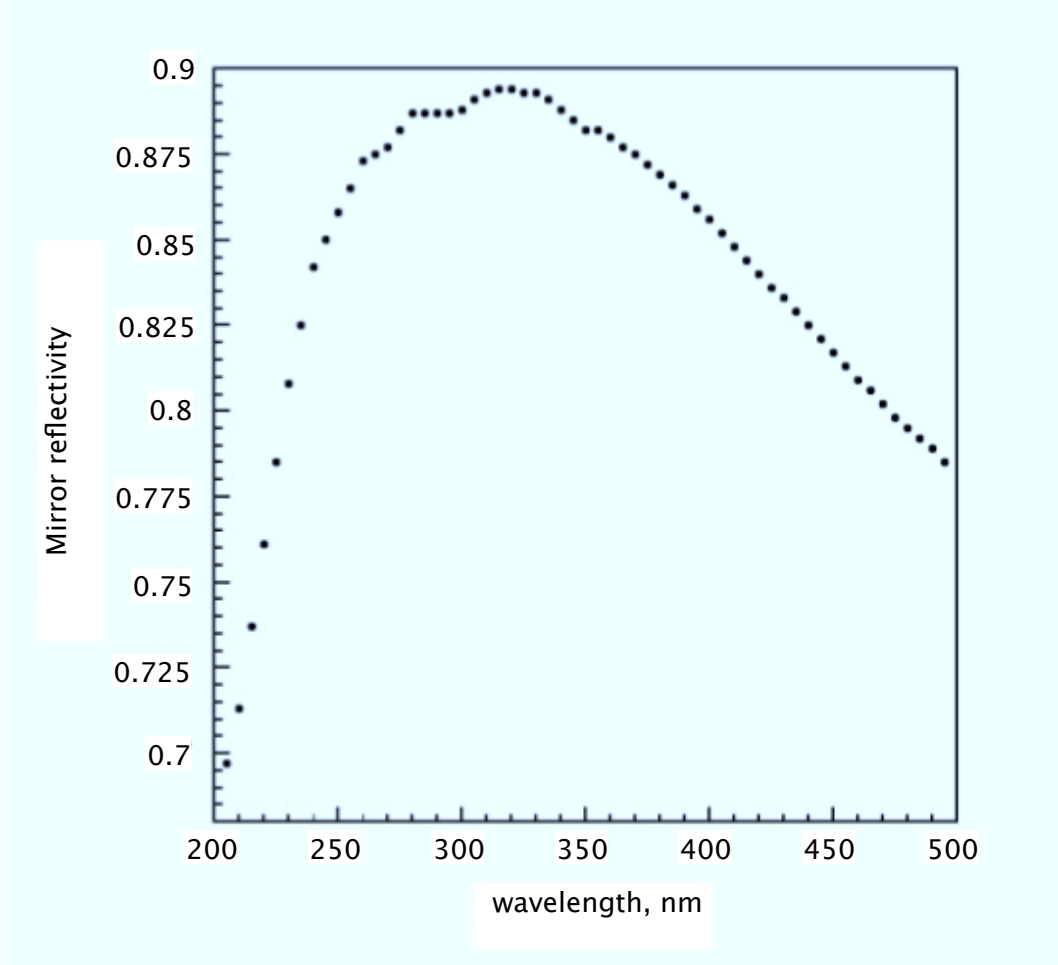

Figure 4.6. Wavelength dependance of mirror reflectivity.

4.2.2 UV Sensitive Camera

The UV sensitive camera is a cluster of 256 photomultiplier tubes arranged in a honeycomb structure of 16×16 tubes. The tube arrangement in the cluster and a photograph of a UV camera are shown in Figures 4.7 and 4.8, respectively. The surface of a cluster box that points towards the mirror is known as the cluster plane. The cluster plane normal vector lies parallel to the imaginary line that connects the center of the cluster plane with the center of the mirror (mirror axis goes through the center of the cluster plane). Each tube views approximately $1^\circ \times 1^\circ$ of the sky and a cluster as a whole has a field of view of about $16^\circ \times 14^\circ$ (horizontal × vertical).

The light signal that is focused on the UV camera by the spherical mirror produces a finite image spot size. The spot size and its shape depends on the direction of the incident light due to spherical aberration. The distance of the cluster from the mirror was optimized to produce a minimum spot size and minimize its off-axis variation. Figure 4.9 shows the variations in the size and the shape of a spot size as a function of spot distance from the mirror axis. Light is better focused if it is incident along the mirror axis.

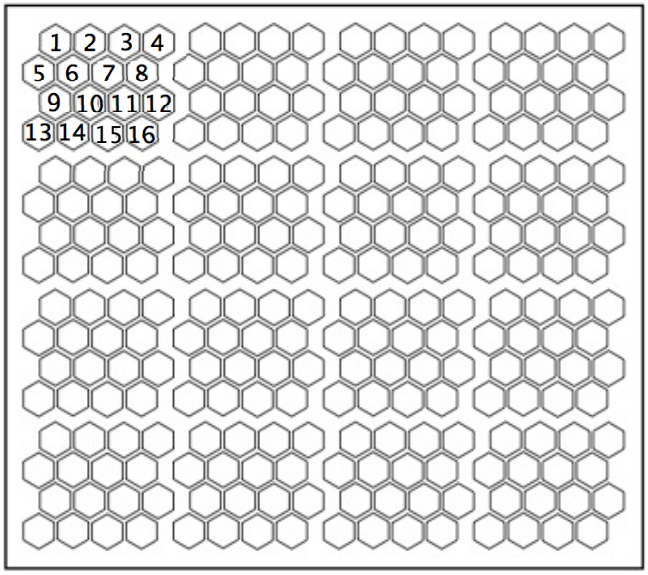

Figure 4.7. Arrangement of PMTs within a cluster. The total number of 256 tubes is arranged in 16 subclusters of 16 PMTs each. The numbering of the PMTs within the subcluster is shown for the top left subcluster. The same numbering system is used to assign numbers to subclusters in a cluster.

Figure 4.8. UV camera of HiRes detector - a cluster of PMTs

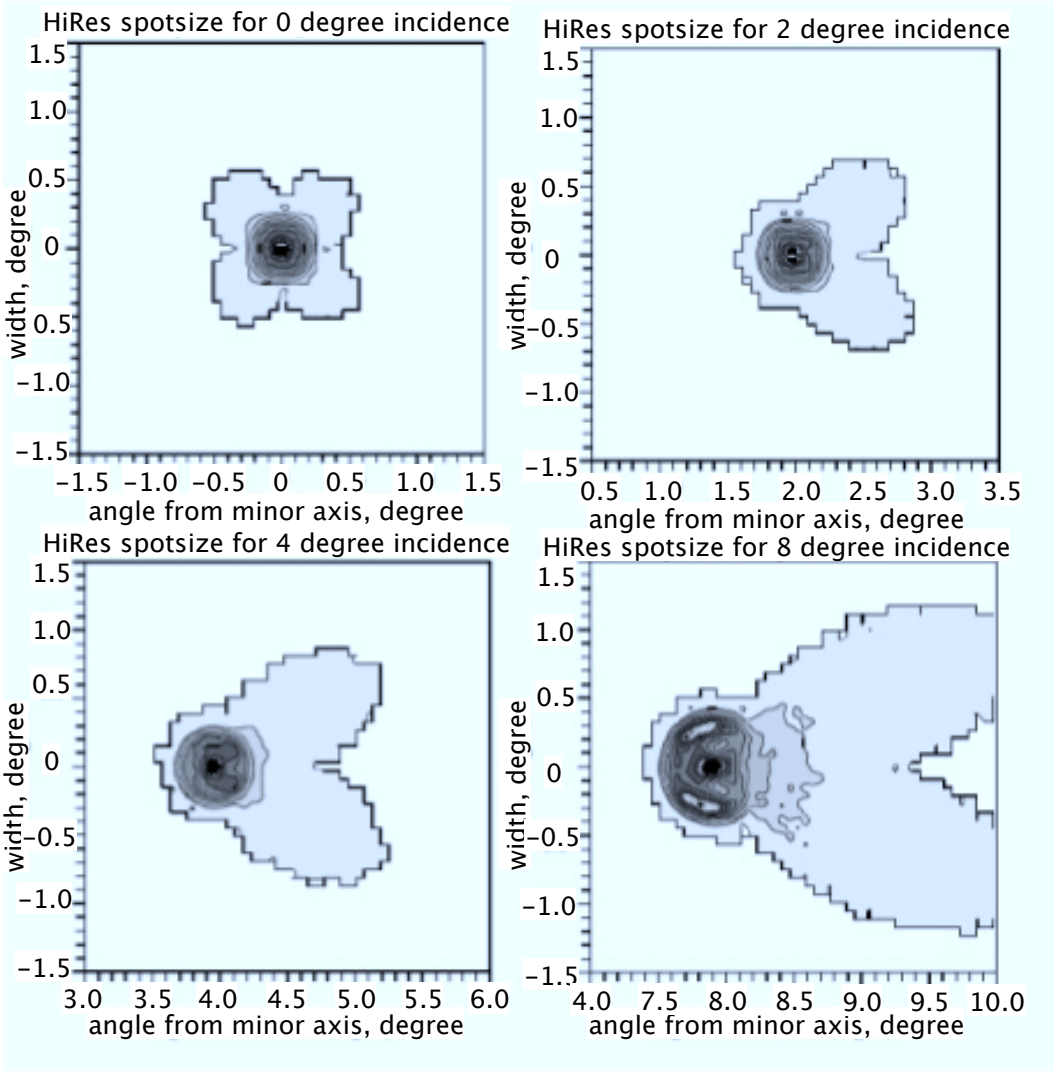

Figure 4.9. Mirror spot size and shape variations. Shape and size of a spot produced by a mirror onto the PMT cluster for the spot location 0°, 2°, 4°, and 8° away from mirror axis.

There are two types of PMTs that are used in HiRes. We distinguish them by manufacturer: EMI and Philips. A photograph of a PMT is shown in Figure 4.10. A photomultiplier tube is a devise widely used for converting a light pulse into a corresponding electrical signal by exploiting the photoelectric effect. The main components of a PMT are the photocathode, several dynodes, and an anode which are kept under high vacuum inside a glass envelope. Incident photons knock out photo-electrons from the cathode material (photoelectric effect), which are then directed by the focusing electrode

Figure 4.10. Photo multiplier tubes used in HiRes Experiment

toward the chain of dynodes, where electrons are multiplied by the process of secondary emission. Each dynode is held at a more positive voltage than the previous one so that electrons are accelerated as they travel between them and more electrons are produced at the next stage of the multiplying process. Finally all electrons reach the anode and produce a current pulse, which is proportional to the total number of original photons.

The main characteristics of PMTs are its quantum efficiency (QE) and gain and they are similar for both types of tubes. The quantum efficiency is given as

$$QE = \frac{number\ of\ photo-electrons}{number\ of\ incident\ photons} \tag{4.1}$$

According to Figure 4.11, QE depends on the wavelength of incident light and ranges from 0% to 30%. It also depends on the material of the photocathode. The fact that QE is not uniform over the photocathode surface must also be considered. Figure 4.12 shows a typical profile of PMT response across the PMT photocathode window. The absolute gain of a PMT as a function of voltage (V) applied between the cathode and anode is given by

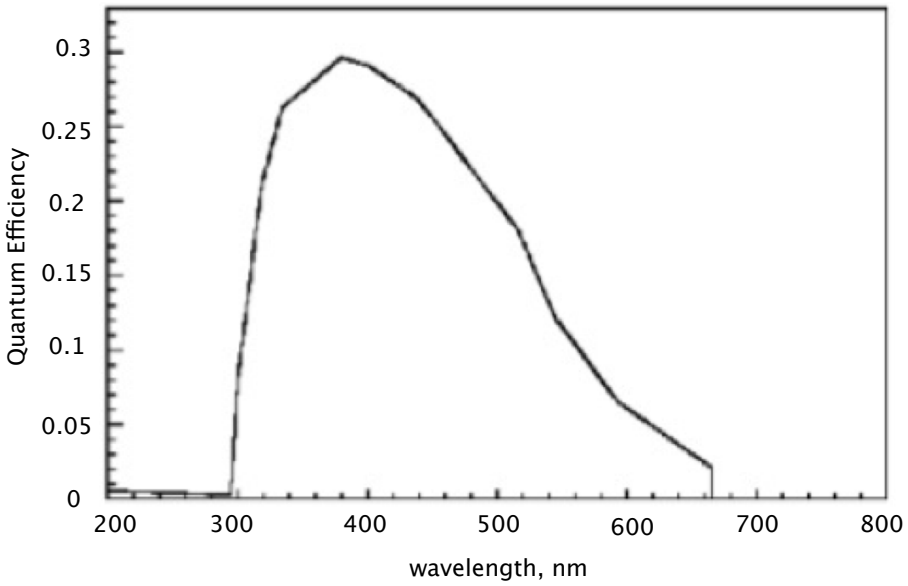

Figure 4.11. Quantum efficiency of a PMT as a function of wavelength

.

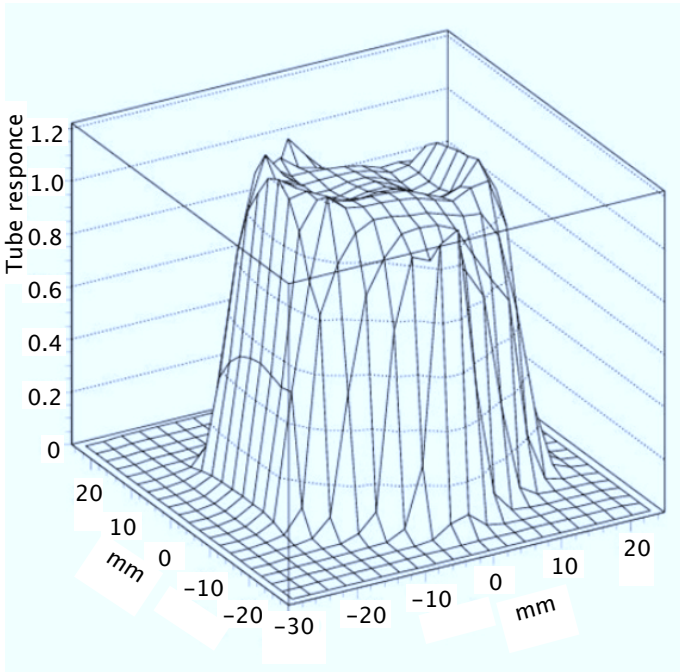

Figure 4.12. PMT response profile in arbitrary units.

.

$$Gain = e^{\alpha} \cdot V^{\beta} \tag{4.2}$$

where α and β are constants and determined during the calibration for each tube. Considering that the high voltage that is applied to the tubes is about 1000 V, $\alpha \approx -30$ and $\beta \approx 6$, the typical gain of HiRes PMTs is about 10^5.

4.2.3 UV Filter

A UV filter is installed in front of each PMT cluster. Figure 4.8 shows a detector camera with an open UV filter. The UV filter is used to improve the signal to noise ratio by cutting outside of the fluorescence wavelengths. Only UV light with wavelengths between 300 and 400 nm passes through the filter. Filter transmittance is plotted in Figure 4.13.

4.3 HiRes Electronics

The amplified signal from the UV camera goes to a mirror electronics rack for further processing. The electronics rack (one rack for each mirror) houses both high voltage (HV) and low voltage (LV) power supplies as well as the mirror readout system. HiRes-1 and HiRes-2 have very different mirror electronics. To expedite the time for HiRes-1 to become fully functional, it was built using "recycled" parts from the HiRes prototype

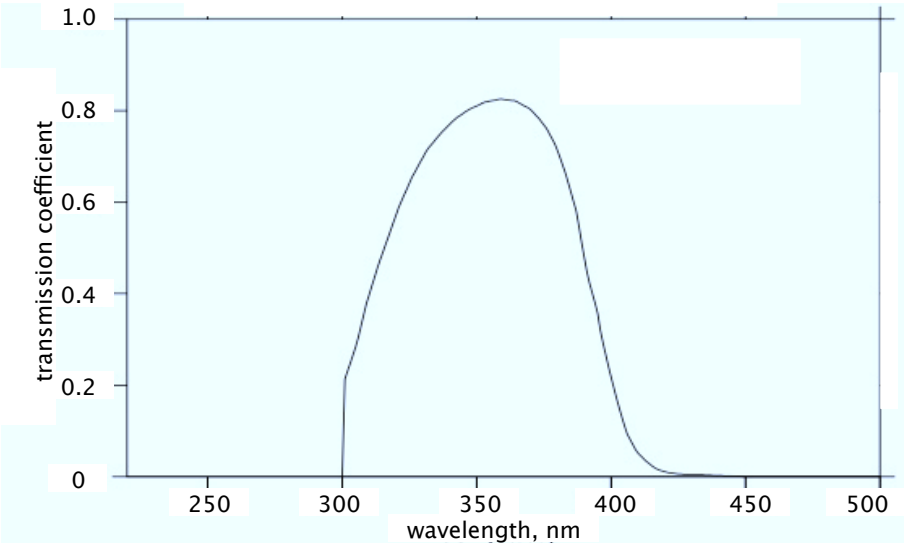

Figure 4.13. UV filter transmittance.

detector. Thus HiRes-1 inherited the"sample and hold" (S&H) electronics. HiRes-2 was built later with more advanced "flash analog to digital" (FADC) electronics.

4.3.1 Mirror Electronics

HiRes readout electronics consists of (also see Figure 4.14):

1. a CPU board
2. a programmable pulse generator (PPG) board
3. a trigger logic board
4. a "garbage" board
5. 16 data acquisition (ommatidial) (OMB) boards

PMT signals are first sent to the ommatidial boards where secondary signal amplification, integration and digitization occurs. Amplification of a signal happens first. After

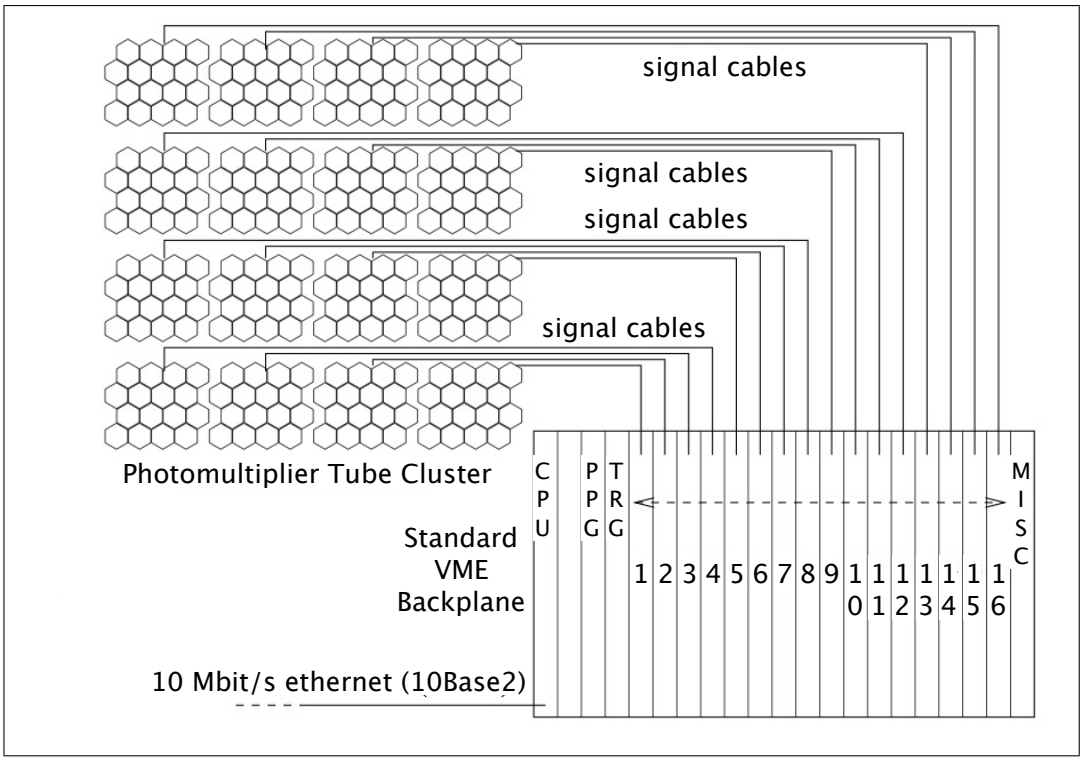

Figure 4.14. HiRes electronics rack diagram.

that it is sent through a low-pass filter that removes pulses with widths shorter than the expected cosmic ray signal pulse width. Next the signal is analyzed by a tube trigger module. If the signal is above a certain threshold, then the PMT is considered to be triggered and the signal integrator is activated. At this step triggering time and the charge are measured. The HiRes-1 S&H electronics records the integrated charge for each pulse within a 5.6 μsec time window, while HiRes-2 FADCs save the pulse forms by continuously digitizing every 100 nsec. To ensure that the entire pulse is integrated and digitized, a PMT signal arrives at the integrator with a delay. Starting from this moment, tube cannot be triggered again for 25 μsec. This time is call tube "hold-off" or "dead" time.

During dead time, the information about all the tubes in the subcluster is analyzed and a decision on subcluster triggering is made. In order to be triggered, a subcluster (explained in Figure 4.7) has to have at least three tube triggers with at least two of them being hexagonally adjacent. From a subcluster the trigger signal is sent to a mirror trigger board, where triggering on the mirror level is considered and an additional 25 μsec are added to the tube "hold-off" time.

A mirror trigger is used when no less than three subclusters are triggered, with two diagonally adjacent. In case of a mirror trigger the tube dead time is increased by another 25 μsec to give other tubes a chance to trigger and contribute to the event. This is done to decrease the possibility of a track cut-off. At the end of the "hold-off" time the mirror trigger signal is sent to Central Timing (CT) for the information on the absolute trigger time. The next 8 msec become mirror dead time. This time is used by the CPU board to read the timing and charge information of every triggered PMT and to send the data packet to the Central Acquisition System. This concludes the readout and the mirror is permitted to trigger again. In order to find a good compromise between measuring signal (CR events) and rejecting noise, trigger thresholds are automatically and dynamically adjusted according to the night sky noise so that average trigger rate was 200 Hz.

The garbage board is multifunctional. It controls the HV readout system, preamplifier power to each PMT subcluster, monitors temperature and remotely controls the garage doors. PPG boards are used to generate square pulses for calibration of the mirror electronics and will be discussed later. For more profound discussion on the HiRes mirror electronics and the difference between HiRes-1 and HiRes-2 electronics, consult the thesis of Belov [38] or Wilkinson [184].

4.3.2 Central Timing

The subject of the HiRes Central Timing (CT) system is covered in great details by Wilkinson in [184]. CT is essential for providing timing records of various HiRes systems. CT exploits a 24 bit, 40 MHz scaler with a resolution of 25 nsec. The scaler is synchronized to absolute UTC by a global position system (GPS) clock. Each site measures event times independently, but relative timing between them is good to the order of 10 ns. The calibration systems of the detector, which will be described next, are also equipped with GPS receivers for easy identification and extraction of calibration related events from the data.

4.4 Calibration

Calibration is a crucial part of HiRes operation. When an EAS moves through the atmosphere, it produces fluorescent light. By measuring this light we can estimate the main shower parameters, which can be used later for determining the shower energy, the type of the primary particle and its arrival direction. This can be done only in case we understand the response of the detector's main components to the fluorescence light and the influence of the atmospheric conditions on light propagation. These are two main sources of errors in the measurement of shower parameters and they should be well understood and controlled when it is possible.

4.4.1 Detector Calibration

Detector calibration is required to know how the detector's main components (PMTs, mirrors, filters) respond the incident fluorescent light.

PMT calibration involves several steps. Before being placed into a cluster, each tube was calibrated using a NIST-calibrated photodiode to study its total photocathode area, variation in the tube sensitivity across the surface and its overall gain. In order to achieve this each tube was illuminated by a 325 nm HeCd normally incident laser beam. The laser produces a 1mm spot, which can be moved horizontally and vertically to measure a total number of 418 points across the surface of the tube. Figure 4.12 shows a typical tube response profile. The response over tube surface is quite homogeneous and was shown not to vary much from tube to tube. There also is not much difference in the response profiles between tubes made by EMI and Philips. The tube gain as a function of applied voltage is measured at seven points on the tube surface. PMTs with small photocathode

area, more that 20% nonuniformity across the surface and low gain are rejected. Tubes with similar properties were grouped into the same cluster.

Since the response of a PMT can change with time, it is checked periodically using the Roving Xenon Flasher (RXF) and every night using a YAG laser.

The RXF is a xenon flash bulb with a strong emission between 300-400 nm (consistent with the spectrum of atmospheric fluorescence). Mounted in a portable housing it can be moved from one camera to another and placed in the center of a mirror to illuminate a cluster directly. The pedestal-subtracted QDC counts can be measured as a function of the number of photo-electrons arriving at each PMT. As the different neutral density filters are placed between the RXF and PMTs, the PMTs response to light pulses with different intensities can be measured. The response of the tubes (QDC counts) is the linear function of the number of photo-electrons hitting the tube (known for each of the different neutral density filters in front of the RXF). For HiRes-1 the gain of a tube is the slope of the plot shown in Figure 4.15 of pedestal subtracted QDC counts vs. the number of photo-electrons. At HiRes-2 the response is used to adjust software-controlled gains to give one FADC count per photo-electron.

The output of the RXF is found to be stable with a pulse-to-pulse variations $\sim 0.3\%$ and within 2% over a night of operation. A single RXF flash is assumed to produce 12,000 photons per tube and have excellent long-term stability.

Since RXF calibration can be applied to one camera at a time, the whole process is quite time consuming and takes place approximately once a month (usually between runs or during bad weather nights).

A YAG laser is used to monitor the PMT responses on a nightly basis. The frequency-tripled YAG laser delivers light at 355 nm to each mirror and each cluster via quartz optical fibers. One of the fibers goes to the center of the mirror and illuminates the cluster directly. A teflon diffuser at the end of the fiber provides uniform illumination of the cluster. Figure 4.15 shows the excellent agreement between RXF and YAG laser gain estimations (a single YAG entry of Figure 4.15 was obtained on the same night with RXF calibration). The second bundle of fibers goes to each side of a PMT cluster and illuminates the mirror, so that changes in the mirror reflectivity can be studied.

The YAG calibration laser is fired several hundreds of times at the beginning and the end of each run at both sites. Calibration is done for both closed and open door conditions to estimate the sky noise at the beginning and the end of the night. YAG

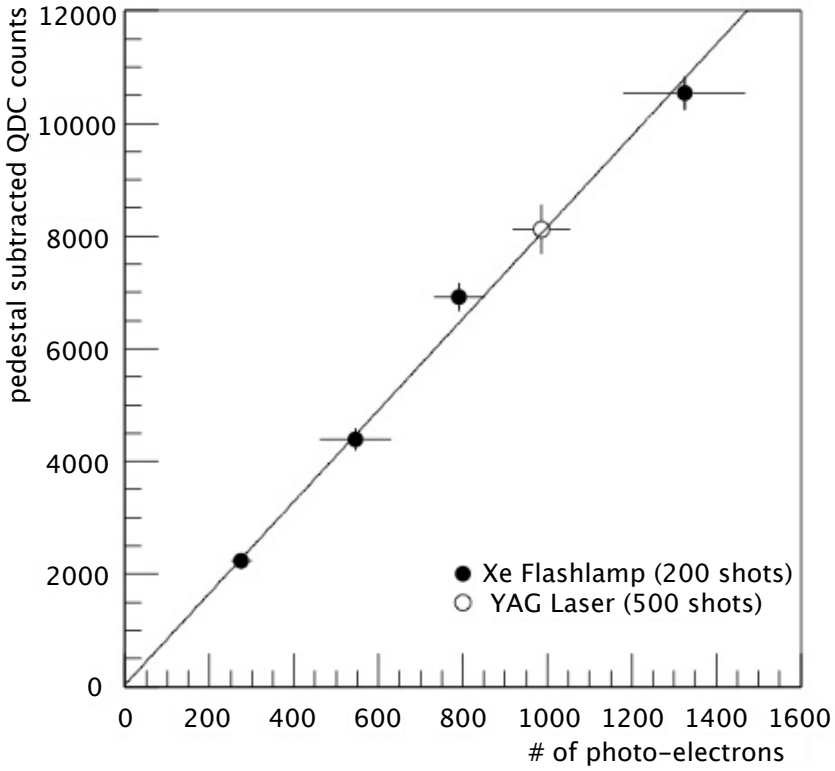

Figure 4.15. Gain fit for a single PMT.

calibration also helps to detect "dead" tubes by failure to respond to the YAG light.

Finally the gains of PMT pre-amplifiers and electronics are measured each night of operation using a Programmable Pulse Generator (PPG).

4.4.2 Atmospheric Calibration

Monitoring the influence of atmospheric conditions on fluorescent light propagation is as vital as understanding the detector response to the received light, since we are aiming to deduce the number of charged particles in the shower. Fluorescent light is scattered as it propagates from the shower to the detecter. Molecular scattering is well understood and can easily be taken into account considering that molecular density profile variations from the U.S. Standard Atmosphere model are small. Aerosol scattering on the contrary is less well known and is complicated by the possibility of sudden and dramatic changes in the aerosol concentration and spatial distribution depending on weather conditions. Atmospheric monitoring tools are employed to monitor the

condition of the atmosphere throughtout detector operation and include observations, cloud monitors, weather stations, xenon Inter-Site Flashers, vertical flashers and steerable YAG lasers.

Weather Codes : A subjective measure of weather is recorded hourly by a detector operator into the operation logs. The information about cloud coverage is provided as a seven digit code. Four digits correspond to the low elevation cloud coverage in all four directions (N, E, S, W) and given in a binary 0 (no clouds) and 1 (some clouds) format. The overhead cloud coverage is estimated by assigning a number from zero to four. 0 corresponds to no clouds, 1 if less than 1/4 of the sky is covered with cloud, 2 if the coverage is more than 1/4 but less than 1/2. Similarly 3 is used between 1/2 and 3/4 and 4 for greater than 3/4 cloud sky coverage. The sixth digit indicates the thickness of the clouds with 0 in case of clear sky conditions and 1 if no stars are visible overhead. Haze indication is given by the last digit (0 - no haze, 1- hazy condition).

Cloud monitors : Cloud monitors provide additional information about the cloud coverage during data taking time. There were 11 infrared sensors inside the buildings at the HiRes-1 site and one high-resolution steerable infrared cloud monitor. The 7-13 μm infrared sensors have a $30^\circ \times 30^\circ$ field of view and detect variations in sky temperature as a function of time. The field of view of the cloud sensor is only 3° in diameter. The sensor is located at the HiRes-1 site and is set up to continuously perform full sky scans during operation time. The information from sensors and the sensor was displayed in real time to assist the operator with identifying clouds and recorded for use in the analysis.

Weather Stations : Two weather monitoring stations installed at the HiRes-2 site (one at the central trailer and the other at the steerable laser building) provided information about temperature, humidity and wind. This information is recorded into the logs on an hourly basis.

Inter-Site Flasher : The Inter-Site Flasher (ISF) was installed at the old Fly's Eye-2 site and is used for local atmospheric monitoring. The ISF is a Xenon flasher with a track that goes through as many as 11 HiRes-1 mirrors. It fired automatically every night which allows to examine weather conditions on a particular night.

Vertical Flasher : Ten vertical xenon flashers are located in the desert between the HiRes-1 and the HiRes-2 sites as shown in Figure 4.16. When flashers are fired their tracks are seen by both detectors. The shape and the intensity of a flasher event will depend on the atmospheric conditions and provides another tool to monitor the atmosphere. Vertical flashers can also be used to measure the inter-site time offset and as tests to the geometry reconstruction routines.

Steerable YAG Lasers : Steerable, frequency-tripled 355 nm YAG lasers are located at each detector site in separate buildings. The lasers were fired periodically (every

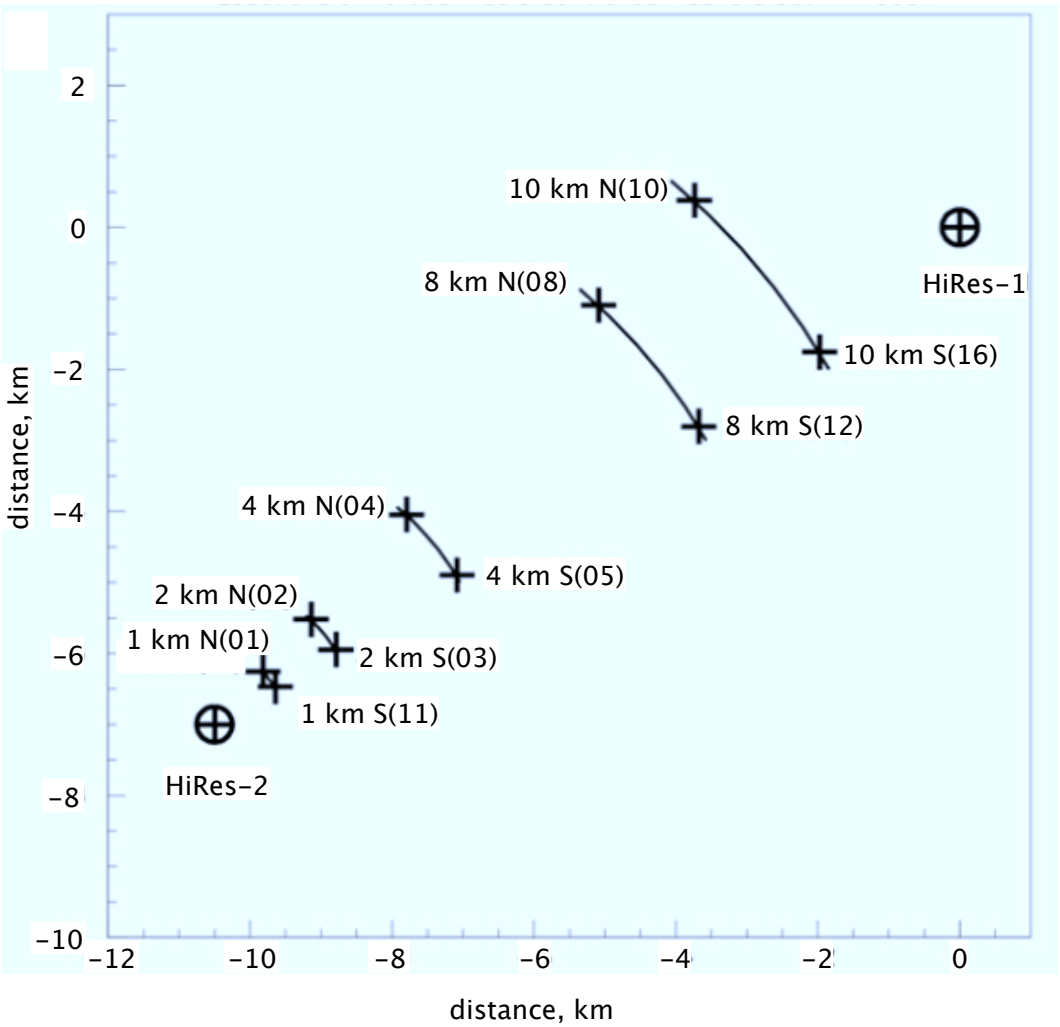

Figure 4.16. Map of locations in the vertical flasher array relative to the HiRes-1 and HiRes-2 sites.

hour) with predefined geometrical patterns and energies. The YAG laser provides a quantitative calibration of atmospheric conditions. In case of an interesting candidate for a very high energy CR even, the laser automatically fires several times in the direction of the shower. This provides important information about the atmospheric conditions in the vicinity of the shower at the time of this CR event.

The so-called Terra Laser is located 22 km from the HiRes-1 and 34 km from the HiRes-2 in Terra and is used to study the atmospheric transmission at the significant distance from the detectors. It provides a fixed geometry vertical beam at the edge of the aperture over the last couple years of HiRes operation for testing the detector aperture at the highest energies [183].

Steerable lasers shots are also used to monitor the UV transmission properties of the atmosphere. This information is important for making a correction for the attenuation of fluorescence light. The most important parameter measured is the vertical aerosol optical depth (VAOD). YAG studies suggest the mean value of the VAOD is 0.04 with a rms variation of 0.02 [194]. A detailed discussion on this measurement is given in [182].

CHAPTER 5

MONTE CARLO SIMULATION

The development of a cosmic ray event in general and a neutrino event in particular from the first interaction in the atmosphere through the generation of the associated EAS and the detector response to the fluorescent light is an extremely complicated process. For cosmic ray primaries in order to test our understanding of the physical processes involved we use a Monte Carlo (MC) simulation to model CR events and compare the results of the simulation to the experimental data. In the case of neutrino primaries, MC simulation helps to find the parameters that distinguish neutrino events from the background of cosmic ray events and applying appropriate cuts to minimize the background.

In order to simulate neutrino events adequately all the processes that govern the creation of a real event should be taken into account, including interaction of the ν primary, shower development, light production and propagation as well as the detector optics and electronics responses. Our simulation process is divided into three steps, each based on its own MC. The interaction of tau neutrino primaries and the subsequent decay of τ leptons is handled by the high-energy neutrino Monte Carlo event generator ANIS (All Neutrino Interaction Simulation) [86]. ANIS was designed for a typical underground neutrino detector such as AMANDA [26], BAIKAL [34], ANTARES [119] or ICECUBE [20] and had to be modified to be suitable for a fluorescence detector (all modifications are discussed in [71]). The second step of shower development in the atmosphere was implemented using the simulation program CORSIKA (COsmic Ray SImulations for KAscade) [98]. The output of CORSIKA was finally fed into the HiRes Detector Monte Carlo (HDMC). All three steps are used to calculate the detector efficiency for tau air showers. All three simulation steps are discussed in this chapter.

5.1 Neutrino Monte Carlo

Simulations of tau neutrino interactions and the subsequent decay of the tau leptons are handled by the high-energy neutrino Monte Carlo event generator ANIS Version

1.8.1 [86]. ANIS was written as a simulation package for high energy underground water/ice Cherenkov neutrino telescopes such as AMANDA [26], BAIKAL [34], ANTARES [119] or ICECUBE [20]. It generates neutrinos of any flavor according to a given flux and propagates them through a model of the Earth that reflects its density profile. All relevant standard model processes are implemented in ANIS and neutrino interactions can be simulated in a specified volume. In order to use ANIS to simulate events for the HiRes detector a few modification have been made by Weiran Deng [71] and they are discussed later in this section.

5.1.1 Description of the Modified ANIS Event Generator

ANIS is a C++ program that exploits the vector package of the CLHEP library [1] and implements the HepMC Monte Carlo event record [72], which holds all interaction vertices with their respective incoming and outgoing particles. The CC, NC neutrino interaction channels as well as Glashow resonant W^- production at $E_{\bar{\nu}_e} \approx 6.3 \times 10^6$ GeV (equation 5.1) are implemented in the MC.

$$\bar{\nu}_e \; e^- \longrightarrow W^- \longrightarrow anything \tag{5.1}$$

At small energies ($E_\nu \leq 10^6$ GeV) neutrino-nucleon deep inelastic cross sections are described using a pQCD (Perturbative Quantum Chromo-Dynamics) framework with the parameterization of the νN structure function according to CTEQ5 [126]. At the highest energies the behavior of the structure function is unknown and thus model dependent. As the Bjorken variable x is getting smaller (momentum transfer Q^2 is getting bigger) the uncertainty in extrapolations of the structure function (and the derived cross section) increases. ANIS provides two options of extrapolating the structure function to small x (large Q^2). The first option and the one that is used in our simulation uses a power-law extrapolation of the pQCD CTEQ5 parameterization. The other one is a hard pomeron (HP) enhanced extrapolation [87]. νN cross section for both prediction are shown in Figure 5.1.

In order to decrease the time of the simulation process cross-section data for CC and NC reactions are provided in terms of pre-calculated tables. The total cross section is then found by interpolation between energy entries in the table.

The final state of any interaction is defined by a pair of Bjorken variable x and y variables. The Bjorken variable x is given by

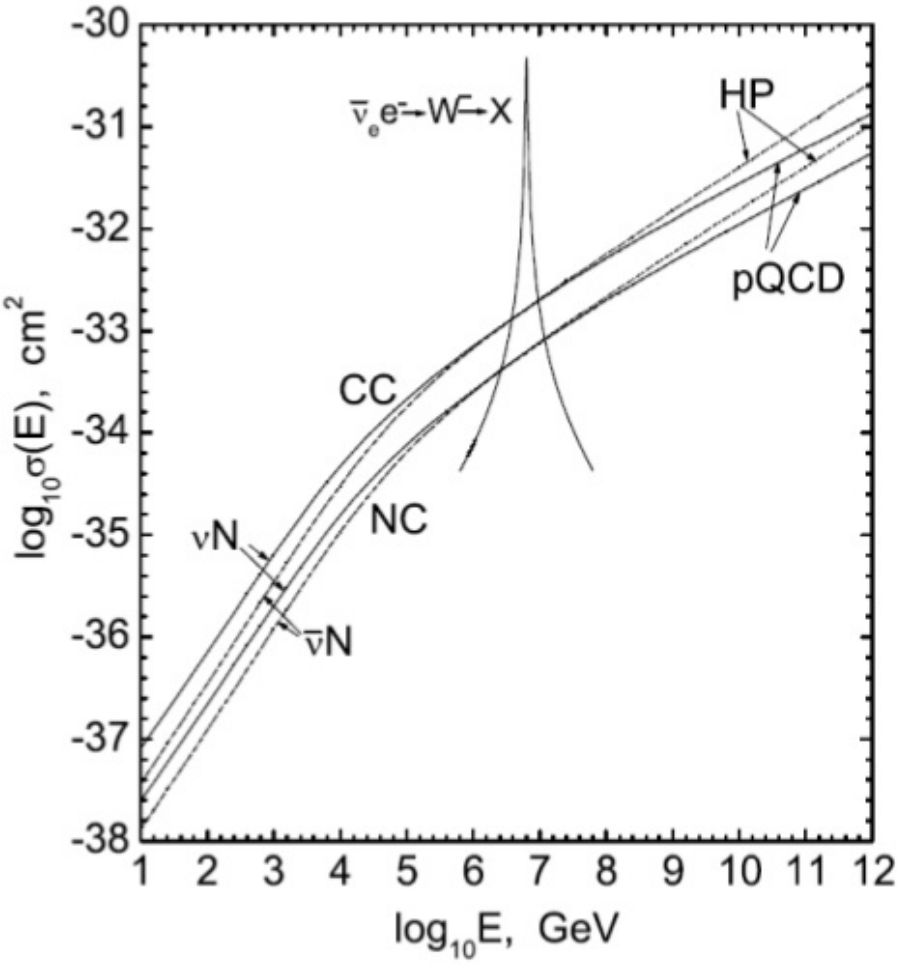

Figure 5.1. Neutrino cross sections: CC and NC νN and resonance $\bar{\nu}_e e^-$ cross-sections for pQCD CTEQ5 and HP extrapolation models. HP predicts approximately 2 times higher cross-sections at the highest energies. Adapted from [86].

$$x = \frac{Q^2}{2M_N(E_\nu - E_l)} \tag{5.2}$$

where E_ν and E_l are the energies of the incoming neutrino and outgoing lepton, M_N is the mass of the target nucleon and $-Q^2 = q^2$ is the four-momentum transfer squared. The 4-momentum $q = P_\nu - P_l$ is given by the difference in momenta between the incoming neutrino and outgoing lepton.

The Bjorken variable y characterizes the energy transfer to the outgoing lepton and to the final hadronic state.

$$y = 1 - \frac{E_l}{E_\nu} \tag{5.3}$$

Neutrino events are generated by randomly picking one such pair that has previously been generated and stored in data tables for different energies. The scattering angle between incoming neutrino and outgoing lepton depends on the parameters x and y as follows:

$$cos\theta = 1 - \frac{xy}{1-y} \cdot \frac{M_N}{E_\nu} \tag{5.4}$$

The propagation and decay of the secondary tau is also implemented in ANIS. Tau leptons are produced in the ν_τ CC interaction or as one of the possible outcomes of the resonance scattering (equation 5.5).

$$\bar{\nu}_e \; e^- \longrightarrow W^- \longrightarrow \bar{\nu}_\tau \; \tau^- \tag{5.5}$$

Due to the increasing tau decay length (equation 5.6) tau energy losses during its propagation have to be taken into account when $E_\tau \geq 10^8$ GeV [86].

$$l_\tau = 49 \; m \; \frac{E_\tau}{PeV} \tag{5.6}$$

ANIS does not account for the stochastic effects in the energy loss rate and uses a continuous approximation of the form:

$$\frac{dE_\tau}{dx} = \alpha + \beta\,(E)\,E_\tau \tag{5.7}$$

where α is approximately constant and determined by ionization energy loss and $\beta = \left(1.508 + 6.3(E/10^9\ GeV)^{0.2}\right) \cdot 10^{-7}$ cm^2/g is weakly dependent on energy and describes the radiative energy loss through bremsstrahlung, pair production and photo nuclear scattering. The second term is dominant above 100 GeV. The continuous approximation is applicable since it introduces only a few percent error. The considerable energy loss at high energies has its effect on the decay length. As can be seen from Figure 5.2 taking into account energy losses will suppress the growth of the tau decay length. The effect is much more pronounced in rock than in air. This means that rock mass around a detector not only provide target mass for the interaction, but also increase the probability of taus to decay inside the detection volume by decreasing their decay length (Figure 5.2).

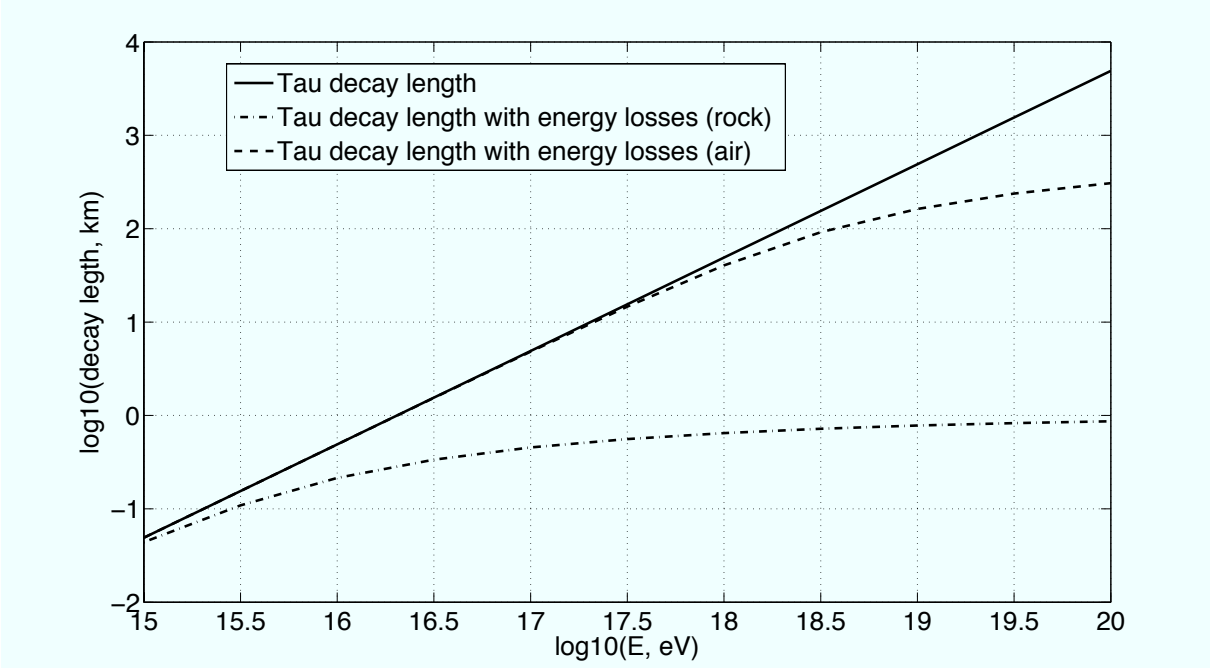

Figure 5.2. Energy dependent tau decay length for two cases: not taking tau energy losses into account (solid line) and including tau energy losses during propagation in the rock (dashed-dotted line) and in the air (dashed line).

Tau decays are simulated using TAUOLA [109] to create tables of fractional energy for different decay final states including hadronic ($\pi^{\pm,0}, K$, ...), electromagnetic (e, γ), muonic and all neutrino types.

The Earth density profile is implemented in ANIS according to the Preliminary Earth Model [74]. This density model was initially proposed by Gandhi et al. [83] and is a good approximation to the complex internal structure of the Earth. The shape of the Earth is assumed to be spherically symmetric. The interior consists of a dense inner and outer core, medium density mantle and the least dense crust. Figure 5.3 illustrates the Earth's density profile according to the Preliminary Earth Model of Ref. [74], which is summarized in equation 5.8.

Figure 5.4 shows the amount of material in terms of slant depth encountered by a neutrino particle passing through the Earth as a function of its incident angle (measured from vertical). The plot suggests that for the incidence angles $< 30°$, the core plays an important role for particle propagation.

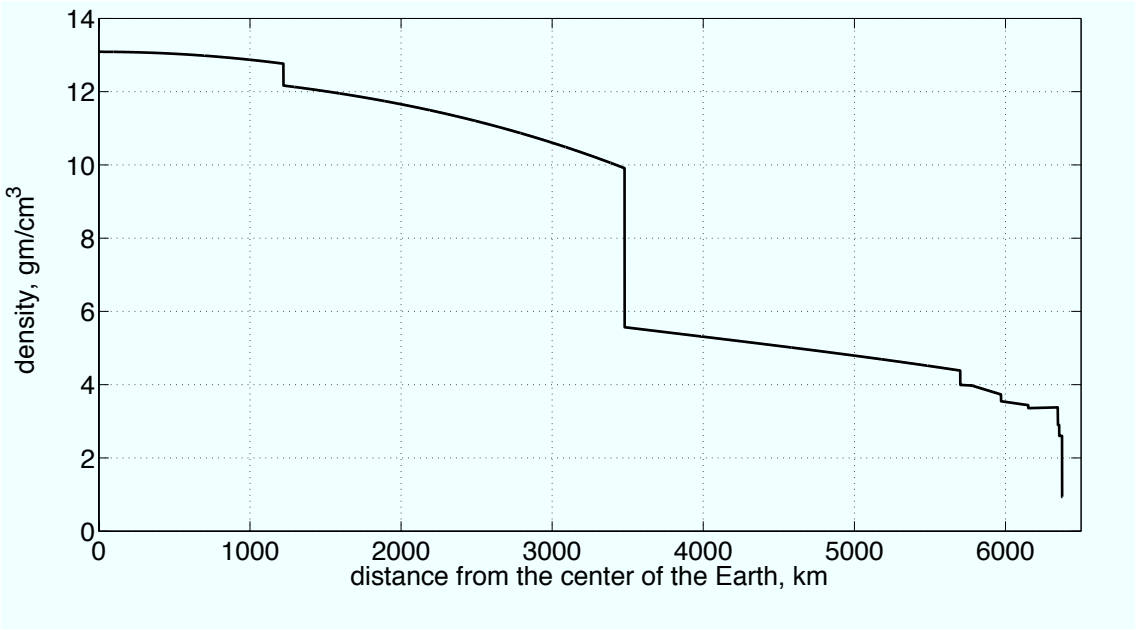

Figure 5.3. Earth density profile as described by the Preliminary Earth Model of Ref. [74].

$$\rho(r) = \begin{cases} 13.0885 - 8.8381\ x^2, & r \leq 1,221.5 \\ 12.5815 - 1.2638\ x - 3.6426\ x^2 - 5.5281\ x^3, & 1,221.5 < r \leq 3,480 \\ 7.9565 - 6.4761\ x + 5.5283\ x^2 - 3.0807\ x^3, & 3,480 \ < r \leq 5,701 \\ 5.3197 - 1.4836\ x, & 5,701 \ < r \leq 5,771 \\ 11.2494 - 8.0298\ x, & 5,771 \ < r \leq 5,971 \\ 7.1089 - 3.8045\ x, & 5,971 \ < r \leq 6,151 \\ 2.691 + 0.6924\ x, & 6,151 \ < r \leq 6,346.6 \\ 2.9, & 6,346.6 < r \leq 6,356 \\ 2.6, & 6,356 \ < r \leq 6,368 \\ 0.93, & 6,368 \ < r \leq R_{Earth} \end{cases} \tag{5.8}$$

where the density is measured in g/cm^3, r is the distance from the center of the Earth in km and the scaled radial variable $x = r/R_{Earth}$ ($R_{Earth} = 6,378$ km).

The effect is even more dramatic when we compare Earth's thickness in gm/cm^2 to the amount of matter each neutrino has to pass before interaction, the plot of which as a function of neutrino energy is shown in Figure 5.5. The interaction length for the neutrinos is between $10^8 - 10^{10}$ gm/cm^2. For UHE neutrinos this is comparable to the slant depth of the Earth for the neutrinos incident at high ($> 70^\circ$) zenith angles. This emphasizes the importance of the near horizon neutrino geometries, since if there is too much target mass, UHE neutrinos will interact far below the surface and secondary tau

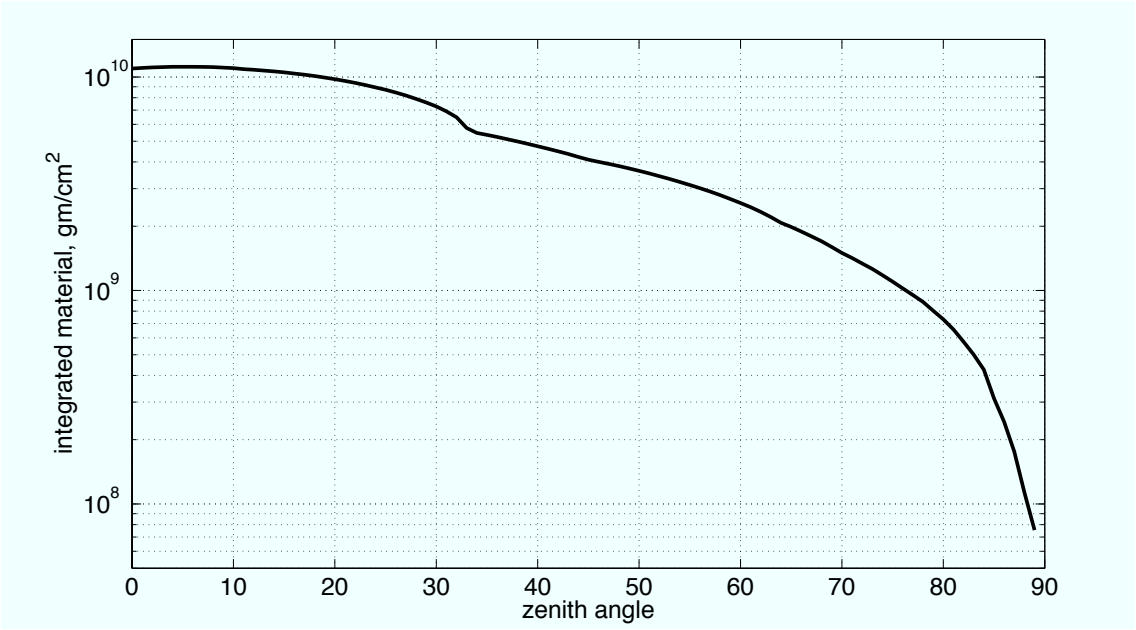

Figure 5.4. Integrated material of the Earth as a function of ν incident angle in zenith direction.

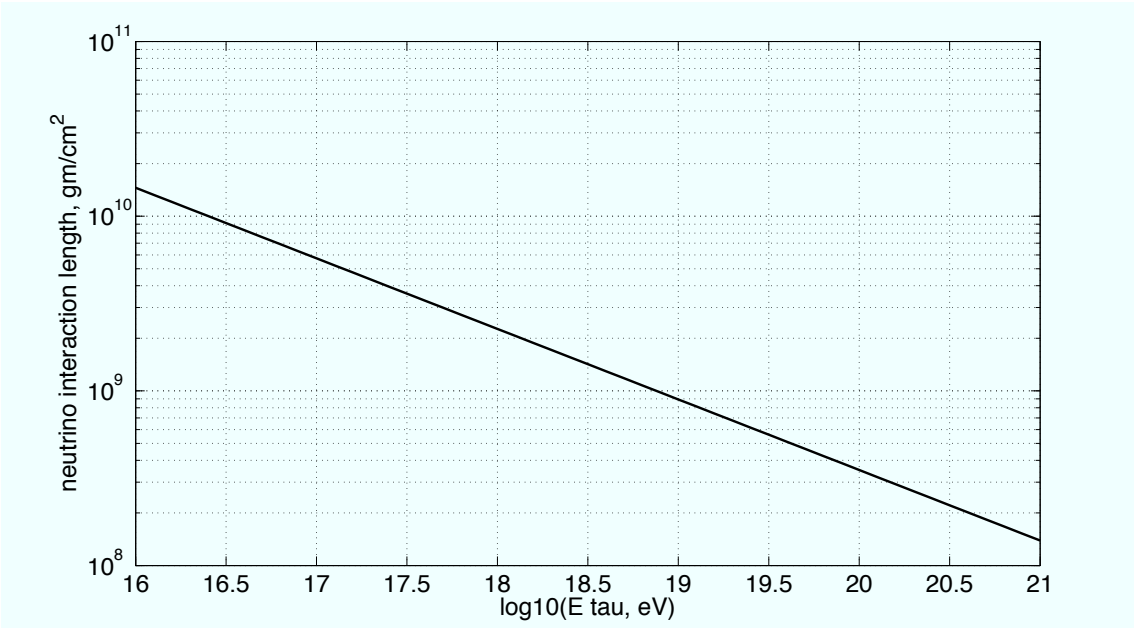

Figure 5.5. Energy dependent neutrino interaction length.

leptons and their decay products will never make it into the atmosphere and will not create EAS because of the significant energy loss.

Since ANIS was designed for underground neutrino detectors, it did not have an atmospheric density profile implemented. Weiran Deng in [71] added the atmospheric density based on the US standard atmosphere of reference [133]. At high zenith angles a flat atmosphere model is not accurate and atmospheric curvature should be taken into account. The atmosphere is parameterized as five vertical layers with the first four following a barometric exponential decrease in density with height, whereas the top layer has a constant density close to zero (see equation 5.9). The transitions between layers are smooth. Figure 5.6 shows the density of the atmosphere as it changes with height. According to Figure 5.7 the slant depth of the atmosphere is only a tiny portion of that of Earth, but is considerably larger for horizontal neutrino events than for vertical ones.

$$\rho(r) = \begin{cases} 12.22/9941.86 \; exp\,(-h/9941.86)\,, & h \leq \; 8.3 \; 10^3 \\ 11.45/8781.54 \; exp\,(-h/8781.54)\,, & 8.3 \; 10^3 < h \leq 12.9 \; 10^3 \\ 13.06/6361.43 \; exp\,(-h/6361.43)\,, & 12.9 \; 10^3 < h \leq 34.0 \; 10^3 \\ \; 5.40/721.70 \;\; exp\,(-h/721.70)\,, & 34.0 \; 10^3 < h \leq 10^5 \\ \; 1.0/10^7, & 10^5 < h \leq 12.0 \; 10^5 \end{cases} \tag{5.9}$$

Surrounding mountains play an important role in shaping the neutrino acceptance for a fluorescence detector. They have two different impacts on the neutrino event. Mountain ranges provide extra target mass for neutrino interaction and they also decrease tau lepton decay lengths, so they are likely to decay in the field of view of a detector. Thus it is important to include local topography around the detector in the simulation program to account for these effects.

The topological information was first implemented in [71] using data from GTOPO30, a global Digital Elevation Model (DEM) [2]. GTOPO30 provides global elevation data with a resolution of about 30-arc seconds (0.0083° or approximately 1 km) referenced to WGS84. Elevation is given in meters above mean sea level ranging from -407 to 8,752 m. GTOPO30 has been divided into 33 smaller pieces, or tiles, covering 50° of latitude and 40° of longitude. The map of the tiles is shown in Figure 5.8. The names of the tiles refer to the longitude and latitude of the upper-left (northwest) corner of a tile. No overlap among the tiles makes it easy to combine the information from adjacent ones.

For the sake of increasing computational speed topographical information was used for only 200 km^2 surface centered at the detector sites. It happened that the detector site was located right at the boundary of two tiles. W140N40 and W140N90 are used

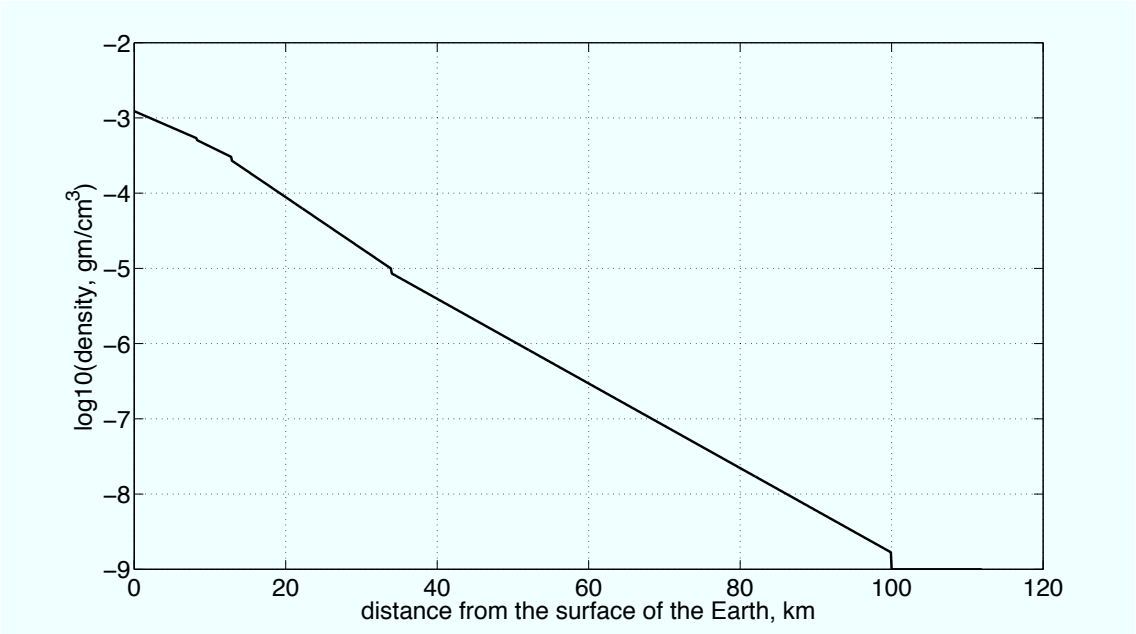

Figure 5.6. Atmospheric density profile: density of the atmosphere as a function of distance from the Earth surface according to Ref. [133].

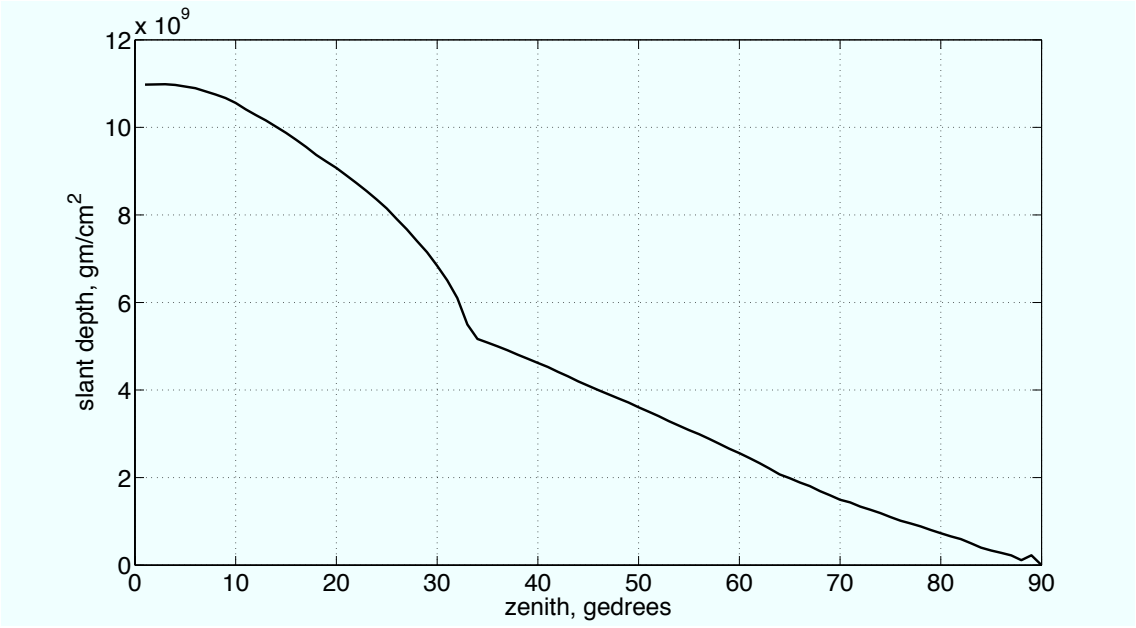

Figure 5.7. Atmospheric slant depth as a function of zenith angle.

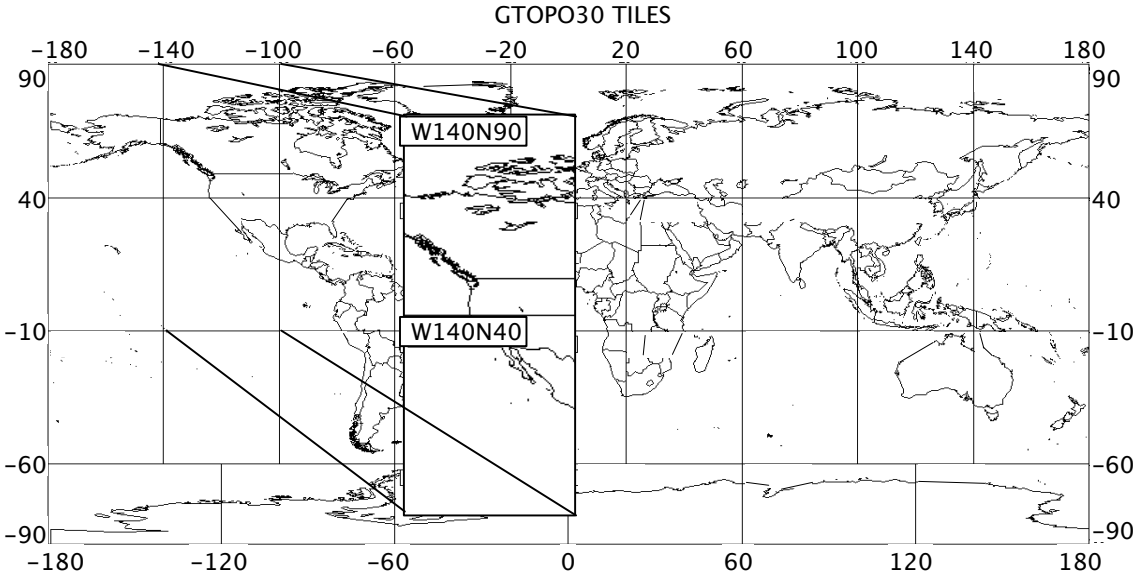

Figure 5.8. The map of the tiles from Global Digital Elevation Model. Adapted from [2].

for extracting information about the detectors' local landscape. Figure 5.9 shows the local topography around the two HiRes sites. The HiRes-1 site position (-112.835799° longitude, 40.195171° latitude, 1597.0 m elevation) and HiRes-2 site position (-112.95897° longitude, 40.13207° latitude, 1553.0 m elevation) are marked by the stars. As indicated by the map the HiRes detector is conveniently surrounded by mountains, which enhance the chance of the neutrino initiated showers to be observed.

For all the arguments above, it is clear that the most probable neutrino events will have close to horizontal trajectories. In this case the ANIS approximation of a spherical Earth does not work any more. We introduce the correction that will account for the Earth nonsphericity based on the WGS 84 Spheroid (the World Geodetic System of 1984) model. This model is also used by GTOPO30 DEM as a more realistic approximation to the shape of the Earth. Table 5.1 provides the parameters for the WGS 84 Spheroid.

5.1.2 Simulation Procedure

A total number of 1,491,325,282 tau neutrinos was thrown into a 75 km spherical volume centered at the midpoint between the two HiRes sites. Neutrino energies were drawn from the interval of 10^9 to 10^{12} GeV according to a power law spectrum that follows E^{-2}. The trajectories of the neutrino events are random in the azimuthal direction but

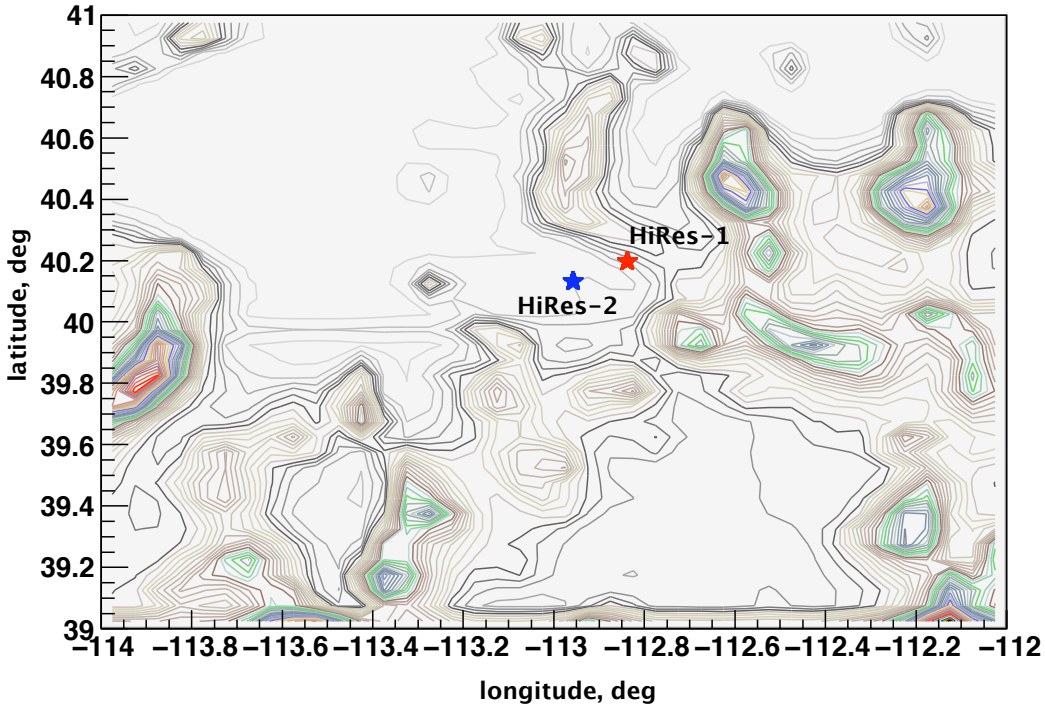

Figure 5.9. Local topography near the HiRes detector. Elevation data is from Ref. [2].

Table 5.1. Parameters for the WGS 84 spheroid

Parameter Name	Value	Units
Semi major axis, a	6,378,137.0	m
Semi minor axis, b	6,356,752.3	m
Inverse flattening, 1/f	298.257	

are constrained in zenith to within 10° from the horizon, since no events are expected to initiate EAS from shallower zenith angles. The effective aperture of the simulation is $4\pi sin(10°) = 2.1821$ str. Zenith angles $< 90°$ correspond to downward going trajectories and those that are $> 90°$ mean upward propagating events.

ANIS propagates neutrinos in small steps along straight trajectories, ignoring the effect of the small angle neutrino scattering. This approximation is adequate for the highest energy neutrinos. At every step of the propagation the interaction probability is calculated. When an interaction occurs one of the active interaction channels is chosen

according to the inclusive cross-section. ANIS accounts for all major neutrino interaction (NC, CC and W^- resonance). In the NC case a tau neutrino is regenerated at lower energies. In case of a CC interaction the ν_τ is absorbed and a short-living τ-lepton is produced. All particles produced in the interaction are added to the event record. Tau neutrinos and tau leptons are propagated through the Earth and the surface topographical features modeled with gtopo30 DEM data or through the atmosphere. Tau leptons are propagated by accounting for their energy losses and their decay routines are called once the tau age exceeds its lifetime. Hadrons, electrons and neutrinos from the decay are added to the particle record. The propagation routine stops when the particle leaves the detection volume or a tau decay happens in the atmosphere.

The selection criteria of events is that secondary taus decay in the atmosphere. Out of 1,491,325,282 input neutrinos only 5,977,051 taus decays were created in the atmosphere.

Figure 5.10 shows the distribution of zenith angles for the surviving MC events with tau decay vertices above ground. All the events are confined between 85° and 100°, which justifies our choice of the range for the input zenith angles. The double peak structure of the distribution comes from the contributions of different types of events. The left line on the plot corresponds to the events with the neutrino interacting beyond a 75 km radius from the detector. These distant events have the most horizontal trajectories. Figure 5.11 shows the locations of interaction points for this type of events (zenith angle is constrained between 89.8° and 90.2°). The interactions for the events with the most horizontal trajectories happen in the mountain ranges located at sufficient distance away from the detector. Earth-skimming neutrinos can also contribute to this event class.

Close by events with the neutrino interaction points within 75 km radius from the detector are shown on the zenith distribution plot 5.10. The contribution to the close-by events comes from up-going and down-going neutrinos. As can be seen from Figure 5.12 the up-going neutrino interaction vertices are almost uniformly distributed over a huge area around the detector location. The interactions are happening inside the Earth and mountains play almost no role. Down-going evens on the other hand are highly dependent on the existence of the close-by mountains, which is shown in Figure 5.13.

5.2 EAS Monte Carlo

The EAS Monte Carlo is used as a link between ANIS and the Detector Monte Carlo, since the latter is not supposed to simulate EAS.

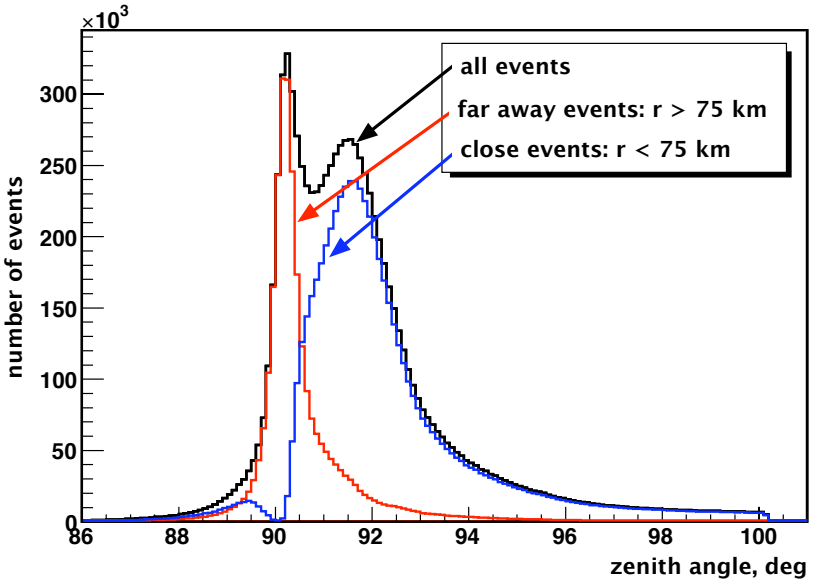

Figure 5.10. Zenith angle distribution of atmospheric τ decays form ν_τ interactions.

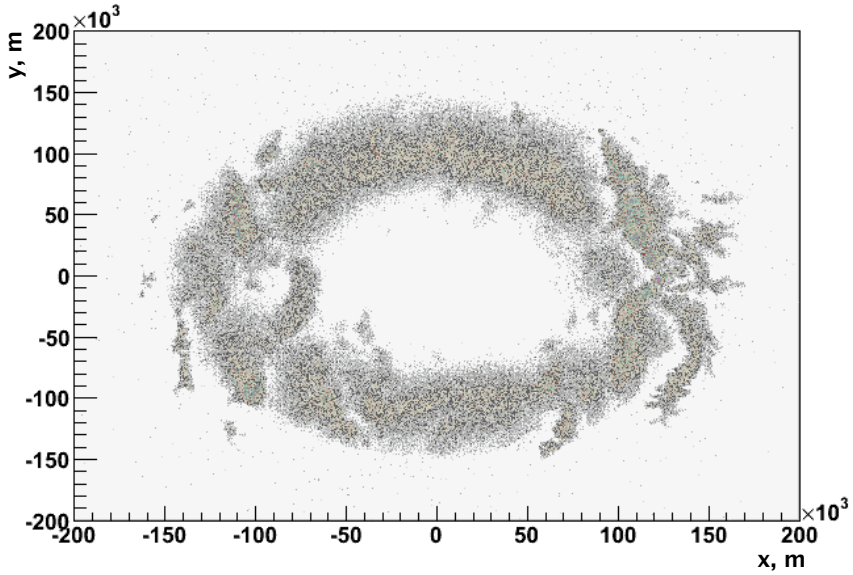

Figure 5.11. Neutrino interaction vertices for the horizontal trajectories limited from 89.8° to 90.2° zenith angles.

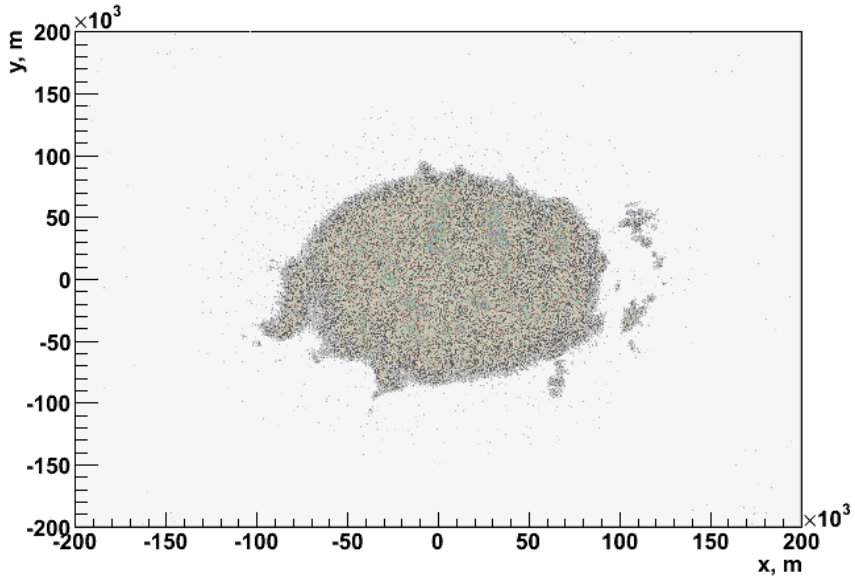

Figure 5.12. Neutrino interaction vertices for the up-going trajectories spreading over 91.1° to 91.5° zenith angles.

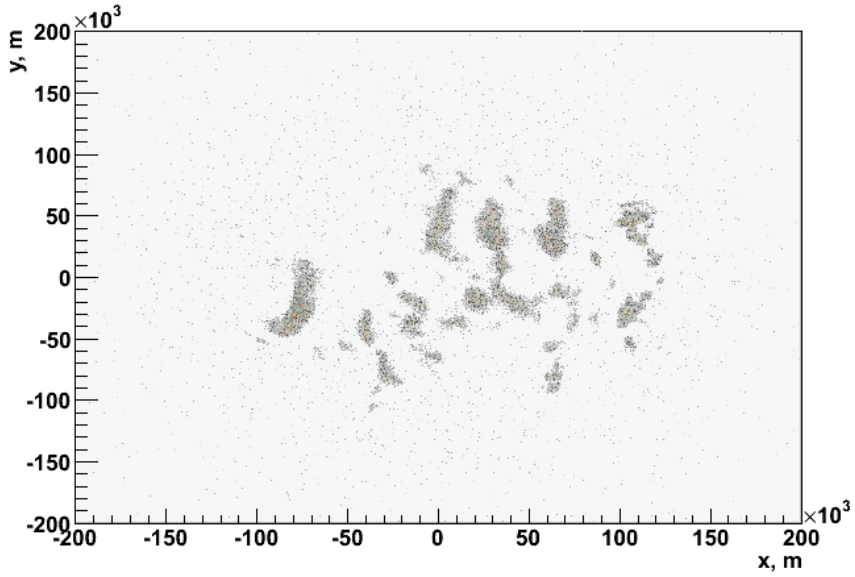

Figure 5.13. Neutrino interaction vertices for the down-going trajectories confined from 89.0° to 89.4° in zenith.

There exist a number of software packages that were designed for the detailed modeling of EASs. Among them are CORSIKA (COsmic Ray SImulation for KAscade) [98], AIRES (AIR shower Extended Simulations) [164], CONEX [45] and others. CORSIKA has been the most popular and widely used in the cosmic ray community and it is used in this analysis.

Originally developed for the KASCADE-Grande experiment in Karlsruhe, Germany, CORSIKA has grown to become a flexible simulation tool, that allows to calculate showers initiated by different types of particles. For hadronic showers at high energies CORSIKA implements different interaction models (VENUS [181], DPMJET [160], NEXUS [56], QGSJet [115] and SIBYLL [77]). We use CORSIKA with QGSJet implementation of the hadronic interaction to simulate hadronic EAS.

Hadrons are produced when a tau decays according to:

$$\tau^- \longrightarrow \nu_\tau \ + \ \pi^{-,\,0} \ / \ K^- \tag{5.10}$$

Electromagnetic showers in CORSIKA are simulated using EGS4 Monte Carlo [144] and NKG lateral distribution functions. Electrons that can initiate e/m showers are produced through

$$\tau^- \longrightarrow \nu_\tau \ + \ \bar{\nu}_e \ + \ e^- \tag{5.11}$$

Neutrino initiated showers have near horizontal trajectories. We use CORSIKA for neutrino induced EASs, since it provides an option to simulate inclined showers with curved atmospheric density profile based on the US standard atmosphere of reference 5.9.

For this study 400 hadronic and 400 electromagnetic showers were generated for different energies (and for hadronic primaries also at different altitudes). Hadronic showers were generated for energies from 10^{15} eV to 10^{21} eV in 1.0 step of log(E/eV) and in 1 km step from 1 km altitude up to 5 km. Similarly EM showers were generated for 7 energy bins from $10^{18} - 10^{21}$ eV and for 5 km above sea level. In the process of shower simulation for a particle with energy E (and height H), a random shower is chosen out of 400 showers in the closest energy, E_{bin} (and height, H_{bin}). In order to adjust this shower to the energy E (and altitude H), proper scale factors are applied to the shower parameters.

Scale factors are calculated for X_{max} and N_{max} parameters as the function of energy and altitude for hadrons and of energy only for EM showers. In case of hadronic showers

mean values of X_{max} and log10(N_{max}) for different energy and height bins were fitted to a 2d-surface. The mean values of $\langle X_{max} \rangle$ and log10($\langle N_{max} \rangle$) are given in Tables 5.2 and 5.3, respectively.

Figures 5.14 and 5.15 shows the distributions of $\langle X_{max} \rangle$ and log10($\langle N_{max} \rangle$) as a function of logarithm of energy in eV and height in km along with the plots of residuals of the fits. $\langle X_{max} \rangle$ was fit to the curved plane parameterized as follows:

$$\langle X_{max} \rangle = -3.53472\, logE^2 + 1.77579 \cdot 10^2\, logE + 1.94\, h^2 - 2.83964\, h - 1.31744 \cdot 10^3; \quad (5.12)$$

where logE is the logarithm of energy in eV and h is height in km. The log10($\langle N_{max} \rangle$) plane is parameterized by

$$log10(\langle N_{max} \rangle) = -1.56060 \cdot 10^{-3}\, logE^2 + 1.04645\, logE - 1.29855 \cdot 10^{-3}\, h - 9.51522; \quad (5.13)$$

$\langle X_{max} \rangle$ and $\langle N_{max} \rangle$ values for electromagnetic showers do not vary with height and have a linear dependence on the logarithm of energy. Figures 5.16 and 5.17 show linear fits to the data and Table 5.4 summarizes the numbers.

Table 5.2. X_{max} energy and height dependence of CORSIKA hadronic EAS

	log10(E, eV)						
H, km	15	16	17	18	19	20	21
1	553.49	616.48	681.08	736.73	772.41	813.37	850.78
2	554.75	617.75	688.54	734.20	780.10	827.37	853.07
3	563.13	626.47	683.49	747.51	801.44	837.01	868.45
4	570.13	634.50	690.83	742.81	796.96	831.16	867.75
5	589.75	642.41	718.60	780.21	821.63	854.56	886.00

Table 5.3. N_{max} energy and height dependence of CORSIKA hadronic EAS

	log10(E, eV)						
H, km	15	16	17	18	19	20	21
1	5.8299	6.8272	7.8255	8.8172	9.80556	10.7906	11.7716
2	5.8276	6.8228	7.8196	8.8109	9.79853	10.7828	11.7690
3	5.8228	6.8207	7.8183	8.8105	9.79855	10.7856	11.7696
4	5.8286	6.8247	7.8207	8.8092	9.79781	10.7829	11.7649
5	5.8249	6.8220	7.8178	8.8102	9.79826	10.7835	11.7668

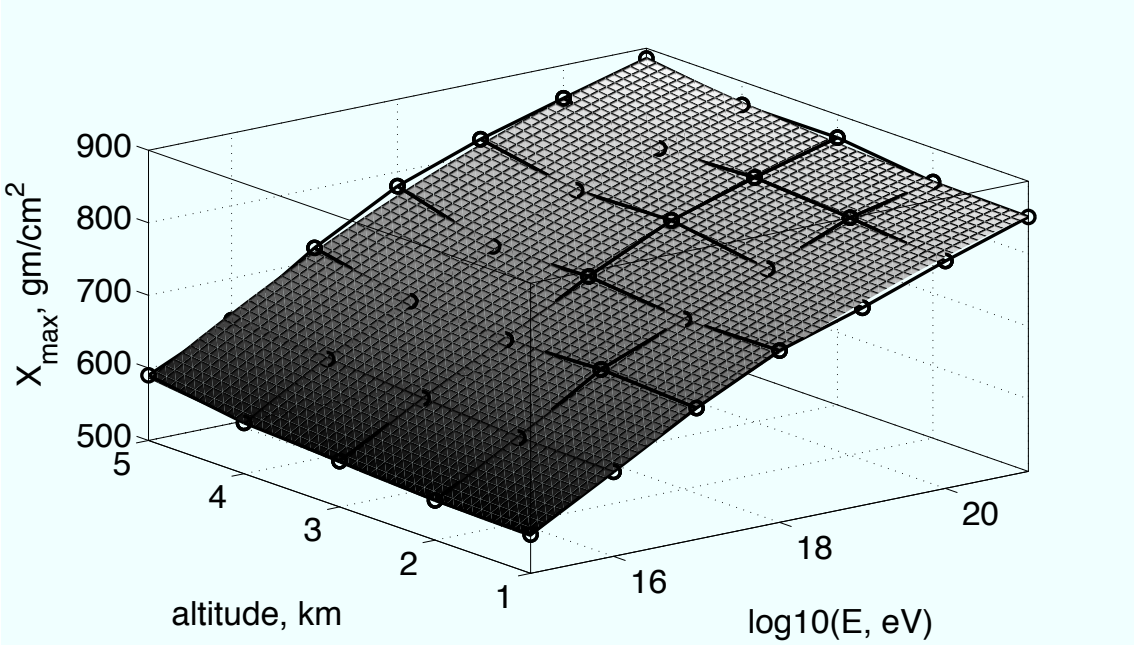

(a) Mean X_{max} data as fitted by the surface parameterized according to 5.12.

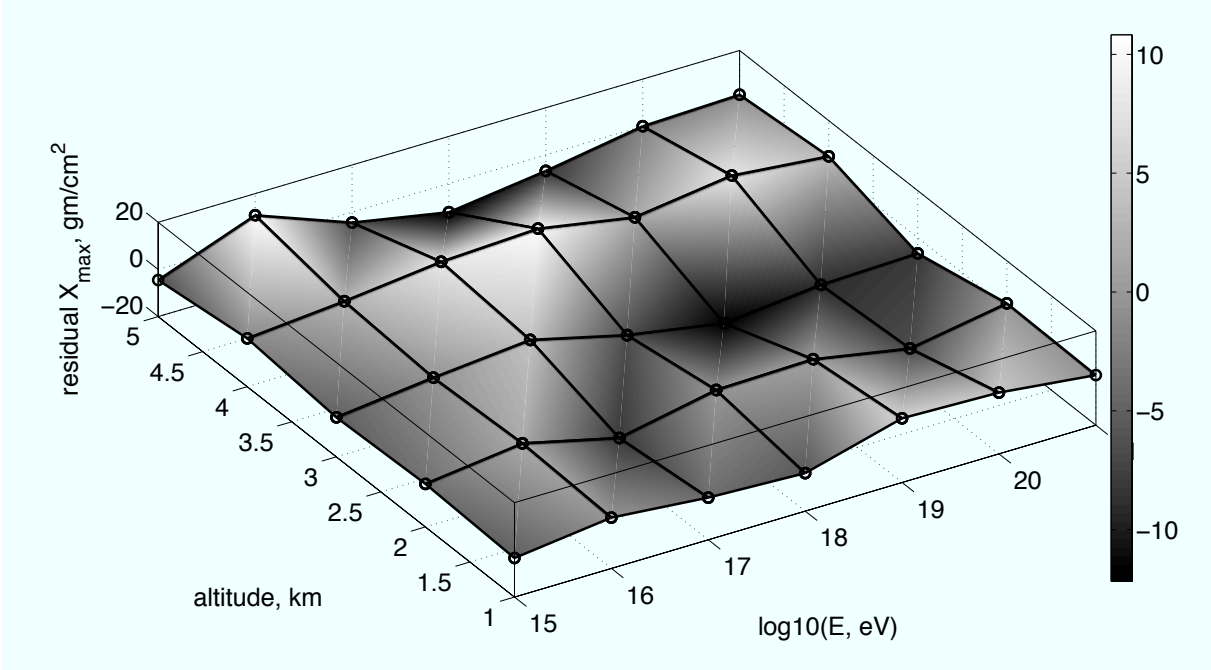

(b) X_{max} fit residuals

Figure 5.14. Surface fit to the mean X_{max} for hadronic showers.

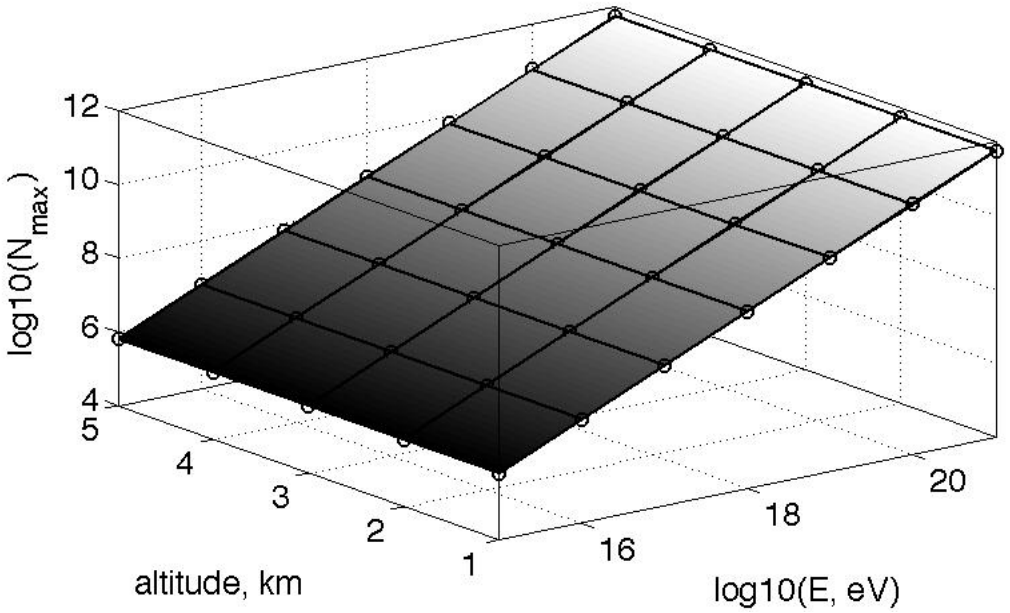

(a) Mean log10(N_{max}) data as fitted by the surface parameterized according to 5.13.

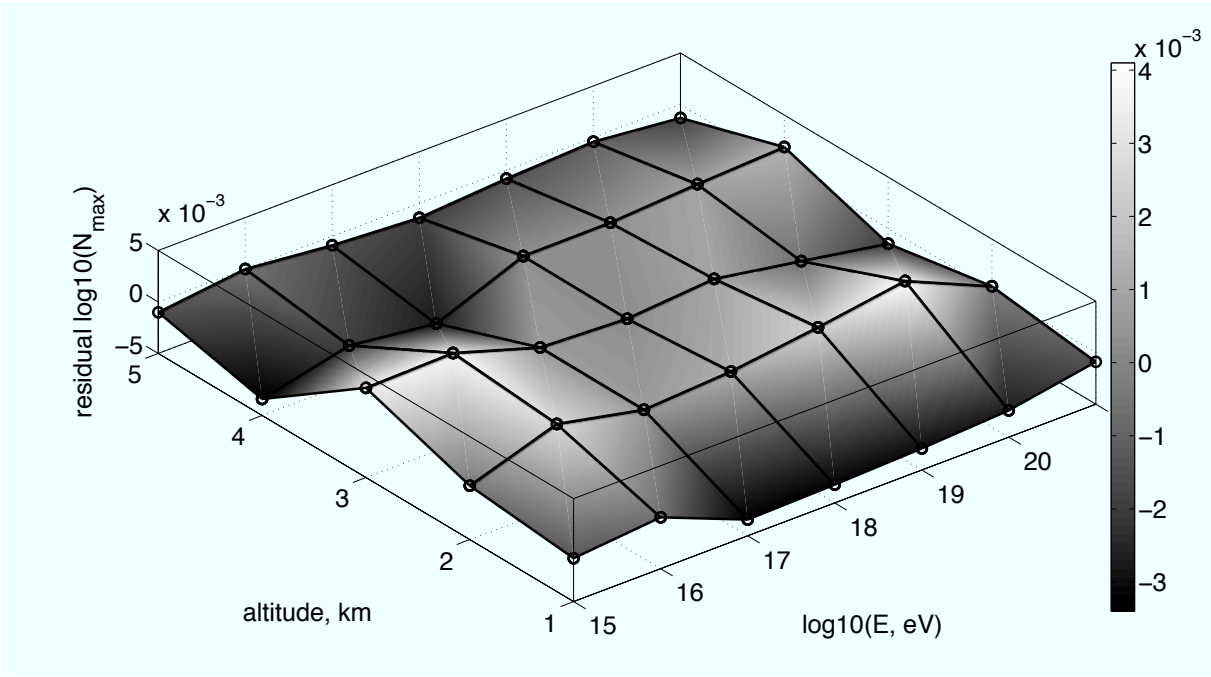

(b) N_{max} Fit Residuals

Figure 5.15. Surface fit to the mean N_{max} for hadronic showers.

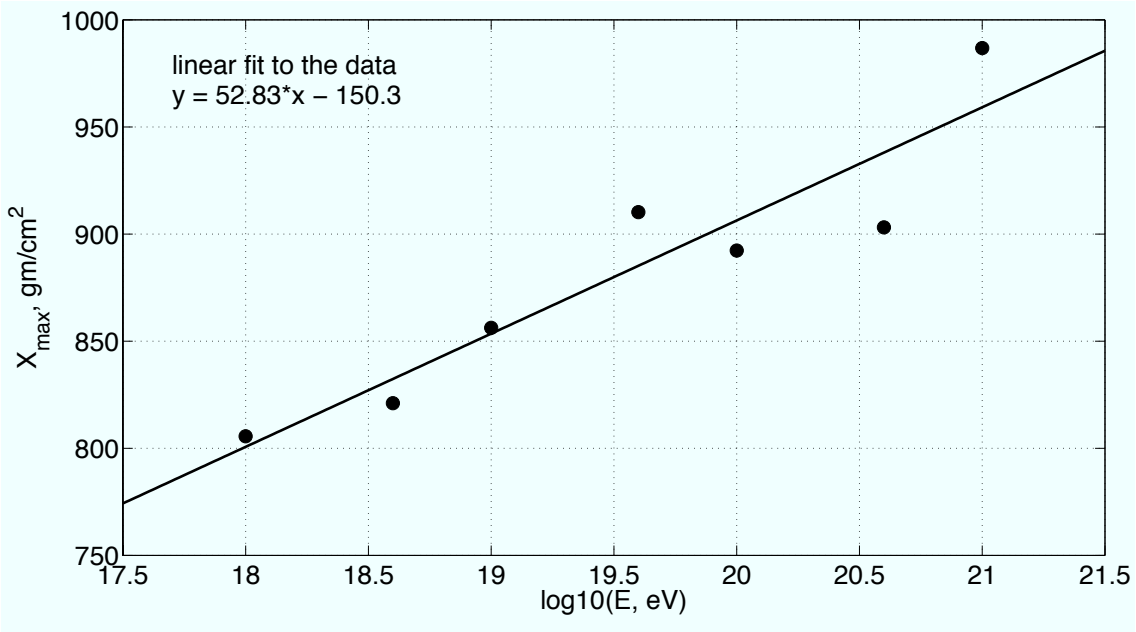

Figure 5.16. Linear fit to the mean X_{max} values for electromagnetic showers.

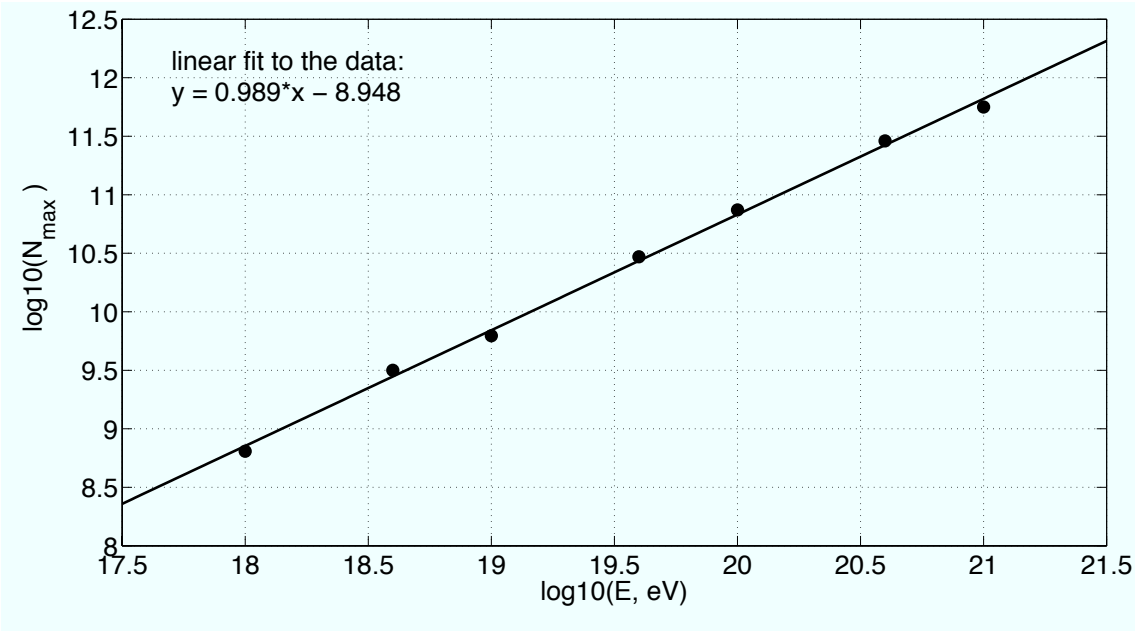

Figure 5.17. Linear fit to the mean log10(N_{max}) values for electromagnetic showers.

Table 5.4. X_{max} and N_{max} energy dependence of CORSIKA e/m EAS.

log10(E, eV)	$\langle X_{max} \rangle$	log10($\langle N_{max} \rangle$)
18	805.6	8.808
18.6	821.0	9.500
19	856.2	9.795
19.6	910.2	10.47
20	892.3	10.87
20.6	903.1	11.46
21	986.8	11.75

Difference in the X_{max} (N_{max}) predictions for the shower with particle energy E and height H and the shower with energy E_{bin} and height H_{bin} are used as scaling factors, which is then applied to the shower depth X (number of particles N) of the shower.

In order to extrapolate for data beyond the edges of the simulated shower, the shower profile is fitted to the Gaussian-in-Age function introduced in 3.19. We are using cubic spline interpolation routines [150] to find the number of particles in the shower in between the centers of the simulated shower depths.

5.3 HiRes Detector Monte Carlo

In order to simulate the detector response to different EASs we run the Detector Monte Carlo (DMC). All the stages of the event development between light propagation from the shower and writing out the electronic signal as an event record are included in the simulation process. These stages include light production by the shower, propagation of this light to the detector, response of the detector optics to the light and finally the electronic response to the optical pulse and event trigger. All the appropriate processes should be included at each stage to achieve the best simulation of real events. In this section a brief description of the DMC program is given. For more detailed information please refer to Ref. [14].

Longitudinal EAS profiles according to CORSIKA output are given to the DMC. The lateral distribution of EAS is parameterized by the NKG function. At the next step UV light is produced according to the shower profile. For the real shower there are two components that contribute to the amount of UV light created at every depth in the atmosphere. The electromagnetic component of an EAS excites Nitrogen of the atmosphere that radiates in the UV range. The amount of fluorescence light from a segment of the shower is directly proportional to the number of electrons in that segment.

Exact formulas are given in section 3.2.2.

Beamed Cherenkov light also contributes to the amount of fluorescent light coming from the shower, but Cherenkov photons are not included into the estimation of the shower profile based on GH and GA. The contribution is maximum for the showers coming towards the detector, since Cherenkov light is highly collimated along the shower direction. Thus it is necessary to model accurately the Cherenkov light contamination in the detected EAS so that this component can be removed. For showers that are coming directly towards a detector, Cherenkov component dominates fluorescent one and these events are removed from the analysis. Section 3.2.1 talks about the Cherenkov radiation and its properties.

During light propagation three processes should be considered: scattering on air molecules, scattering on aerosol particles suspended in the atmosphere, and absorption by Ozone molecules. The scattering effect is twofold. Scattering of Cherenkov light into the field of view of the detector builds the unwanted Cherenkov contamination of the shower signal. Fluorescence photons are scattered out of the field of view of the detector, which weakens the optical signal. Description of the light attenuation during its propagation from EAS to the detector is discussed in 3.2.2.

A detailed overview of the simulations of the response of HiRes optics to the attenuated pulse from EAS is given in [14]. Here the main points of that discussion are presented. HiRes response to the external light (e.g., light coming from EAS) is in the form of a set of triggered PMTs with their respective triggering times and signals (or FADC traces for HiRes-2). A tube is triggered when the number of photo-electrons (*pe*) produced by the incident light rises above a pre-determined threshold. The process of simulation of the number of the photo-electrons resulting from the passage of the shower through the detector's field of view starts with an analytical calculation of the number of *pe* according to:

$$N_{pe} = \sum_{\lambda=300}^{420} \left(\frac{dN_\gamma}{d\Omega}(\lambda,\theta_e)\Big|_{Scin.} + \frac{dN_\gamma}{d\Omega}(\lambda,\theta_e)\Big|_{Rayl.} + \frac{dN_\gamma}{d\Omega}(\lambda,\theta_e) \right) \Big|_{Mie} \times \\ \times T_{Rayleigh}(\lambda) T_{Mie}(\lambda)\ T_{O_3}(\lambda) R_m Q E(\lambda) \delta\Omega \qquad (5.14)$$

The number of photons N_γ with different emission directions θ_e in the solid angle $d\Omega$ produced by a shower segment due to scintillation (Scin.), aerosol scattering of Cherenkov light (Mie) and Rayleigh scattering of Cherenkov light (Rayl.) are multiplied by light

transmission coeffisients ($T_{Rayleigh}, T_{Mie}, T_{O_3}$), UV filter transmission coefficient, mirror reflectivity (R_m), PMT quantum efficiency (QE) and finally the solid angle $\delta\Omega$. To get the contributions from all the wavelengths, a summation over λ is performed in 1nm steps.

This formula describes the average value of *pe* collected by spherically shaped mirror with the solid angle extended to the source location given by:

$$\delta\Omega = \frac{A^0_{eff} cos(\theta_m)}{d^2} \tag{5.15}$$

where A^0_{eff} is the effective area of the mirror, θ_m is the off-axis angle of the source point and d is the distance to the source. The number of photons due to fluorescence as a function of wavelength can be derived from Figure 3.6. The number of Cherenkov photons and attenuation effects can be found by applying formulas of sections 3.2.1 and 3.2.2. The transmission coefficient of the UV filter is shown as a function of wavelength in Figure 4.13. The mirror reflectivity is set to the constant value of 0.8. Figure 4.11 shows the wavelength dependence of the PMT quantum efficiency.

Formula 5.14 can not be used directly, since it only gives the average value for N_{pe} and fails to account for following issues: lateral spread of electrons in the shower, actual 4-leaf clover shape of HiRes mirrors, reduced effective area of the mirror due to the presence of the PMT cluster in front of it, mirror spherical aberrations, nonuniform PMT response profile. To correct for these effects as well as to introduce the fluctuation due to stochastic nature of the physical processes a Monte Carlo technique is used.

Fluctuations in the number of photo-electrons as the result of fluctuations in the number of photons hitting the surface of a mirror is implemented by a ray tracing algorithm. The position of each γ is chosen randomly along the longitudinal direction and according the NKG formula in the lateral direction from the shower axis. Ray tracing find if a photon hits the active surface of the mirror and is reflected onto the front face of the cluster. To estimate the effect of the mirror spot size the position of a photon on the PMT cluster surface is drawn from a gaussian of $\sigma = 0.25$ cm. If the position of a photon falls within the field of view of a PMT, the photon is added to the signal of that PMT, weighted by the PMT response profile (Figure 4.12). Formula 5.14 is used as a mean for the poisson distribution of the numbers of *pe*.

The simulation of electronic response of the HiRes detector is implemented in order to reproduce the trigger requirements and model the interaction between S/H electronics and

tube signal. The simulation starts with the estimation of the total time the propagating shower can enable tube triggering for each mirror. The total time interval that has to be considered is:

$$T_{tot} = T_e + T_s + T_h \tag{5.16}$$

In the above equation T_e is the time it takes for a shower to transit through the mirror field of view based on the geometry of the event. $T_s = 25$ μs is added to the transit time due to the possibility of the tube noise triggers formed prior to the transit of the shower. 25 μs is the time individual tube triggers are saved. Another 50μs are added at the end of the T_e interval as T_h to permit additional individual tube triggers to be included in the event.

At the next step the total interval T_{tot} is divided into 20 ns time bins. This array of time bins is assigned to each tube of the PMT cluster, which is than filled with the corresponding *pe* signal (found by ray-tracing) from the shower plus an additional Poisson distributed sky noise with the mean of 40 pe/μs.

After that testing for individual tube triggers is done for every 20 ns of T_{tot}. The testing is done by comparing the processed tube signal with a fixed threshold of 500 mV (this threshold is automatically readjusted during the operation of the real detector). Processing of tube signal include simulation of the PMT, preamplifier and electronics gain, passage of the signal through a low pass filter and splitting the signal to send it to both, the trigger and the integration circuit. If the tube signal exceeds the threshold the time of the trigger is saved by the TDC and the signal is integrated in a 5.6 μsec time window and digitized.

All the triggered tubes are sorted in time ascending order to test for subcluster and mirror triggers. A subcluster is triggered if at least three tubes two of which are adjacent are in the triggered tube list. A mirror triggers if two subclusters satisfies trigger requirements. In case of a mirror trigger the time of the event is set as the trigger time of the first tube in the time ordered list. The information about the event is then saved in the same format as the real data recorded at the detectors.

5.4 Monte Carlo Summary

In our Monte Carlo study we simulated a total number of 1,491,325,282 ν_{tau} particles, that had been thrown into a spherical volume of 75 km radius centered on the middle

point between the two HiRes detectors. The energies of the neutrinos were randomly selected according to E^{-2} spectrum. The events were simulated with random azimuths but limited within 10° from the horizon in zenith. Neutrinos were propagated along straight lines following their injection directions. Both Earth and atmospheric density profiles were approximated to reflect the changes in the interaction probabilities, which were evaluated at each propagation step. Local topography around HiRes was included to account for the matter distribution around the detectors. The outgoing particles from neutrino interactions were also propagated. Their interaction probabilities and energy losses were taken into account.

All the hadrons, electrons and gamma rays that were created in the atmosphere were selected to initiate the total number of 5,977,051 EASs. These EASs are divided into three categories according to a primary particle type. There were 1,664,667 events with hadrons only. Their interaction location as well as propagation direction were used to simulate pure hadronic showers. The number of electrons only counted to 1,384,847. They were picked to generate pure electromagnetic showers in the atmosphere. 2,927,537 events had both a hadronic and an e/m shower emerging from the same tau decay vertex. Since the current version of the Detector Monte Carlo only propagates light from the GH-like shower shape, a possible double peak structure for these mixed composition events was not simulated and instead the energies of the two particles were added for the simulation of a more energetic hadronic shower.

After the simulation of the detector response to 5,977,051 showers, 4,416 of them were found to trigger the detector and were retained for further analysis.

CHAPTER 6

NEUTRINO EVENT SEARCH IN THE HIRES DATA

The Monte Carlo studies of section 5.1 have shown that neutrino events have close to horizontal (both up-going and down-going) trajectories. Also, small neutrino interaction cross sections lead to showers initiated deep in the atmosphere. This makes them distinguishable from cosmic ray events, that start an EAS at the top of the atmosphere. Low in the atmosphere means close to the detector, and thus these horizontal trajectories have a good chance to be detected. In order to perform a neutrino search in the HiRes data, we need to build the event selection criteria that will isolate the subset of quasi-horizontal close-by events.

The HiRes-1 data is recorded and stored as a collection of PMTs with corresponding trigger times and signal strengths (charge). Based on this information and the pointing direction of the tubes, the showers spacial location can be reconstructed to see if the event geometry resembles that of a neutrino event. The HiRes-1 and The HiRes-2 detectors have different electronics (the HiRes-1 uses S/H and the HiRes-2 uses Flash ADC) In our analysis we applied the HiRes-1 reconstruction techniques to both detectors without using the full detail of Flash ADC information in the HiRes-2 data.

A test of the reconstruction algorithms is performed by applying them to Monte Carlo simulated data, since only for those data do we know the true geometry. The Monte Carlo helps to decide what type of the event geometry can be reconstructed well and may be used for analysis. Criteria that help to discriminate neutrino-like events from cosmic-rays are established by comparing MC simulated events to HiRes data. Finally, since we do not have real neutrino events, we use MC events for calculating the efficiency of the HiRes detector. This is legitimate as our MC has been proven to have excellent agreement with data in the analysis of CRs [193].

Even before any reconstruction is done, HiRes data should be stripped of numerous incidental events triggered by electronic and sky noise. Events corresponding to artificial

flashers and lasers should also be removed from the data, especially as horizontal laser tracks might be wrongly classified as neutrinos.

The HiRes-1 and HiRes-2 detectors collect data separately, so they can be analyzed in monocular mode. If an event is seen by both detectors it can be reconstructed in stereo mode. Since tau neutrino showers are initiated by the tau decay products that have already lost some energy, they are usually not very energetic. Monocular data sets are the ones appropriate for neutrino search, simply due to the fact that HiRes is more sensitive to lower energy events in monocular mode. Although stereo reconstruction is much more robust and accurate, stereo events are confined to a smaller detection volume and have a higher energy thresholds. MC studies confirm that monocular dataset is more appropriate for neutrino search. From 8,904,588 neutrino induced showers, HiRes-1 was triggered by 2,918 showers, HiRes-2 was triggered by 1,498 showers and only 393 showers triggered both detectors.

This chapter describes all the stages of data processing, event reconstruction and data reduction. The upper limit on the tau neutrino fluxes for three energy bins based on the detector sensitivity to tau neutrino events are given at the end of the chapter together with the limit over the whole range.

6.1 Data Processing

Before being used for analysis, the HiRes data is processes by a well established set of routines. A good description of data processing steps is found in [14, 156]. Here we give a brief discussion of the workflow.

At the early stage of data processing, the number of photo-electrons is calculated using the calibration data. Measured mirror reflectivity, UV filter transmission, PMT gain and quantum efficiency are also taken into account according to the data taking conditions. In case several mirrors were triggered, they are all included in the event.

Removal of known light sources is the next stage of data processing (see [156] for more details). The HiRes controlled light sources (steerable laser and flashers) are used for data calibration and the monitoring of atmospheric conditions. Starting from September 2000 the steerable lasers have easily identifiable time stamps. Lasers at the HiRes-1 site fired at 222, 472, 722, and 972 ms after the GPS second. The HiRes-2 laser system fired exclusively at 111, 361, 511, and 761 ms after the GPS second. All events within $+1.0/-0.2$ ms of these times are removed as lasers. Prior to September of 2000 laser

events must be removed based on their geometries.

Laser events fired from the roving steerable laser system that is used for systematic checks of the detector operation are also removed by their time stamps at 0, 250, 500, and 750 ms after the GPS second. Finally the events associated with the intersite and vertical flashers are removed based on the known geometry of these events. Events with repetitive geometries are removed from the data set. A calculation in [156] shows that the laser events make about 6% of the total number of events while the vertical flashers account for about 2%.

A much bigger number of events comes from noise. Noise events are removed by applying a Random Walk (Rayleigh) filter. When a cosmic ray event develops in the detector field of view it leaves a track-like pattern of triggered tube triggers. Noise triggers are random in nature and noise events usually do not have a well defined or consistent pattern of tubes. The Rayleigh filter is a fast and simple filter that compares the signal in the detector to a signal that could be created by a two-dimensional random walk. The principle is as follows:

In 2d random walk case the probability distribution of the length of a resulting vector $r = |\vec{r}|$ after 10 random steps is given by a Rayleigh probability density function:

$$P(r) = \frac{r}{\sigma^2} exp\left(-\frac{r^2}{2\sigma^2}\right) \tag{6.1}$$

where $r = |\sum_{i=0}^{N} \vec{r}_i|$ is a sum of N independent random unit vectors and $\sigma^2 = N/2$. Thus the probability to observe a net displacement $r > R$ after N steps falls as:

$$P(r > R) = \int_R^\infty P(r)dr = exp\left(-\frac{R^2}{2\sigma^2}\right) \tag{6.2}$$

Log likelihood test suggests that the probability that this vector is a result of a random walk is given by

$$plog = \frac{R^2}{Nln10} \tag{6.3}$$

plog value of 2 corresponds to 1% chance of the vector resulting from a random walk. A 0.1% probability gives a *plog* value of 3.

The 2d random walk filter is applied to the HiRes data with established trigger time order, the resulting displacement vector is built from the first triggered tube to the next until the last triggered tube is reached. Next the probability of a random walk event is

calculated according to 6.3. If this probability is greater than 1% ($plog < 2.0$) the event is removed as noise. Additionally, if no adjacent tube pairs can be found, events are rejected by this cut. Up to 90% of data is removed as noise at this stage.

6.2 Data Reconstruction and Reduction

After most of the noise events and time tagged laser events have been removed, reconstruction routines and neutrino event selection criteria can be applied to the remaining data to produce a set of best neutrino candidates. This section describes the algorithm that we developed to select well reconstructed neutrino-like events.

Event geometry reconstruction is the key element of τ-neutrino search. Reconstruction of the event geometry starts with identifying the shower detector plane (SDP). When a shower moves through the atmosphere at the speed of light, a line along the shower together with the position of the observing detector define a unique plane in space, which is called the SDP. Figure 6.1 illustrates the concept of the SDP.

The SDP can be found by using the pointing directions of the triggered PMTs. The viewing directions of those tubes that are triggered by the light emitted from the shower lie in or close to its SDP.

The second part of geometry reconstruction is localizing a shower track within the SDP. When it is observed by two detectors at the same time in stereo mode, the track of an air shower can be found by crossing the SDPs reconstructed by each of the detectors. This option is not available for a monocular event and the position of the shower axis has to be estimated from the analysis of the tube timing records.

Within the SDP each shower trajectory can be characterized by a set of parameters. The first parameter is called Rp (Figure 6.2), which is given by the shortest distance from the detector center to the reconstructed or MC shower axis. The point where the EAS reaches zero of z-coordinate is called the "impact" point and the distance to its position from the detector is R_{impact}. Angle Ψ in Figure 6.2 is the incline angle of the track.

As a shower develops and its image moves across an array of PMTs the time sequence of triggered PMTs is recorded. Assuming that a shower travels at the speed of light, the following relationship holds between the trigger time t_i and the angle between the shower track and the pointing direction of a triggered tube θ_i:

$$t_i(\theta_i) = t_0 + \frac{Rp}{c} tan\left(\frac{\theta_i}{2}\right) \tag{6.4}$$

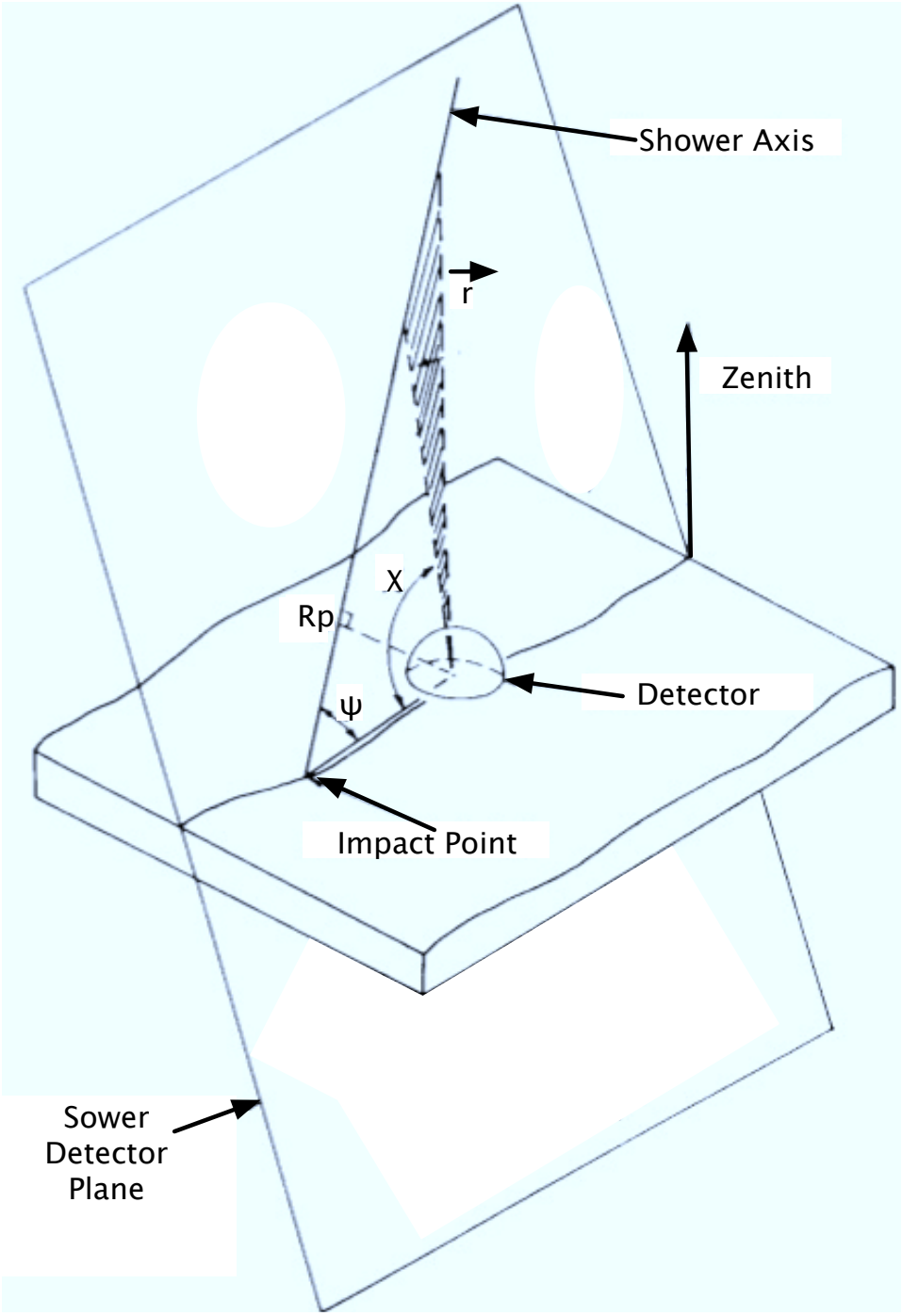

Figure 6.1. The shower detector plane defined as the plane going through the center of the detector and containing the shower track. Adapted from [14].

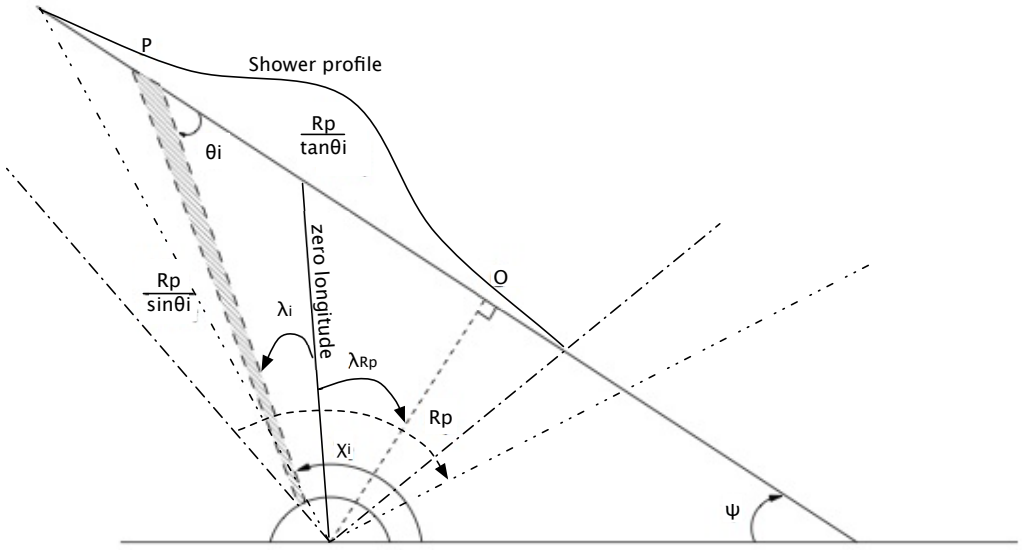

Figure 6.2. Shower timing reconstruction. Adapted from [14].

where t_0 is the time at which the shower front passes the point of closest approach and c is the speed of light. The angle θ_i is related to the tube viewing angle χ_i through:

$$\theta_i = \pi - \Psi - \chi_i \tag{6.5}$$

The unknown geometry parameters R_p and Ψ are found by using tube trigger times and tube viewing angles.

6.2.1 Tube Categories

Many of the events coming from the data processing stage will have residual noise triggered tubes that lie far from the main track both spatially and in time. An example of an event with spatial outliers is given in Figure 6.3. This figure shows a HiRes-2 CR event recorded by mirrors 33 and 35. The event has a nice long track and also several outliers. If considered these outliers can cause a significant decrease in the efficiency of its reconstruction. Assigning tubes to three different categories helps us to eliminate outliers.

Every tube in the HiRes event is assigned to one of three categories:

Core Tubes: A tube is assigned to the core tube class if it has at least two neighbors that are also triggered at the tube level. As the name of the category suggests these

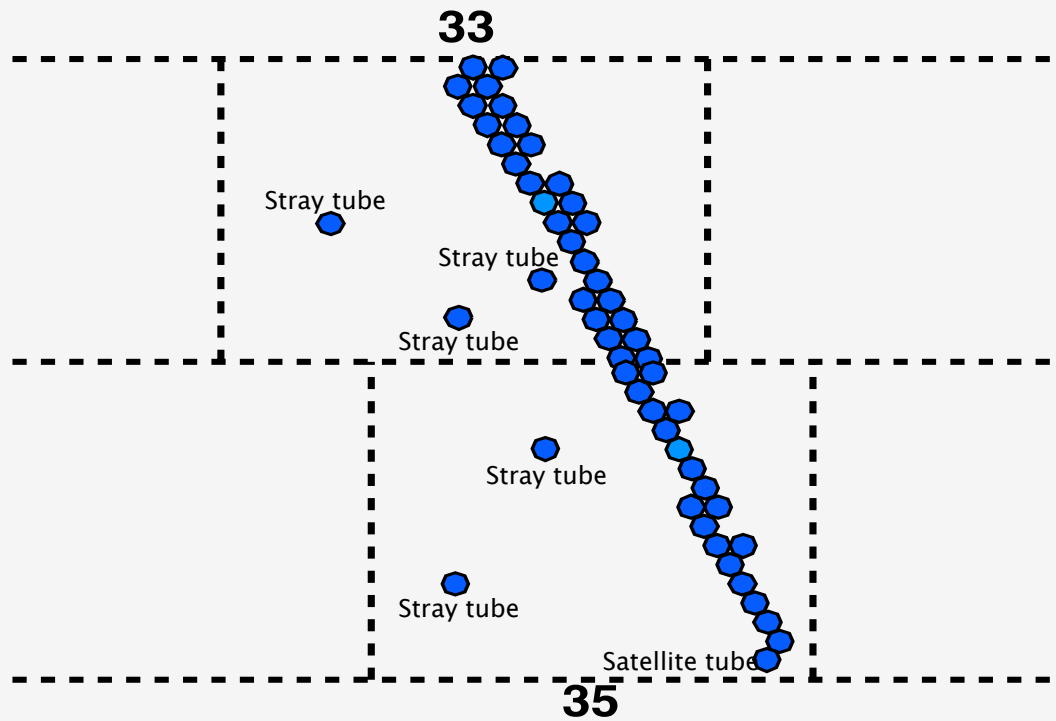

Figure 6.3. A HiRes-2 event with categorized tubes. Three categories of tubes are distinguished. The event has 1 satellite, 5 stray and 48 core tubes. Core tubes are left unsigned.

are the best tubes for the reconstruction, since they are most likely to form a track structure. The event in Figure 6.3 has 48 core tubes (left unmarked).

Satellite Tubes: Satellite tubes have only one neighbor, but this neighbor is a core tube. Satellite tubes are usually located at the ends of a track. Only one satellite tube is found in the Figure 6.3 event.

Stray Tubes: All the rest tubes are marked as stray tubes, meaning they either do not have any neighbors or have just one neighbor, which is not a core tube. Figure 6.3 has an event with five stray tubes.

Stray tubes are not considered in the early stages of the reconstruction. But in case any of these tubes is identified as a signal on the later stages of the analysis they are easily included into the main scope of "working" tubes.

Figure 6.4 shows the distribution of the core and satellite tubes of the well reconstructed neutrino Monte Carlo events (angle between reconstructed and true SDP normal

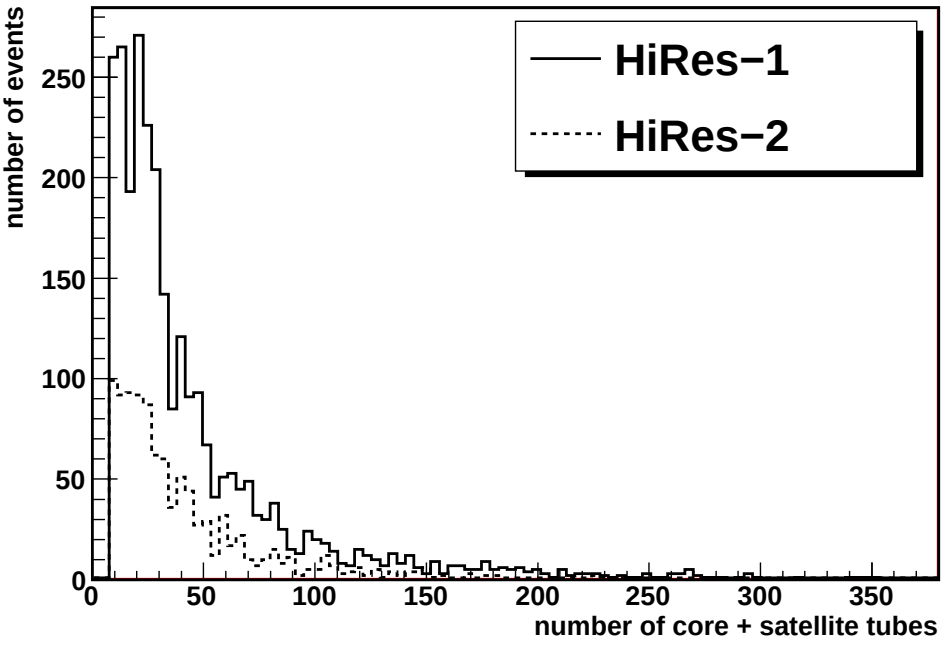

Figure 6.4. Distribution of the number of core plus satellite triggered tubes of MC events for well reconstructed events.

vectors is less than 0.1 radians). Based on this distribution a minimum and maximum core and satellite tube cut was set for both HiRes-1 and HiRes-2. Events with only few tubes will not be reconstructed, simply due to the fact that there is not enough information in the event record. We set a minimum for a combined number of core and satellite tubes at seven tubes per event, since almost no well reconstructed MC event has less than seven tubes. The event is also not considered in the further analysis if the number of tubes is very large (> 500), since this is characteristic of a typical laser event.

6.2.2 Plane Reconstruction

The SDP can be found by using the pointing directions of the triggered PMTs. But the tube directions can not be used directly, since every event contains some number of noise tubes, pointing in random directions and the discrete pointing directions of the tubes will not generally align perfectly with the true SDP of the shower. Thus a plane reconstruction algorithm should be developed that will determine the SDP effectively.

In this study the SDP normal vector is found by adding up the cross products of

pointing direction unit vectors of the time ordered core and satellite tubes in the event. The cross products are calculated between all the different combinations of tube pairs. The contribution of a pair to the estimation of the plane normal direction is weighted by $(1 - cos\theta)$, where θ if the angle between the pointing directions of the tubes. Weighting the tube contribution in this manner allow us to minimize the contributions from the pairs of close-by tubes and give more weight to the pairs of tubes which are far apart.

The quality of the reconstruction of a SDP vector can be measured by studying how much the length of the resulting vector differs from the summed lengths of all the vectors from the contributing pairs. The exact formula is as follows:

$$PQF = \frac{\sum_{i=1}^{N} |\vec{r}_i| - |\sum_{i=1}^{N} \vec{r}_i|}{\sum_{i=1}^{N} |\vec{r}_i|} \tag{6.6}$$

PQF stands for plane quality factor. Vector r is a vector resulting from the cross product of the directions of two tubes weighted by the $1 - cos\theta$. N is the number of participating pairs. Figure 6.5 compares the distributions of the PQF for the Monte Carlo and HiRes data events for both detectors. Data and Monte Carlo look very different on the PQF plot. As expected there are many data events at the higher values of PQF indicating failure of the plane reconstruction. If there is much scatter in the vectors from cross products of different tube pairs the event is poorly reconstructable and the parameter is close to 1. This is characteristic of the noise events with no well defined track structure (triggered tubes are pointing in random directions). We ged rid of these events by applying a PQF cut. The value for the cut was optimized to get the highest signal to noise ratio (SNR = MC/$\sqrt{Data}$), assuming that data is mostly background and not ν-events. For HiRes-1 the cut is set at 0.60 and for HiRes-2 it is set at by 0.25 (see Figure 6.5).

The locations of the cuts are quite different due to different shape of distributions of HiRes-1 and HiRes-2 data. Such difference in data distributions of two detectors is mainly due to differences in the detectors themselves. The HiRes-2 detector has two rings of mirrors and thus records less energetic events happening higher in the atmosphere. Along with the lower energy cosmic ray tracks, HiRes-2 saves significantly many more noise triggered events, which is reflected in Figure 6.5.

Once the plane normal is identified, we reject tubes which lie far from the plane. Assuming that the majority of tubes in the event are real signal and only some are triggered by noise we cut all the tubes that are more than 0.02 in cosine away from the

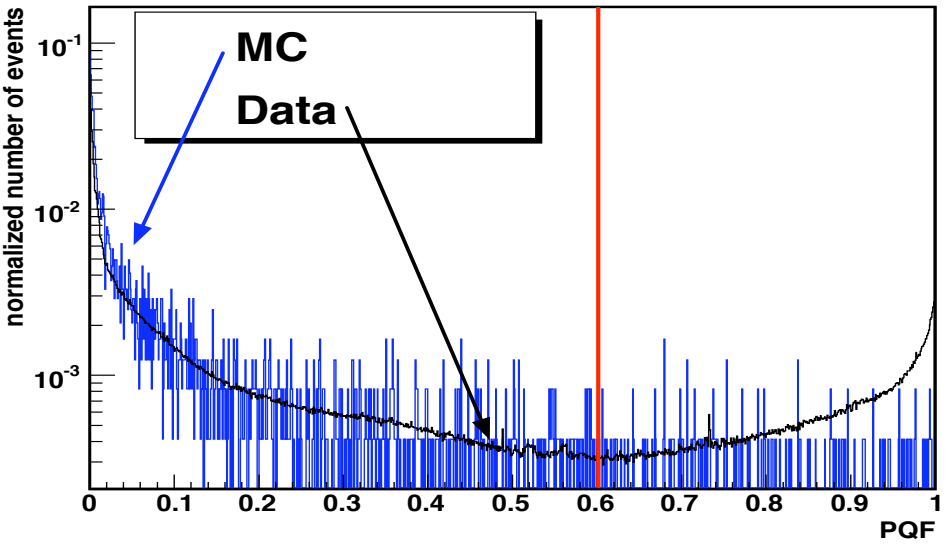

(a) HiRes-1: cut at 0.60

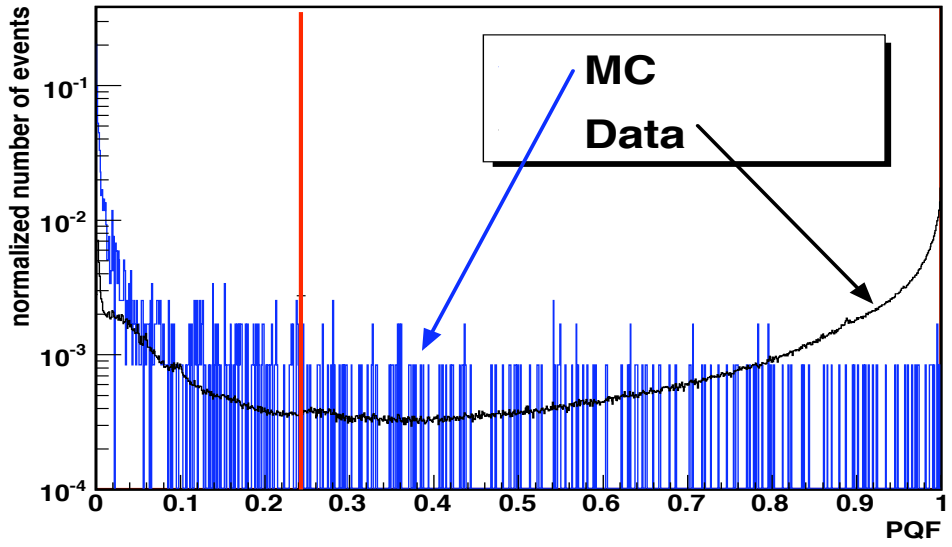

(b) HiRes-2: cut at 0.25

Figure 6.5. The comparison of the normalized PQF distributions on MC and data. The peak near 1 for the data corresponds to the events with poorly reconstructable SDP, which is characteristic of the events with no well defined track structure. Vertical line shows the location of the cut.

plane, since noise tubes are supposed to be spatially uncorrelated with the actual track. Figure 6.6 shows the justification for the 0.02 cut. Stray tubes that pass the 0.02 cut become "good" tubes and are included for further analysis.

The plane normal and the remaining tubes are used to built a SDP based coordinate system, that allows to refer to tube directions relative to the SDP in terms of longitudes and latitudes respectively. Longitude describes the angular position of a tube pointing vector within a plane relative to some fixed direction. Latutude accounts for the position of a tube pointing vector relative to SDP. The reference direction for a longitude coordinate is the projection onto the SDP plane of the charge weighted sum of all tube directions (Figure 6.2). This vector is used to define zero longitude. The third vector to form an orthogonal unit vector system relative to the plane is found by the cross product of the first two, which also defines the positive direction of the longitudes. All the longitudes are measured from -180° to +180°. From the construction of the SDP normal vector the time evolution of the tubes in the plane proceeds towards higher longitudes.

Our study shows that the ratio of the number of "good" tubes (tubes that are within

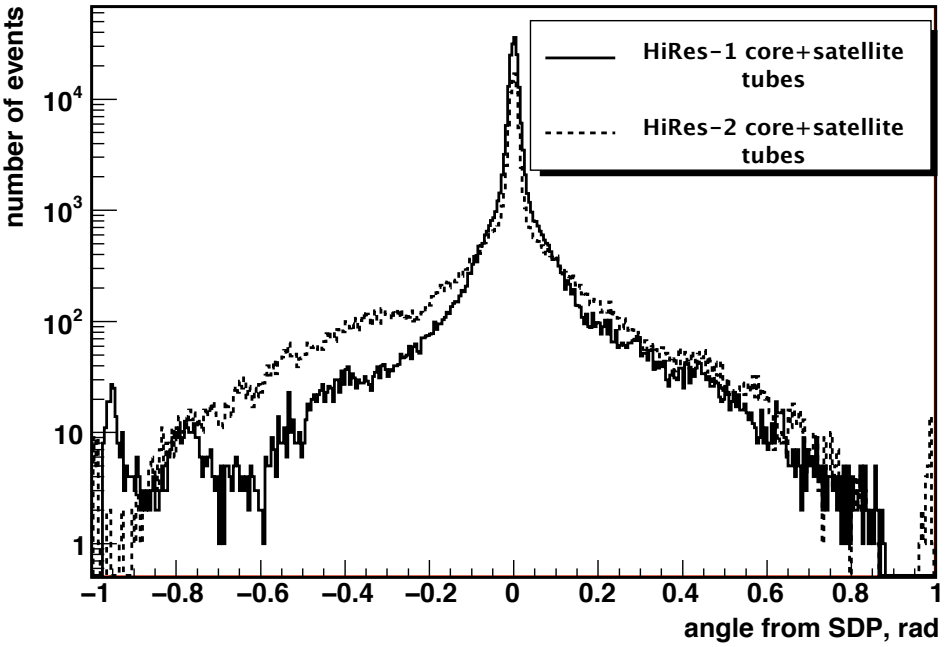

Figure 6.6. Distribution of the tube directions relative to SDP.

0.02 radians from the SDP) in the event to the total angle spanned in the longitudinal direction can be used to effectively enrich neutrino events as is done for CR event in other analyses. We define a plane cut parameter (PCP) as follows:

$$PCP = \frac{Number\ of\ Tubes}{Shower\ Angular\ Extend} \tag{6.7}$$

The number of tubes include all the "good" tubes in the event. The shower angular extent (SAE) is the longitude difference between the two extremes in longitude tubes in the event. Short events with many tubes will result in a large PCP value and very long events or events with few tubes will correspond to a small PCP.

Figure 6.7 shows the distribution of PCP for the MC and data events. The majority of neutrino MC events for both HiRes-1 and HiRes-2 are located in between 50 and 80 in PCP. Data look very different. The distribution of data events peak around 120-130, meaning that there are a lot of quite short events and/or events with large number of tubes. Badly reconstructed MC events (the angle between reconstructed plain normal vector and true plain normal vector exceeds 0.1 radians) are shown on the plots. These events correspond to the lowest PCP values due to small number of tubes in these events. Based on these plots we define a minimum and maximum cuts on PCP to select well reconstructed neutrino-like events. For both detectors the minimum PCP cut is 40. This cut will help us to reduce the amount of poorly reconstructed events and save most of well reconstructed ones. Events with large PCP are both lasers and noise events, since they are most likely to have lots of triggered tubes within relatively short SAE. The maximum PCP cut was again based on the maximum SNR. For HiRes-1 it is found to be 84 and for HiRes-2 data it is 100.

HiRes-1 and HiRes-2 data events have different distributions in Figure 6.7. HiRes-2 data shows a double peak structure. One of the peaks is similar to the peak of HiRes-1 data and the other is locater where the MC says the data should be (the second peak is missing in HiRes-1 distribution). Such a difference in the data distributions arise from the different cuts on PQF. As compared to HiRes-1 most of HiRes-2 noise events were rejected when we apply PQF cut, thus the ratio of cosmic ray to noise events is higher for HiRes-2. HiRes-1 data after PQF cut is still contaminated with noise events, which dominate over cosmic ray events.

The plane fitting algorithm used in this analysis differs from the conventional HiRes plane fitting routine. Standard HiRes plane fitting is accomplished by minimizing a χ^2

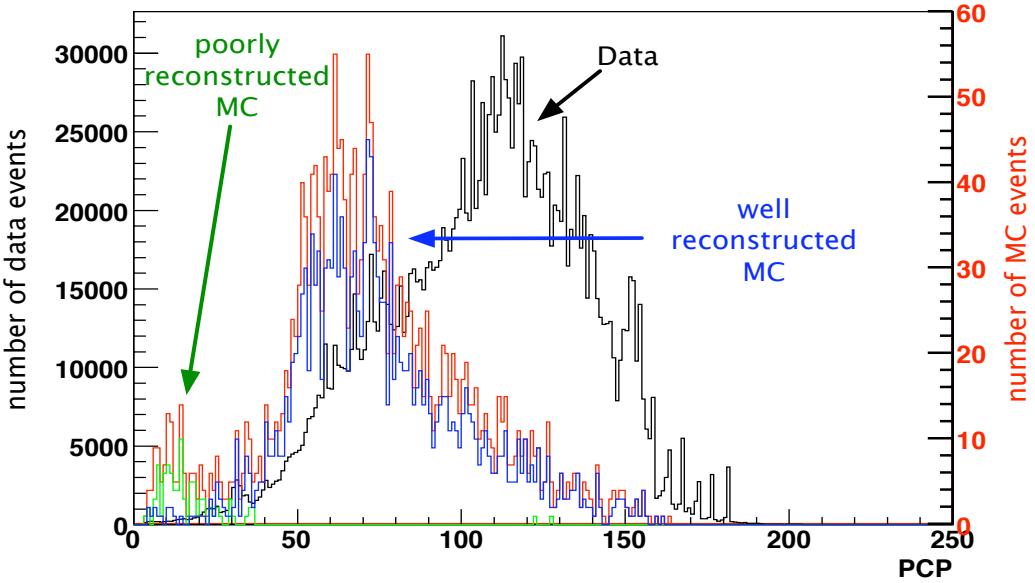

(a) HiRes-1: cut at 30 and 84

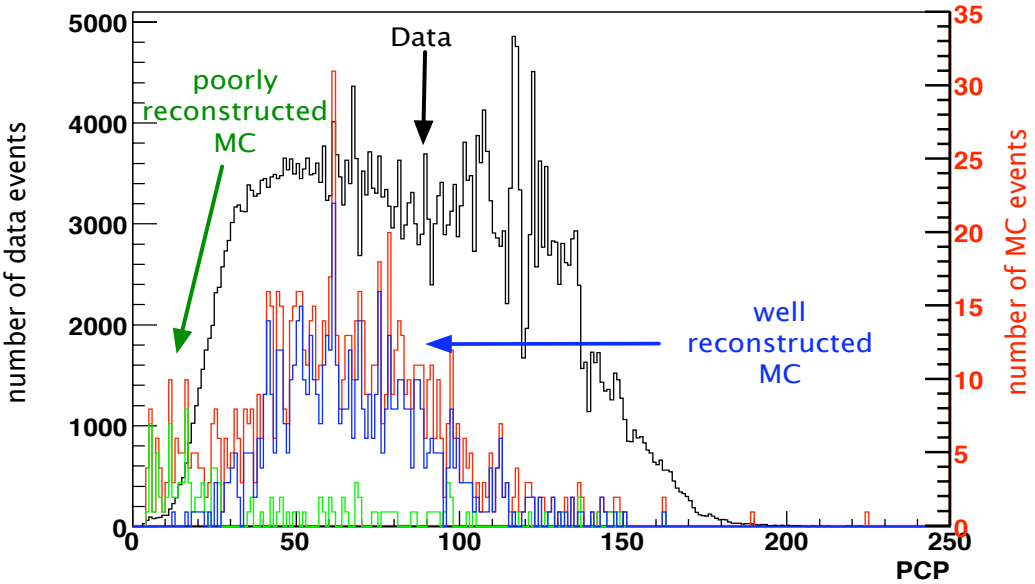

(b) HiRes-2: cut at 30 and 100

Figure 6.7. Distribution of the PCP for the MC and HiRes data. MC events with good and poor plane reconstruction are shown.

function given by:

$$\chi^2 = \frac{\sum_i (\vec{n} \cdot \vec{r}_i)^2 w_i}{\sigma_i^2} \tag{6.8}$$

where the sum is over all tubes in the event, $\vec{n}$ is the plane normal, $\vec{r}_i$ is the tube viewing direction vector and w_i is the number of photo-electrons seen by tube i, and σ_i^2 is an angular error assumed assumed to be 1 for all tubes. More information on HiRes standard plane fitting is found in [14].

Figure 6.8 shows the quality of the two analyses in terms of angular difference between the reconstructed and true plane normal vectors. There are not significant differences between the standard approach to plane fitting and the one used in this study. Distributions have overall similar shapes. Figure 6.8 is built for HiRes-1 data. Similar plot for HiRes-2 dataset leads to the same conclusions.

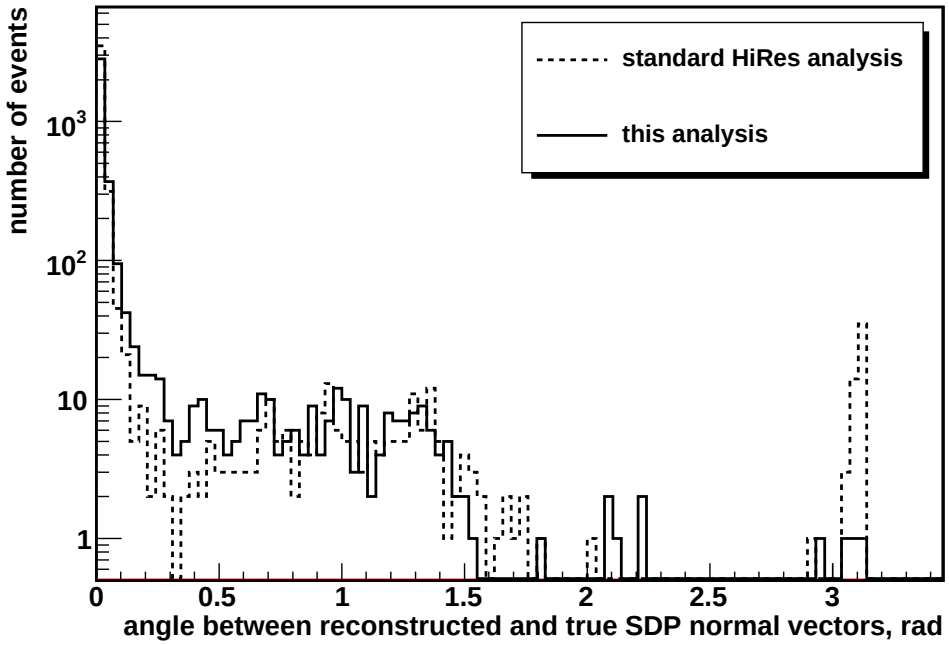

Figure 6.8. Comparison between plane fitting algorithms on MC data. Standard HiRes plane fitting and plane fitting algorithm used in this analysis are compared in terms of angular difference between the reconstructed and true plane normal vectors of MC events.

Our study shows that our new method works better when applied to the data, even though on the MC side no significant difference was noticed. Figure 6.9 helps to illustrate our point. The figure shows the scatter plots of x and y components of the reconstructed plane normal vectors for two methods (based on positive z HiRes-1 data). On this kind of plots in HiRes data we expect to see structure, caused by events with repetitive geometries (lasers). Both plane fitters result in similarly shaped structure on x-y plots in Figures 6.9(a) and 6.9(b). But as compared to the plane fitter used in this analysis, HiRes fitter produced structure with poorly defined shape. One can say that Figure 6.9(a) is a blurred version of Figure 6.9(b). This is due to the fact that some of the events that are well reconstructed by our fitter are misreconstructed by standard HiRes fitter. Since the rejection of laser events is crucial for our analysis and for the remaining laser events will have to be based entirely on reconstructed geometry, our newly developed plane fitting method is clearly better suited for the analysis.

6.2.3 Removing Lasers

Lasers are the biggest obstacle for the neutrino search in the HiRes data. The geometries of laser events are upward or close to horizontal, which is similar to the neutrino event geometries. Only for data collected after August of 2000 can laser events be cut out by their trigger timing. Lasers operated by the military in the Dugway pose a serious problem, since we have no information about when these lasers were fired and what their geometries are.

Fortunately many of the calibration laser shots are fired at pre-defined geometries. Thus these geometries will be repeated over and over again (within some variation due to changing atmospheric condition and detector response). Figure 6.9 shows clustering of such events in the x and y domain of their plane normal vector coordinates. These events are artificial light events that have to be removed.

In order to remove clusters associated with laser events, we use laser rejection maps. Rejection maps are built from the analysis of all data events surviving the plane cuts (424,095 for HiRes-1 and 233,592 for HiRes-2). These events are considered to have well reconstructed SDP normals. The x and y components of plane normal vectors of these events are entered into two dimensional histograms with 800 bins in each direction. The histograms are further divided into tiles of 5×5 pixels each. If any of the pixels exceeds max number of entries (5 for HiRes-1 and 15 for HiRes-2) it is kept for next step of

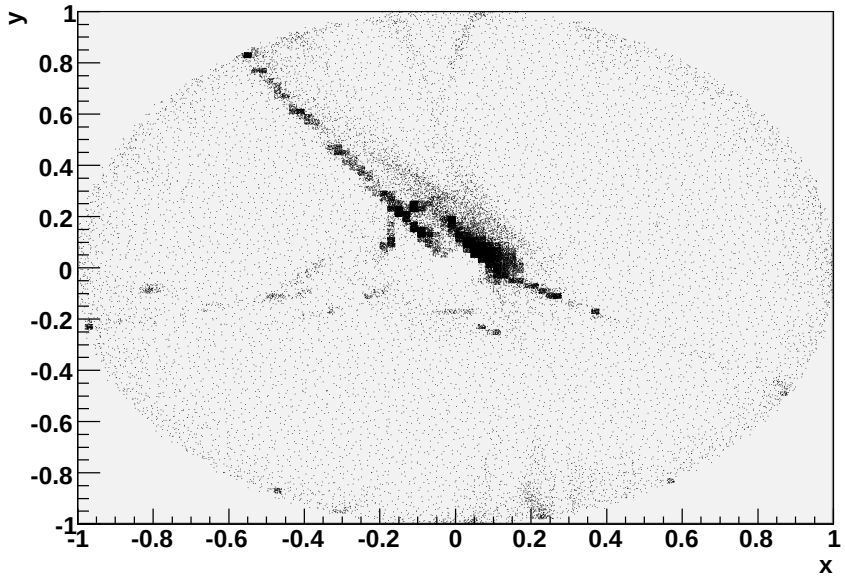

(a) Standard HiRes plane fitting.

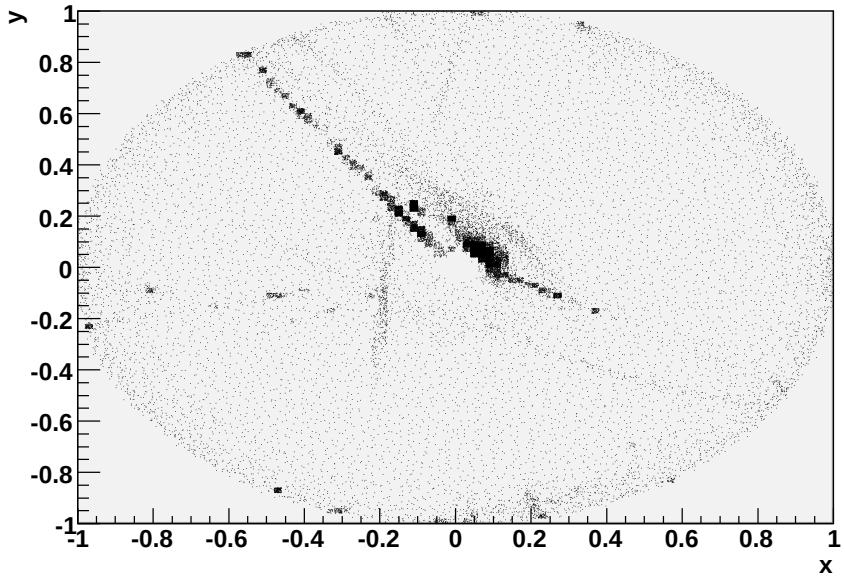

(b) Plane fitting method used in this analysis.

Figure 6.9. Comparison between plane fitting algorithms on HiRes data. The scatter plots of x and y components of the reconstructed plane normal vectors for standard HiRes plane fitting and the one used in this analysis.

building laser rejection maps. If this criteria is not satisfied the pixels are filled with zero. Laser rejection maps are built from tiles that have more than two nonzero pixels, after the first step.

Figure 6.10 shows rejection maps for both detectors separated into z-positive and z-negative projections. These maps are used to tag potential laser events. If the DSP of an event happens to correspond to one of the filled pixels on the rejection map, this even is tagged as a potensial laser events and removed from the analysis.

6.2.4 Time Pruning

Before timing reconstruction can be applied to the events that survived the plane fit, previous cuts, and laser rejection, we need to clean the events from outliers in the time evolution of the tubes. The presence of outliers is detrimental to time fitting and results in a dramatic decrease of fitting efficiency. To reduce this possibility we apply a data pruning algorithm to remove outliers before time fitting.

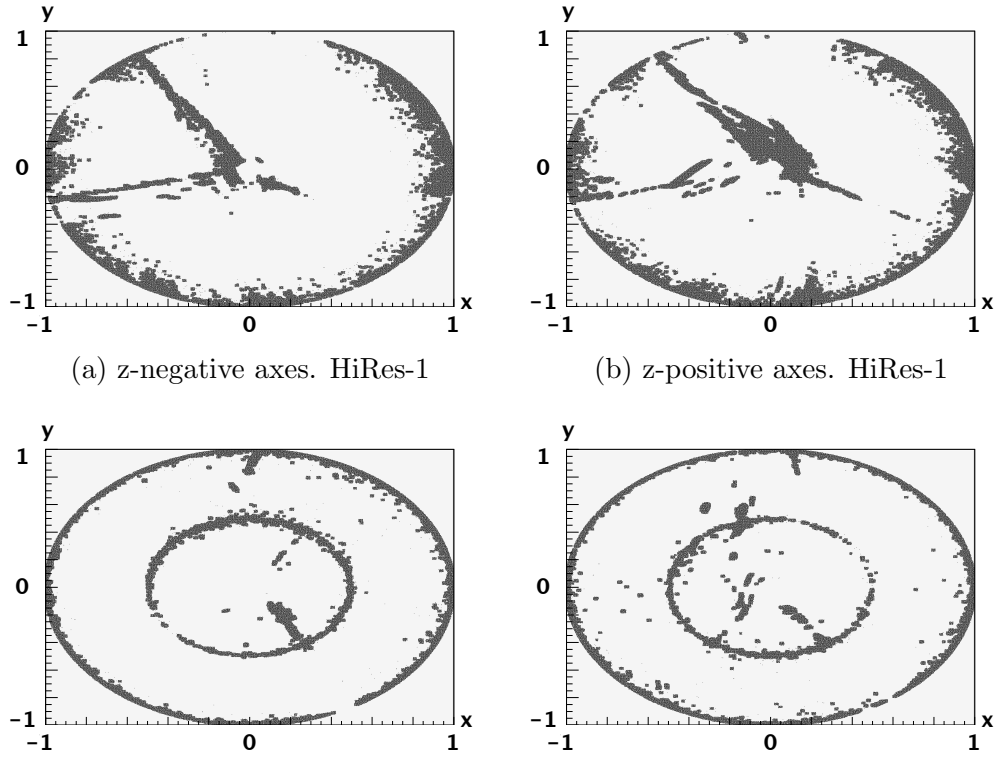

(a) z-negative axes. HiRes-1

(b) z-positive axes. HiRes-1

(c) z-negative axes. HiRes-2

(d) z-positive axes. HiRes-2

Figure 6.10. Laser rejection maps.

The main idea of the method is based on the fact that noise signals do not follow the overall time evolution of the good event tubes on a time vs. longitude plot (Figure 6.11).

Inclined neutrino tracks are usually quite long, but may consist of several segments recorded in different mirrors, sometimes with missing parts in between. If the angular distance between two adjacent tubes in a track is more than 0.15 radian, the track is broken into segments and the data pruning algorithm is applied to each segment seperately.

The algorithm starts by looping through tubes (that are incrementally ordered by longitude) from both ends and counting the number of tubes and their time range. In case the timing of the tube is off from the rest of the tubes it is marked as an outlier. After the first set of the outliers is removed a second order polynomial fit is performed on three points selected from the beginning, the middle and the ending part of the segment. Although tube trigger times relate to their longitudes through the tangential function given in equation 6.4, a second order polynomial function is considered to be a good

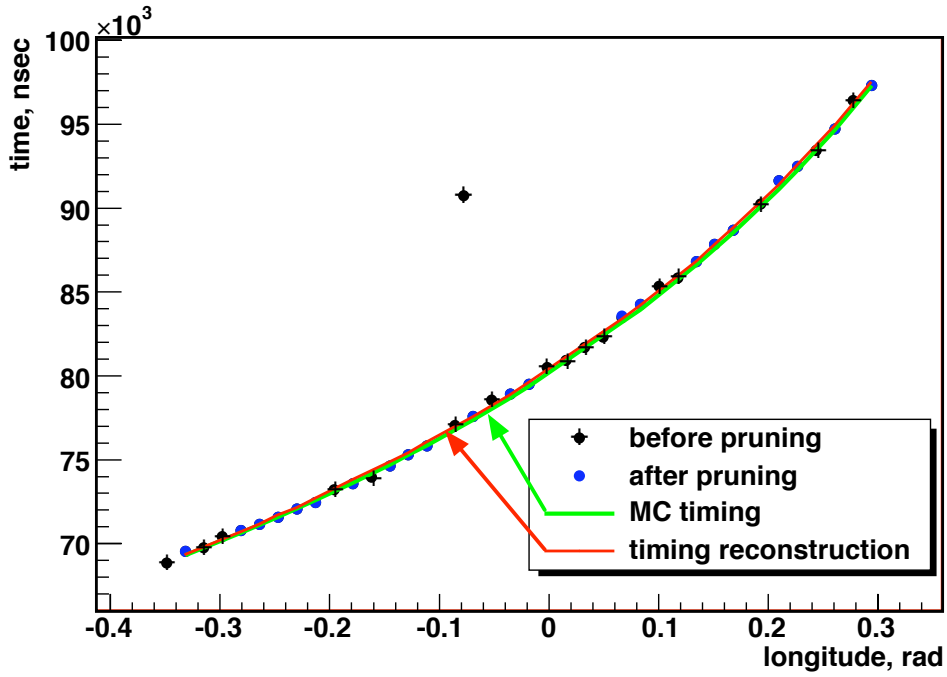

Figure 6.11. Outlier removal with the data pruning algorithm. Dots with crosses are the outliers found by the method. Dots are the surviving tubes. Solid lines are MC and Reconstructed time vs. longitude profiles respectively.

approximation at this level. Any tube with a time residual greater than 100 nanosecond with respect to this fitted polynomial is eliminated as an outlier. The 100 ns cut is based on an estimation of the time resolution of the HiRes-1 electronics.

Figure 6.11 shows a track on the trigger time versus longitude angle plot. Dots with crosses are the tubes that did not survive after the pruning algorithm was applied. These are tubes with greater than 100 ns time residuals from the fit and are deleted from the event. Simple dots are the tubes left after pruning. The lower solid line shows the original MC time vs longitude profile for the event. Upper line is the reconstructed timing profile. We can see that the timing reconstruction is exellent for the event since it coincides with the original MC profile.

6.2.5 Timing Reconstruction

Timing reconstruction includes using equation 6.10 to locate the shower track within its SDP. In our shower plane based coordinate system the angle θ_i can be rewritten as:

$$\theta_i = \pi - \lambda_{rp} - \lambda_i \tag{6.9}$$

λ_i is the longitude coordinate of the tube and λ_{rp} is the longitude coordinate of the Rp vector. In our coordinate system the timing equation is thus given by (Figure 6.2):

$$t_i(\theta_i) = t_0 + \frac{Rp}{c} tan\left(\frac{\pi - \lambda_{rp} - \lambda_i}{2}\right) \tag{6.10}$$

There are three unknowns in this equation: t_0, R_p and λ_{rp}. The last two are required for finding the shower track position in the SDP. To find the unknown parameters in the equation 6.10 we first assume some value for λ_{rp} and perform a least squares linear fit to this equation as suggested in Ref. [150]. The linear regression to the function t_i of argument $tan\left(\frac{\pi-\lambda_{rp}-\lambda_i}{2}\right)$ will return t_0 as an intercept and $\frac{Rp}{c}$ as a slope. We iterate λ_{rp} through all possible values in 1° steps to find the best parameters that minimize the function:

$$\chi^2_{tim} = \sum_i \frac{1}{\sigma_i^2}\left\{t_i - t_0 + \frac{Rp}{c} tan\left(\frac{\pi - \lambda_{rp} - \lambda_i}{2}\right)\right\}^2 \tag{6.11}$$

σ_i^2 is assumed to be constant and set equal to 1.

The range of the possible values of λ_{rp} is restricted from the angle 90° smaller than the maximum of the tube longitudes to the angle 90° larger than the minimum of the tube

longitudes, since no light can come from longitude more than 90° away from λ_{rp}. This algorithm will work only if a minimum value exists in this range (limits in *Rp* scanning angles are shown in Figure 6.2 as a dashed arrow between two dashed lines). If there is no true minimum, the least value will be found at the limits of *Rp* range (either at the beginning or the end of the scanning range).

Figure 6.12 shows the distribution of angular distance of *Rp* to the edge of the scanning range. The peak at the smaller anguar distances in the figure corresponds the case when the minimum is assumed at the edge. Because the step size is 0.0175 radians (about 1°) the peak is around 1° wide. The cut based on the longitudinal angular difference of *Rp* to the scanning edge is set at 1.5×0.0175 radians to remove events that can not be reliably reconstructed.

Once the *Rp* vector is determined, we can find the direction of the air shower track as the cross product of the $\vec{Rp}$ and the SDP normal vector $\vec{n}$. From that point all other parameters related to the shower geometry are easily found (e.g., azimuth, zenith, ϕ, χ).

Our ability to determine the three unknown parameters in equation 6.10 depends on the degree to which the relation between t_i and λ_i is nonlinear. For long tracks the nonlinearity is usually clearly evident. Shorter tracks can be fitted well to straight lines as well as the correct tangential form which results in a poor estimation and larger

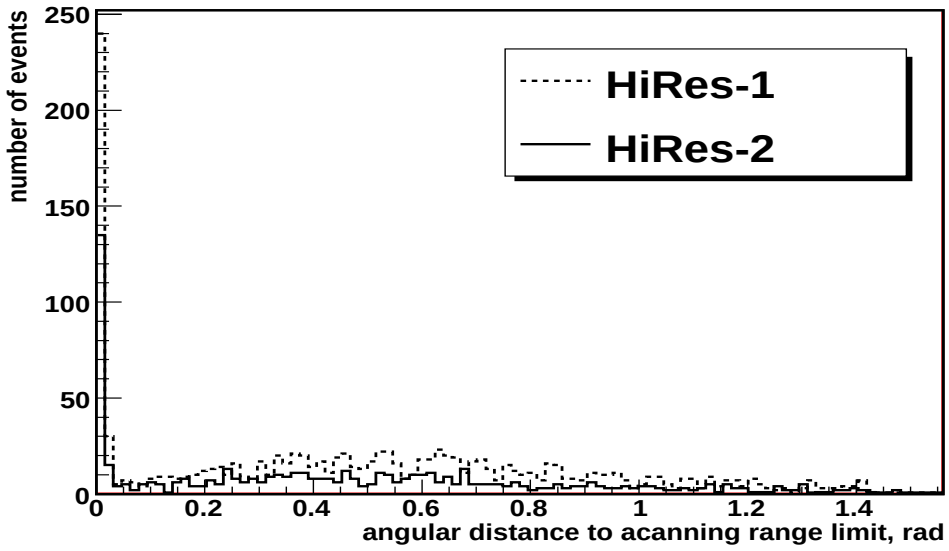

Figure 6.12. Distribution of *Rp* angular distance to the edge of scanning range.

uncertainties in locating the shower within the SDP. Without any curvature our algorithm of searching for a minimum of the least squares is unstable and will fail to reconstruct the proper event geometry.

The shower angular extent (SAE) parameter is clearly of great importance to our ability to reconstruct. It directly measures the length of our "lever arm". Figure 6.13 plots SAE for well and badly reconstructed Monte Carlo events. Well reconstructed events defined here are the events with angular difference between true zenith angle of the event and reconstructed one less than 2°. Everything else falls into the poorly reconstructed event catagory.

The distribution of poorly reconstructed MC events in Figure 6.13 peaks at low SAE values, while most of well reconstructed events have higher SAE and thus longer tracks in longitudinal direction. SAE cuts of 0.4 radians for HiRes-1 and 0.6 radians for HiRes-2 help to illuminate most of misreconstructed events while keeping most well reconstructed ones.

After SAE cut there are still misreconstructed events left in MC data as suggested by Figure 6.13. A cut on zenith angles serves two purposes. First, according to Figure 6.14 it elliminates almost all of the misreconstructed events left after the SAE cut. Second, it removes nonhorizontal CR events from data. Based on the zenith distribution of the remaining MC events (Figure 6.14) the cut is made between 90° and 93°.

One way to check how well the previous two cuts (SAE and ZA) worked to illuminate misreconstructed events from MC dataset is to look at the distribution of angular difference between true and reconstructed zenith angles. Figure 6.15 shows this distribution. Unlike the distribution of events before the cuts, almost all events that survived cuts have less than two degree angle between their true and reconstructed zenith angles, which make them well reconstructed by our convention.

Since neutrino related air showers are initiated by decay products of tau leptons, neutrino events are lower in energy as compared to cosmic ray events. Low energy events will only trigger the detector if they happen relatively close to the detector (i. e. if they have small Rp distance). Thus the natural parameter to cut on to eliminate horizontal cosmic ray tracks coming from the top of the atmosphere from the data is Rp. Figure 6.16 shows the distribution of Rp angles of reconstructed neutrino MC events after all the cuts discussed above were applied. The value for the Rp cut at 8 km was based on this plot.

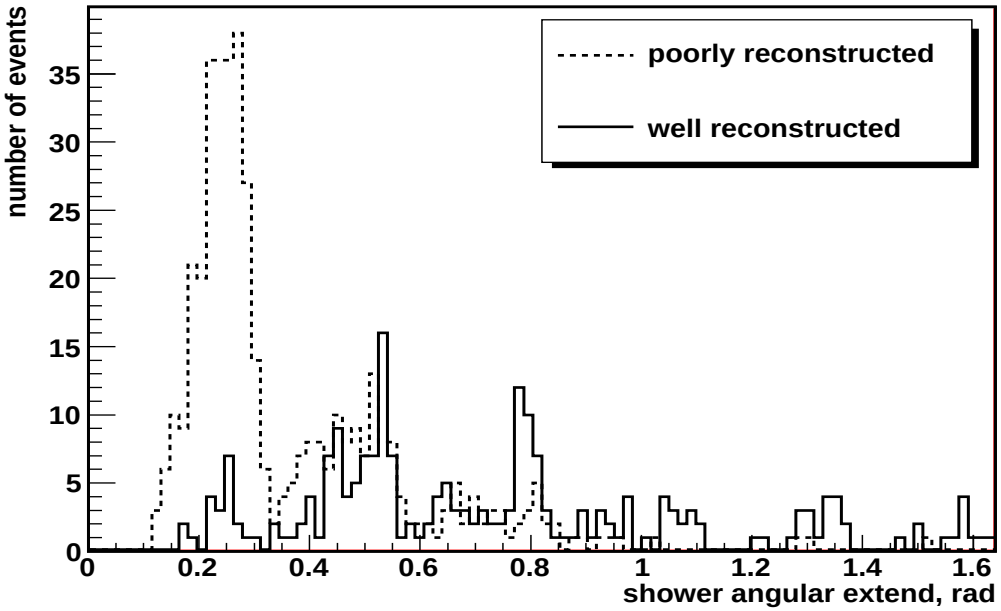

(a) HiRes-1

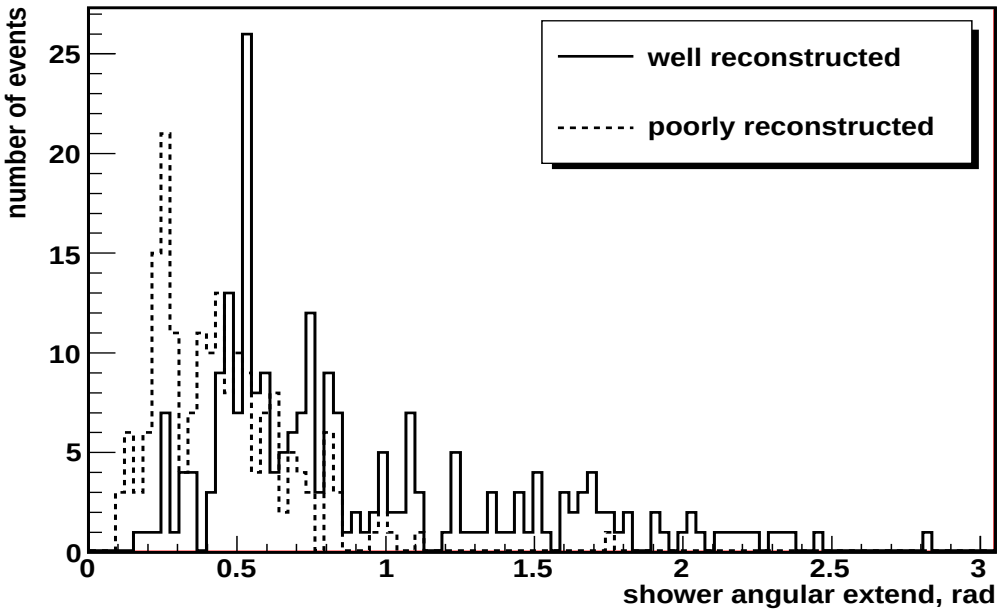

(b) HiRes-2

Figure 6.13. SAE distribution of MC events for well and poorly reconstructed events.

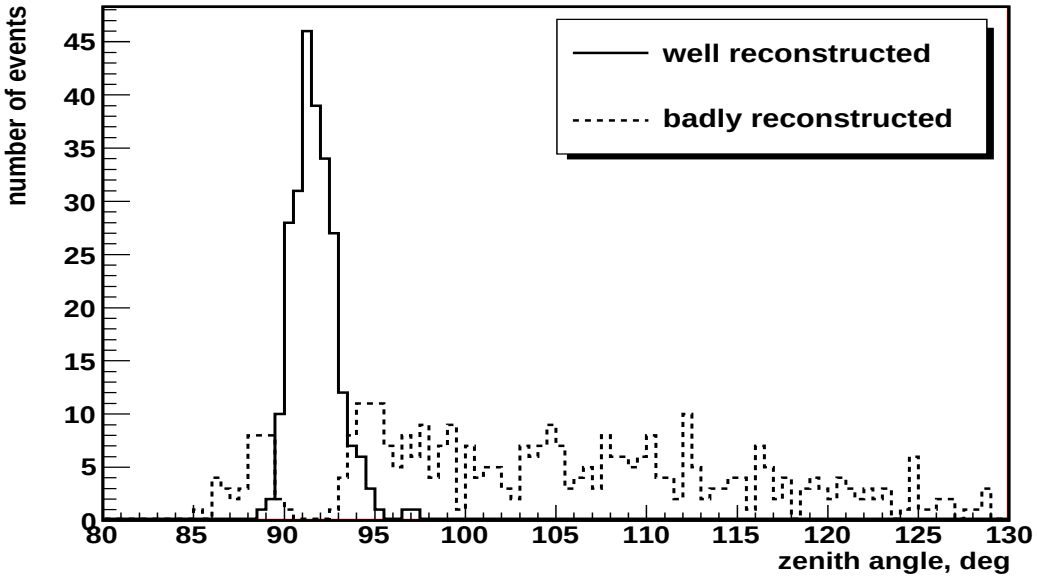

(a) HiRes-1

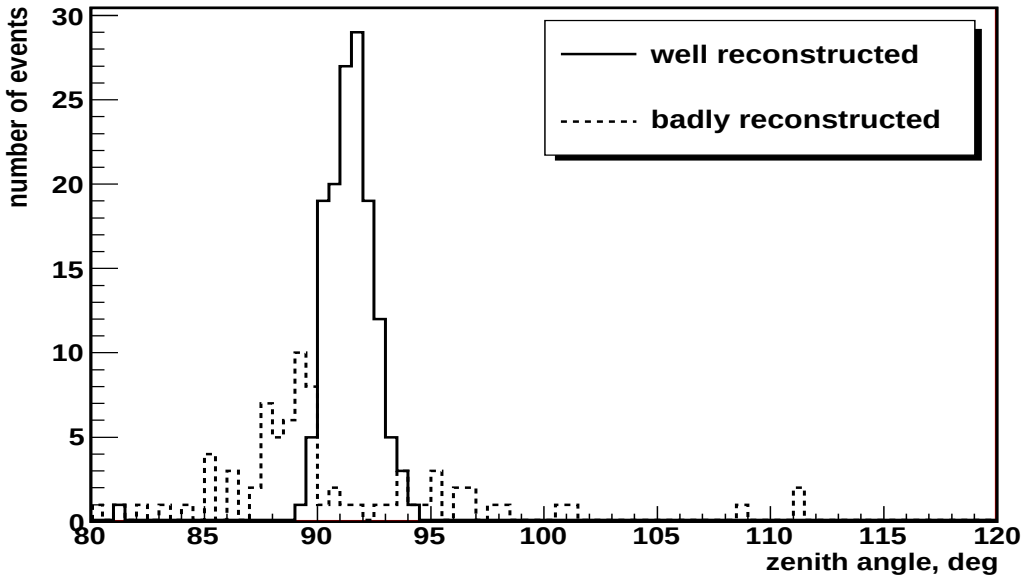

(b) HiRes-2

Figure 6.14. Zenith angle distribution of MC events for well and poorly reconstructed events.

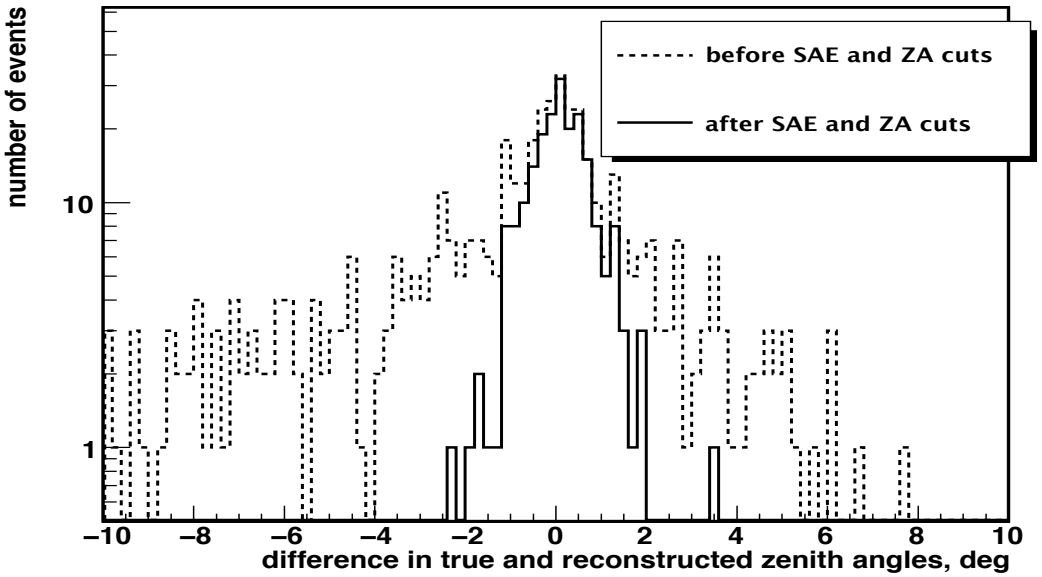

(a) HiRes-1

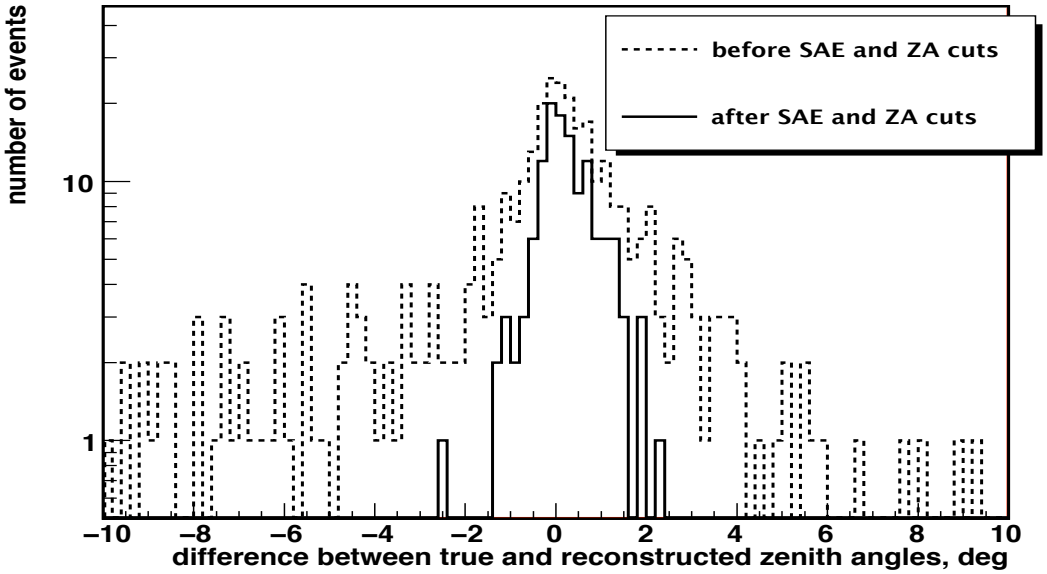

(b) HiRes-2

Figure 6.15. Difference between true and reconstructed zenith angles of MC events before and after SAE and ZA cuts are applied.

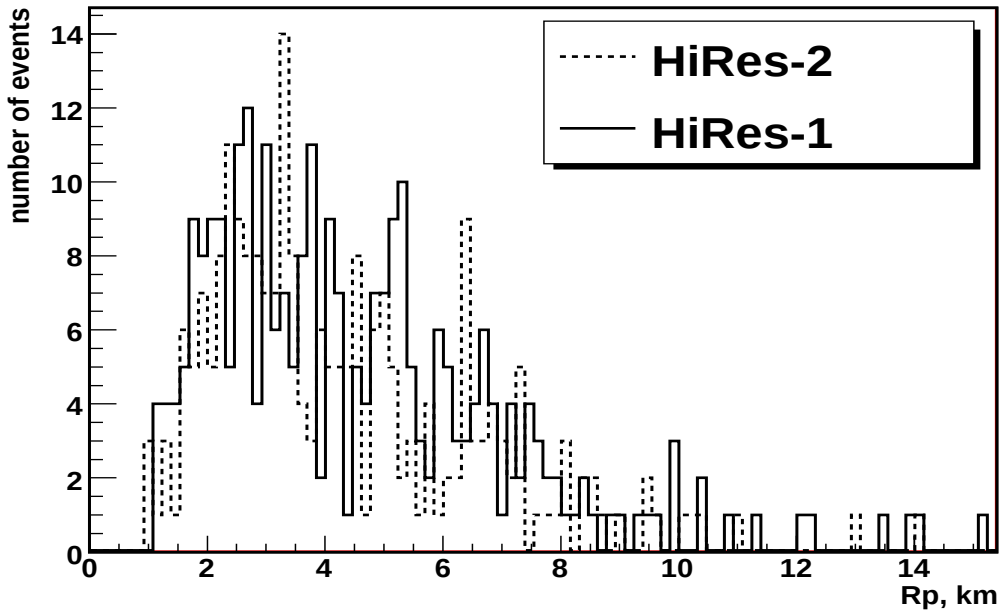

Figure 6.16. Rp distribution of MC events.

6.2.6 Analysis of the Residual Events

After all cuts discussed above were applied to the HiRes monocular dataset, 28 HiRes-1 and 23 HiRes-2 events pass all our cuts. We call these events residual events. They are well reconstructed quasi-horizontal close-by events and in principal should be our best candidates for neutrino events. Examples of two MC residual neutrino events seen by both detectors are shown in Figure 6.17. MC neutrino events surviving the cuts have long almost horizontal tracks. We were looking for the similar features in our data residual events.

Each of these residual events was studied with a HiRes event display program to see how they compare with MC neutrinos. All the residual events as they appear on HiRes event displays are given in Appendix D. We conclude that none of HiRes events is a neutrino event. Our reasoning is given below.

Looking at HiRes-1 residual events, most of them can be identified as noise or lasers right away. HiRes-1 events dated by 1997/09/12 and 2004/06/09 (see Appendix D) are full mirror triggered events that are clearly not an image of a EAS. Most of the remaining events are identified as lasers because we can find repetitive events with identical tube

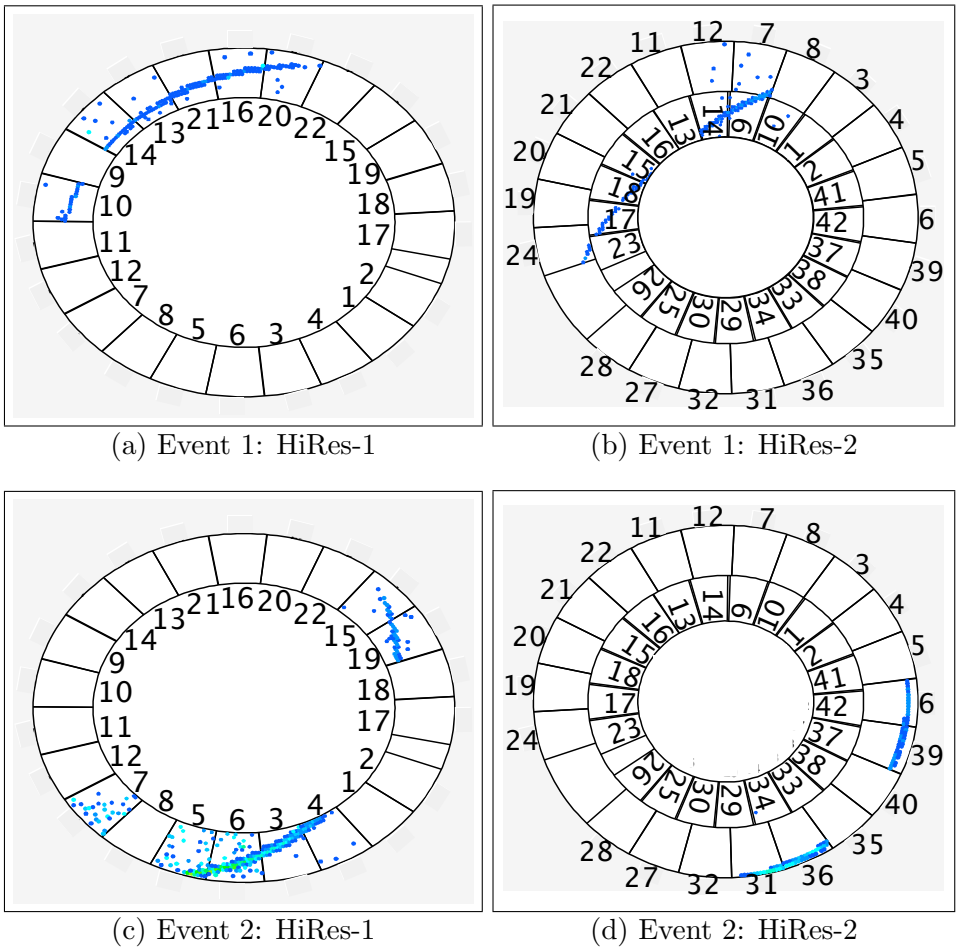

(a) Event 1: HiRes-1 (b) Event 1: HiRes-2

(c) Event 2: HiRes-1 (d) Event 2: HiRes-2

Figure 6.17. Examples of MC residual neutrino events seen by both detectors.

patterns. Geometry of event 1999/01/17 repeats itself in the event 2000/02/02. The same argument applies to events recorded on 1999/06/14, which also were recorded during the same night. A series of noise-like events dated by 2000/01/31, 2000/09/24 through 2000/09/27, 2004/05/20, and 2004/10/07 through 2004/10/14 with similar shapes occurring over many nights are also laser-related events. For them most of the laser track is located below the FOV of the detector and only a part of a track with scattered light is recorded along the edge of the FOV of the detector. Events dated by 2003/05/30 do not show any track structure, although they appear in the same mirrors. They are also most likely related to the same laser geometry, but were recorded in worse weather conditions. Events 2003/02/28 and 2003/10/23 may or may not be related to lasers, but in any case they are lacking track structure and are not considered as probable neutrino events.

Some of the lasers are harder to identify. For example, events recorded on 1999/07/13 are produced by the same laser fired several times through the night, but the geometries of the events are a bit different. Scattered light from adverse atmospheric conditions changed the way this overall fixed geometry laser event appears on the HiRes-1 display. Looking through the event record of the same night we find more events with identical geometries. Figure 6.18(a) gives an example of a residual HiRes-1 event recorded on 1999/07/13, which geometry was found in a different event of the same night 6.18(b). Events 1999/02/16, 1999/06/13, 2000/04/03 are laser events for the same argument.

Most of the residual HiRes-2 events are again events that lack any track structure and/or replicate known laser geometries (1999/10/03 through 2000/02/07, 2000/03/03 through 2000/04/08, and 2002/07/08). Laser track structure is recognized for some of them (e.g., 2000/03/31). Events dated by 2002/05/03 have identical geometries and are recorded on the same night. Events 2000/02/28 is noise. The nice long tracks tracks of events 2000/12/30 and 2005/03/14 are identified as lasers. The last two were recorded on the same night and have similar geometries. Events 2003/04/29 and 2003/04/30 are too noisy to determine their cause (probably light scattered from the laser shot and recorded in bad weather), but they are definitely not neutrino candidates since they do not show a recognizable track structure. The last two events to consider are 2004/12/18 and 2006/02/03. These events have very similar shapes, but are recorded by different sets of mirrors. One interpretation of these events is that they are produced by the light

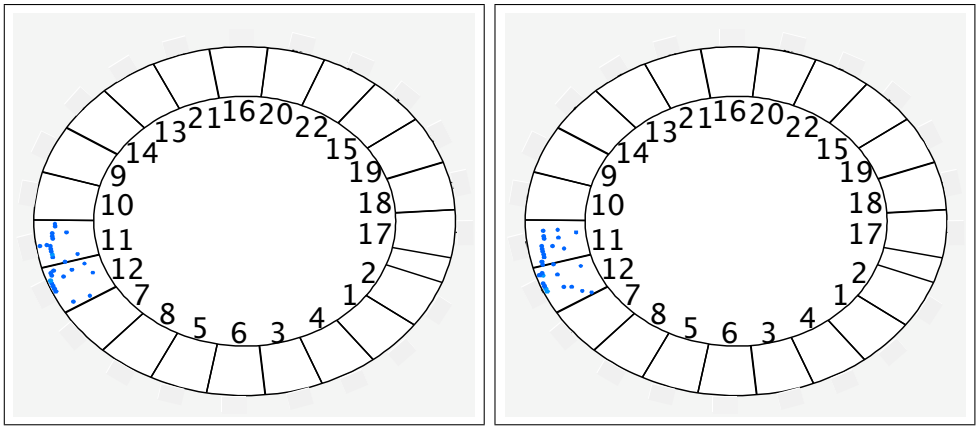

(a) 1999/07/13 part 13 (b) 1999/07/13 part 13

Figure 6.18. HiRes-1 events with repetitive geometry. Event 6.18(a) and event 6.18(b) were recorded at the same night.

scattered from an airplane passing the FOV of the detector. Another interpretation is that they might be cosmic ray showers coming directly towards the detector, so that highly beamed Cherenkov light produces a bright spot of triggered PMTs on the display. The important issue is that they do not look anything like MC neutrino events of Figure 6.17.

All residual HiRes events were explained in terms of noise, lasers and airplanes or CRs moving towards the detectors. None of these events were identified as possible neutrino candidates.

6.3 Results and Discussion

After data reconstruction and reduction was completed and the remaining events were carefully analyzed, we conclude that no neutrino events are found in the HiRes data. The summary of each step of the data and MC reduction are provided in Tables 6.1 and 6.2.

With the MC events we can calculate the overall efficiency of the HiRes detector and then use the fact that zero τ-neutrinos were found to set an upper limit on the isotropic cosmogenic neutrino flux.

The general formula for finding the flux of events as a function of energy following the assumed power law spectrum with spectral index γ is :

$$j(E) = \phi \cdot E^{-\gamma} = \frac{d}{dE}\left[\frac{N_{event}}{\epsilon T A \Omega}\right] \tag{6.12}$$

Table 6.1. Data reduction summary

Step	HiRes-1		HiRes-2	
	Cut, %	Events Remaining	Cut, %	Events Remaining
input	-	223,601,203	-	51,711,048
lasers and flashers	7.9	206,034,783	17.6	42,634,453
Rayleigh filter	89.3	22,133,395	56.8	18,403,966
number of tubes cut	88.9	2,457,269	90.2	1,807,956
plane quality cut	23.1	1,890,627	77.1	413,344
shower coordinates	0.3	1,884,017	0.6	410,803
plane parameter cut	77.5	424,095	43.1	233,592
laser elimination	88.4	49,304	53.6	108,300
data pruning	54.2	22,573	28.1	77,903
Rp edge cut	43.5	12,744	40.7	46,231
max longitude cut	95.9	524	98.4	748
zenith angle cut	93.1	36	96.5	26
maximum Rp cut	22.2	28	11.5	23

Table 6.2. MC reduction summary

Step	HiRes-1		HiRes-2		Stereo	
	Cut, %	Events Remaining	Cut, %	Events Remaining	Cut, %	Events Remaining
input	1,491,325,279					
showers in atmosphere	5,977,051					
showers triggered	-	2,918	-	1,498	-	393
number of tubes cut	17.0	2,421	21.0	1,184	12.0	346
plane quality cut	5.8	2,280	15.2	1,004	4.3	331
shower coordinates	0.8	2,261	1.5	989	1.5	326
plane parameter cut	39.9	1,358	29.5	697	43.6	184
laser elimination	24.0	1,032	11.2	619	37.5	115
data pruning	11.0	918	12.8	540	18.3	94
Rp edge cut	23.7	700	23.0	416	11.7	83
max longitude cut	44.6	388	56.7	180	22.9	64
zenith angle cut	46.6	207	28.9	128	39.1	39
maximum Rp cut	8.7	189	7.0	119	12.8	34

ϕ is the flux constant, N_{event} is the number of events, ϵ is the overall efficiency of the detector to this kind of events, T is the total time of operation, A is the area and Ω is the solid angle acceptance of the detector.

Assuming E^{-2} we find ϕ so that

$$\phi = \frac{N_{event}}{(\epsilon_1 T_1 + \epsilon_2 T_2 - \epsilon_3 T_3) A\Omega \, (1/E_{min} - 1/E_{max})} \tag{6.13}$$

In our case N_{event} is the unified confidence upper limit for a background free observation of zero events as proposed by Feldman and Cousin [85]. For zero neutrino events found in data we expect no more than 2.44 (3.09) events at confidence level of 90% (95%). ϵ_1, ϵ_2 and ϵ_3 are the efficiencies for HiRes-1, HiRes-2 and stereo data recording as inferred form our MC simulation. E_{min} and E_{max} are the upper and the lower bound of the energy bin under investigation. As we exclusively use mono datasets that possibly contain stereo events, in order not to count one event twice, the contributions from stereo events have to be subtracted. Aperture, $A\Omega$, for MC simulated neutrino events thrown into a 75 km radius sphere within $\pm 10^\circ$ of the horizon around the detector is culculated to be $4\pi^2 \sin(10^\circ) r^2 = 3.8542\ 10^{14}$ str cm^2. These numbers are corrected for mirrors that are not operational during parts of the time.

Table 6.3 summarizes the necessary information for calculating the flux constant of cosmogenic neutrinos for three energy (10^{18} eV - 10^{19} eV, 10^{19} eV - 10^{20} eV, 10^{20} eV -

Table 6.3. Cosmogenic neutrino flux constant

Parameter	log10(Energy, eV)			
	18-19	19-20	20-21	18-21
number of input ν_τ	1,343,527,548	134,363,076	13,434,655	1,491,325,279
surviving HiRes-1 MC events	155	34	0	189
surviving HiRes-2 MC events	94	23	2	119
surviving Stereo MC events	29	5	0	34
ϕ (90%CL), eV·cm^{-2}·sr^{-1}·s^{-1}	$2,329^{201}_{172}$	$10,108^{2,048}_{1,458}$	$360,784^{871,011}_{149,441}$	$1,883^{146}_{126}$
ϕ (95%CL), eV·cm^{-2}·sr^{-1}·s^{-1}	$2,949^{256}_{217}$	$12,800^{2,594}_{1,846}$	$456,895^{1,103,042}_{189,252}$	$2,385^{184}_{160}$

10^{21} eV) and integrated flux (10^{18} eV - 10^{21} eV) assuming E^{-2} input spectrum. Predicted flux constants ϕ for confidence levels of 90% and 95% are also given for the same energy bins. In our analysis we used data collected by HiRes-1 from May 1997 till April 2006 and by HiRes-2 form October 1999 till April 2006. The lifetime of HiRes-1 is 20,132,360 seconds for all mirror equivalent operation. HiRes-2 has a lifetime of 13,096,693 seconds. There are 10,128,727 seconds of stereo operation.

Figure 6.19 compares the HiRes upper limits on the isotropic cosmogenic τ-neutrino flux (three thick squares that incorporate statistical uncertainty for three energy bins and dashed thick line for integrated flux at a 90% condence level) with limits set by other experiments and studies (Fly's Eye 85 [36], AGASA 01 [186], RICE 06 [124], Pierre Auger 08 [11], AMANDA 2 [16], Semikoz and Sigl [165]). It also shows our GZK CR spectrum derived ν flux expectations and HiRes limits on e-neutrino flux of Ref. [8].

The largest uncertainty of our limit estimation that we control is due to limited MC statistics. Among the systematic uncertainties the largest one are introduced by the extrapolation of neutrino cross sections to the highest energies. As estimated by [8] new cross section models will affect ν_τ limits by as much as 10% for lowest energy bin and 40% for the highest energies. Models of neutrino interactions are also a big source of systematic uncertainties. The amount of energy transferred to the secondary electron or hadron is important especially for the lowest energy bins. As it was suggested in [11], uncertainties in the τ energy losses are governed by the photonuclear cross section, which differs by as much as 40% among existing estimations.

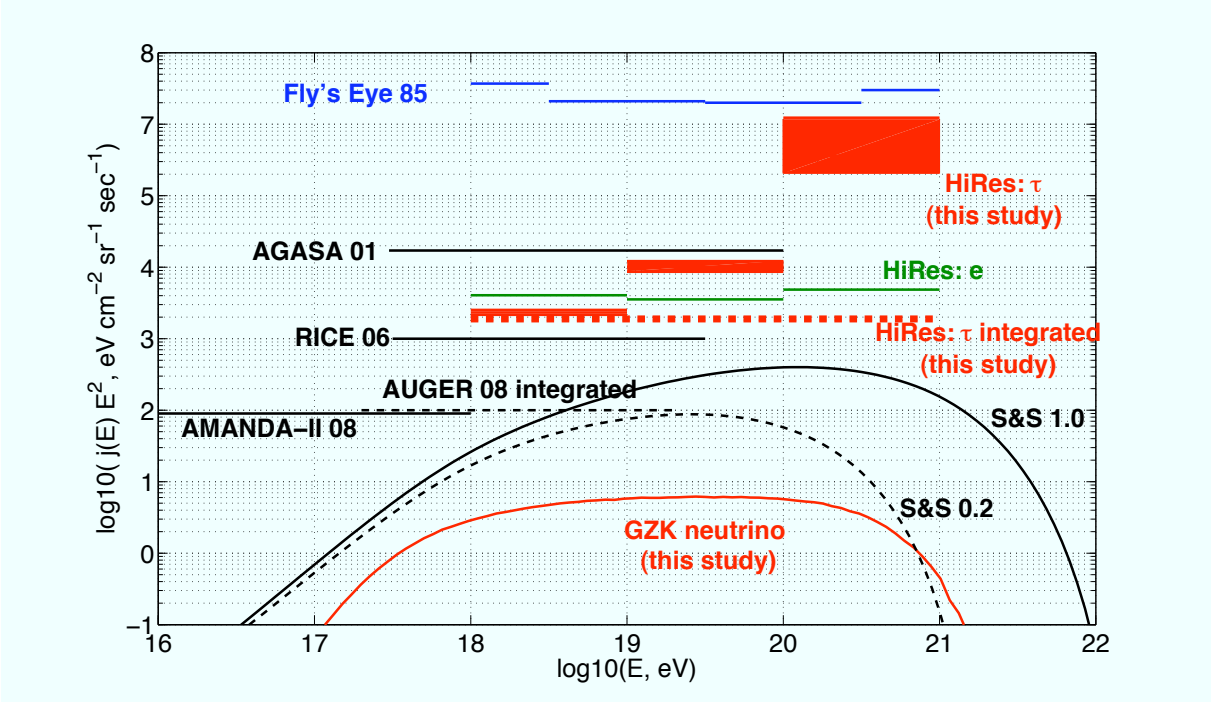

Figure 6.19. Upper limits on cosmogenic neutrino flux from HiRes experiment for 90% confidence level and from other studies.

HiRes neutrino limits have significantly improved as compared to those given for the Flys Eye [36], but they are still much above even the most optimistic predictions [165]. This result is not surprising, since HiRes is not a dedicated neutrino experiment.

APPENDIX A

COSMOLOGY

Present knowledge of cosmology suggests that our universe is spatially homogeneous and isotropic on the large scale and can expand or contract as a function of time. One of the evidences that the universe looks the same in all directions comes from the isotropy of cosmic microwave background radiation. The spacial distribution of galaxies and radio sources agrees with the hypothesis that our universe is homogeneous. This model is also known as the Standard Model of modern cosmology [46].

The most general space-time metric that is consistent with the Standard Model is the Robertson-Walker (RW) metric [157, 158, 159, 180]. In the spherical polar coordinates (ρ, θ, ϕ) it has the form:

$$ds^2 = c^2dt^2 - a^2(t)\left[d\rho^2 + f^2(\rho)\left(d\theta^2 + sin^2\theta d\phi^2\right)\right] \tag{A.1}$$

where s is a four-dimensional interval, t is the proper time, measured by the observer, $a(t)$ is the scale factor responsible for the expansion/contraction of the universe (in units of length). ρ, θ and ϕ are three spacial unit vectors, and $f(\rho)$ can be of three values $(sin(\rho), \rho, sinh(\rho))$.

In the radial coordinate system the metric is given by:

$$ds^2 = c^2dt^2 - a^2(t)\left[\frac{dr^2}{1-kr^2} + r^2\left(d\theta^2 + sin^2\theta d\phi^2\right)\right] \tag{A.2a}$$

where

$$k = \begin{cases} +1, & \text{if } f(\rho) = sin(\rho) \\ 0, & \text{if } f(\rho) = \rho \\ -1, & \text{if } f(\rho) = sinh(\rho) \end{cases} \tag{A.2b}$$

Constant parameter k describes the curvature of space at constant time. $k = +1$ suggests positive curvature of space, $k = 0$ corresponds to the flat space and $k = -1$ rises negative curvature.

The metric has an analytical solution to Einstein's field equation $G_{\mu\nu} - \Lambda g_{\mu\nu} = \frac{8\pi G}{c^4} T_{\mu\nu}$. The resulting solutions describe the dynamics of the universe [120] and are known as the first A.3a and the second A.3b Friedmann equations [79, 80]:

$$\left(\frac{\dot{a}}{a}\right)^2 + \frac{kc^2}{a^2} - \frac{\Lambda c^2}{3} = \frac{8\pi G}{3}\rho \tag{A.3a}$$

$$2\frac{\ddot{a}}{a} + \left(\frac{\dot{a}}{a}\right)^2 + \frac{kc^2}{a^2} - \Lambda c^2 = \frac{8\pi G}{c^2}p \tag{A.3b}$$

Subtracting A.3a from A.3b, we have the following simplified form of solution:

$$\left(\frac{\dot{a}}{a}\right)^2 = \frac{8\pi G}{3}\rho - \frac{kc^2}{a^2} + \frac{\Lambda c^2}{3} \tag{A.4a}$$

$$\frac{\ddot{a}}{a} = -\frac{4\pi G}{3}\left(\rho + \frac{3p}{c^2}\right) + \frac{\Lambda c^2}{3} \tag{A.4b}$$

where differentiation is with respect to time t. $\rho(t)$ is the mean density of matter, $p(t)$ is the isotropic hydrodynamic pressure of universe matter and radiation. G is the gravitational constant, Λ is called cosmological constant and k determines the curvature of the universe.

It can be inferred from the result above that the expansion rate of the universe $\dot{a}$ increases with the decrease of pressure p and density ρ and the increase with cosmological constant Λ. This means that vacuum dominated universe will be acceleration.

Now it is time to define some important parameters. In 1929 Edwin Hubble found a simple linear relationship between the recessional velocity of a galaxy and the distance from the galaxy to the observer [107]. This observation is now known as the Hubble Law:

$$v = HD \tag{A.5}$$

H is Hubble's constant at the time of observation and is time dependent. The Hubble's parameter can also be defined through the scale factor introduces above as:

$$H \equiv \frac{\dot{a}}{a} \tag{A.6}$$

or substituting A.4a in the equation A.6 above

$$H = \sqrt{\frac{8\pi G}{3}\rho - \frac{kc^2}{a^2} + \frac{\Lambda c^2}{3}} \tag{A.7}$$

Deceleration parameter is defined as

$$q = -\frac{\ddot{a}}{aH^2} = -\frac{\ddot{a}a}{\dot{a}^2} = -\frac{1}{H^2}\left[\frac{\Lambda c^2}{3} - \frac{4\pi G}{3}\left(\rho + \frac{3p}{c^2}\right)\right] \tag{A.8}$$

Density parameter Ω_t describes the total density of matter (Ω_m) and radiation (Ω_r) of the universe. Here $\rho_c = \frac{3H^2}{8\pi G}$ is the critical density.

$$\Omega_t = \frac{\rho}{\rho_c} = \frac{8\pi G\rho}{3H^2} \tag{A.9}$$

Now, when all the necessary parameter are defined, equation A.4a can be rewritten as:

$$a = \frac{c\sqrt{k}}{H}\frac{1}{\sqrt{\Omega_t + \frac{\Lambda c^2}{3H^2} - 1}} \tag{A.10}$$

This equation defines the radius of curvature of the three-dimensional space at time t.

From equations A.4a and A.9 we can write:

$$\dot{a} = Ha\sqrt{\Omega_m + \Omega_r + \frac{\Lambda c^2}{3H^2} - \frac{kc^2}{a^2H^2}} \tag{A.11}$$

and by taking matter conservation into account ($\rho a^3 = \rho_0 a_0^3$) we can rewrite equation A.11 in terms of present present epoch values of cosmological parameters (denoted by subscript o).

$$\dot{a} = H_0 a_0\sqrt{\Omega_{m0}\left(\frac{a_0}{a}\right) + \Omega_{r0}\left(\frac{a_0}{a}\right)^2 + \frac{\Lambda c^2 a^2}{3H_0^2 a_0^2} - \frac{kc^2}{a_0^2H_0^2}} \tag{A.12}$$

The second and the third terms in the above equation are density parameters of two types of energies: "spacial curvature" energy Ω_k, and vacuum energy Ω_Λ (sometimes called the normalized cosmological parameter).

$$\Omega_k = \frac{\rho_k}{\rho_c} = \frac{kc^2}{a_0^2H_0^2} \tag{A.13a}$$

$$\Omega_\Lambda = \frac{\rho_\Lambda}{\rho_c} = \frac{\Lambda c^2}{3H^2} \tag{A.13b}$$

Then equation A.12 is reduced to

$$\dot{a} = H_0 a_0\sqrt{\Omega_{m0}\left(\frac{a_0}{a}\right) + \Omega_{r0}\left(\frac{a_0}{a}\right)^2 + \Omega_\Lambda\left(\frac{a}{a_0}\right)^2 - \Omega_k} \tag{A.14a}$$

or

$$H = H_0\sqrt{\Omega_{m0}\left(\frac{a_0}{a}\right)^3 + \Omega_{r0}\left(\frac{a_0}{a}\right)^4 + \Omega_\Lambda - \Omega_k\left(\frac{a_0}{a}\right)^2} \tag{A.14b}$$

As the universe expands, the density of matter decreases as a^3 (since the university expands in all three spatial dimensions). Total matter energy density includes contributions from baryon density Ω_b and dark matter density Ω_d. The radiational energy density decreases inversely proportional to a^4 (a^3 due to the space expansion and another power comes from redshift contribution defined below). Vacuum energy does not change with universe expansion (vacuum is created proportional to the space creation). The curvature component shows how much energy is lacking compared to a flat universe and is a second power function of a.

It is also very interesting to see how different terms in the equation A.14b played a role in different ages of our universe. When it was young and small ($a << 1$), the radiational term Ω_r/a^4 dominated over the rest of them. But when a became larger, the mass component, Ω_m/a^3, started to play the most important role. As time goes by for $a >> 1$ and Ω_Λ becomes the most dominant energy density contribution.

By definition

$$\Omega_k = 1 - \Omega_{m0} - \Omega_{r0} - \Omega_\Lambda = 1 - \Omega_0 \tag{A.15}$$

This allows us to relate the total energy density Ω_0 in the universe to its local geometry via

$$\Omega_0 \begin{cases} > 1, & k = +1 \\ = 1, & k = \ \ 0 \\ < 1, & k = -1 \end{cases} \tag{A.16}$$

In cosmology the concept of redshift is very important. As photons (or another particle) move through the space, the wavelength λ, which is associated with it, stretches as the result of stretching space. A particle, emitted with the wavelength λ at the time when the expansion factor was a, will have an increased wavelength $\lambda_o = \lambda/a$ at the current epoch with $a_o = 1$. This is indicated by the equation below:

$$z = \frac{\delta\lambda}{\lambda} = \frac{a_o}{a} - 1 \tag{A.17}$$

The parameter z is called the cosmological redshift. The expansion factor in terms of redshift is:

$$a = \frac{a_o}{z+1} \tag{A.18}$$

It is possible to define the redshift between two objects, both of which are cosmologically shifted relative to us. The redshift z_{12} between object at redshift z_2 relative to the object at z_1 ($z_1 < z_2$):

$$1 + z_{12} = \frac{a_1}{a_2} = \frac{1+z_2}{1+z_1} \tag{A.19}$$

Eq. A.14b in terms of z looks like:

$$H = H_0\sqrt{\Omega_r(1+z)^4 + \Omega_m(1+z)^3 - \Omega_k(1+z)^2 + \Omega_\Lambda} \tag{A.20}$$

Redshift is one of the several parameters that are needed to calculate the distances between the extragalactic objects.

Combining equation A.14a and A.18 we get

$$\frac{dz}{dt} = -H_0(1+z)\sqrt{\Omega_r(1+z)^4 + \Omega_m(1+z)^3 - \Omega_k(1+z)^2 + \Omega_\Lambda} \tag{A.21a}$$

or

$$dt = -H_0\frac{1}{(1+z)\sqrt{\Omega_r(1+z)^4 + \Omega_m(1+z)^3 - \Omega_k(1+z)^2 + \Omega_\Lambda}} \tag{A.21b}$$

However, distance $ds = cdt$

$$ds = -\frac{c}{H_0}\frac{dz}{(1+z)\sqrt{\Omega_r(1+z)^4 + \Omega_m(1+z)^3 - \Omega_k(1+z)^2 + \Omega_\Lambda}} \tag{A.22}$$

Equation A.22 is a very important relationship that allows to find the unit length ds for any redshift z.

The light travel-time distance between two objects located at redshifts z_1 and z_2 respectively is found by integration A.22 over dz from z_1 to z_2

$$S = \frac{c}{H_0}\int_{z_2}^{z_1}\frac{dz}{(1+z)\sqrt{\Omega_r(1+z)^4 + \Omega_m(1+z)^3 - \Omega_k(1+z)^2 + \Omega_\Lambda}} \tag{A.23}$$

where minus sign from equation A.22 is equivalent to the swapped limits of integration.

Since in case of no expansion proper distance D_{p0} at the present time will be equal to the light travel-time distance [120], the former can be calculated by multiplying A.22 by $(1+z)$ and integration.

$$D_{p0} = \frac{c}{H_0} \int_{z_2}^{z_1} \frac{1}{\sqrt{\Omega_r(1+z)^4 + \Omega_m(1+z)^3 - \Omega_k(1+z)^2 + \Omega_\Lambda}} \tag{A.24}$$

Due to the fact the D_p scales linearly with the expansion of the universe at some other time t, the proper distance is given by:

$$D_p = \frac{c}{H_0(1+z)} \int_{z_2}^{z_1} \frac{1}{\sqrt{\Omega_r(1+z)^4 + \Omega_m(1+z)^3 - \Omega_k(1+z)^2 + \Omega_\Lambda}} \tag{A.25}$$

APPENDIX B

RELATIVISTIC KINEMATICS

The purpose of this appendix is to remind the reader of the essentials of relativistic kinematics of particle reactions. Section B.1 introduces the notations that are used throughout this appendix and also provides a summary of the basic principles and transformations of relativistic kinematics. In sections B.2 and B.3, two- and three-body decays of unstable particles are covered. Section B.4 describes particle collisions.

B.1 General Principles

Since high energy particles are moving with a speed close to the speed of light, classical kinetic relationships are not valid any more and they have to be generalized for the relativistic case.

The theory of relativity is based on two main principles:

1. The laws of nature are the same in all inertial reference frames.

2. In vacuum, light propagates with respect to any inertial frame and in all directions with the universal speed c. This speed is a constant of nature.

In special relativity, total energy and total momentum of a particle with rest mass m_0 moving with the speed $\vec{v}$ are defined as

$$E = mc^2 = \frac{m_0 c^2}{\sqrt{1-(v/c)^2}} = \gamma m_0 c^2 \tag{B.1}$$

$$\vec{p} = m\vec{v} = \frac{m_0 \vec{v}}{\sqrt{1-(v/c)^2}} = \gamma m_0 \vec{v} \tag{B.2}$$

where m is particle's relativistic mass, $\gamma = E/mc^2$ is called a Lorentz factor and we can substitute $v/c = \beta$, which is just velocity in speed of light units.

Squaring B.1 and B.2 and doing simple algebra, we get the following relationship between the total energy and the momentum of a particle:

$$E^2 = p^2c^2 + m^2c^4 \tag{B.3}$$

In relativistic kinematics, a particle is also described by a four-momentum, generalization of the classical three-dimensional momentum to four-dimensional space-time. The first three components of the four-momentum are three spatial components of a particle's momentum and the fourth component is its energy divided by c. In order to keep particle energies, momenta and masses of the same dimension (units of energy), the speed of light is set to be $c = 1$. In new notation particle's four-momentum is

$$P = (E, \vec{p}) = \begin{pmatrix} E \\ p_x \\ p_y \\ p_z \end{pmatrix} \tag{B.4}$$

For the system of two particles the sum of four-momenta is

$$P_1 + P_2 = (E_1 + E_2, \vec{p_1} + \vec{p_2}) \tag{B.5}$$

The length of the four-vector is a Lorenz invariant, meaning it does not change as we move from one reference system to another. The length of four-momenta (also called invariant mass) is

$$s = m_0^2 = E^2 - \vec{p}^{\,2} = E^2 - p_x^2 - p_y^2 - p_z^2 \tag{B.6}$$

The length of total four-momenta of the two particle system is

$$\begin{aligned} s_{12} &= (E_1 + E_2)^2 - (\vec{p_1} + \vec{p_2})^2 \\ &= E_1^2 + E_2^2 + 2E_1E_2 - \vec{p_1}^{\,2} - \vec{p_2}^{\,2} - 2\vec{p_1} \cdot \vec{p_2} \\ &= (E_1^2 - \vec{p_1}^{\,2}) + (E_2^2 - \vec{p_2}^{\,2}) + 2(E_1E_2 - \vec{p_1} \cdot \vec{p_2}) \\ &= m_{01}^2 + m_{02}^2 + 2(E_1E_2 - |\vec{p_1}||\vec{p_2}|cos\theta) \\ &= m_{01}^2 + m_{02}^2 + 2E_1E_2(1 - \beta_1\beta_2 cos\theta) \end{aligned} \tag{B.7}$$

Although the length of the four-momentum is invariant under Lorenz transformation, its components are not. If a particle four-momentum is given as $P = (E, p_x, p_y, p_z)$, its

components in the reference frame that is moving with relative velocity $\vec{v} = \vec{v}_x$ are given by the following transform

$$\begin{pmatrix} E^{'} \\ p_x^{'} \\ p_y^{'} \\ p_z^{'} \end{pmatrix} = \begin{pmatrix} \gamma & -\gamma\beta & 0 & 0 \\ -\gamma\beta & \gamma & 0 & 0 \\ 0 & 0 & 1 & 0 \\ 0 & 0 & 0 & 1 \end{pmatrix} \times \begin{pmatrix} E \\ p_x \\ p_y \\ p_z \end{pmatrix} \tag{B.8a}$$

$$E^{'} = \gamma(E - \beta p_x) \tag{B.8b}$$

$$p_x^{'} = \gamma(p_x - \beta E) \tag{B.8c}$$

$$p_y^{'} = p_y \tag{B.8d}$$

$$p_z^{'} = p_z \tag{B.8e}$$

$$\gamma = 1/\sqrt{1 - \beta^2} \tag{B.8f}$$

The inverse transformation involves just the change in the sign of β:

$$\begin{pmatrix} E \\ p_x \\ p_y \\ p_z \end{pmatrix} = \begin{pmatrix} \gamma & \gamma\beta & 0 & 0 \\ \gamma\beta & \gamma & 0 & 0 \\ 0 & 0 & 1 & 0 \\ 0 & 0 & 0 & 1 \end{pmatrix} \times \begin{pmatrix} E^{'} \\ p_x^{'} \\ p_y^{'} \\ p_z^{'} \end{pmatrix} \tag{B.9}$$

There are several different reference systems that are usually useful to understand the processes of particle interactions. The center-of-mass frame (CMF) is the reference frame in which the total momentum of the system is equal to zero ($\sum_{i=1}^{n} \vec{p}_i{}^* = \vec{p}_1{}^* + \vec{p}_2{}^* + \ldots + \vec{p}_n{}^* = 0$). Quantities in the CMF will be marked by the asterisk. The reference frame in which one of the initial particles is at rest ($\vec{p}^{\,'} = 0$) is called a rest frame (RF). Quantities in the rest frame are denoted by a prime, and quantities in the observer's frame are left unmarked.

B.2 Kinematics of Two-Body Particle Decay

Two-body decay of unstable particle is probably the simplest kind of particle reactions. In 2-body decay the unstable "mother" particle with rest mass M decays into two "daughter" particles with rest masses m_1 and m_2. Let us consider the general case when particle M is moving along z-axis in the observer's frame (OF) with energy E and momentum $\vec{p} = \vec{p}_z$. The four-momenta for the three particles in the OF are $P = (E, 0, 0, p)$ for the "mother" particle and $P_1 = (E_1, p_{1x}, 0, p_{1z})$, $P_2 = (E_2, p_{2x}, 0, p_{2z})$ for the "daughter"

particles (also see diagram a of Figure B.1). The momentum conservation in x direction immediately implies that:

$$p_z = p_{1z} + p_{2z} \tag{B.10}$$

It is easy to find the relationships for energy and momenta in the rest frame of M and then go back to the observer's frame (see plot b in Figure B.1). In the rest frame (RF) of particle M, its four-momenta is $P^{'} = (M, 0, 0, 0)$. We will denote the four-momenta of the two secondary particles as $P_1^{'} = (E_1^{'}, p_{1x}^{'}, 0, p_{1z}^{'})$ and $P_2^{'} = (E_2^{'}, p_{2x}^{'}, 0, p_{2z}^{'})$. By momentum conservation in RF we have:

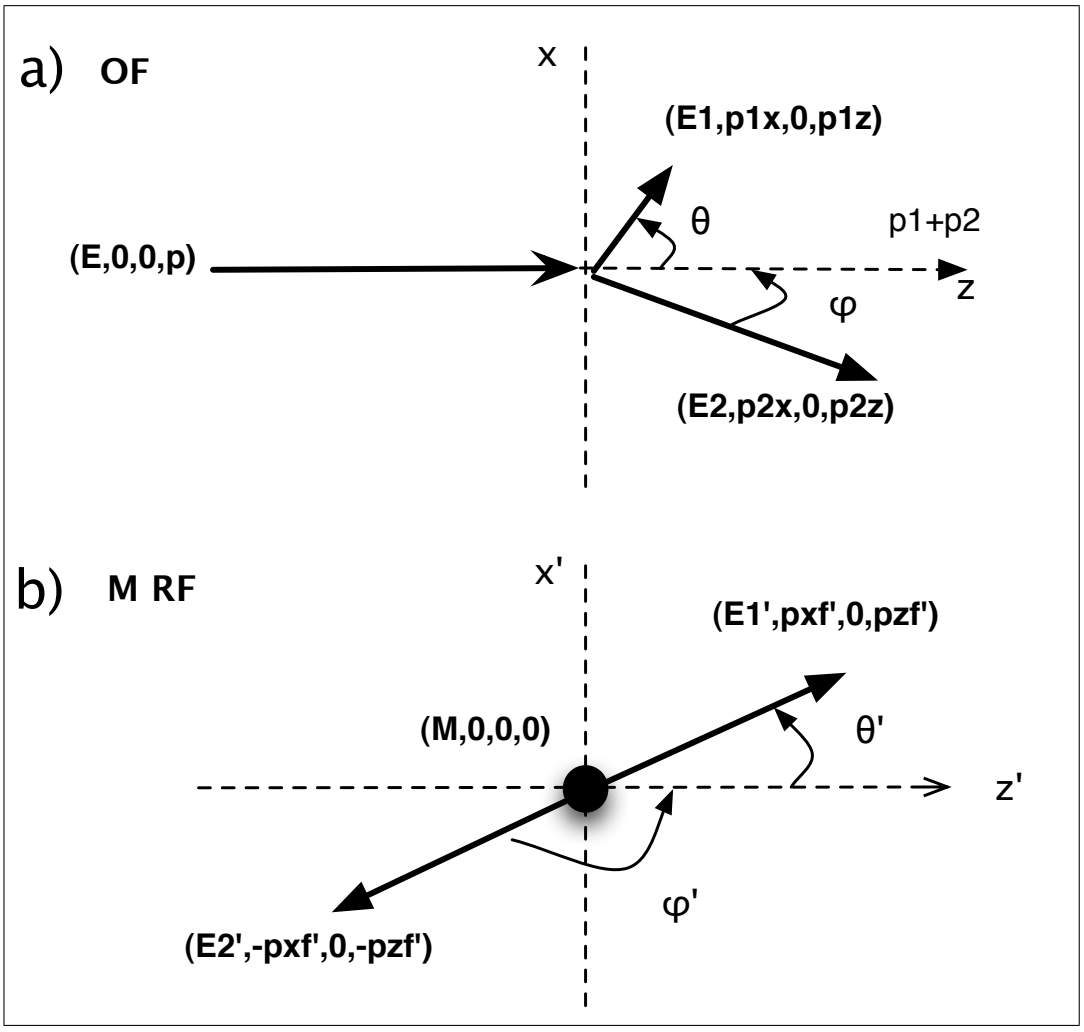

Figure B.1. Two-body decay diagram in different reference frames: a - observer's frame (OF), b - rest frame (RF) of M.

$$\vec{p}^{\,'} = \vec{p}_1^{\,'} + \vec{p}_2^{\,'} = 0 \tag{B.11}$$

or

$$\vec{p}_1^{\,'} = -\vec{p}_2^{\,'} \tag{B.12}$$

Energy conservation requires that

$$M = E_1^{'} + E_2^{'} \tag{B.13}$$

By combining energy and momentum conservation law, we can find the relationships for the energy and momenta for the decay products.

$$\begin{aligned}
\vec{p}_1^{\,'2} &= \vec{p}_2^{\,'2} \\
E_1^{'2} - m_1^2 &= E_2^{'2} - m_2^2 \\
E_1^{'2} - E_2^{'2} &= m_1^2 - m_2^2 \\
(E_1^{'} - E_2^{'})(E_1^{'} + E_2^{'}) &= m_1^2 - m_2^2 \\
(E_1^{'} - E_2^{'})M &= m_1^2 - m_2^2 \\
ME_1^{'} - ME_2^{'} &= m_1^2 - m_2^2 \\
ME_1^{'} - ME_2^{'} + ME_1^{'} - ME_1^{'} &= m_1^2 - m_2^2 \\
2ME_1^{'} - M(E_2^{'} + E_1^{'}) &= m_1^2 - m_2^2 \\
2ME_1^{'} - M^2 &= m_1^2 - m_2^2
\end{aligned} \tag{B.14}$$

Thus, the energy of the "daughter" particles in the RF of M

$$E_{1(2)}^{'} = \frac{M^2 + m_{1(2)}^2 - m_{2(1)}^2}{2M} \tag{B.15}$$

The momenta of the particles $p_{12}^{'}$ is given by

$$p_{12}^{'} = \sqrt{E_{12}^{'2} - m_{1(2)}^2} = \frac{\sqrt{(M^2 - (m_1 + m_2)^2)(M^2 - (m_1 - m_2)^2)}}{2M} \tag{B.16}$$

We can see that a particle will decay only if its mass equals or exceeds the sum of the masses of its decay products ($M \geq m_1 + m_2$). This also means if the mass of the particle is greater than the masses of other particles combined, then this particle will be unstable and will decay, unless the decay is prohibited by another conservation law.

It is also important to notice that there is no preferable direction for the daughter particles in the RF (the decay is said to be isotropic). This means that we can chose the direction $\theta^{'}$ of one of the decay products randomly, and the direction of the other one by the conservation of momentum is $\phi^{'} = 180^{\circ} + \theta^{'}$.

The energies and momenta in RF related to the same quantities in OF through the inverse Lorentz transforms B.9

$$
\begin{aligned}
E_{1(2)} &= \gamma^{'}(E^{'}_{1(2)} + (-)\beta^{'} p^{'}_{1(2)} cos(\theta^{'})) && \text{(B.17)} \\
p_{1(2)z} &= \gamma^{'}(p^{'}_{1(2)} cos(\theta^{'}) + (-)\beta^{'} E^{'}_{1(2)}) && \text{(B.18)} \\
p_{1(2)x} &= p^{'}_{1(2)} sin(\theta^{'}) && \text{(B.19)} \\
p_{1(2)} &= \sqrt{p^2_{1(2)x} + p^2_{1(2)z}} && \text{(B.20)} \\
& && \text{(B.21)}
\end{aligned}
$$

where $\gamma^{'} = E/M$ and $\beta^{'} = p/E = \sqrt{1 - \frac{1}{\gamma^{'2}}}$. It is also easy to show that the angle θ that particle 1 makes with the direction of M in OF is related to its production angle $\theta^{'}$ in RF through:

$$
tan(\theta) = \frac{sin(\theta^{'})}{\gamma^{'}(cos(\theta^{'}) + \frac{E^{'}_1 \beta^{'}}{p^{'}_1})} \qquad \text{(B.22)}
$$

The same applies for angle ϕ.

B.3 Kinematics of Three-Body Particle Decay

Let us consider a particle reaction when a "mother" particle of rest mass M decays into three particles with rest masses m_1, m_2 and m_3. As in the case of the two-body decay (section B.2), we assume that M is moving in positive z direction in OF with energy E and momentum $\vec{p} = \vec{p}_z$. The four-momentum of initial particles in the OF is $P = (E, 0, 0, p)$. $P_1 = (E_1, p_{1x}, 0, p_{1z})$, $P_2 = (E_2, p_{2x}, 0, p_{2z})$ and $P_3 = (E_3, p_{3x}, 0, p_{3z})$ are four-momenta for the decay products (also see diagram a of Figure B.2). The momentum conservation implies that:

$$
\vec{p} = \vec{p}_1 + \vec{p}_2 + \vec{p}_3 \qquad \text{(B.23)}
$$

To simplify the problem, we go to the rest frame of particle M, where energy and momentum conservation laws require that:

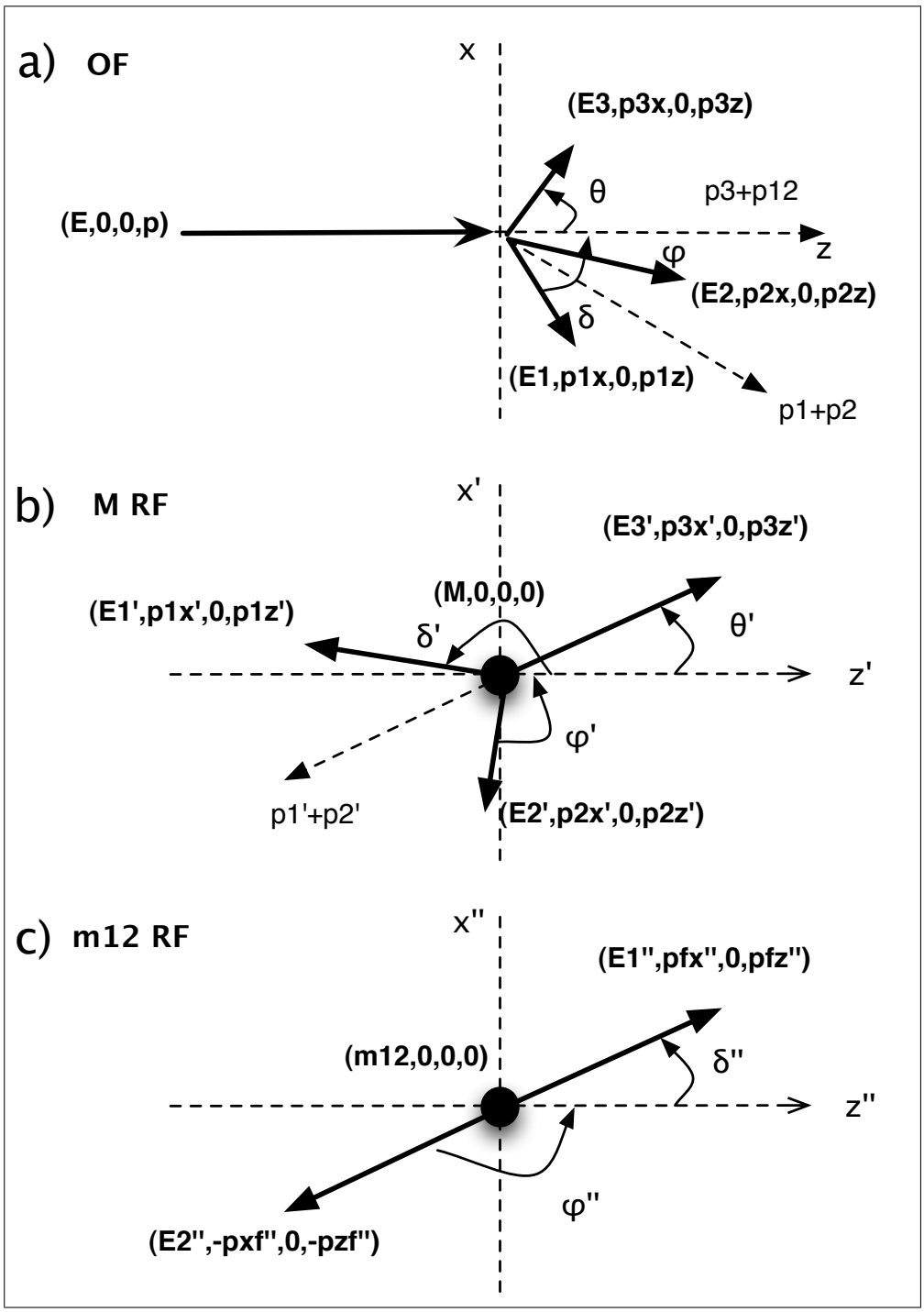

Figure B.2. Three-body decay diagram in different reference frames: a - observer's frame (OF), b - rest frame (RF) of M, c - rest frame (RF) of the $m_1 + m_2$ particle system.

$$M = E_1^{'} + E_2^{'} + E_3^{'} \tag{B.24}$$

$$0 = \vec{p}_1^{\,'} + \vec{p}_2^{\,'} + \vec{p}_3^{\,'} \tag{B.25}$$

Energy conservation B.24 allows the decay if

$$M \geq m_1 + m_2 + m_3 \tag{B.26}$$

Unlike the two-body decay, in case of three-body decay there are limits on the available energies among the three decay particles. We first explore the motivation for these limits in the RF of M. The least energy that a particle m_3 can have is when it is produced at rest

$$E_{3_{min}}^{'} = m_3 \tag{B.27}$$

$$p_{3_{min}}^{'} = 0 \tag{B.28}$$

Then the energy available for the $m_1 + m_2$ system is equal to $E_{12} = M - m_3$ and the problem reduces to the two-body decay problem considered in section B.2. Then the particle energies can be found according to B.15:

$$E_{1(2)}^{'} = \frac{(M - m_3)^2 + m_{1(2)}^2 - m_{2(1)}^2}{2(M - m_3)} \tag{B.29}$$

The greatest energy of m_3 is achieved when the energy of the particle system $m_1 + m_2$ is the least. Thus applying equation B.15:

$$E_{3_{max}}^{'} = \frac{M^2 + m_3^2 - (m_1 + m_2)^2}{2M} \tag{B.30}$$

The maximum momentum of the decay particle is

$$p_{3_{max}}^{'} = \frac{\sqrt{(M^2 - (m_1 + m_2 + m_3)^2)(M^2 - (m_1 + m_2 - m_3)^2)}}{2M} \tag{B.31}$$

The energies of m_1 and m_2 particles can be found by considering that

$$E_1^{'} + E_2^{'} = M - E_{3_{max}}^{'} \tag{B.32}$$

and

$$E_1^{'} + E_2^{'} = \gamma^{'}(m_1 + m_2) = \gamma^{'} m_1(1 + \frac{m_2}{m_1}) = E_1^{'}(1 + \frac{m_2}{m_1}) \tag{B.33}$$

Finally for the energy of m_1 and m_2 in case of the maximum energy of particle 3, we have

$$E_{1(2)}^{'} = \frac{m_1(M - E_{3_{max}}^{'})}{m_1 + m_2} \tag{B.34}$$

Now assuming that $E_3^{'}$ lies in the permitted range of allowed values ($E_{3_{min}}^{'} \leq E_3^{'} \leq E_{3_{max}}^{'}$), we need to find what the values for $E_1^{'}$ and $E_2^{'}$ are. As the first step, we consider the system of particles 1 and 2. The invariant mass of $1 + 2$ system in the M rest frame is given by:

$$\begin{aligned}
s_{12} &= (P_{12}^{'})^2 \\
&= m_{12}^2 \\
&= (P^{'} - P_3^{'})^2 \\
&= (E^{'} - E_3^{'})^2 - (\vec{p}^{\,'} - \vec{p}_3^{\,'}) \\
&= M^2 + E_3^{'2} - 2ME_3^{'} - \vec{p}_3^{\,'2} \\
&= M^2 + (E_3^{'2} - \vec{p}_3^{\,'2}) - 2ME_3^{'} \\
&= M^2 + m_3^2 - 2ME_3^{'}
\end{aligned} \tag{B.35}$$

The energy and momentum of the 1+2 system in the rest frame of initial particles are

$$E_{12}^{'} = M - E_3^{'} \tag{B.36}$$

$$p_{12}^{'} = \sqrt{E_{12}^{'} - m_{12}^2} \tag{B.37}$$

To find the values for $E_1^{'}$ and $E_2^{'}$ we need to go to the rest frame of the $m_1 + m_2$ system. All the quantities in this system will be denoted double double prime. The Lorentz factor to go from the M rest frame to $m_1 + m_2$ rest frame is:

$$\gamma^{''} = \frac{E_{12}^{'}}{m_{12}} \tag{B.38}$$

In this reference frame, a hypothetical particle m_{12}, which is initially at rest, is decaying into two particle m_1 and m_2 according to the laws of the two-body decay process.

Thus, it is straightforward to find the energies and momenta of the decay particles in m_{12} rest frame.

$$E^{''}_{1(2)} = \frac{s_{12} + m^2_{1(2)} - m^2_{2(1)}}{2\sqrt{s_{12}}} \tag{B.39}$$

and

$$p^{''}_{12} = \sqrt{E^{''}_{12} - m^2_{12}} \tag{B.40}$$

Since the decay is isotropic, we can choose a random production angle $\delta^{''} = 180^{\circ} + \phi^{''}$ (see plot c in Figure B.2). Now in order to go back to the M rest frame, we have to apply the inverse Lorentz transformation according to B.9:

$$\begin{aligned} E^{'}_{1(2)} &= \gamma^{''}(E^{''}_{1(2)} + (-)\beta^{''} p^{''}_{1(2)} cos(\delta^{''})) \\ p^{'}_{1(2)z} &= \gamma^{''}(p^{''}_{1(2)} cos(\delta^{''}) + (-)\beta^{''} E^{''}_{1(2)}) \\ p^{'}_{1(2)x} &= p^{''}_{1(2)} sin(\delta^{''}) \\ p^{'}_{1(2)} &= \sqrt{p^{'2}_{1(2)x} + p^{'2}_{1(2)z}} \end{aligned} \tag{B.41}$$

And the production angles m_1, m_2 and m_3 in M RF are found by

$$\delta^{'} = cos^{-1}\left(\frac{p^{'}_1}{p^{'}_{1z}}\right) \tag{B.42}$$

$$\phi^{'} = cos^{-1}\left(\frac{p^{'}_2}{p^{'}_{2z}}\right) \tag{B.43}$$

$$\theta^{'} = cos^{-1}\left(\frac{p^{'}_3}{p^{'}_{3z}}\right) \tag{B.44}$$

and $\vec{p}^{\,'}_{3z} = -(\vec{p}^{\,'}_{1z} + \vec{p}^{\,'}_{2z})$. There is one final step left. This step is to go from the M RF to OF by applying inverse Lorentz transforms with $\gamma^{'} = E/M$.

$$\begin{aligned} E_i &= \gamma^{'}(E^{'}_i + \beta^{'} p^{'}_{iz}) \\ p_{iz} &= \gamma^{'}(p^{'}_{iz} + \beta^{'} E^{'}_i) \\ p_{ix} &= p^{'}_{ix} \\ p_i &= \sqrt{p^2_{ix} + p^2_{iz}} \end{aligned} \tag{B.45}$$

where $i = 1, 2, 3$.

B.4 Kinematics of Particle Collisions

Consider a particle m_1 with energy E_1 and momentum $\vec{p}_1$ colliding with a particle m_2, having energy E_2 and momentum $\vec{p}_2$ in the observer's reference frame. θ is the angle between the directions of propagation of the particles. As a result of the interaction, two new particles are produced: m_3 at angle ϕ and m_4 at an angle δ. Refer to plot a of Figure B.3.

$$P_1(E_1,0,0,p_1)\ P_2(E_2,p_{x2},0,p_{z2}) \longrightarrow P_3(E_3,p_{x3},0,p_{z3})\ P_4(E_4,p_{x4},0,p_{z4}) \tag{B.46}$$

P_i is the four-momentum of $i-th$ particle with energy E_i and momentum p_i. In the case of the two-body collision, we can define the Lorentz-invariant Mandelstam variables by the following equations:

$$s = (P_1+P_2)^2 = (P_3+P_4)^2 = m_1^2+m_2^2+2E_1E_2-2\vec{p}_1\cdot\vec{p}_2 \tag{B.47a}$$

$$t = (P_1-P_3)^2 = (P_2-P_4)^2 = m_1^2+m_3^2-2E_1E_3+2\vec{p}_1\cdot\vec{p}_3 \tag{B.47b}$$

$$u = (P_1-P_4)^2 = (P_2-P_3)^2 = m_1^2+m_4^2-2E_1E_4+2\vec{p}_1\cdot\vec{p}_4 \tag{B.47c}$$

and they satisfy

$$s+t+u = m_1^2+m_2^2+m_3^2+m_4^2 \tag{B.48}$$

It is more convenient to work in the reference frame where one of the particles is at rest. In the rest frame of the first particle (see diagram b of Figure B.3), we have:

$$P_1^{'}(m_1,0,0,0)\ P_2^{'}(E_2^{'},p_{x2}^{'},0,p_{z2}^{'}) \longrightarrow P_3^{'}(E_3^{'},p_{x3}^{'},0,p_{z3}^{'})\ P_4^{'}(E_4^{'},p_{x4}^{'},0,p_{z4}^{'}) \tag{B.49}$$

The total four-momentum of initial particles is the sum of the momenta of individual particles ($P^{'} = P_1^{'}+P_2^{'}$). The Lorentz invariant length of the four-momentum in the case of two initial particles is $s = (P_1^{'}+P_2^{'})^2 = (E_1+E_2)^2-(\vec{p_1}+\vec{p_2})^2$.

In the RF of particle 1, according to equation B.47a, invariant mass of the system before interaction is:

$$s = m_1^2+m_2^2+2m_1E_2^{'} \tag{B.50}$$

or by rearranging the terms in equation B.50, the energy of the second particle in the reference frame of the first is easily found by:

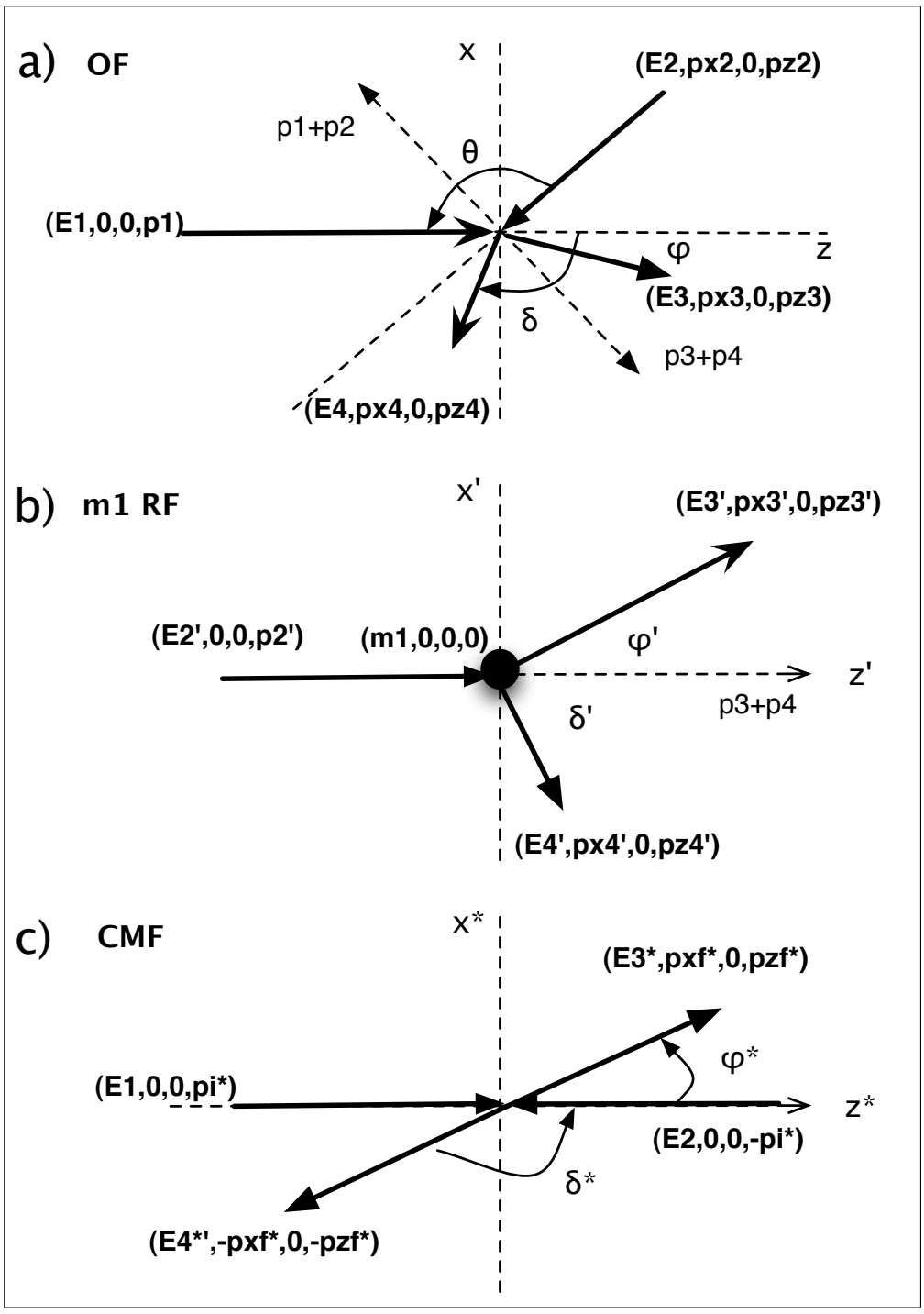

Figure B.3. Diagram of particle collision in different reference frames: a - observer's frame (OF), b - rest frame (RF) of m_1, c - center of mass frame (CMF).

$$E_2^{'} = \frac{s - m_1^2 - m_2^2}{2m_1} \tag{B.51}$$

and hence, substituting $E_2^{'} = \sqrt{p_2^{'} + m_2^2}$ and solving for $p_2^{'}$ we get

$$p_2^{'} = \frac{1}{2m_1}\left[(s - (m_1 - m_2)^2)(s - (m_1 + m_2)^2)\right]^{1/2} \tag{B.52}$$

It can be shown that the energies for the particles 3 and 4 are expressed through:

$$E_3^{'} = \frac{m_1^2 + m_3^2 - t}{2m_1} \tag{B.53}$$

$$E_4^{'} = \frac{m_1^2 + m_4^2 - u}{2m_1} \tag{B.54}$$

t and u are Lorentz-invariant Mandelstam variables defined by B.47b and B.47c.

The production angles of the emerging particles satisfy the following relationships:

$$cos(\phi^{'}) = \frac{u - m_2^2 - m_3^2 + 2E_2^{'}E_3^{'}}{2\vec{p}_2^{\,'}\vec{p}_3^{\,'}} \tag{B.55}$$

$$cos(\delta^{'}) = \frac{t - m_2^2 - m_4^2 + 2E_2^{'}E_4^{'}}{2\vec{p}_2^{\,'}\vec{p}_4^{\,'}} \tag{B.56}$$

In the CMF both incoming particles have equal none zero momentum, pointing in opposite directions ($\vec{p}_1{}^* + \vec{p}_2{}^* = 0$ or $|\vec{p}_1{}^*| = |\vec{p}_2{}^*| = p_i^*$). The same applies for the outgoing particles (($\vec{p}_3{}^* + \vec{p}_4{}^* = 0$ or $|\vec{p}_3{}^*| = |\vec{p}_4{}^*| = p_f^*$)

$$P_1^*(E_1^*, 0, 0, p_i^*)\ P_2^*(E_2^*, 0, 0, p_i^*) \longrightarrow P_3^*(E_3^*, p_{xf}^*, 0, p_{zf}^*)\ P_4^*(E_4^*, p_{xf}^*, 0, p_{zf}^*) \tag{B.57}$$

The expression for invariant mass in CMF is:

$$s = (E_1^* + E_2^*)^2 \tag{B.58}$$

According to B.3, the energies of the two particles in the CMF are $E_1^* = \sqrt{m_1^2 + p^{*2}}$ and $E_2^* = \sqrt{m_2^2 + p^{*2}}$. Substituting this expressions into equation B.58 and solving for p^* we get

$$p_i^* = \frac{1}{2\sqrt{s}}\left[(s - (m_1 - m_2)^2)(s - (m_1 + m_2)^2)\right]^{1/2} \tag{B.59a}$$

The energies of the original particles in the CMF can be found as:

$$E^*_{1,2} = \frac{s + m^2_{1,2} - m^2_{2,1}}{2\sqrt{s}} \tag{B.59b}$$

The final momenta of the particles m_3 and m_4 produced as the result of this interaction in CMF and their energies are

$$p^*_f = \frac{1}{2\sqrt{s}} \left[(s - (m_3 - m_4)^2)(s - (m_3 + m_4)^2) \right]^{1/2} \tag{B.60a}$$

$$E^*_{3,4} = \frac{s + m^2_{3,4} - m^2_{4,3}}{2\sqrt{s}} \tag{B.60b}$$

If ϕ^* is the angle between $\vec{p}_1{}^*$ and $\vec{p}_4{}^*$ (or $\vec{p}_2{}^*$ and $\vec{p}_3{}^*$), we have

$$cos(\phi^*) = 1 - \frac{u - u_0}{2\vec{p}_1{}^*\vec{p}_4{}^*} = 1 - \frac{t_0 - t}{2\vec{p}_1{}^*\vec{p}_3{}^*} \tag{B.61}$$

where $u_0 = m^2_1 + m^2_4 - 2(E^*_1 E^*_4 + \vec{p}_1{}^*\vec{p}_4{}^*) = m^2_2 + m^2_3 - 2(E^*_2 E^*_3 + \vec{p}_2{}^*\vec{p}_3{}^*)$ and $t_0 = m^2_1 + m^2_3 - 2(E^*_1 E^*_3 - \vec{p}_1{}^*\vec{p}_3{}^*) = m^2_2 + m^2_4 - 2(E^*_2 E^*_4 - \vec{p}_2{}^*\vec{p}_4{}^*)$

Comparing equation B.52 with B.59a we find that

$$p^* = p_2^{'} \frac{m_{01}}{\sqrt{s}} \tag{B.62}$$

and hence

$$E^*_{1,2} = (m^2_{1,2} + m_1 E^{'}_2)/\sqrt{s} \tag{B.63}$$

In the ultra-relativistic case (when energies of the particles are much greater, than their rest masses), we get from equation B.50 and B.63

$$E^*_1 \approx E^*_2 \approx \sqrt{\frac{1}{2} m_1 E^{'}_2} \tag{B.64}$$

CMF energy grows as the square-root of the RF energy

We can also find the center of mass velocity of the initial particles in the rest frame of reference (the Lorentz boost from CMF to RF). The total energy of initial particles in the RF in terms of their energies and momenta in CMF is

$$\begin{aligned} \sqrt{s} &= m_1 + E^{'}_2 \\ &= \gamma^*(E^*_1 - \beta^* p^*_{1z}) + \gamma^*(E^*_2 - \beta^* p^*_{2z}) \end{aligned}$$

$$= \quad \gamma^* \left[E_1^* + E_1^* - \beta^*(p_{1z}^* + p_{2z}^*)\right] \tag{B.65}$$

Using that in the CMF $p_{1z}^* + p_{2z}^* = 0$ we get the relationships for γ^* and β^*

$$\gamma^* = \frac{m_1 + E_2^{'}}{E_1^* + E_1^*} = \frac{m_1 + E_2^{'}}{\sqrt{s}} \tag{B.66a}$$

and

$$\beta^* = \sqrt{1 - \frac{1}{\gamma^{*2}}} = \frac{p^*}{m_1 + E_2^{'}} \tag{B.66b}$$

It is more useful to find the relationship that relates particles energies and momenta in the observer reference frame to the corresponding parameters in the CMF. For that we have to use formulas B.8b and B.8c. Thus for any of the four particles that participate in the reaction $i = 1, 2, 3, 4$, we can write:

$$E_i = \gamma_i^*(E_i^* - \beta_i^* p_i^* cos(\theta^*)) \tag{B.67a}$$

and

$$p_i = \beta_i E_i \tag{B.67b}$$

Here θ^*, the angle between p_i^* and p_{xi}^*, transforms to ORF as $cos(\theta) = \frac{cos(\theta^*)+\beta^*}{1+\beta^* cos(\theta^*)}$ and $\gamma_i^* = \frac{E_{1(3)}+E_{2(4)}}{\sqrt{s}}$. Inserting B.59a and B.59b into B.67a results in:

$$E_i = (E_{1(3)} + E_{2(4)}) \left(\frac{s + m_i^2 - m_j^2}{2s} - \frac{\beta_i^*}{2s} \sqrt{(s - (m_i - m_j)^2)(s - (m_i + m_j)^2)} cos(\theta^*) \right) \tag{B.68}$$

if $i = 1, 2, 3, 4$, than $j = 2, 1, 4, 3$.

APPENDIX C

PHOTON OPTICAL DEPTH

This Appendix provides the derivation of general formulas of optical depth and corresponding survival probability for high energy photons traveling through blackbody CMB according to Ref. [89].

The process of the pair creation through the photon interaction on CMB this a very effective photon absorption mechanism, when we consider HE photon propagation over cosmological distances.

Let us consider a collision between a high energy photon E_γ and a low energy free CMB photon ϵ in the observer's reference frame, in which a gamma ray is moving along the positive z direction and a low-energy CMB photon is incident at an angle θ. As the result of this interaction, a electron-positron pair is created.

$$\gamma + \gamma_{cmb} \longrightarrow e^+ + e^- \tag{C.1}$$

The total cross section for this process is well known and given by [110]:

$$\sigma = \frac{1}{2}\pi r_0^2(1-\beta^2)\left[(3-\beta^4)ln\frac{1+\beta}{1-\beta} - 2\beta(2-\beta^2)\right] \tag{C.2}$$

where $r_0 = e^2/mc^2$ is the classical electron radius and β is the electron/positron velocity in the units of speed of light in the center of mass frame.

The Lorentz invariant mass suggests the following relationship between the photon and the electron energies:

$$2E_\gamma\epsilon(1-cos(\theta)) = 4E_e^{*2} \tag{C.3}$$

where E_e^* is the electron/proton energy in the CMF.

Following [89] we divide C.3 by $4m_e^2c^4$:

$$s = (E_e/m_ec^2)^2 = (\gamma_e)^2 = (E_\gamma\epsilon/2m_e^2c^4)(1-cos(\theta)) \tag{C.4}$$

We can rewrite $\beta = \sqrt{1-1/\gamma_e^2} = \sqrt{1-1/s}$

The threshold condition for pair production in case of head-on photon collision is $s = 1$ or:

$$E_\gamma \epsilon = 2m_e^2 c^4 \tag{C.5}$$

The absorption probability per unit path length dx for photons of energy E_γ passing through the isotropic photon gas is given by:

$$dP_{abs} = \frac{d\tau_{abs}}{dx} \tag{C.6}$$

where $d\tau_{abs}$ is the absorption "optical depth". The differential density of photons at energy ϵ moving in the differential cone at angle θ and within θ and $\theta + d\theta$ is:

$$dn = \frac{1}{2} n(\epsilon) sin(\theta) d\epsilon d\theta \tag{C.7}$$

with the number of photons per unit volume per unit of interval energy $n(\epsilon)$.

Taking into account the velocity of the low energy CMB photons on the direction of high energy photons in OF is $c(1 - cos(\theta))$, then the absorption probability per unit length is

$$\frac{d\tau_{abs}}{dx} = \int_{\frac{m_e^2 c^4}{E_\gamma}}^{\infty} \int_0^{2\pi} \frac{1}{2} \sigma n(\epsilon)(1 - cos(\theta)) sin(\theta) d\theta d\epsilon \tag{C.8}$$

It is convenient to change variables of integration from θ to s in C.8. Since $s = (E_\gamma \epsilon / 2m_e^2 c^4)(1 - cos(\theta))$, then $ds = (E_\gamma \epsilon / 2m_e^2 c^4)(sin(\theta) d\theta)$ and the absorption probability in the new variables takes the form:

$$\frac{d\tau_{abs}}{dx} = 2 \left(\frac{m_e^2 c^4}{E_\gamma} \right)^2 \int_{\epsilon_0}^{\infty} \int_{s_{min}}^{s_0(\epsilon)} \frac{\sigma n(\epsilon) s}{\epsilon^2} ds d\epsilon \tag{C.9}$$

where $s_0(\epsilon) = \frac{E_\gamma \epsilon}{m_e^2 c^4}$, $\epsilon_0 = \frac{m_e^2 c^4}{E_\gamma}$ and $s_{min} = 1$.

For the blackbody CMB radiation we have

$$n(\epsilon) = \frac{1}{\pi^2 (\hbar c)^3} \frac{\epsilon^2}{e^{\epsilon / kT} - 1} \tag{C.10}$$

Thus the photon absorption probability on the blackbody CMB is

$$\frac{d\tau_{abs}}{dx} = \frac{2}{\pi^2 (\hbar c)^3} \left(\frac{m_e^2 c^4}{E_\gamma} \right)^2 \int_{\epsilon_0}^{\infty} \int_1^{s_0(\epsilon)} \frac{\sigma s}{e^{\epsilon / kT} - 1} ds d\epsilon \tag{C.11}$$

If we define the dimensional cross section as $\sigma' = 2\sigma / \pi r_0^2 = (1 - \beta^2) \left[(3 - \beta^4) ln \frac{1+\beta}{1-\beta} - 2\beta(2 - \beta^2) \right]$, then the equation is modified to

$$\frac{d\tau_{abs}}{dx} = \frac{1}{\pi(\hbar c)^3}\left(\frac{r_0 m_e^2 c^4}{E_\gamma}\right)^2 \int_{\epsilon_0}^{\infty}\int_{1}^{s_0(\epsilon)} \frac{\sigma^{'} s}{e^{\epsilon/kT}-1} ds d\epsilon \tag{C.12}$$

We can further simplify this equation by introducing the dimensionless energy of the CMB photons $\epsilon^{'} = \epsilon/kT$:

$$\frac{d\tau_{abs}}{dx} = \frac{(r_0\nu)^2}{\pi}\left(\frac{kT}{\hbar c}\right)^3 \int_{\nu}^{\infty} \frac{\int_1^{\epsilon^{'}/\nu} \sigma^{'} s \; ds}{e^{\epsilon^{'}}-1} d\epsilon^{'} \tag{C.13}$$

where $\nu = \epsilon_0/kT = \frac{m_e^2 c^4}{E_\gamma kT}$.

According to C.13 the absorption probability is maximum for $\nu = 1$ or $E_\gamma = m_e^2 c^4/kT$ and small when $\nu << 1$ or $E_\gamma >> m_e^2 c^4/kT$.

APPENDIX D

CANDIDATES FOR NEUTRINO EVENTS IN HIRES DATA

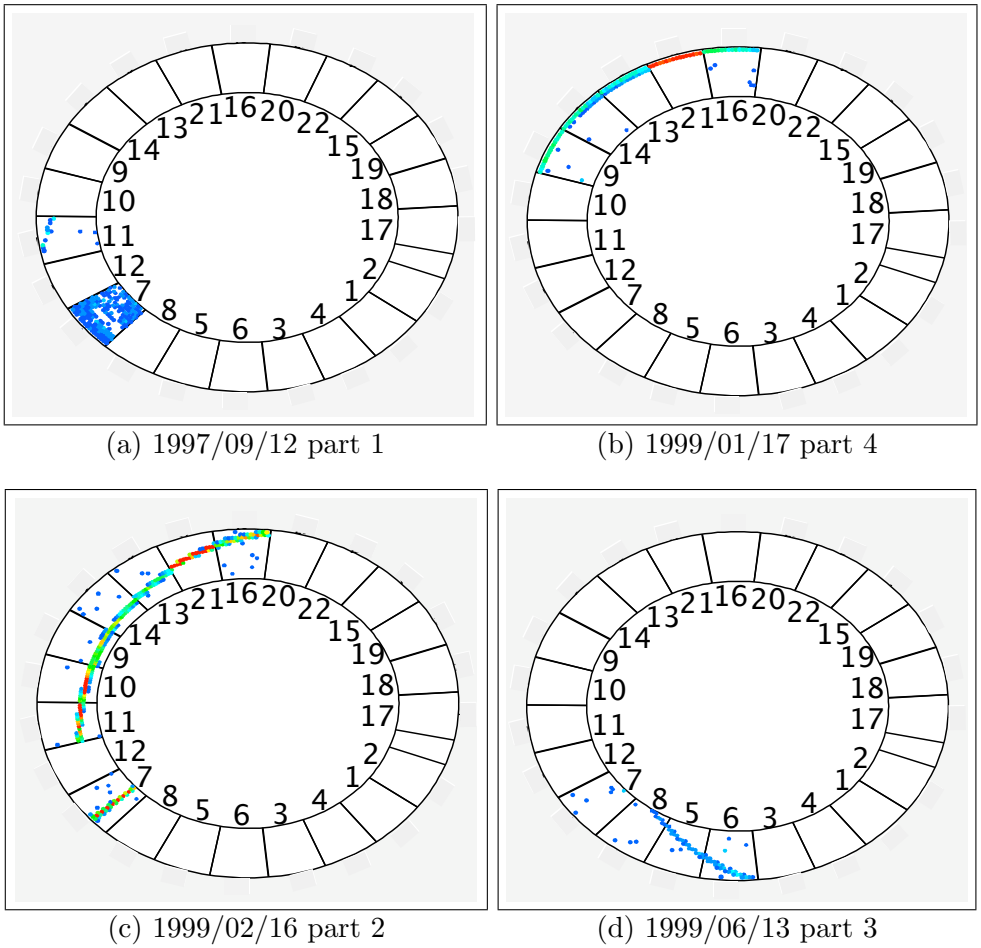

(a) 1997/09/12 part 1

(b) 1999/01/17 part 4

(c) 1999/02/16 part 2

(d) 1999/06/13 part 3

Figure D.1. HiRes-1 candidates for neutrino events: events 1-4.

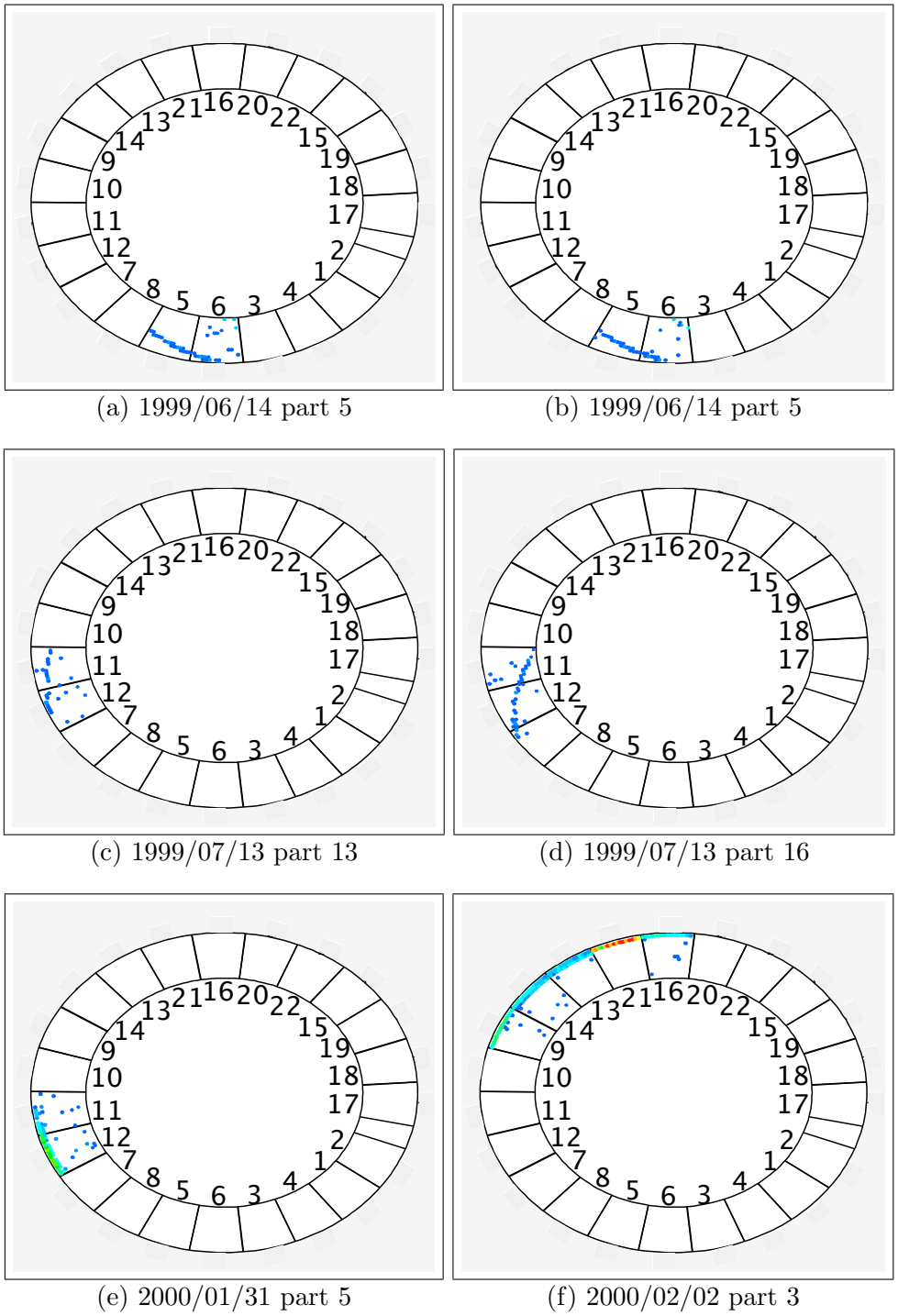

(a) 1999/06/14 part 5

(b) 1999/06/14 part 5

(c) 1999/07/13 part 13

(d) 1999/07/13 part 16

(e) 2000/01/31 part 5

(f) 2000/02/02 part 3

Figure D.2. HiRes-1 candidates for neutrino events: events 5-10.

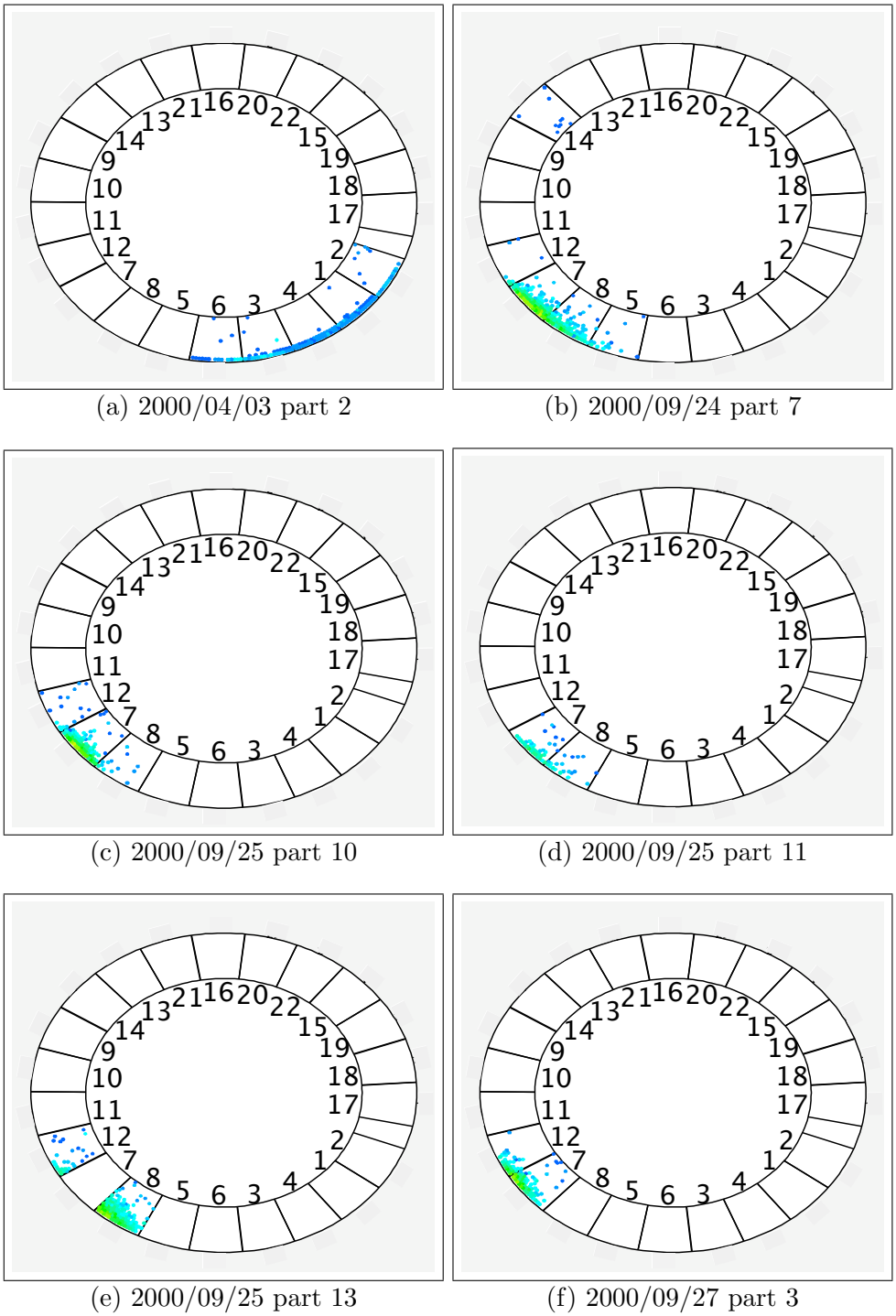

(a) 2000/04/03 part 2

(b) 2000/09/24 part 7

(c) 2000/09/25 part 10

(d) 2000/09/25 part 11

(e) 2000/09/25 part 13

(f) 2000/09/27 part 3

Figure D.3. HiRes-1 candidates for neutrino events: events 11-16.

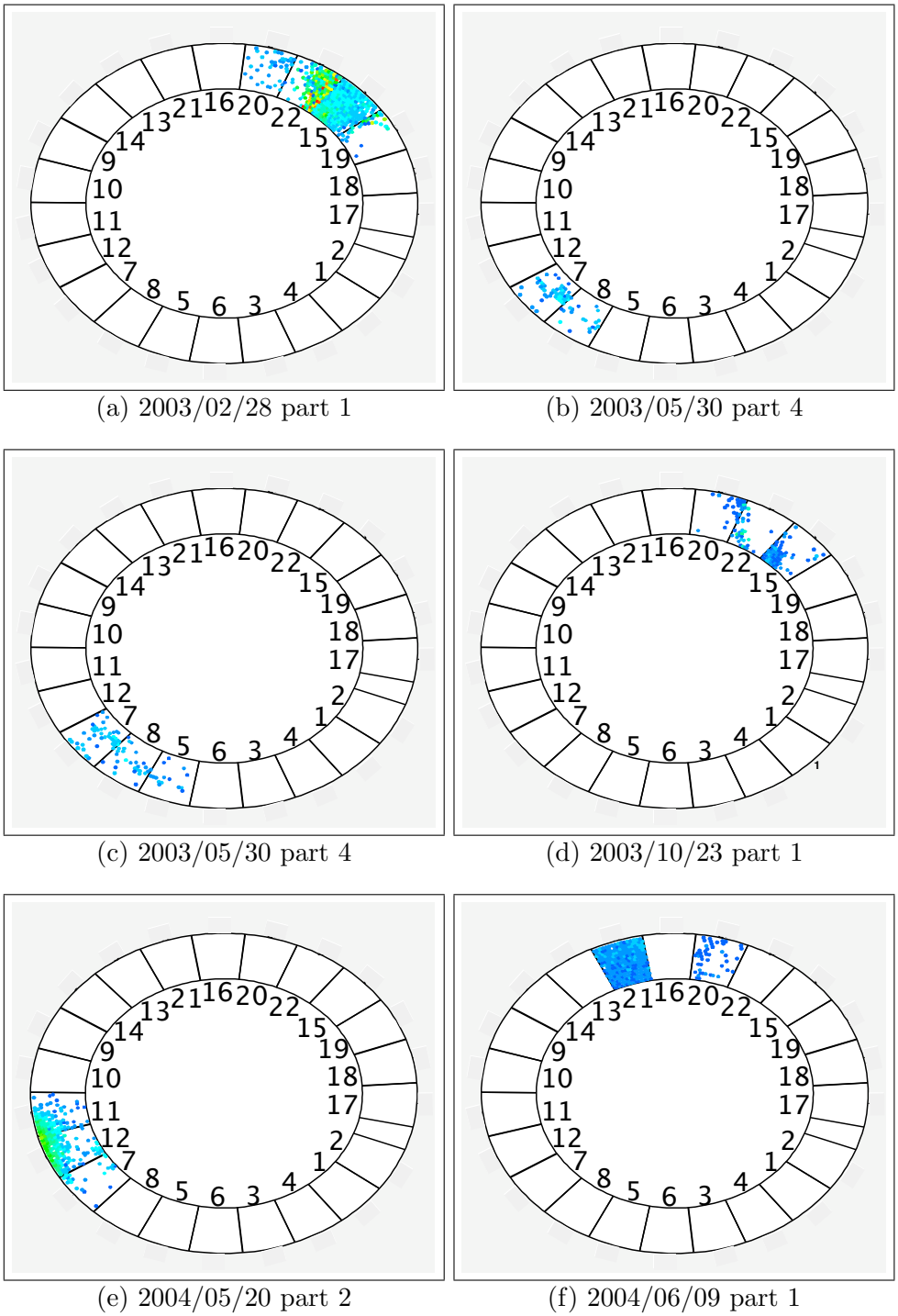

(a) 2003/02/28 part 1 (b) 2003/05/30 part 4

(c) 2003/05/30 part 4 (d) 2003/10/23 part 1

(e) 2004/05/20 part 2 (f) 2004/06/09 part 1

Figure D.4. HiRes-1 candidates for neutrino events: events 17-22.

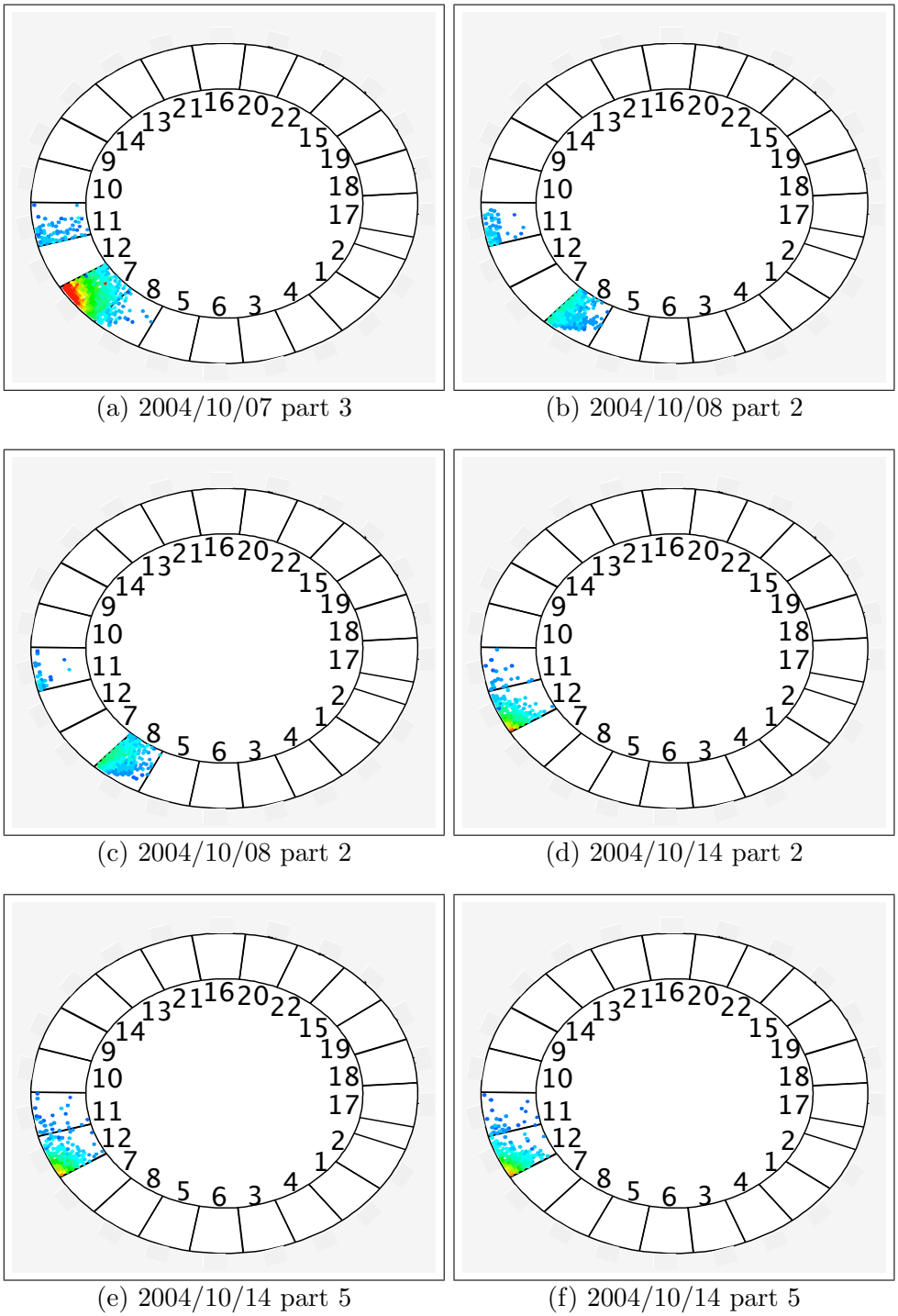

(a) 2004/10/07 part 3 (b) 2004/10/08 part 2

(c) 2004/10/08 part 2 (d) 2004/10/14 part 2

(e) 2004/10/14 part 5 (f) 2004/10/14 part 5

Figure D.5. HiRes-1 candidates for neutrino events: events 23-28.

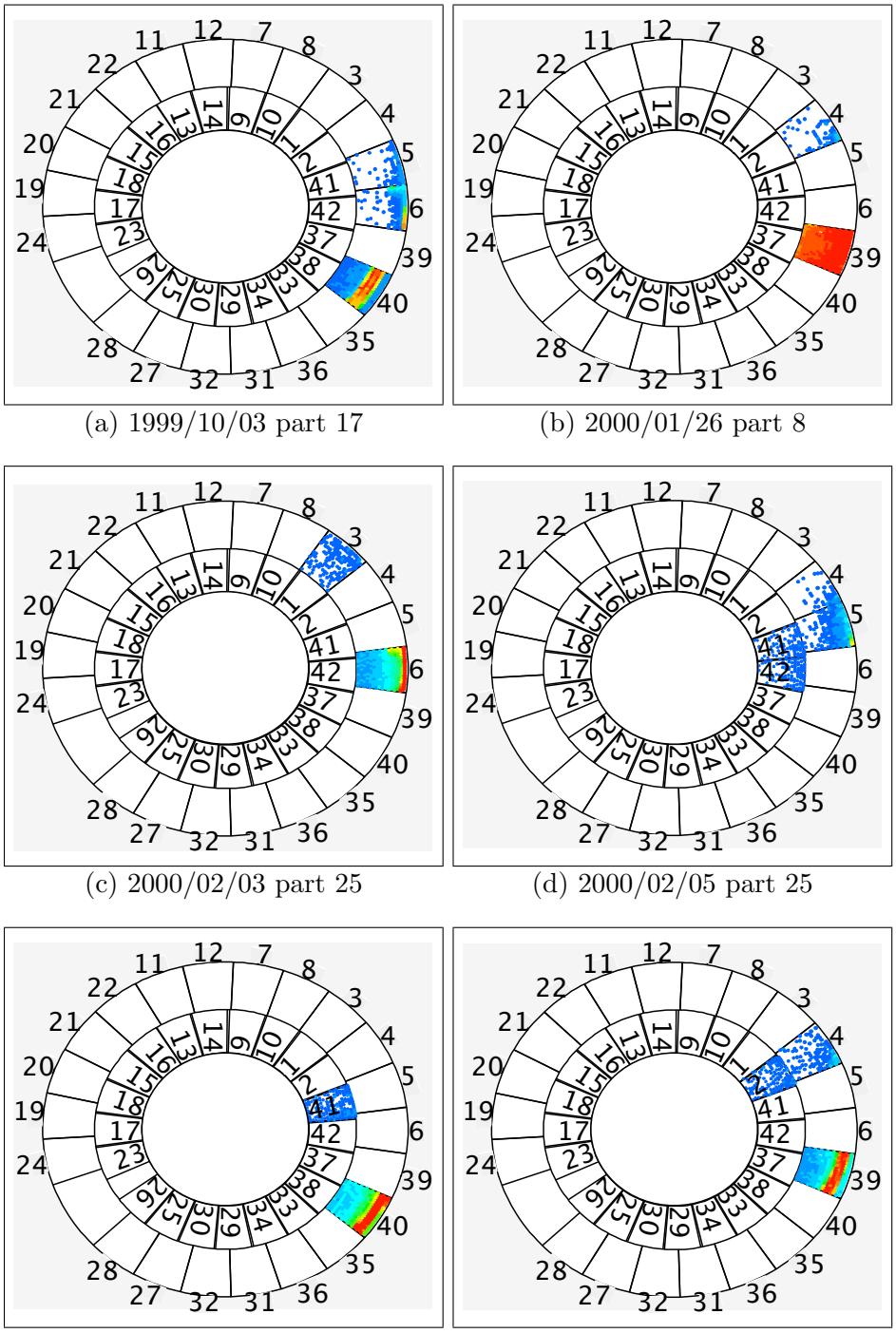

(a) 1999/10/03 part 17

(b) 2000/01/26 part 8

(c) 2000/02/03 part 25

(d) 2000/02/05 part 25

(e) 2000/02/07 part 12

(f) 2000/02/07 part 18

Figure D.6. HiRes-2 candidates for neutrino events: events 1-6.

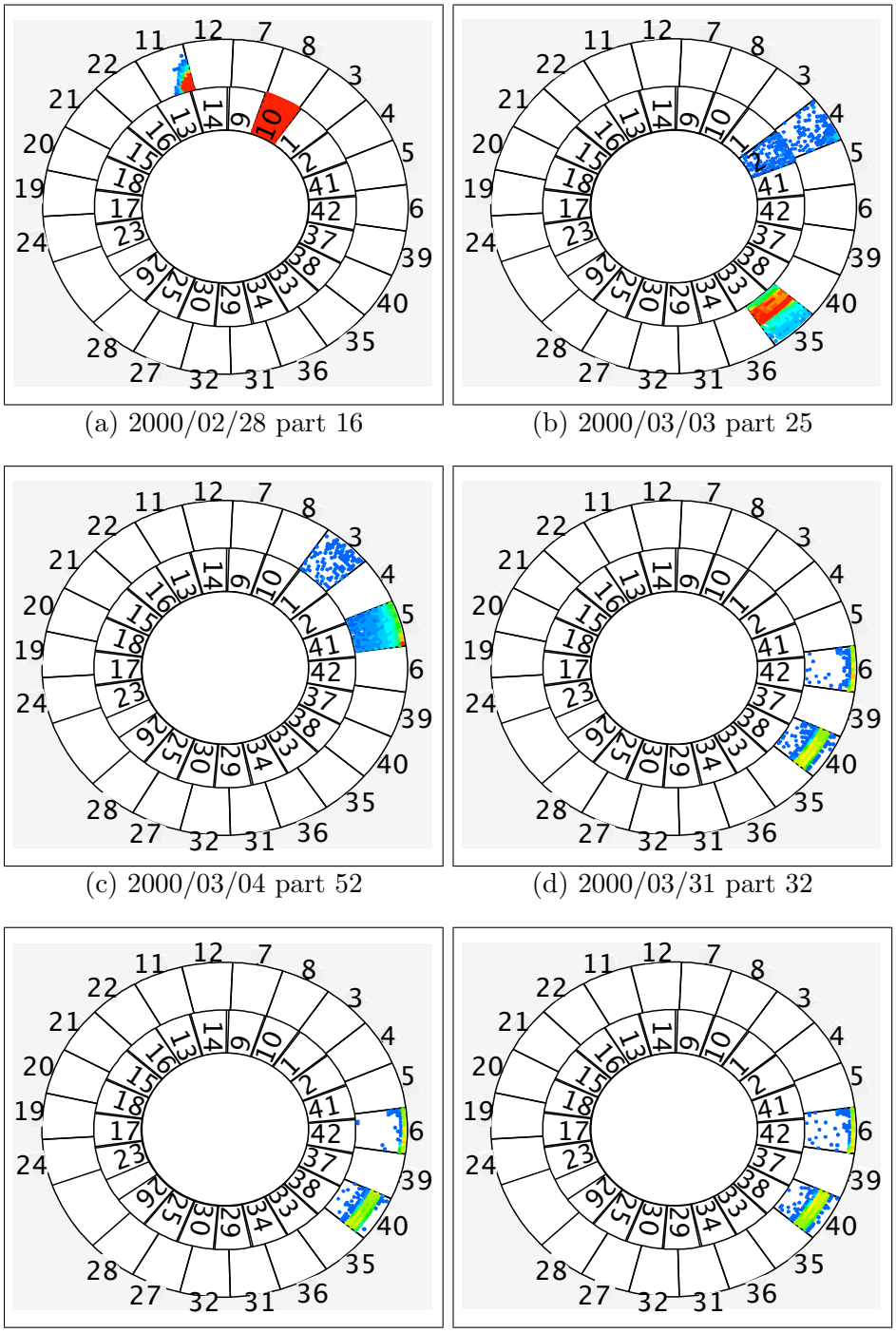

(a) 2000/02/28 part 16

(b) 2000/03/03 part 25

(c) 2000/03/04 part 52

(d) 2000/03/31 part 32

(e) 2000/04/04 part 31

(f) 2000/04/08 part 9

Figure D.7. HiRes-2 candidates for neutrino events: events 7-12.

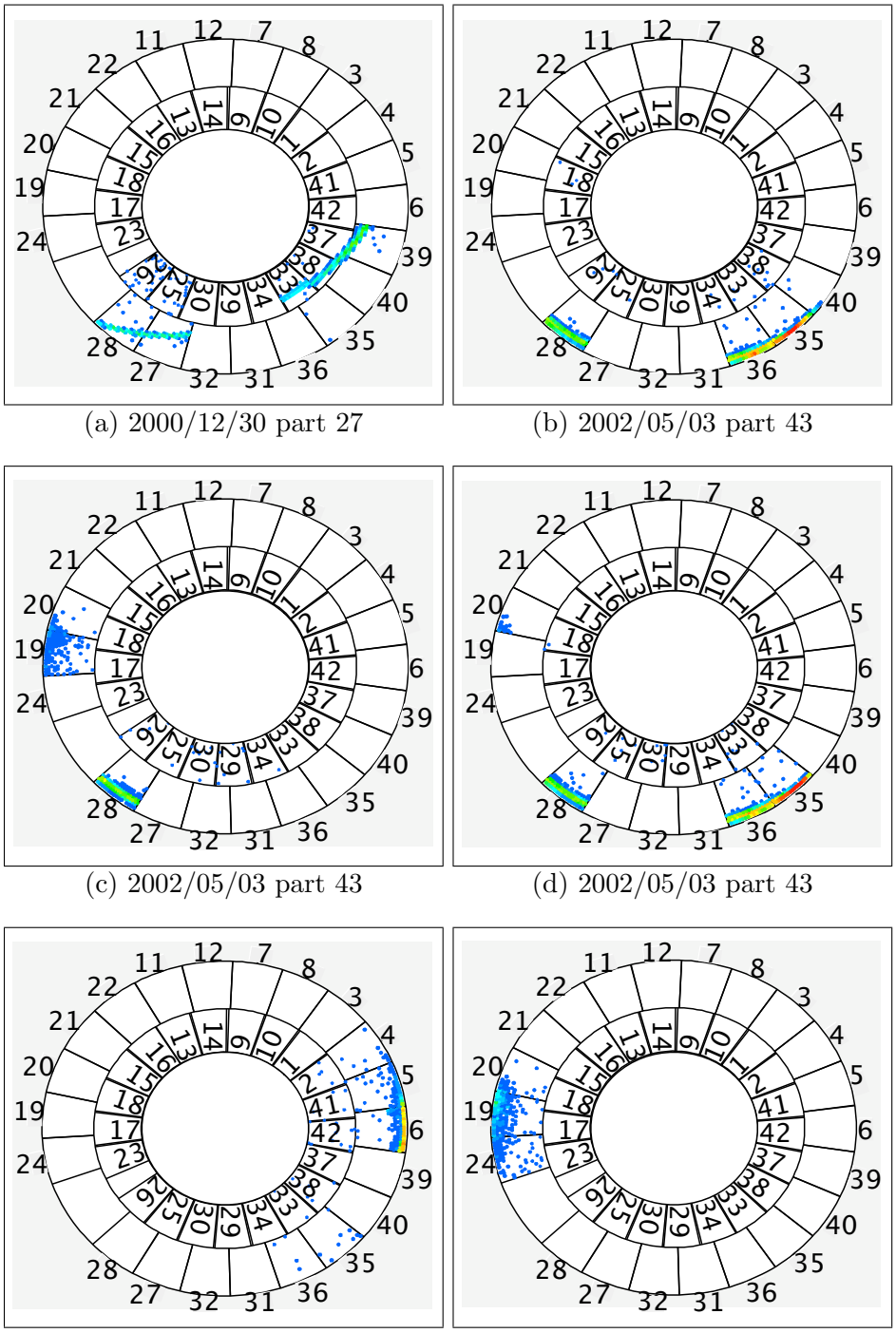

(a) 2000/12/30 part 27

(b) 2002/05/03 part 43

(c) 2002/05/03 part 43

(d) 2002/05/03 part 43

(e) 2002/07/08 part 21

(f) 2003/04/29part 19

Figure D.8. HiRes-2 candidates for neutrino events: events 13-18.

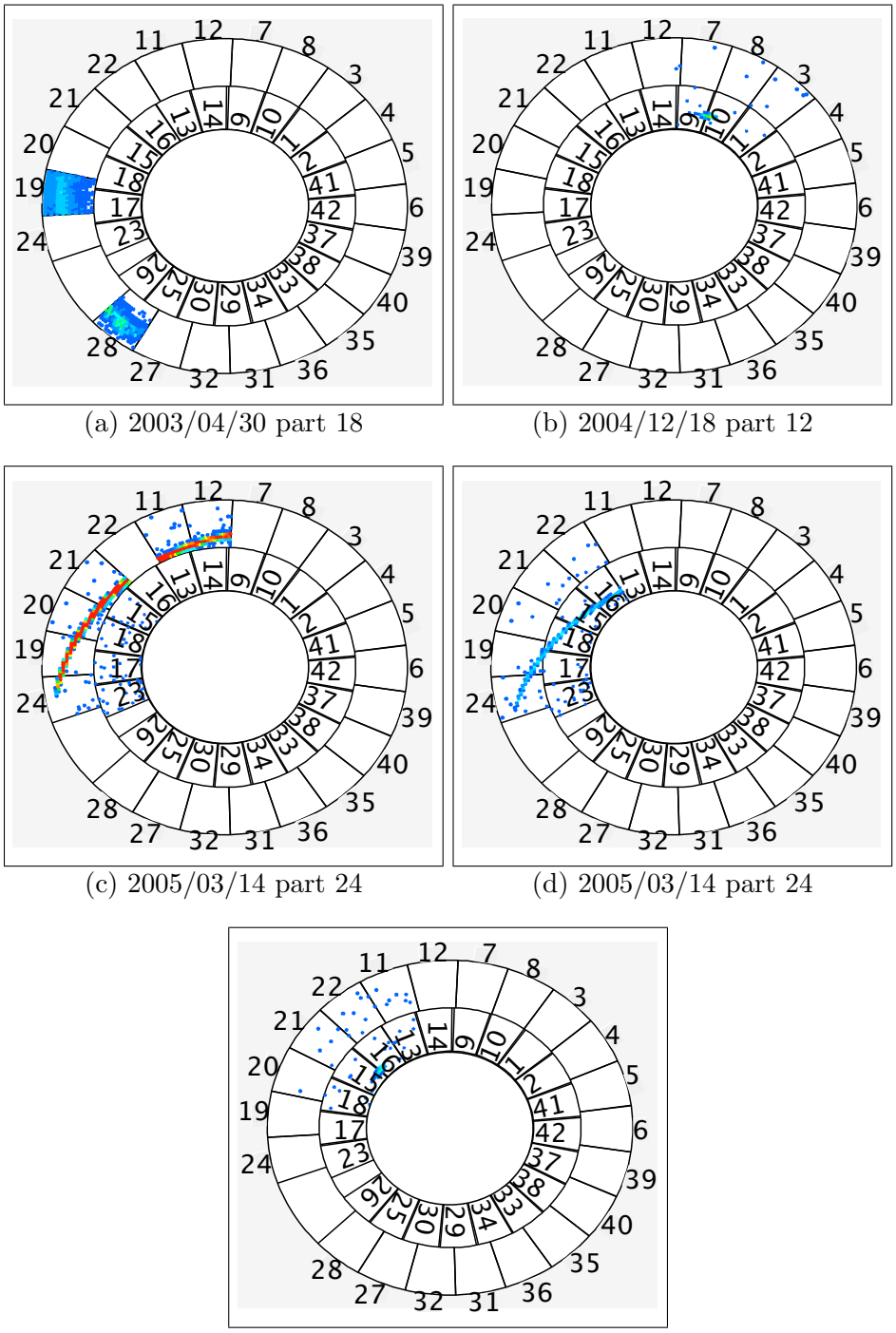

(a) 2003/04/30 part 18

(b) 2004/12/18 part 12

(c) 2005/03/14 part 24

(d) 2005/03/14 part 24

(e) 2006/02/03 part 18

Figure D.9. HiRes-2 candidates for neutrino events: events 19-23.

REFERENCES

[1] http://wwwasd.web.cern.ch/wwwasd/lhc++/clhep/. CLHEP - A Class Library for High Energy Physics.

[2] . Global 30 Arc-Second Elevation (GTOPO30).

[3] *Nobel Lectures, Physics 1922-1941.* Elsevier Publishing Company, Amsterdam, 1965.

[4] R. U. Abbasi et al. Measurement of the flux of ultrahigh energy cosmic rays from monocular observations by the High Resolution Fly's Eye experiment. *Phys. Rev. Lett.*, 92(15):151101, 2004. arXiv:astro-ph/0208243v7.

[5] R. U. Abbasi et al. Monocular measurement of the spectrum of UHE cosmic rays by the FADC detector of the HiRes experiment. *Astropart. Phys.*, 23(2):157–174, 2005.

[6] R. U. Abbasi et al. Observation of the ankle and evidence for a high-energy break in the cosmic ray spectrum. *Phys. Lett.*, B619:271–280, 2005.

[7] R. U. Abbasi et al. A study of the composition of ultra high energy cosmic rays using the High Resolution Fly's Eye. *Astrophys. J.*, 622(2):910–926, 2005. arXiv:astro-ph/0407622v3.

[8] R. U. Abbasi et al. An upper limit on the electron-neutrino flux from the HiRes detector. *Astrophys. J.*, 684:790–793, 2008. arXiv:0803.0554v2.

[9] R. U. Abbasi et al. First observation of the Greisen-Zatsepin-Kuzmin suppression. *Phys. Rev. Lett.*, 100:101101, 2008. arXiv:astro-ph/0703099v2.

[10] J. Abraham et al. *Science*, 318:938, 2007.

[11] J. Abraham, G. Snow, et al. Upper limit on the diffuse flux of ultrahigh energy tau neutrinos from the Pierre Auger observatory. *Phys. Rev. Lett.*, 100:211101, 2008.

[12] T. Abu-Zayyad et al. The prototype high-resolution Fly's Eye cosmic ray detector. *Nucl. Inst. Meth. Sect. A*, 450(2-3):253–269, August 2000.

[13] T. Abu-Zayyad et al. Measurement of the cosmic ray energy spectrum and composition from 10^{17} to $10^{18.3}$ eV using a hybrid fluorescence technique. *Astrophys. J.*, 557:686–699, 2001. arXiv:astro-ph/0010652v1.

[14] T. Z. AbuZayyad. *The Energy Spectrum of Ultra High Energy Cosmic Rays.* PhD thesis, University of Utah, 2000.

[15] A. Achterberg, Y. Gallant, C. A. Norman, and D. B. Merlose. Intergalactic propagation of the cosmic rays. *Astron. Astrophys.*, (Mon. Not. R. Astron. Soc.), 2008. arXiv:astro-ph/9907060v1.

[16] M. Ackermann et al. Search for ultra high-energy neutrinos with AMANDA-II. *Astrophys. J.*, 675:1014, 2008. arXiv:0711.3022v1.

[17] Afanasiev et al. In M. Nagano, editor, *Proceedings Int. Symposium of Extremely High Energy Cosmic Rays: Astrophysics and Future Observatories*, page 32, Institute for Cosmic Ray Research, Tokyo, 1996.

[18] M. Aglietta et al. *Astropart. Phys.*, 27:244, 2007. arXiv:astro-ph/0607382.

[19] F. A. Aharonian and J. W. Cronin. Influence of the universal microwave background radiation on the extragalactic cosmic-ray spectrum. *Phys. Rev. D*, 50:1892–1900, 1994.

[20] J. Ahrens et al. Sensitivity of the IceCube detector to astrophysical sources of high energy muon neutrinos. *Astropart. Phys.*, 20(5):507–532, February 2004.

[21] H. R. Allan. Radio emission from extensive air showers. *Progress in Elementary Particle and Cosmic Ray Physics*, 10:169–302, 1971.

[22] D. Allard, M. Ave, N. Busca, M. A. Malkan, A. V. Olinto, E. Parizot, F. W. Stecker, and T. Yamamoto. Cosmogenic neutrinos from the propagation of ultra high energy nuclei. *Journal of Cosmology and Astroparticle Physics*, 0609:005, 2005. arXiv:astro-ph/0605327v2.

[23] S. W. Allen, R. W. Schmidt, and A. C. Fabian. Cosmological constraints from the X-ray gas mass fraction in relaxed lensing clusters observed with Chandra. *Monthly Notices of the Royal Astronomical Society*, 334(2):L11–L15, 2002.

[24] L. A. Anchordoqui, D. Hooper, S. Sarkar, and A. M. Taylor. High-energy neutrinos from astrophysical accelerators of cosmic ray nuclei. *Astropart. Phys.*, 29:1–13, 2008. arXiv:astro-ph/0703001v4.

[25] C. D. Anderson. The apparent existence of easily deflectable positives. *Science*, 76(1967):238–239, September 1932.

[26] E. Andres. The AMANDA neutrino telescope: principle of operation and first results. *Astropart. Phys.*, 13:1–20, 2000. arXiv:astro-ph/9906203v1.

[27] A. V. Apanasenko et al. Primary cosmic ray spectra observed by RUNJOB - proton and alpha spectra. In M. Salamon D. Kieda and B. Dingus, editors, *Proceedings of the* 26^{th} *International Cosmic Ray Conference*, volume 3, page 163, Salt Lake City, Utah, USA, August 1999.

[28] E. Armengaud, G. Sigl, T. Beau, and F. Miniati. CRPropa: a numerical tool for the propagation of UHE cosmic rays, gamma-rays and neutrinos. *Astropart. Phys.*, 28:463–471, 2007. arXiv:astro-ph/0603675v2.

[29] S. Yoshida at al. *Astropat. Phys.*, 3(The Cosmic Ray Energy Spectrum above 3×10^{18} eV measured by the Akeno Giant Air Shower Array):105–124, 1995.

[30] W. Au, J. Boyer, Y. Chi, Y. Ho, W. Lee, et al. Description and status of the High Resolution (HiRes) Fly's Eye experiment. In *Proceedings of the* 22^{th} *International Cosmic Ray Conference*, volume 2, pages 692–695, Dublin, 1991.

[31] P. Auger, R. Maze, and J. Robley. *C. R. Acad. Sci. Paris*, 208:1641, 1938.

[32] M. Ave, N. Busca, A. V. Olinto, A. A. Watson, and T. Yamamoto. Cosmogenic neutrinos from ultra-high energy nuclei. *Astropart. Phys.*, 23:19–29, 2005. arXiv:astro-ph/0409316v2.

[33] A. Baldini, V. Flaminio, W. G. Moorhead, and D. R. O. Morrison. *Total Cross Sections for Reactions of High Energy Particles*. Springer, Berlin, 1988.

[34] V. A. Balkanov et al. An upper limit on the diffuse flux of high energy neutrinos obtained with the Baikal detector NT-96. *Astropart. Phys.*, 14(2):61–66, September 2000.

[35] R. M. Baltrusaitis, R. Cady, G. L. Cassiday, R. Cooper, J. W. Elbert, et al. The Utah Fly's Eye detector. *Nuclear Instruments and Methods in Physics Research*, 240(A):410–428, 1985.

[36] R. M. Baltrusaitis, G. L. Cassiday, P. R. Gerhardy, E. C. Loh, Y. Mizumoto, P. Sokolsky, and D. Steck. Limits on the deeply penetrating particles in the ¿ 10^{17} eV cosmic-ray flux. *Phys. Rev. D*, 31(9):2192–2198, 1985.

[37] H. Becquerel. On the invisible radiation emitted by phosphorescent substances. *C. R. Acad. Sci. Paris*, 122:501, 1896.

[38] K. V. Belov. *Proton-Air Inelastic Cross-Section at the Energies above* 10^18 *eV*. PhD thesis, University Of Utah, 2005.

[39] J. Bennett, M. Donahue, N. Schneider, and M. Voit. *The Cosmic Perspective, 2nd Edition*. Addison Wesley, 2002.

[40] V. Berezinsky. Ultra high energy cosmic rays. *Nucl. Phys. Proc. Suppl.*, 70:419, 1999.

[41] V. S. Berezinsky and S. I. Grigorieva. *Astron. Astrophys.*, 1:199, 1988.

[42] V. S. Berezinsky, S. I. Grigorieva, and G. T. Zatsepin. *Astrophys. Space. Sci.*, 36:3, 1975.

[43] H. E. Bergeson et al. Measurement of light emission from remote cosmic-ray air showers. *Phys. Rev. Lett.*, 39(13):847–849, 1977.

[44] D. R. Bergman. Fitting the HiRes spectra and monocular composition. *Nucl. Phys. Proc. Suppl.*, 136:40–45, 2004. arXiv:astro-ph/0407244v1.

[45] T. Bergmann, R. Engel, D. Heck, N. N. Kalmykov, S. Ostapchenko, T. Pierog, T. Thouw, and K. Werner. One-dimensional hybrid approach to extensive air shower simulation. *Astropart. Phys.*, 26:420–432, 2007. arXiv:astro-ph/0606564v1.

[46] Lars Bergström and Ariel Goobar. *Cosmology and Particle Astrophysics*. Springer, 2 edition, 2006.

[47] P. Bhattacharjee and G. Sigl. Origin and propagation of extremely high energy cosmic rays. *Phys. Rept.*, 327:109–247, 2000. arXiv:astro-ph/9811011v2.

[48] P. L. Biermann. In *Proceedings of the* 23^{th} *International Cosmic Ray Conference*, volume Rapporteur, page 45, Calgary, Canada, 1993.

[49] P. L. Biermann. The origin of the highest energy cosmic rays. *J. Phys. G*, 23:1–27, 1997.

[50] D. J. Bird et al. The Cosmic-Ray Energy Spectrum Observed by the Fly's Eye. *Astrophys. J.*, 424:491–502, March 1994.

[51] D. J. Bird et al. *Astrophys. J.*, 441:144, 1995.

[52] D. J. Bird et al. Study of Broad Scale Anisotropy of Cosmic Ray Arrival Direction from 2×10^{17} to 10^{20} ev from Fly's Eye Data. *Astrophys. J.*, 511:739–749, February 1999. arXiv:astro-ph/9806096v1.

[53] J. D. Bjorken and E. A. Paschos. Inelastic electron-proton and γ-proton scattering and the structure of the nucleon. *Phys. Rev.*, 185(5):1975–1982, 1969.

[54] P. M. S. Blackett and G. P. S. Occhialini. Some photographs of the tracks of penetrating radiation. *Proc. Roy. Soc.*, A139:699, 1933.

[55] G. R. Blumenthal. Energy Loss of High-Energy Cosmic Rays in Pair-Producing Collisions with Ambient Photons. *Phys. Rev. D*, 1(6):1596–1602, 1970.

[56] G. Bossard, H. J. Drescher, N. N. Kalmykov, S. Ostapchenko, A. I. Pavlov, T. Pierog, E. A. Vishnevskaya, and K. Werner. Cosmic Ray Air Shower Characteristics in the Framework of the Parton-Based Gribov-Regge Model NEXUS. *Phys. Rev.*, D63:054030, 2001. arXiv:hep-ph/0009119v1.

[57] A. J. Bunker et al. The star formation rate of the Universe at z $\approx$ 6 from the Hubble Ultra-Deep Field. *Mon. Not. R. Astron. Soc.*, 355(2):374–384, 2004.

[58] A. N. Bunner. *Cosmic Ray Detection by Atmospheric Fluorescence*. PhD thesis, Cornell University, 1967.

[59] S.M. Carroll, W.H. Press, and E.L. Turner. The cosmological constant. *Ann. Rev. Astron. Astrophys.*, 30:499, 1992.

[60] G. L. Cassiday. Observatory for Ultra High-Energy Processes: The Fly's Eye. *Ann. Rev. Nucl. Part. Sci.*, 35:321–349, December 1985.

[61] G. Clark and L. W. Brown J. K. Alexander. Spectrum of the Extra-galactic Background Radiation at Low Radio Frequencies. *Nature*, 228(28):847–849, 1970.

[62] G. Clark et al. An Experiment on Air Showers Produced by High Energy Cosmic Rays. *Nature*, 180:353, 1957.

[63] J. Clay. *Proc. Roy. Acad. of Amsterdam*, 30:1115, 1927.

[64] G. Cocconi, A. Loverdo, and V. Tongiorgi. Penetrating Particles in Air Showers. *Phys. Rev.*, 70:852–854, 1946.

[65] A. H. Compton. A Geographic Study of Cosmic Rays. *Phys. Rev.*, 43:387, 1933.

[66] The Auger Cpllaboration. Pierre Auger project design report, 2nd editions. Technical report, March 1997. http://www-f9.ijs.si/auger/private/DesignReport/.

[67] The Pierre Auger Cpllaboration. Correlation of the highest-energy cosmic rays with nearby extragalactic objects. *Science*, 318(5852):938–943, 2007. arXiv:0711.2256v1.

[68] J. W. Cronin. Cosmic Rays: The most energetic particles in the universe. *Rev. Mod. Phys.*, 71:S165–S172, 1999.

[69] J. W. Cronin, T.K. Gaisser, and S.P. Swordy. Cosmic rays at the energy frontier. *Scientific American*, 276(1):32–37, 1997.

[70] J. Daudin. *Ann. de Phys.*, 20:563, 1945.

[71] W. Deng. *A HiRes Limit of the Flux of the Cosmic Neutrinos*. PhD thesis, University of Utah, 2007.

[72] M. Dobbs and J. B. Hansen. The HepMC C++ Monte Carlo event record for High Energy Physics. *Computer Physics Communications*, 134(1):41–46, February 2001.

[73] S. L. Dubovsky and P. G. Tinyakov. Galactic anisotropy of ultra-high energy cosmic rays produced by CDM-related mechanisms. *Phys. Rev. Lett.*, 79:4302, 1997.

[74] A. Dziewonski. *The Encyclopedia of Solid Earth Geophysics*. Springer, New York, USA, 1989.

[75] D. Fargion, B. Mele, and A. Salis. Ultrahigh energy neutrino scattering onto relic light neutrinos in galactic halo as a possible source of highest energy extragalactic cosmic rays. *Astrophys. J.*, 517:725–733, 1999. arXiv:astro-ph/9710029v2.

[76] E. Fermi. On the Origin of the Cosmic Radiation. *Phys. Rev.*, 75(8):1169–1174, 1949.

[77] R.S. Fletcher, T.K. Gaisser, P. Lipari, and T. Stanev. SIBYLL: An Event Generator for Simulation of high energy cosmic ray cascades. *Phys. Rev. D*, 5:5710–5731, 1994.

[78] A. Franceschini, H. Aussel, C. J. Cesarsky, D. Elbaz, and D. Fadda. *Astron. Astrophys.*, 378:1, 2001.

[79] A. Friedman. *Ü*ber die krümmung des raumes. *Zeitschrift für Physik A*, 10:337–386, 1922.

[80] A. Friedman. *Ü*ber die möglichkeit einer welt mit konstanter negativer krümmung des raumes. *Zeitschrift für Physik A*, 21:326–332, 1924.

[81] T. K. Gaisser. *Cosmic Rays and Particle Physics*. Cambridge Univ. Press, 1990.

[82] T. K. Gaisser and A. M. Hillas. In *Proceedings of the* 15^{th} *International Cosmic Ray Conference*, volume 8, page 353, Plovdiv, Bulgaria, 1977.

[83] R. Gandhi, C. Quigg, M. H. Reno, and I. Sarcevic. Ultrahigh-energy neutrino interactions. *Astropart. Phys.*, 5:81–110, 1996. arXiv:hep-ph/9512364v1.

[84] R. Gandhi, C. Quigg, M. H. Reno, and I. Sarcevic. Neutrino interactions at ultrahigh energies. *Phys. Rev. D*, 58:093009, 1998.

[85] Robert D. Cousins Gary J. Feldman. A unified approach to the classical statistical analysis of small signals. *Phys. Rev. D*, 57(7):3873–3889, 1998. arXiv:physics/9711021v2.

[86] A. Gazizov and M. P. Kowalski. ANIS: High Energy Neutrino Generator for Neutrino Telescopes. *Comput. Phys. Commun.*, 172:203–213, 2005. arXiv:astro-ph/0406439v1.

[87] A. Z. Gazizov and S. I. Yanush. *Phys. Rev. D*, 39:941, 2002.

[88] Neil Gehrelsa and Peter Michelsonb. GLAST: the next-generation high energy gamma-ray astronomy mission. *Astropart. Phys.*, 11(1-2):277–282, 1999.

[89] R. J. Gould and G. P. Schreder. *Phys. Rev.*, 155:5, 1967.

[90] K. Greisen. The Extensive Air Showers. *Progress in Elementary Particle and Cosmic Ray Physics*, 1:1–141, 1956.

[91] K. Greisen. Cosmic Ray Showers. *Ann. Rev. Nucl. Part. Sci.*, 10:63, 1960.

[92] K. Greisen. End to the Cosmic-Ray Spectrum? *Phys. Rev. Lett.*, 16(17):748–750, 1966.

[93] Grigorov et al. In *Proceedings of the* 12^{th} *International Cosmic Ray Conference*, volume 5, page 1746, Hobart, 1971.

[94] D. Harari, S. Mollerach, E. Roulet, and F. Sanchez. Lensing of ultra-high energy cosmic rays in turbulent magnetic elds. *JHEP*, 0203:45, 2002. arXiv:astro-ph/0202362v2.

[95] N. Hayashida et al. *J. Phys. G: Nucl. Part. Phys.*, 21:1101, 1995.

[96] N. Hayashida et al. Possible Clustering of the Most Energetic Cosmic Rays within a Limited Space Angle Observed by the Akeno Giant Air Shower Array. *Phys. Rev. Lett.*, 77(6):1000–1003, 1996.

[97] N. Hayashida et al. The anisotropy of cosmic ray arrival direction around 10^{18} eV. In M. Salamon D. Kieda and B. Dingus, editors, *Proceedings of the* 26^{th} *International Cosmic Ray Conference*, volume 3, page 256, Salt Lake City, Utah, USA, August 1999.

[98] D. Heck, G. Schatz, T. Thouw, J. Knapp, and J. N. Capdevielle. CORSIKA: A Monte Carlo Code to Simulate Extensive Air Showers. Technical Report FZKA 6019, Forschungszentrum Karlsruhe, 1998.

[99] W. Heitler. *Quantum Theory of Radiation, 2nd Edition.* Oxford University Press, Oxford, 1994.

[100] V. F. Hess. Observation of Penetrating Radiation in Seven Balloon Flights. *Phys. Zeitschr*, 13:1084, 1912.

[101] C. T. Hill and D. N. Schramm. *Phys. Rev. D*, 31:5648, 1985.

[102] A. M. Hillas. *Cosmic Rays*. Pergamon Press, Oxford, 1972.

[103] A. M. Hillas. In *Proceedings of the* 16^{th} *International Cosmic Ray Conference*, volume 8, page 7, Kyoto, Japan, 1979.

[104] A. M. Hillas. In *Proceedings of the* 17^{th} *International Cosmic Ray Conference*, volume 13, page 69, Paris, France, 1981.

[105] A. M. Hillas. The origin of ultra-high energy cosmic rays. *Ann. Rev. Astron. Astrophys.*, 22:425–444, 1984.

[106] G. Hinshaw et al. Five-Year Wilkinson Microwave Anisotropy Probe (WMAP) Observations: Data Processing, Sky Maps, and Basic Results. *Astrophysical Journal Supplement Series*, 180:225–245, 2009. arXiv:0803.0732v2.

[107] Edwin Hubble. A relation between distance and radial velocity among extra-galactic nebulae. In *Proceedings of the National Academy of Sciences of the United States of America*, volume 15, pages 168–173, 1929.

[108] J. D. Jackson. *Classical Electrodynamics*. John Wiley & Sons, New York, USA, 2 edition, 1975.

[109] S. Jadach, Z. Ws, R. Decker, and J. H. Kühn. The τ decay library TAUOLA, version 2.4. *Computer Physics Communications*, 76(3):361–380, August 1993.

[110] J. M. Jauch and F. Rohrlich. *The Theory of Photons and Electrons*. Springer-Verlag, New York, USA, 2 edition, 1980.

[111] J. R. Jokipii and G. E. Morfil. *Astrophys. J.*, 190, 1985.

[112] A. S. Jursa. *Handbook of Geophysics and the Space Environment*. Air Force Geophysics Laboratory, 4 edition, 1985.

[113] F. Kakimoto, E.C. Loh, M. Nagano, H. Okuno, M. Teshima, and S. Ueno. A measurement of the air fluorescence yield. *Nuclear Instruments and Methods in Physics Research A*, 372:527–533, 1996.

[114] N. N. Kalmykov and S. S. Ostapchenko. *Physics of Atomic Nuclei*, 56(3):346, 1993.

[115] N. N. Kalmykov, S. S. Ostapchenko, and A. I. Pavlov. Quark-gluon string model and EAS simulation problems at ultra-high energies. *Nucl. Phys. Proc. Suppl.*, 52B:17, 1997.

[116] N.N. Kalmykov et al. *Physics of Atomic Nuclei*, 58:1728, 1995.

[117] K. Kamata and J. Nishimura. *Prog. Theor. Phys. Suppl.*, 6:93, 1958.

[118] M. F. Kaplon, B. Peters, and H. L. Bradt. Evidence for multiple meson and γ-ray production in cosmic-ray stars. *Phys. Rev.*, 76:1735, 1949.

[119] U. F. Katz and ANTARES Collaboration. Status of the ANTARES Project. *Eur. Phys. J.*, C33:S971–S974, 2004. arXiv:astro-ph/0310736v1.

[120] Rainer Kayser, Phillips Helbig, and Thomas Schramm. A general and practical method for calculating cosmological distances. *Astron. Astrophys.*, 318:680–686, 1997.

[121] T. W. Kibble. Topology of cosmic domains and strings. *J. Phys. A*, 9:1387, 1976.

[122] Knop et al. New constraints on ω_m, ω_Λ, and w from an independent set of eleven high-redshift supernovae observed with hst. *Astrophys. J.*, 598:102, 2003. arXiv:astro-ph/0309368v1.

[123] W. Kolhörster, A. A. Ivanov, V. A. Kolosov, A. D. Krasilnikov, K. N. Makarov, et al. Anisotropy of Intensity of Cosmic Rays with $E_0 > 10^{17}$ eV. In *Proceedings of the* 18^{th} *International Cosmic Ray Conference*, volume 2, pages 145–148, Bangalore, India, 1983.

[124] I. Kravchenko et al. RICE limits on the diffuse ultrahigh energy neutrino flux. *Phys. Rev. D*, 73(8):082002, 2006.

[125] P. O. Lagage and C. J. Cesarsky. The maximum energy of cosmic rays accelerated by supernova shocks. *Astron. Astrophys.*, 125:249, 1983.

[126] H. L. Lai, J. Huston, S. Kuhlmann, J. Morfin, F. Olness, J. F. Owens, J. Pumplin, and W. K. Tung. Global QCD Analysis of Parton Structure of the Nucleon: CTEQ5 Parton Distributions. *Eur. Phys. J*, C12:375–392, 2000. arXiv:hep-ph/9903282v3.

[127] L. D. Landau and I. J. Pomeranchuk. *Dok. Akad. Nauk. SSSR*, 92:535, 1953.

[128] K. R. Lang. *Astrophysical Formulae, 3rd Edition.* Springer, 2006.

[129] Lawrence, Reid, and Watson. *J. Phys. G.*, 17:733, 1991.

[130] J. G. Learned and K. Mannheim. High-Energy Neutrino Astrophysics. *Ann. Rev. Nucl. Part. Sci.*, 50(1):679–749, 2000.

[131] S. Lee. Propagation of extragalactic high energy cosmic and γ rays. *Phys. Rev. D*, 58(4):043004, 1998.

[132] S. Lee et al. Extragalactic Magnetic Field and the Highest Energy Cosmic Rays. *Astrophys. J.*, 455:L21–L24, 1995. arXiv:astro-ph/9508088v2.

[133] D. R. Lide, editor. *Handbook of Chemistry and Physics.* CRC Press, Boca Raton, Florida, USA, 75 edition, 1994.

[134] J. Linsley. Evidence for a primary cosmic-ray particle with energy $10^{20}eV$. *Phys. Rev. Lett.*, 10:146–148, 1963.

[135] J. Linsley. Primary cosmic rays of energy 10^{17} to 10^{20} eV; the energy spectrum and arrival direction. In *Proceedings of the* 8^{th} *International Cosmic Ray Conference*, volume 4, pages 77–79, Jaipur, 1964.

[136] J. Linsley, L. Scarsi, and B. Rossi. Energy spectrum and structure of large air showers. *J. Phys. Soc. Japan*, 17(suppl. A-III):91–102, 1962.

[137] M. S. Longair. *High Energy Astrophysics, 2nd Edition.* Cambridge University Press, Cambridge, England, 1997.

[138] P. Madau et al. *Mon. Not. R. Astron. Soc.*, 238:1388, 1996.

[139] A. B. Migdal. Bremsstrahlung and Pair Production in Condensed Media at High Energies. *Phys. Rev.*, 103(6):1811–1820, 1956.

[140] R. A. Millikan and G. H. Cameron. The origin of the cosmic rays. *Phys. Rev.*, 32:522, 1928.

[141] M. Nagano et al. *J. Phys. G*, 10:1295, 1984.

[142] M. Nagano et al. *J. Phys. G*, 18:423, 1992.

[143] S. H. Neddermeyer and C. D. Anderson. Note on the nature of cosmic-ray particles. *Phys. Rev.*, 51:884, 1937.

[144] W. R. Nelson, H. Hirayama, and D. W. O. Rogers. The EGS4 code system. Technical report, SLAC Report 265, Stanford Linear Accelerator Center, Stanford, California, March 1985. http://www-f9.ijs.si/auger/private/DesignReport/.

[145] S. I. Nikolsky. *Nucl. Phys. B, Proc. Suppl.*, 36A:228, 1995.

[146] J. F. Ormes and J. Protheroe. *Astrophys. J.*, 272:757, 1983.

[147] A. A. Penzias and R. W. Wilson. A measurement of excess antenna temperature at 4080 mc/s. *Astrophys. J.*, 142, 1965.

[148] P. G. Perez-Gonzalez et al. Spitzer view on the evolution of star-forming galaxies from z =0 to z∼3. *Astrophys. J.*, 630:82–107, 2005. arXiv:astro-ph/0505101v1.

[149] D. H. Perkins. Nuclear disintegration by meson capture. *Nature*, 159:126, 1947.

[150] W. H. Press, S. A. Teukolsky, W. T. Vetterling, and B. P. Flannery. *Numerical recipes: the art of scientific computing.* Cambridge University Press, Cambridge, 3 edition, 2007.

[151] J. R. Primack, J. S. Bullock, and R. S. Somerville. Observational Gamma-ray Cosmology. *AIP Conf. Proc.*, 745:23, 2001. arXiv:astro-ph/0502177v1.

[152] R .J. Protheroe and P. L. Biermann. A new estimate of the extragalactic radio background and implications for ultra-high-energy gamma-ray propagation. *Astropart. Phys.*, 6:45–54, 1996. arXiv:astro-ph/9605119v1.

[153] J. L. Puget, F. W. Stecker, and J. H. Bredekamp. *Astrophys. J.*, 205:638, 1976.

[154] J. P. Rachen and P. L. Biermann. *Astron. Astrophys.*, 272:161, 1993.

[155] J. Ranft. Dual parton model at cosmic ray energies. *Phys. Rev. D*, 51:64–84, 1995.

[156] K. Reil. *The Energy Spectrum of Ultra High Energy Cosmic Rays Measured by the High Resolution Fly's Eye Detector.* PhD thesis, University of Utah, 2002.

[157] H. P. Robertson. Kinematics and world-structure. *Astron. Astrophys.*, 82:284–301, 1935.

[158] H. P. Robertson. Kinematics and world-structure ii. *Astron. Astrophys.*, 83:187–201, 1936.

[159] H. P. Robertson. Kinematics and world-structure iii. *Astron. Astrophys.*, 83(4):257–271, 1936.

[160] S. Roesler, R. Engel, and J. Ranft. DPMJET-III, a hadronic interaction model for cascade simulations. In *Proceedings of the* 27^{th} *International Cosmic Ray Conference*, volume IUPAP, page 439, Hamburg, Germany, 2001.

[161] B. Rossi. Cosmic rays. pages 8–12, 1964.

[162] B. Rossi and K. Greisen. *Rev. Mod. Phys.*, 13:240, 1941.

[163] M. Roth et al. Measurement of the UHECR energy spectrum using data from the surface detectors of the Pierre Auger observatory. In *Proceedings of the* 30^{th} *International Cosmic Ray Conference*, Merida, 2007. arXiv:0706.2096v1.

[164] S. J. Sciutto. AIRES: A system for air shower simulations (Version 2.2.0). arXiv:astro-ph/9911331v1.

[165] D. Semikoz and G. Sigl. Ultra-High Energy Neutrino Fluxes: New Constraints and Implications. *JCAP*, 0404:003, 2004. arXiv:hep-ph/0309328v1.

[166] Seo et al. *Astrophys. J.*, 378:763, 1991.

[167] G. Sigl, S. lee, and P. Coppi. Highest Energy Cosmic Rays, Grand Unified Theories, and the Diffuse Gamma-Ray Background. *Phys. Rev. Lett.*, 1996. arXiv:astro-ph/9604093v2.

[168] J. A. Simpson. Elemental and isotopic composition of the galactic cosmic rays. *Ann. Rev. Nucl. Part. Sci.*, 33:323–381, 1983.

[169] K. M. Simpson. *Studies of Cosmic Ray Composition using a Hybrid Fluorescence Detector*. PhD thesis, University of Adelaide, 2001.

[170] D. V. Skobelzyn. A new type of very fast beta rays. *Z. Phys.*, 54:686, 1929.

[171] P. Sokolsky. *Introduction to Ultrahigh Energy Cosmic Ray Physics*. Addison Wesley, New York, 1989.

[172] D. N. Spergel et al. First-Year Wilkinson Microwave Anisotropy Probe (WMAP) Observations: Determination of Cosmological Parameters. *Astrophysical Journal Supplement Series*, 148:175–194, 2003.

[173] P. Sreekumar et al. EGRET observations of the extragalactic gamma ray emission. *Astrophys. J.*, 494:523–534, 1998. arXiv:astro-ph/9709257v1.

[174] T. Stanev. Arrival Directions of the Most Energetic Cosmic Rays. *Phys. Rev. Lett.*, 75(17):3056–3059,, 1995.

[175] T. Stanev. Ultra High Energy Cosmic Rays. *ECONF*, C040802:L020,, 2004.

[176] T. Stanev* and D. De Marco. Cosmogenic neutrinos from cosmic ray interactions with extragalactic infrared photons. *Phys. Rev. D*, 73:043003 ,, 2006.

[177] B. T. Stokes. *A Search for Anisotropy in the Arrival Directions of Ultra High Energy Cosmic Rays Observed by the High Resolution Fly's Eye Detector*. PhD thesis, University of Utah, 2006.

[178] M. Takeda et al. *JETT Lett. Pisma Zh. Eksp. Teor. Fiz.*, 81:1163–1166, 1998.

[179] Diego F. Torres and Luis A. Anchordoqui. Astrophysical origins of ultrahigh energy cosmic rays. *Rept. Prog. Phys.*, 67:16631730, 2004.

[180] A. G. Walker. On milne's theory of world-structure. *Proc. London Math. Soc.*, s2-42:90–127, 1937.

[181] K. Werner. *Phys. Rep.*, 232:87, 1993.

[182] L. R. Wiencke, , et al. In *Proceedings of the* 27^{th} *International Cosmic Ray Conference*, pages 635–638, Hamburg, Germany, 2001.

[183] L. R. Wiencke, , et al. In *Proceedings of the* 28^{th} *International Cosmic Ray Conference*, Trukuba, Japan, 2003.

[184] C. R. Wilkinson. *The Application of High Precision Timing in the High Resolution Flys Eye Cosmic Ray Detector*. PhD thesis, University of Adelaide, 1998.

[185] T. Wulf. *Phys. Z*, 11:811, 1910.

[186] S. Yoshida, , et al. A search for horizontal air showers induced by extremely high energy cosmic neutrinos observed by Akeno Giant Air Shower Array. In *Proceedings of the* 27^{th} *International Cosmic Ray Conference*, pages 1142–1145, Hamburg, Germany, 2001.

[187] S. Yoshida and H. Dai. The extremely high energy cosmic rays. *J. Phys. G: Nucl. Part. Phys.*, 24:905938, 1998.

[188] S. Yoshida et al. Charged particles in giant air showers above 1eev. *J. Phys.*, G20:651, 1994.

[189] S. Yoshida, G. Sigl, and S. lee. Extremely High Energy Neutrinos, Neutrino Hot Dark Matter, and the Highest Energy Cosmic Rays. *Phys. Rev. Lett.*, 81:5505, 1998.

[190] S. Yoshida and M. Teshima. Prog. theor. phys. *Energy Spectrum of Ultra-high Energy Cosmic Rays with Extra-Galactic Origin*, 88:833, 1993.

[191] H. Yukawa. On the interaction of elementary particles. *Proc. Phys. Math. Soc.*, 17:48, 1935.

[192] G. T. Zatsepin and V. A. Kuzmin. Upper limit of the spectrum of cosmic rays. *Sov. Phys. JETP Lett. (Engl. Transl.)*, 4:78–80, 1966.

[193] A. Zech. Testing the HiRes detector simulation against UHECR data. In *Proceedings of the* 28^{th} *International Cosmic Ray Conference*, Trukuba, Japan, 2003.

[194] A. Zech. *A Measurement of the Ultra-High Energy Cosmic Ray Flux with the HiRes FADC Detector*. PhD thesis, Rutgers University, 2004.

[195] Fodor Zoltan, Sandor D. Katz, and Andreas Ringwald. *J. High Energy Phys.*, 6:46, 2002.